Acoustic interference fields in the ocean

Thesis

ACOUSTIC INTERFERENCE FIELDS IN THE OCEAN

Burton G. Hurdle
February 1988

Naval Research Laboratory
Washington, D.C.

ACOUSTIC INTERFERENCE FIELDS IN THE OCEAN

Thesis Submitted By
Burton G. Hurdle BS MS
for the degree of
Doctor of Philosophy
February 1988

Department of Engineering Mechanics
Faculty of Technology
Open University
Milton Keynes
England.

ABSTRACT

Two areas of underwater acoustics are investigated: ocean-bottom scattering and acoustic fields in geometrically dispersive sound channels. The purpose is to describe and provide an understanding of the physical mechanisms in these two areas by comparing analyzed results from ocean experiments with theoretical computations.

Experiments using directive 19.5-kHz transducers illustrate temporal and spacial behavior of signals scattered from the ocean bottom. The signals fluctuate, as a function of acoustic geometry, in linear relation to source and receiver motion and to signal frequency. Spacial structure of the acoustic field depends on frequency and acoustic geometry and is independent of motion and bottom roughness. Data supporting these observations are included as well as data showing the effects of bottom type on the scattered returns, that is, the existence of subbottom returns in some data. Volume-scattering-strength profiles are also provided from data obtained in these experiments.

Continuous-wave (CW) and impulsive sources covering frequencies 5 to 260 Hz were towed and deployed respectively over ranges up to 3000 km, with reception on fixed hydrophones. Analyses of measured propagation losses of these low-frequency acoustic signals in the dispersive channel provide insights into the nature of the propagation and the acoustic channel. Both the CW signals and the arrivals of the impulsive signals are analyzed in terms of transmission loss, convergence-zone structure, source-motion effects, interference structure, and channel characteristics. The systematic variation (internal tides) of the medium and its influence on the interference field are discussed. The state of modeling, both simple and complicated, is reviewed and compared with results of the ocean experiments. Relationships are provided between this work and the broader field of underwater acoustics. Suggested areas for future research are made.

PREFACE

Experimental underwater acoustic research in the ocean environment has a particular fascination for its practitioners. In many ways this research is similar to geophysical research in the ocean environment. Its conduct requires a team of scientists and technicians living and working, usually around the clock, on special ships, submarines, aircraft, and other unique platforms. An experiment with multiple ships and fixed receivers, covering thousands of kilometers, requires tight coordination of all its far-flung components and tight communications. The team is always at the mercy of the weather and must have a flexible agenda, even to riding out a storm for several days. Also, ships have been known to have casualties, causing changes in plans. However, although conducting the experiment has fascination, the greatest reward is in successfully completing an analysis that illuminates a physical mechanism or explains a previously perceived anomaly.

In an experiment of this type three major classes of data must be monitored and recorded. Obviously the acoustic data are of prime importance. Of almost equal significance, however, is the geometry, including the navigation, the relative positions of all acoustic components, and the properties of the experiment's environment. Preplanning analysis and simulation provides strong guidance in structuring the experiment, in determining what data are required, and in selecting the form for recording the data. The data set must be as complete as possible. Ocean acousticians do not have the luxury of repeating an experiment the next day in the laboratory. They cannot repeat the experiment for months or even years.

One objective in this work is to demonstrate the nature of acoustic interference fields in space and time for two relatively different areas of underwater acoustics: scattering from the bottom and propagation in the ocean's dispersive sound channels. A further objective is a physical interpretation of the various mechanisms encountered. This work is an attempt to consolidate the information in each of the two areas and to show the interaction between them. Also important is to see where they fit into the broader context of underwater acoustics.

This work begins with a discussion of acoustic monostatic scattering from the ocean bottom at a frequency around 20 kHz. An analysis provides a detailed description of the fluctuation in the received scattered signal. This description includes the influence of the source and receiver velocities and the acoustic geometry on the form and fluctuation rate of the received signals. Also described is the configuration of the acoustic field in the medium and how the field's form and dynamics depend on the same velocities of source and receiver and on the acoustic geometry. In the discussion the temporal form of the received signal is compared with a model based on a conical beam geometry for a broad range of grazing angles and transmitted pulse lengths. Both the fluctuation and the field characteristics are compared to simple physical theory. Following the discussion is an analysis of the statistics of the monostatic returns, employing probability density functions.

The work continues with a discussion extended to bistatic scattering of energy in the half-space above the ocean bottom. Analyzed and compared are two experiments that are from different ocean environments and have significantly different results. The reasons for the differences are discussed. The acoustic power scattered into the upper half-space is computed and compared to the power incident on the boundary.

The work presents measurements of the scattered returns from the ocean volume as a function of depth, depression angle, and pulse length. The isotropy of the scattering is tested. Scattering-strength profiles are obtained for two ocean areas as a function of the diurnal/nocturnal cycle.

The work continues next with a discussion of the nature of low-frequency propagation of CW and impulsive acoustic energy in a geometrically dispersive channel, the deep sound channel of the oceans. The sound fields, with particular emphasis on the interference nature of the fields, are described in both space and time. The dynamics of moving fields including the resulting effects on the received signals is analyzed. Further, statistics of measured fluctuations are compared with statistics from mathematical simulations, and good agreement is found. A model is developed for predicting the statistical variations of low-frequency signals propagated over long ranges in an ocean channel.

Propagation models are employed to simulate the behavior of the interference fields and the resulting received signals for periodic variations of the sound-speed profile. Simulations are also made of the spacial behavior of the fields.

Also provided is a summary of the research contained in this work, a discussion of the relation of this research to applied needs, and a number of suggestions for future research.

The work includes a description of the instrumentation, procedures, and environmental-data computations of the experiments in ocean acoustic scattering. This description ends the work, as an appendix.

Underwater acoustic research not only has fascination for its practitioners and for theorists in developing new models from its results but also has importance for practical applications in both passive and active acoustic systems for both commercial and military uses and for the furthering of our knowledge of ocean characteristics. For example, reverberation, the scattering of acoustic energy from the bottom, surface, and volume of the ocean, provides the principal interfering background in all active sonar systems. Further, when a low-frequency active system is operated in a dispersive channel, the propagation in the channel combines with the scattering from the boundaries and produces a complicated signal-to-background situation. Therefore a complete understanding of the interactions for a particular design and use of an acoustic system in a given environment is vitally important.

CONTENTS

Chapter 1

TEMPORAL AND SPACIAL STRUCTURE OF SIGNALS SCATTERED FROM THE OCEAN BOTTOM*

INTRODUCTION

In a geophysical environment such as the ocean, fluctuation is one of the dominating characteristics of acoustic signals. It is generally conceded that the major cause of fluctuation can be attributed to motion of one or more of the following: source, receiver, boundary, or medium. One of the mechanisms that is well-understood and has been experimentally verified is the image or Lloyd-mirror effect. (This is the simplest interference mechanism to be found in underwater acoustics. It results from the interference ot two paths from the source to a receiver that is moving in or out in range. One path is a direct path from source to receiver, with the second path being specularly reflected from the surface. Lloyd-mirror interference will be discussed further in Chapter 7 in the section on interference and fluctuation. It is also discussed by Wood (1960).) However, many situations are experienced in which the cause of the fluctuation is not adequately understood. One such situation is discussed in this chapter.

TEMPORAL FLUCTUATION OF BOTTOM-SCATTERED SIGNALS

An investigation has been made of the time fluctuations of acoustic signals scattered from the ocean bottom when transmission and reception are made from a moving platform. The geometry of the experiment is illustrated in Fig. 1 and consists of an acoustic beam that can be directed toward the sea bottom at any chosen angle of azimuth and tilt in the half-space below the sea surface.

An experimental pulsed sonar operating at 19.5 kHz was used. Special features of this sonar included a plane piston transducer, stabilized in pitch and roll, and a streamlined dome

*Some of this material was presented earlier (Hurdle and Ferris, 1962, Hurdle et al. 1964, and Hurdle, 1966a, 1966b).

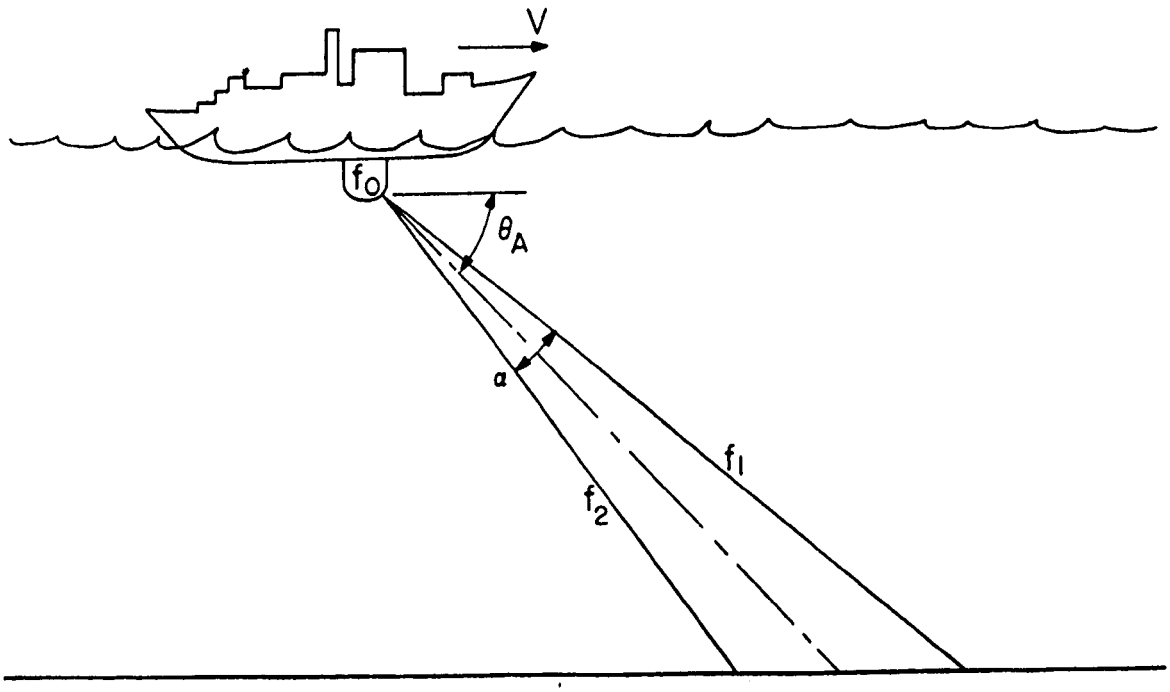

Fig. 1. Acoustic geometry employed in obtaining bottom returns.

mounted below the keel of the ship. Its beamwidth was approximately 8° at the half-power points, with all sidelobes being down 17 dB or more. Instrumentation was provided for photographic recording of the bottom-scattered signals, with features for time-base and amplitude calibration. In order to observe signal returns over a number of cycles of the fluctuation, sufficiently long pulses were required, necessitating operation in water depths such that reverberations and secondary reflections did not interfere. Pulse lengths were long relative to the projected extension in range of the insonified area. Measurements were made in water depths of 365 to 2500 m. This experiment included three types of bottom: sand; mud and sand; and sand, shell, and coral.

Details of the conduct of the experiments, the instrumentation, and the environment for this chapter and for Chapters 2, 3, 4, and 6 are contained in APPENDIX A (at the end of this work).

Figure 2 illustrates two representative samples of the echoes obtained for each of the different speeds. These are returns from a sand bottom but could just as easily represent returns from the other bottom types. The water depth was approximately 900 m. The transducer was trained in the direction of the ship's heading with a downward tilt of 60°. A transmitted

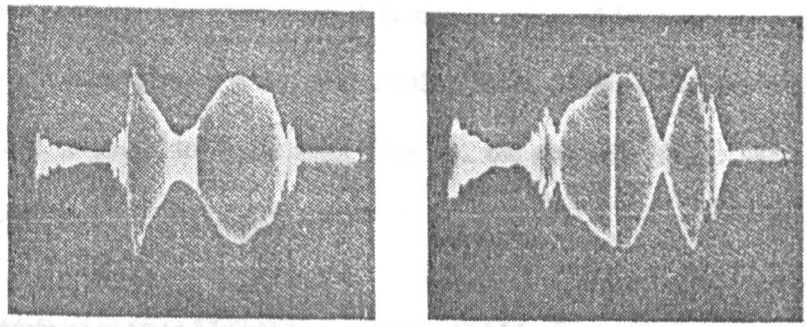

1 knot

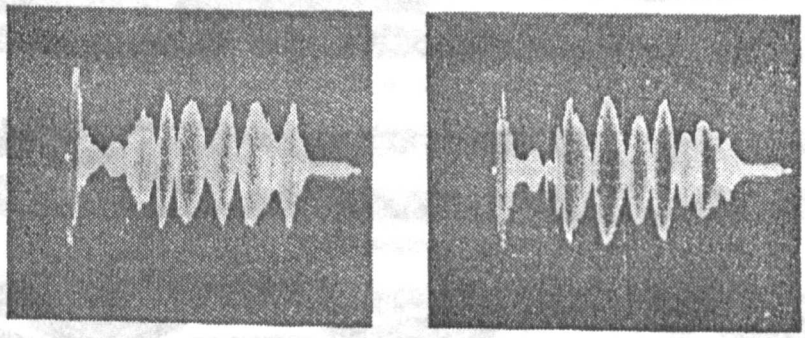

6 knots

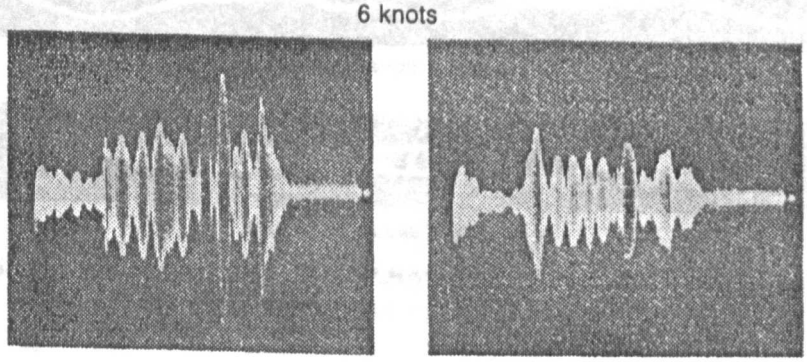

9 knots

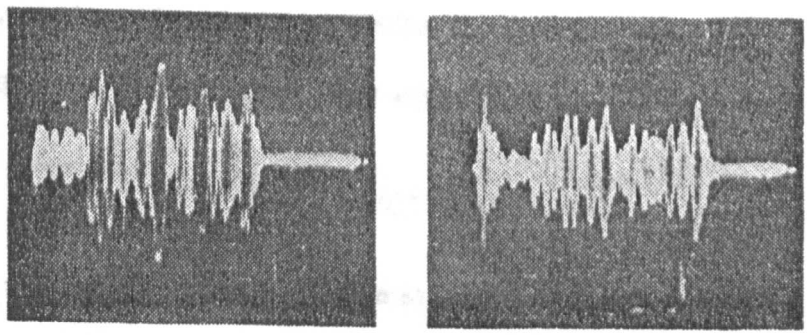

15 knots

Fig. 2. Two samples of returns from a sand bottom at a depth of 915 m. The pulse length is 1 sec, and the frequency is 19.5 kHz.

pulse length of 1 sec was used. There are two points of interest in these returns. The first is the form of the variation in the signal envelope. This form is that of a beat, characterized by the linear summation of two or more sine waves of slightly different frequencies:

$$r \sin \gamma t = a \sin \omega_1 t + b \sin \omega_2 t, \tag{1}$$

as developed in Appendix 1A. The second is the increase of beat rate as ship's speed is increased. Figure 3 illustrates sections from another series of returns in which the time scale has been expanded in order to show more detail of the envelope form, particularly at the higher ship speeds.

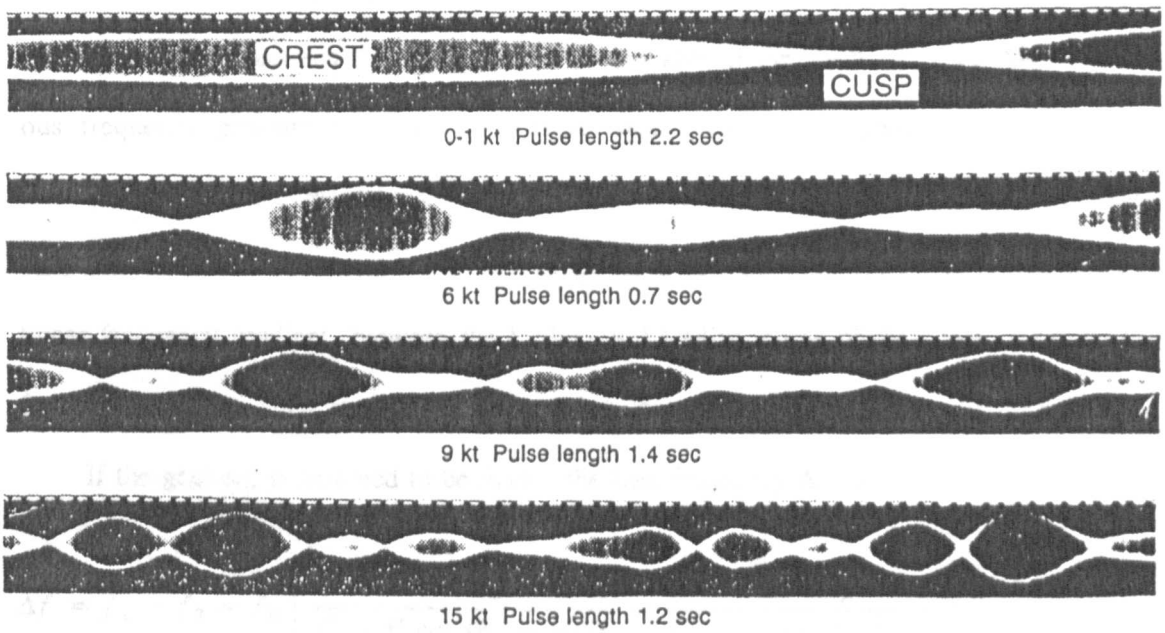

Fig. 3. Bottom returns photographically recorded such that the time scale is expanded relative to that in Fig. 2.

Let us now consider a hypothesis that predicts this type of return. When a source is in motion in a medium, the frequency observed at any point on a ray is

$$f = f_0(1 - VC^{-1} \cos \theta)^{-1},$$

where f_0 is the transmitted frequency, C is the sound speed, V is the magnitude of the velocity of the source, and θ is the angle between the velocity vector and the acoustic ray.

The signal scattered from the point of intersection of the ray and boundary arrives back at the moving source point with a frequency of

$$f_r = f_0(C + V \cos \theta)/(C - V \cos \theta). \tag{2}$$

This equation neglects the change of angle between the time of transmission and reception, and it assumes that the medium is stationary with respect to the boundary. The medium can be either isotropic or refractive, if the return path is essentially the same as the outgoing path.

Since practical acoustic beams subtend a finite angle, each of the rays contributing at the receiver will have its appropriate frequency, defined by Eq. 2. If a narrow strip or element on the boundary, between the leading and trailing edges of the beam, is examined, a continuous frequency gradient is found. For small beam angles, this gradient is approximately linear, and a constant frequency is assumed to be received from points on the boundary falling on a line normal to the element. If one integrates a constant-amplitude sine function, with a linear frequency gradient, between the leading and trailing edges of the beam, a simple beat function that is the difference between two sinusoids representing the limits is obtained.

If the gradient is assumed to be linear, the beat frequency Δf is

$$\Delta f = f_1 - f_2 = f_0 \left[\frac{C + V\cos(\theta_A - \alpha/2)}{C - V\cos(\theta_A - \alpha/2)} - \frac{C + V\cos(\theta_A + \alpha/2)}{C - V\cos(\theta_A + \alpha/2)} \right]$$

$$= \frac{2f_0 CV[\cos(\theta_A - \alpha/2) - \cos(\theta_A + \alpha/2)]}{C^2 - CV[\cos(\theta_A - \alpha/2) + \cos(\theta_A + \alpha/2)] + V^2\cos(\theta_A - \alpha/2)\cos(\theta_A + \alpha/2)}. \quad (3)$$

If the last two terms of the denominator of Eq. 3 are neglected as being small as compared to the C^2 term (resulting in an error of less than 2% for speeds up to 30 knots), Eq. 3 reduces to

$$\Delta f = 4f_0 VC^{-1} \sin(\alpha/2) \sin\theta_A . \quad (4)$$

This equation says that the frequency difference, or beat frequency, or beat rate, is directly proportional to the transmitted frequency and the ship's speed. It also varies as the sine of both the half-beamwidth angle and the angle between the beam axis and the velocity vector.

Several series of bottom returns for various ship speeds and tilt angles were recorded and analyzed for comparison with the simple model. To measure the frequency difference or

beat rate at a given speed and tilt angle, the period T of the beats was measured, by measuring the time interval between cusps of a large number of returns, similar to the returns illustrated in Fig. 3. As the experimental data show, the period of a beat varies from beat to beat. Figure 4 illustrates three of the experimental distributions, for speeds of 6.5, 10.5, and 14.5 knots. The median value of $1/T$, the median beat rate, occurs very near the peak of the distribution.

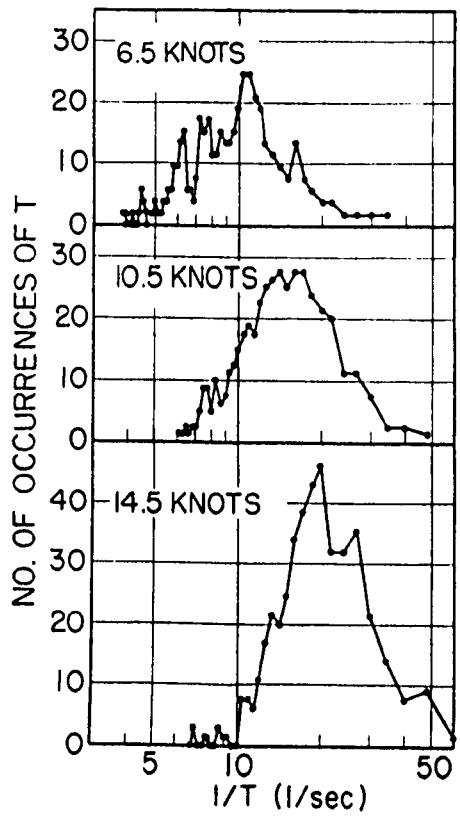

Fig. 4. Distributions of beat periods.

The median beat rates from the distributions are plotted as a function of speed in Fig. 5 and compared with computations from Eq. 4 to illustrate the linear dependency of the median beat rate or ship's speed. The lower point is elongated because of uncertainty in the speed measurement. In a similar manner the sine dependency of the tilt angle was experimentally verified when the tilt angle was varied with all other conditions held constant. Although the 90° point in tilt represents a specular condition, the behavior of the fluctuation follows the same trend as at the other angles. The effective beamwidth for these observations was found

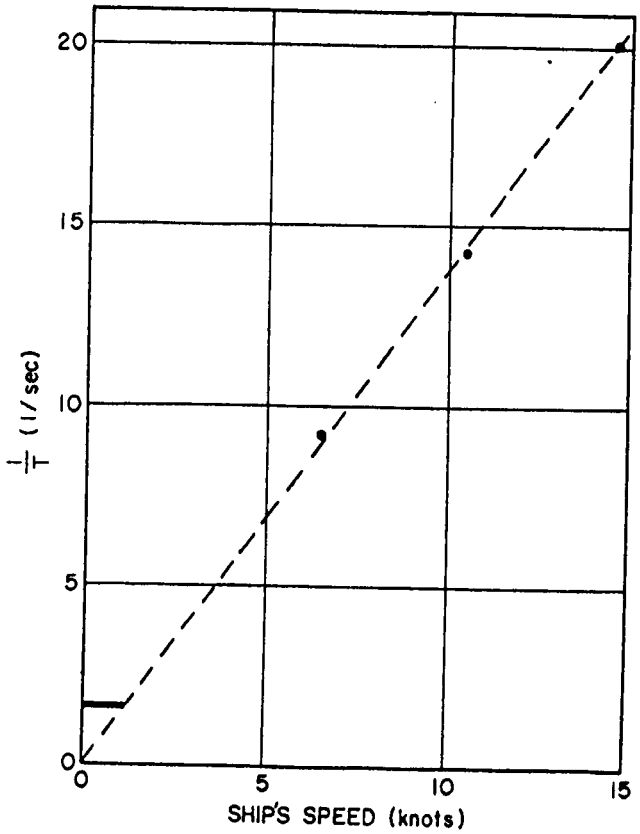

Fig. 5. Dependence of the median beat period on ship's speed. The three data points other than the elongated point are from Fig. 4, and the dashed line is from Eq. 4.

to be approximately 7°. If a beamwidth is computed from the maximum beat rate found in the distribution, the value falls within the major lobe of the transducer beam pattern.

As a further check on the hypothesis, it was postulated that the beat rate of the return signal could be controlled by adjusting the frequency gradient across the insonified area on the bottom. Since the signal arrives at various points on the bottom as a function of time, a time variation of the transmitted frequency would affect the gradient. In this chapter's Appendix B an expression is derived for the beat rate, based on a linear gradient across the beam, as a function of the rate of change of the transmitted frequency:

$$\Delta f = (A-B)f_0 + (At - Bt - A\Delta t)\delta, \tag{5}$$

where f_0 is the midfrequency of the transmitted band, t is the elapsed time in the transmitted pulse, 2nd δ is the rate of change of the transmitted frequency (df/dt) and where

$$A = [C + V \cos(\theta_A - \alpha/2)]/[C - V \cos(\theta_A - \alpha/2)],$$

$$B = [C + V \cos(\theta_A + \alpha/2)]/[C - V \cos(\theta_A + \alpha/2)],$$

and

$$\Delta t = \frac{2d}{C}\left[\frac{1}{\sin(\theta_A - \alpha/2)} - \frac{1}{\sin(\theta_A + \alpha/2)}\right]$$ is the time difference of limiting paths,

in which C is the sound speed, V is the source velocity, θ_A is the angle between the velocity vector and the beam axis, and α is the beamwidth. This expression shows that the beat rate depends linearly on the rate of change of the transmitted frequency for constant acoustic geometry and constant speed.

In Fig. 6, the solid lines illustrate the function for a ship's speed of 4 knots and two water depths: 815 and 3800 m. The points are experimental values obtained by measuring the periods of the beats from records exemplified in Fig. 7 in the same manner as described previously. Reasonable agreement is obtained between the analytical and experimental values, considering the sample size of the experimental data. The Vs near the zero beat rate indicate the value is less than shown. This condition is encountered when the beat period exceeds the pulse length. Thus, by varying the rate of change of the transmitted signal properly, the beat or fluctuation rate of the scattered returns can be controlled.

EFFECT OF PULSE LENGTH

An observation was made of the effect of pulse length on this mechanism. For this part of the experiment, pulses of 90 msec duration were produced by gating a continuously running oscillator, and the repetition rate was adjusted to approximately 4 times that for a round trip to the bottom, so that the transmitted-pulse or volume reverberations did not obscure the bottom return. Figure 8 is a photograph of a series of the 90-msec returns. The transmitted pulse and volume reverberations have been masked out. A ship speed of a fraction of a knot was used for these observations in order to have the pulse-repetition period short with respect to the beat period associated with the return of a single long-duration transmission. As can be

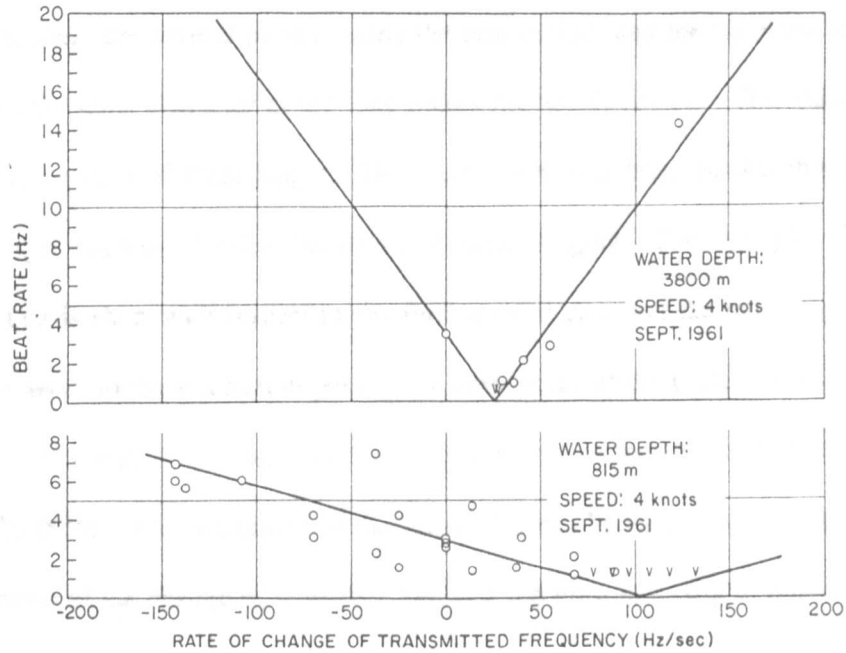

Fig. 6. Comparison of measured and computed beat rates as a function of rate of change of transmitted frequency.

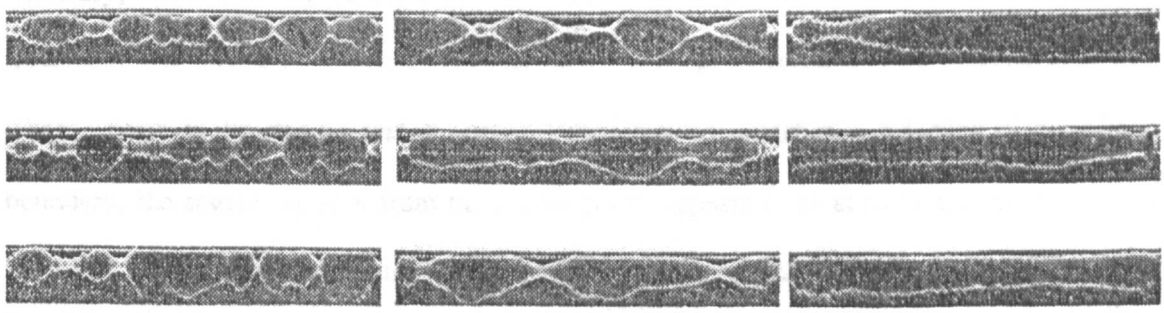

Fig. 7. Examples of the fluctuation of bottom returns (Blake Plateau area) as a function of rate of change of the transmitted frequency. The water depth is 815 m, the ship speed is 4 knots, the pulse length is 0.910 sec, and the basic frequency is 19.5 kHz.

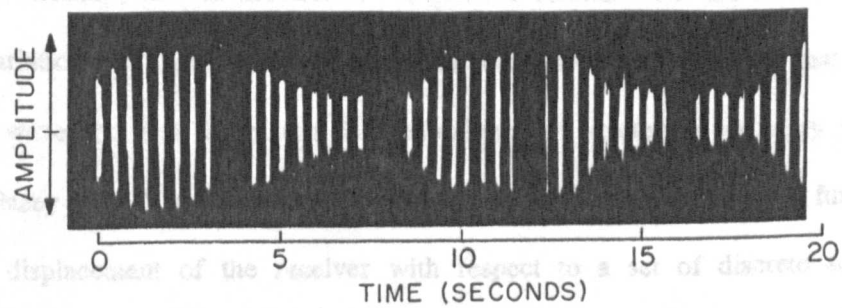

Fig. 8. Amplitude variation of short pulses with time. The pulse length is 90 msec, the water depth is 1100 m, and the tilt angle is 80°.

seen in Fig. 8, there are several pulses during the beat period, and the envelope of the composite pulses has the same character as the long pulses previously shown. This indicates that the beat rate is independent of pulse length. More important, it is believed that this demonstrates one of the major sources of echo fluctuation in echo ranging. For example, if one uses a pulse length that is short with respect to the fluctuation period and the pulse repetition period is long with respect to the fluctuation period, the amplitudes of the pulse returns would appear to be random. If the pulse is long with respect to the beat period, the beats represent fluctuation within the pulse. The magnitude of the fluctuation can be as great as 40 dB, as indicated by measurements of the change of amplitude between the crest and cusp of observed beats.

Let us examine the nature of the boundary that is required to produce this type of return. To my knowledge no one has rigorously treated the reflected field from a perfect reflecting boundary, with velocities of the source and the receiver included. In the absence of such a treatment, one has to rely on the classical image concept of reflection. This concept is that when a beam is directed so that it impinges normally on a perfectly reflecting plane infinite boundary, the source, as seen from the source point, appears to be at twice the distance to the boundary. With any part on the boundary being indistinguishable from any other part, the reflection and image points would move along uniformly with the source. Under these conditions the signal received back at the source point would have the characteristics of reception near the center of the major lobe of the beam and display negligible amplitude variation with time. Experimentally, as was illustrated, we observe returns from the bottom having large amplitude variations with time for these geometric conditions. This implies that the return is not a plane wave and that the bottom is predominantly a scattering boundary rather than a reflector. Gazey (1963) has provided an analysis of signal fluctuation as a function of the geometrical displacement of the receiver with respect to a set of discrete scatterers and scattering areas.

SPACIAL STRUCTURE OF SCATTERED FIELDS

Each of the beats of the received scattered signals illustrated in Figs. 2 and 3 can be assumed to be a lobe* of the complicated interference field. This assumption is based on the form of the envelope and on the presence of the characteristic phase shift at the amplitude cusps. Amplitudes and phases of signal portions from several echoes are compared in Fig. 9. The vertical height of each phase plot represents 360° of phase, as indicated by the arrow at the left of each plot. It can be seen that the abrupt phase shifts coincide with the deep cusps of the amplitude envelope and that the slope of the phase increases with the depth of the cusp, as expected in a beat or in passing from one lobe to another in an interference field.

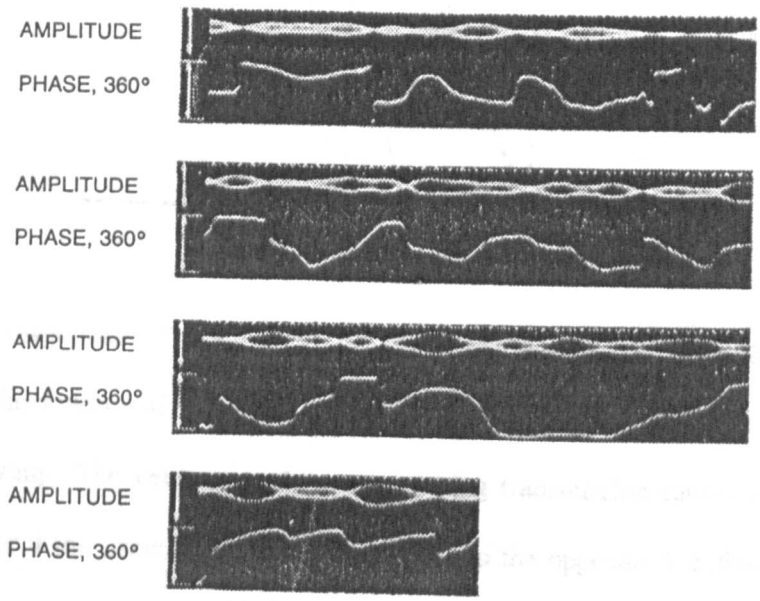

Fig. 9. Simultaneous recordings of amplitudes and phases of scattered signals.

Based on the preceding assumption, the geometry of Fig. 10 can be drawn, defining h, the horizontal distance, at the source point, between the cusps of a scattered lobe; s, the distance across the lobe normal to its direction; and ϕ, the lobe angle. Then

$$h = 2VT, \tag{6}$$

*The word *lobe* in this chapter is correct for only the far field and should be construed as *interference interval* for the near field.

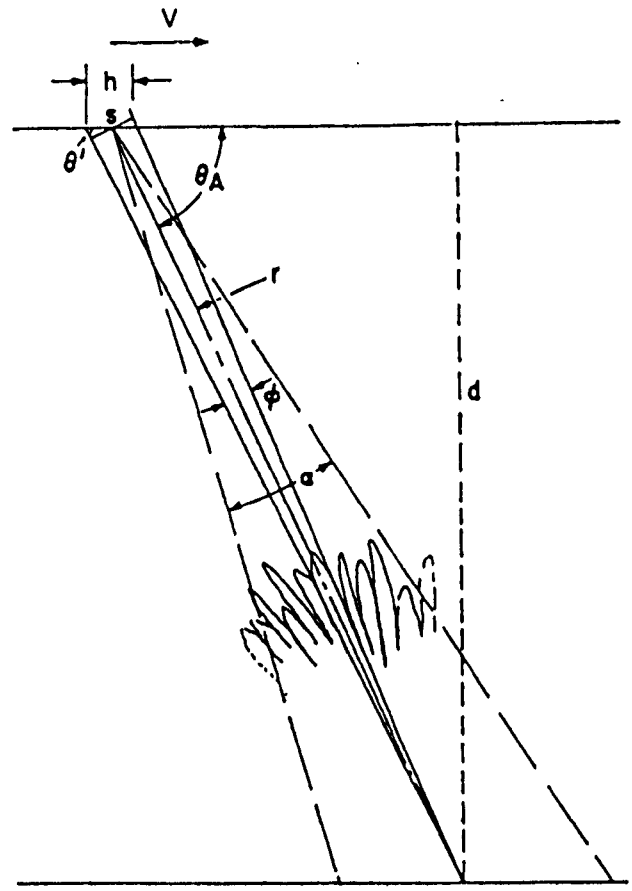

Fig. 10. Acoustic geometry.

where V is the magnitude of the velocity of the source/receiver and T is the period of the fluctuation, or the inverse of the beat rate Δf. The 2 arises because both the source and receiver are moving. The velocity of the source during transmission causes the fine lobes to seem to rotate about the insonified area on the bottom in the opposite direction to the velocity vector. Then the velocity during reception causes the lobe to be intercepted at twice the rate. It has been observed that the fluctuation rate is reduced by approximately 1/2 when the receiver velocity is zero, all other conditions being the same. The factor is only approximately 1/2 because of the nonlinear Doppler equation for the moving-source case.

The approximate form of the fluctuation equation, Eq. 4, is rewritten as

$$VT = \lambda_0[4 \sin(\alpha/2) \sin\theta_A]^{-1}, \tag{7}$$

where $\lambda_0 = C/f_0$. Equation 7 is substituted into Eq. 6, giving

$$h = \lambda_0[2 \sin(\alpha/2) \sin\theta_A]^{-1}. \tag{8}$$

For small angles of ϕ such that θ' is assumed to be equal to θ_A,

$$s = h \sin \theta_A . \tag{9}$$

Equation 8 is substituted into Eq. 9, giving

$$s = \lambda_0 [2 \sin (\alpha/2)]^{-1}. \tag{10}$$

From the geometry, when s is assumed to be equal to the arc length for small angles of ϕ,

$$\phi = sd^{-1} \sin \theta_A . \tag{11}$$

To obtain the angular lobe width, Eq. 10 is substituted into Eq. 11, giving

$$\phi = \lambda_0 \sin \theta_A [2d \sin (\alpha/2)]^{-1}. \tag{12}$$

One should note that, as hypothesized by Eqs. 8, 10, and 12, h, s, and ϕ are functions of the wavelength and the geometry of the original beam and are independent of the velocity of the source or receiver.

To compare the experimental data of the previous section with this hypothesis, the distributions of fluctuation rate for various speeds illustrated in Fig. 4 are employed. The data are replotted in Fig. 11 with $1/T$ converted to h. The result is that the distributions of h are now invariant with speed, within experimental error. To more clearly show this result, the median h from each of the distributions is plotted versus speed in Fig. 12, similar to the plot of beat rate (Fig. 5). Also included in Fig. 12 is a lobe-width scale. Thus the experimental data support the hypothesis that the lobe width is invariant with speed and a further hypothesis that for zero speed there would be a spatially stationary interference field, without beats. This invariance with speed allows a correlation coefficient to be obtained in both time and space, in time relative to the moving field and in space relative to the field itself.

If one assumes that the correlation angle C_ϕ (to the first zero crossing) is approximately half of the scattered beamwidth, $\phi/2$, then the correlation angle is

$$C_\phi = \lambda_0 \sin \theta_A [4d \sin (\alpha/2)]^{-1} . \tag{13}$$

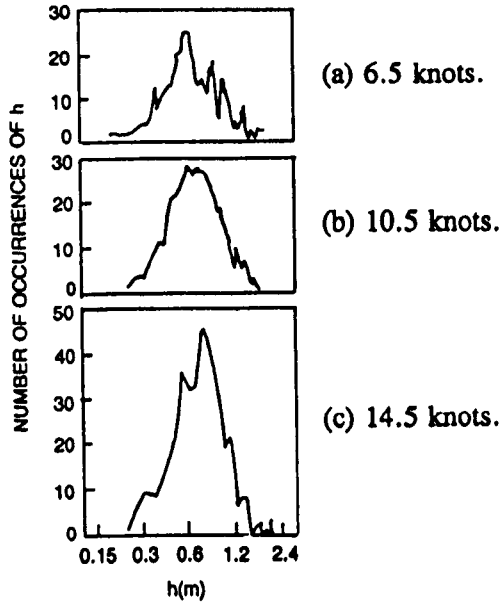

Fig. 11. Distribution of h, the horizontal lobe intercept.

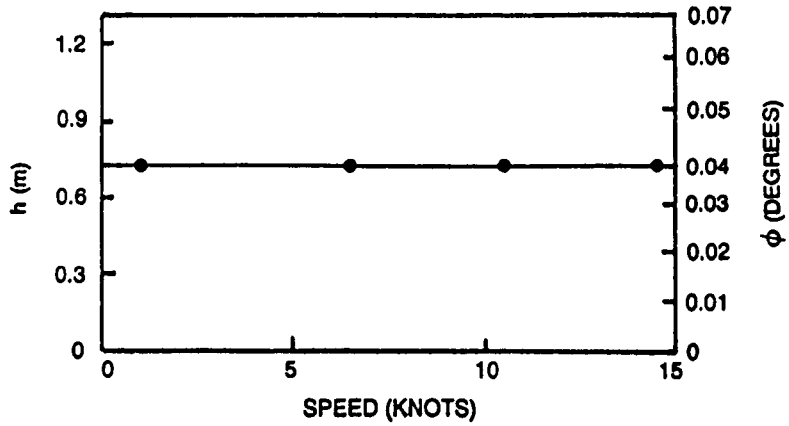

Fig. 12. Dependence of h and ϕ on the ship speed.

Also, if one assumes that the correlation time C_t (to the first zero crossing) in a beat is approximately $T/2$, then the correlation time for the fluctuation is

$$C_t = C[8f_0V \sin(\alpha/2) \sin\theta_A]^{-1} \tag{14}$$

and the correlation distance is

$$C_d = [8f_0 \sin(\alpha/2) \sin\theta_A]^{-1}. \tag{15}$$

Both the correlation angle and distance are independent of the velocity.

This same mechanism has been observed by several workers, Rigden and Gordon (1962), Oliver (1963), Langmuir (1963), Huntley (1964), and Goldfisher (1965), in coherent light scattered from rough surfaces using lasers. Intensity statistics of the speckle field were obtained by Dainty (1971) and McKehnie (1974). Additional applications of speckle fields are found in a special issue of the Journal of the Optical Society of America (1976) and in Erf (1978) and Francon (1979). When a laser beam is directed toward a scattering surface, the illuminated area sparkles with many bright spots. In this case the complex scattered field is described as having many fine interference lobes, randomly distributed in space, and stationary as long as there is no motion of the source or boundary and no instability of the monochromatic source. Further the total illuminated area contributes to each lobe. Near the boundary, the field seems to display the Fresnel characteristics. As the distance from the boundary becomes great, the lobes of the farfield radiation pattern are developed and obey the inverse-square law for the intensity.

The statistical lobe structure of the fields appears to be invariant with the roughness characteristic of the boundary, when the roughness is sufficiently great to preclude geometric reflection. This invariance was experimentally observed by Rigden and Gordon (1962) using surfaces made from densely packed particles ranging from 0.1-μm alumina powder to coarse carborundum grit. It has been found that surface-height statistical estimates can be obtained by correlating multiple speckle patterns from different directions and distances (Welford, 1977, Leger and Perrin, 1976, and Ohtsubo, 1982). A number of workers have tried to obtain surface characteristics from a single pattern but have not been successful.

Observations of the acoustic returns from a number of bottom types with different roughnesses (the exact characterization of the roughnesses not being known) indicate that scattering from the ocean bottom may have the same statistical invariance. For a limited example, Fig. 13 illustrates two distributions of s, the distance across the lobe at the receiving point, normal to its direction, obtained at 14.5 knots: one for a sand bottom in a water depth of 0.7 km with a tilt angle of 75°, and a second for a mud bottom in a water depth of 3 km

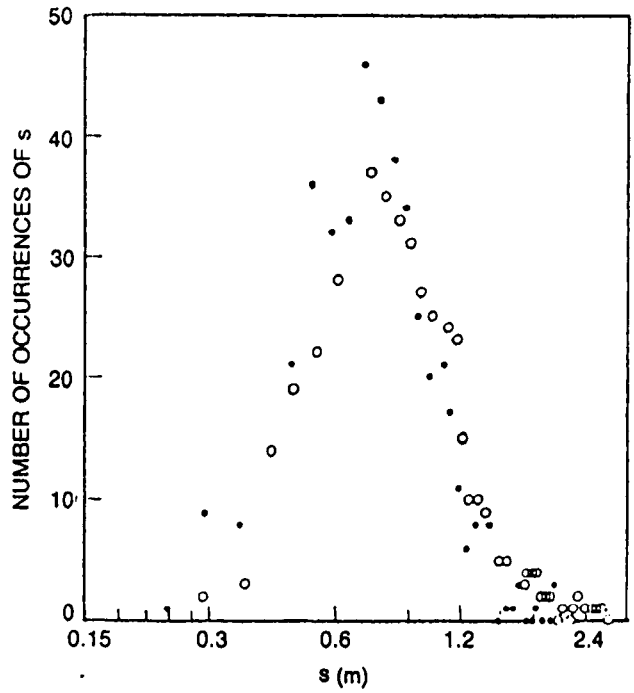

Fig. 13. Distributions of s for (●) a sand bottom ($\theta_A = 75°$ and $d = 0.7$ km) and (○) for a mud bottom ($\theta_A = 85°$ and $d = 3$ km).

with a tilt angle of 85°. The coincidence of the distributions supports Eq. 13, indicating the independence of depth and also the independence of the fine structure on the type of bottom.

CONCLUSIONS

All of the acoustical data in the experiments discussed were obtained in the Fresnel region of the scattered fields. In fact, when one considers the scale factors, most of the practical scattering situations in underwater acoustics are limited to this region.

It is concluded that motion produces a continuous Doppler shift across a beam and that the scatter from a boundary adds linearly, resulting in a beat or interference structure in the signal. The amplitude variations of the interference structure can be large for small velocities of source, scatterer, or receiver. Time characteristics of experimentally observed beats are in good agreement with those predicted by a simple theory.

Each of the beats can be visualized as a lobe of the scatter source, rotating about the scatter area in the opposite direction to the velocity vector. If there were no motion, the rotation would cease and the field would be stationary. The angular width, linear width, and

correlation distances to the lobes are independent of velocity. These observations are in good agreement with a simple theory. A number of these characteristics have been observed in optical experiments with lasers.

REFERENCES

L.I. Goldfischer, "Autocorrelation Function and Power Spectral Density of Laser-Produced Speckle Patterns," J. Opt. Soc. Am. **55**, 247-253 (1965).

W.H. Huntley, Jr., "New Coherent Light Diffraction Techniques," IEEE Spectrum **1**, 114-122 (1964).

B.K. Gazey, "Sea-bed Echo Amplitude Fluctuations Arising from Ship Motion," J. Brit. IRE **26**, 125-134 (1963).

B.G. Hurdle and R.H. Ferris, "Effect of Transducer Velocity on the Structure of Signals Reflected from the Ocean Bottom," J. Acoust. Soc. Am. **34**, 742 (1962).

B. G. Hurdle, R. H. Ferris, and K. D. Flowers, "Effect of Transducer Velocity on the Structure of Signals Scattered from the Ocean Bottom," J. Acoust. Soc. Am. **36**, 1936-1942 (1964).

B.G. Hurdle, "Fine Structure of Scattered Acoustic Fields," J. Acoust. Soc. Am. **39**, 1241 (1966a).

B.G. Hurdle, "Fine Structure of Acoustic Fields Scattered from the Ocean Bottom," J. Acoust. Soc. Am. **40**, 255-257 (1966b).

R.V. Langmuir, "Scattering of Laser Light," Appl. Phys. Letters **2**, 29-30 (1963).

B.M. Oliver, "Sparkling Spots and Random Diffraction," Proc. IEEE Correspondence **51**, 220-221 (1963).

J.D. Rigden and E.I. Gordon, "The Granularity of Scattered Optical Maser Light," Proc. IEEE Correspondence **50**, 2367-2368 (1962).

APPENDIX 1A: DERIVATION OF EQ. 1

A beat, the sum r of two or more vectors of amplitudes a, b, etc., and slightly different rotational frequencies, $\omega_1 t$, $\omega_2 t$, etc. is illustrated in Fig. 1A1. From the figure

$$r \sin \gamma = a \sin \omega_1 t + b \sin \omega_2 t$$

and

$$r \cos \gamma = a \cos \omega_1 t + b \cos \omega_2 t \ .$$

Also

$$r^2 = a^2 + b^2 + 2ab \cos (\omega_2 t - \omega_1 t)$$

$$= (a \cos \omega_1 t + b \cos \omega_2 t)^2 + (a \sin \omega_1 t + b \sin \omega_2 t)^2$$

and

$$\tan \gamma = \frac{a \sin \omega_1 t + b \sin \omega_2 t}{a \cos \omega_1 t + b \cos \omega_2 t} .$$

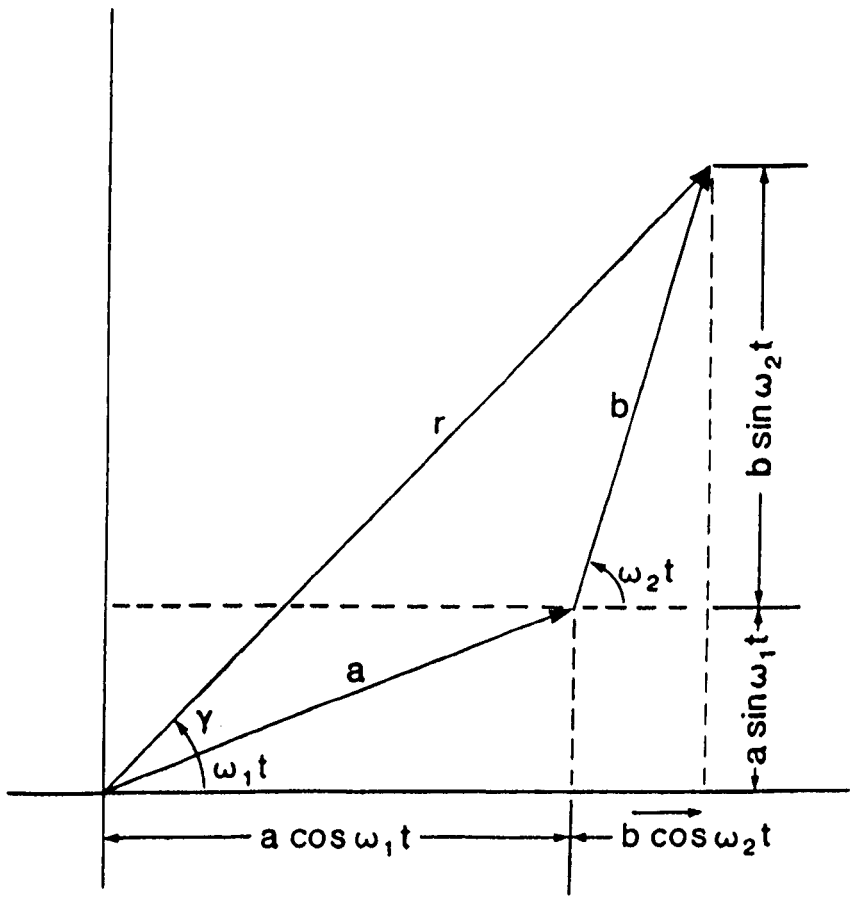

Fig. 1A1. Sum of two vectors.

In general the sum of n vectors is

$$\sum_{i=1}^{n} a_i \cos \omega_i t = R \cos \gamma,$$

where

$$\tan \gamma = \frac{\sum_{i=1}^{n} a_i \sin \omega_i t}{\sum_{i=1}^{n} a_i \cos \omega_i t}$$

and

$$R = \left[\left(\sum_{i=1}^{n} a_i \cos \omega_i t \right)^2 + \left(\sum_{i=1}^{n} a_i \sin \omega_i t \right)^2 \right]^{1/2}.$$

APPENDIX 1B: DERIVATION OF EQ. 5

Returning to Eq. 2, which gives the frequency received along any ray from the bottom, one obtains for the frequency f_1 received for the upper edge of the beam

$$f_1 = f_0[C + V \cos (\theta - \alpha/2)]/[C - V \cos (\theta - \alpha/2)]. \quad (1B1)$$

In like manner one obtains for the frequency f_2 received for the lower edge of the beam

$$f_2 = f_0[C + V \cos (\theta + \alpha/2)]/[C - V \cos (\theta + \alpha/2)]. \quad (1B2)$$

Figure 1B1 shows the geometry corresponding to Eqs. 1B1 and 1B2.

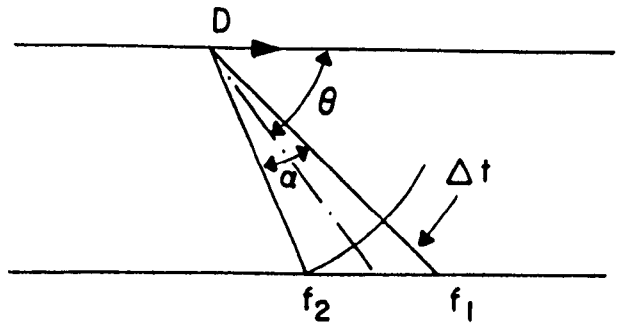

Fig. 1B1. Geometry of reflected rays.

It is proposed that the difference between f_1 and f_2 can be controlled by modulating the transmitted frequency as a function of time: $f \rightarrow f_0 + (df/dt)t$, where t is the time during transmission.

When the two frequencies f_1 and f_2 are compared, upon reception at point D, then f_1 will be lagging f_2 by a time Δt because of the longer path length. Therefore

$$f_1 = \left[f_0 + \frac{df}{dt} (t + \Delta t) \right] \left[\frac{C + V \cos (\theta - \alpha/2)}{C - V \cos (\theta - \alpha/2)} \right] \tag{1B3}$$

and

$$f_2 = \left[f_0 + \frac{df}{dt} t \right] \left[\frac{C + V \cos (\theta + \alpha/2)}{C - V \cos (\theta + \alpha/2)} \right] . \tag{1B4}$$

The difference between f_1 and f_2 is

$$\Delta f = f_0 \left[\frac{C + V \cos (\theta - \alpha/2)}{C - V \cos (\theta - \alpha/2)} - \frac{C + V \cos (\theta + \alpha/2)}{C - V \cos (\theta + \alpha/2)} \right]$$

$$+ t \frac{df}{dt} \left[\frac{C + V \cos (\theta - \alpha/2)}{C - V \cos (\theta - \alpha/2)} - \frac{C + V \cos (\theta + \alpha/2)}{C - V \cos (\theta + \alpha/2)} \right]$$

$$- \Delta t \frac{df}{dt} \left[\frac{C + V \cos (\theta - \alpha/2)}{C - V \cos (\theta - \alpha/2} \right] . \tag{1B5}$$

Referring to Fig. 1B2, one may write Δt in terms of the geometry and sound speed:

$$DF - DE = \Delta l / 2 \tag{1B6}$$

or

$$\frac{d}{\sin (\theta - \alpha/2)} - \frac{d}{\sin (\theta + \alpha/2)} = \frac{\Delta l}{2} \tag{1B7}$$

or

$$\Delta l = 2d \left[\frac{1}{\sin (\theta - \alpha/2)} - \frac{1}{\sin (\theta + \alpha/2)} \right] , \tag{1B8}$$

so that

$$\Delta t = \frac{\Delta \ell}{C} = \frac{2d}{C} \left[\frac{1}{\sin (\theta - \alpha/2)} - \frac{1}{\sin (\theta + \alpha/2)} \right] . \tag{1B9}$$

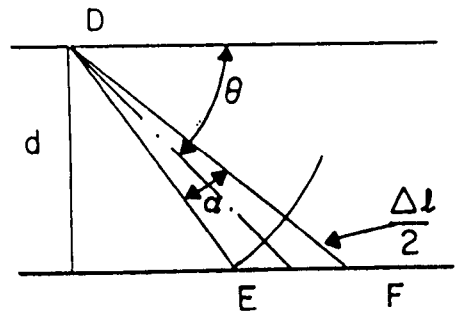

Fig. 1B2. Geometry for determining Δt.

Substituting Eq. 1B9 in Eq. 1B5, one has

$$\Delta f = f_0 \left[\frac{C + V\cos(\theta - \alpha/2)}{C - V\cos(\theta - \alpha/2)} - \frac{C + V\cos(\theta + \alpha/2)}{C - V\cos(\theta + \alpha/2)} \right]$$

$$+ t \frac{df}{dt} \left[\frac{C + V\cos(\theta - \alpha/2)}{C - V\cos(\theta - \alpha/2)} - \frac{C + V\cos(\theta + \alpha/2)}{C - V\cos(\theta + \alpha/2)} \right]$$

$$- \frac{2d}{C} \frac{df}{dt} \left[\frac{1}{\sin(\theta - \alpha/2)} - \frac{1}{\sin(\theta + \alpha/2)} \right] \left[\frac{C + V\cos(\theta - \alpha/2)}{C - V\cos(\theta - \alpha/2)} \right]. \qquad \text{(1B10)}$$

Equation 1B10 reduces to Eq. 3 of the text if $(df/dt) = 0$, that is, if a constant frequency is transmitted.

If the velocity and geometry are held constant, it can be seen from Eq. 1B10 and the curves of Fig. 6 that the transmitted frequency can be varied such that Δf will go to zero. For Δf to remain at zero over the length of the received pulse, it must be nonlinear with time. However, for the pulse lengths, geometry, and velocities used in this experiment, a constant df/dt was used because the magnitude of the second term of Eq. 1B10 was small with respect to the first and third terms.

Chapter 2

EFFECT OF GEOMETRY ON SIGNALS SCATTERED MONOSTATICALLY FROM THE OCEAN BOTTOM*

INTRODUCTION

When an area of the ocean bottom is insonified, a portion of the energy penetrates into and is lost in the bottom, and the remainder is returned to the water. If the directivity function of the original source is preserved in that portion returned to the water, the process can be considered to be that of reflection. If on the other hand the directivity function of the energy returned from the bottom is distorted, the process can be considered to be that of scattering. The degree of scattering can change from that causing small distortions to that causing radical distortions of the original directivity function, such that the insonified area behaves like a new source.

This chapter is concerned with the scattering of sound from the bottom back to the source point (the monostatic case, that is, with the source point and the receiver point coincident) when a directive source is employed. The purpose of this chapter is to determine the degree of correspondence between the scattering indicated by isotropic scattering theory and that measured in a monostatic scattering experiment.

THEORY

The analysis of this chapter is based on the isotropic scattering model by Eckart (1946) except following Urick (1954) scattering strength is used rather than the scattering coefficient. Scattering Strength, s is defined as the ratio of the scattered intensity, I_s (at a distance of one yard) to the incident intensity, I_i from a surface area of one square yard. The model states that

$$I_s = sI_iA\,, \tag{1}$$

*Some of this material was presented earlier (Hurdle and Flowers, 1964, 1967).

where I_s is the intensity of the scattered signal at unit distance (1 yard or 1 m) from the boundary, s is the scattering strength, I_i is the incident intensity, and A is the insonified area contributing to the scattered signal at a particular instant.

A practical acoustical experiment employing transducers having a beam function requires the integration of the incident intensity over the insonified area. When Cartesian coordinates are used, the scattered intensity is

$$I_s(\psi) = \int_A \int s(x,y) I_i(x,y)\, dxdy, \tag{2}$$

where $s(x,y)$ is the scattering strength of $dxdy$ in the direction ψ.

In extending the isotropic model to accommodate a directive source, it is convenient to use polar coordinates. Equation 2 is rewritten as

$$I_S(\psi) = \int_R \int s(\delta,\theta) I_i(r,\delta,\theta) dR\,, \tag{3}$$

where I_s is the scattered intensity at unit distance in the direction ψ as shown in Fig. 1, with ψ being an angle of scatter observation, R is the region of insonification, s is the scattering strength, r is the distance between the source and dR, δ is the angle between the direction of incident intensity and the horizontal or grazing angle, and I_i is the incident intensity on dR.

In the monostatic case $\psi = \beta$, where

$$\beta = \frac{\delta_{max} + \delta_{min}}{2} \tag{4}$$

is the angle of the center ray of the source/receiver beam function with respect to the horizontal (Figs. 1 and 2). The model will here be restricted to a beam with circular symmetry about the beam axis.

Although the scattering strength depends on the geometry, particularly on β, if $|s(\delta) - s(\beta)|$ for $\delta_{min} \leq \delta \leq \delta_{max}$ is sufficiently small, a constant $s(\beta)$ over the interval may be used. This allows s to be removed from the integral but restricts the model to small beamwidths. Including the above restrictions in Eq. 3 results in

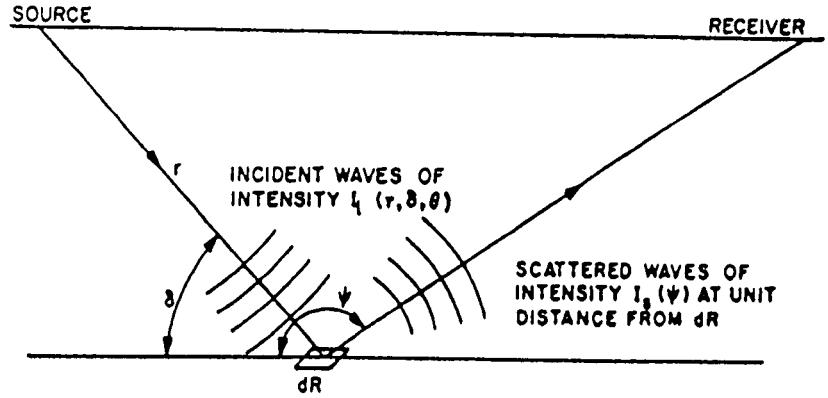

Fig. 1. General scattering geometry.

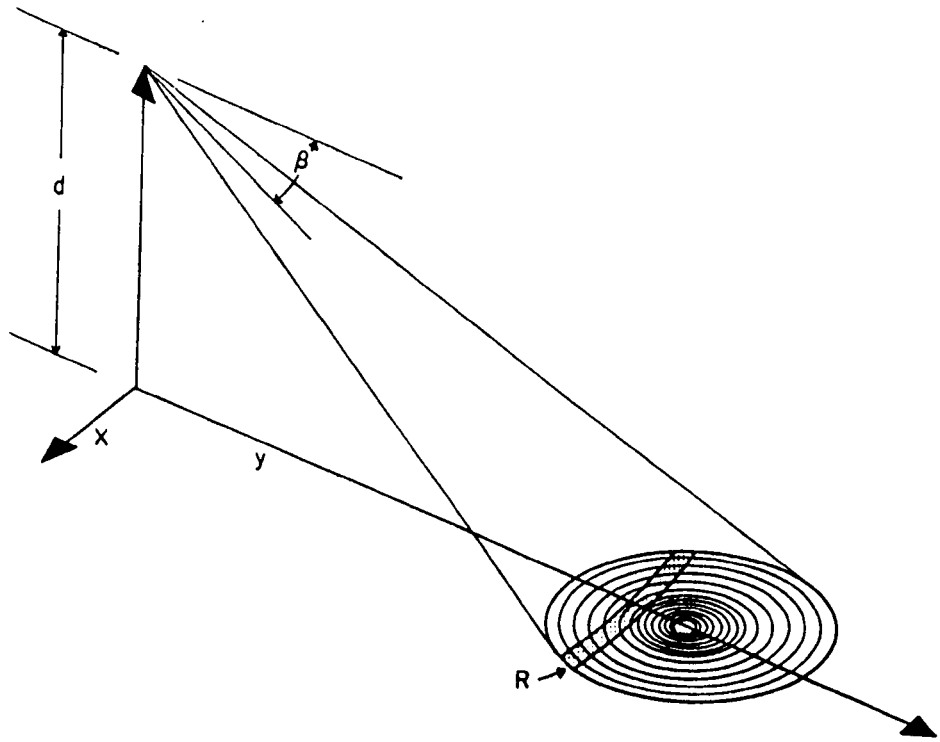

Fig. 2. Geometry for monostatic scattering with a directive source.

$$I_s(\beta) = s(\beta)\int_R\int I_i(r,\delta,\theta)\, dR\,, \tag{5}$$

where the geometry is illustrated in Fig. 2. Then

$$NP_i = \int_R\int I_i(r,\delta,\theta)\, dR\,, \tag{6}$$

where P_i is the normalized incident power and N is a constant.

Since the incident power on the bottom boundary is the integral of the incident intensity over the insonified area, it is independent of distance, except for attenuation. That is, there is

no power loss in transit from the source to the bottom except for attenuation losses. This enables P_i to be evaluated at unit distance from the source-receiver.

In taking account of the beam function, which is directly proportional to $I_i(r,\delta,\theta)$, it is found that most functions are sufficiently complicated to make the necessary integration intractable. Further, when making a computation for a particular transducer that is to be employed in obtaining experimental data, it is considered better to use the measured function of the transducer, which is never exactly analytic. For these reasons the measured beam function was used and incremented to enable a numerical integration of P_i.

Since the same directivity function is used in transmission and reception, it is convenient to use the square of the function rather than deal with it independently in both transmission and reception. Therefore, the square of the directivity function is illustrated in Fig. 3.

By introducing the propagational velocity, a transformation of the variable is made so that the incident power can be evaluated as a function of time for the parameters pulse length and grazing angle. The details of the P_i solution are contained in Appendix 2A of this chapter.

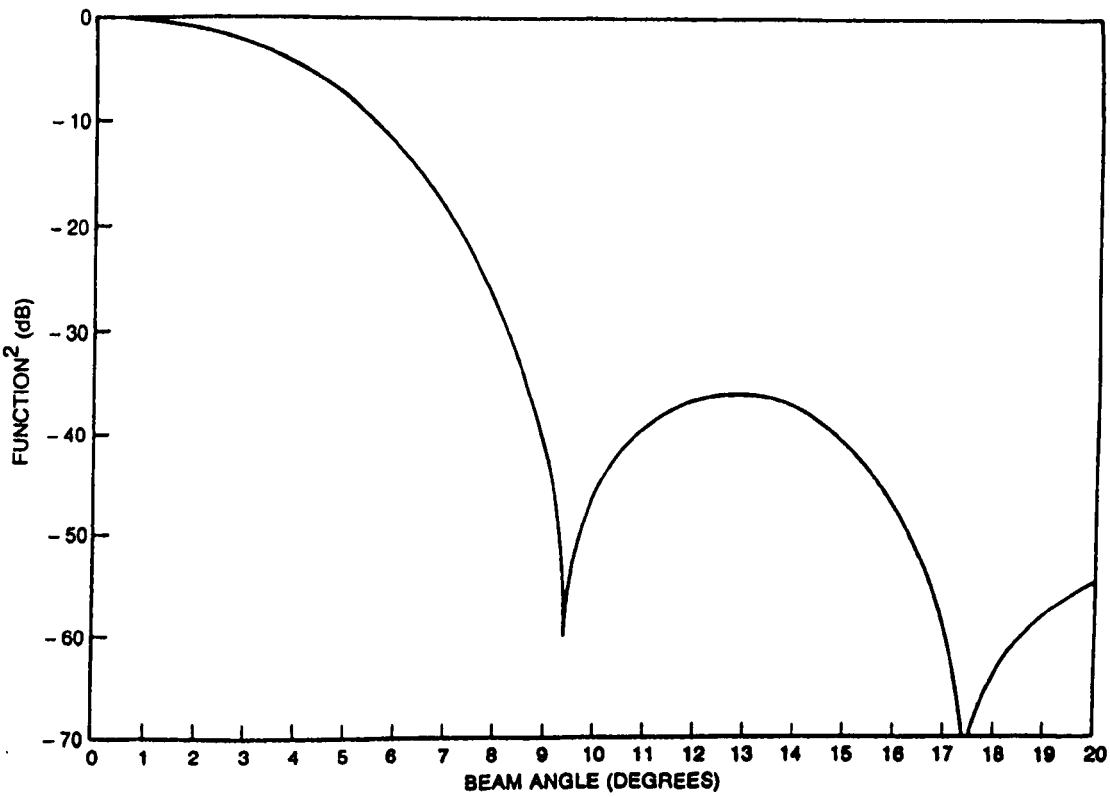

Fig. 3. Square of the source/receiver beam function at 19.5 kHz.

A computer program providing the numerical integration of P_i was constructed to make the evaluation. Several curves of P_i versus time for a variation of pulse length and a constant grazing angle are illustrated in Fig. 4. A similar set illustrated in Fig. 5 gives P_i as a function of time for a constant pulse length and several grazing angles. All of the curves are for a constant-amplitude transmitted pulse of constant length τ. The steady-state normalized value of P_i of -19.1 dB indicated by the flat portion of the 500-msec curve in Fig. 4 is in agreement with the value of the integral over the beam function computed for the transducer using the Christensen (1943) method.

The discussion to this point has been concerned with quantities near the scattering boundary. In practice both source and receiver are a distance r from the boundary, which requires that the propagation to and from the boundary be included. The transducer characteristics must also be included. Thus for the incident path (using the dB form)

$$10 \log NP_i = L + 20 \log i - D - Kr + 10 \log P_i , \tag{7}$$

where L is the transmitting response (dB re 1 μbar at 1 yard/ampere or dB re 1 μPa at 1 m/A), i is the source current (amperes), D is the dome loss (dB), and K is the absorption coefficient (dB/yard or dB/m).

Taking account of the receiving characteristics, for experimental purpose,

$$10 \log I_s = E - M - G + 20 \log r + Kr + D , \tag{8}$$

where E = 20 log (amplitude of the received signal) (dB re 1 volt), M is the receiving sensitivity (dB re 1 volt/μbar or dB re 1 V/μPa), G is the receiving gain (dB), K is the absorption coefficient (dB/yard or dB/m), and D is the dome loss (dB). Then converting the linear form of the scattering strengths to the logarithmic S ($S = 10 \log s$)

$$S = (E - M - G + 20 \log r + Kr + D) - (L + 20 \log i - D - Kr + 10 \log P_i). \tag{9}$$

For an isotropic medium Eq. 9 is written in terms of depth d and depression angle β using the relation $r \sin \beta = d$:

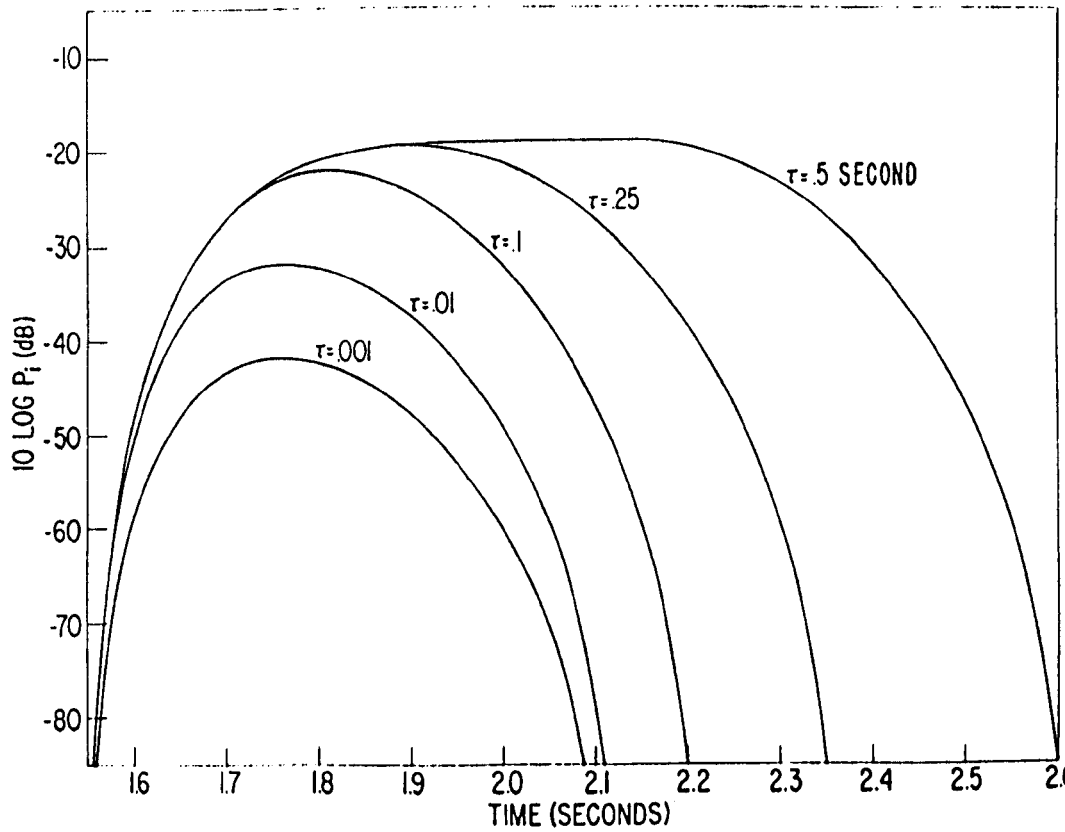

Fig. 4. Normalized incident power as a function of time for various pulse lengths with the depression angle β constant (45°) and with d = 0.9 km (1000 yards) and C = 1460 m/sec (1600 yards/sec).

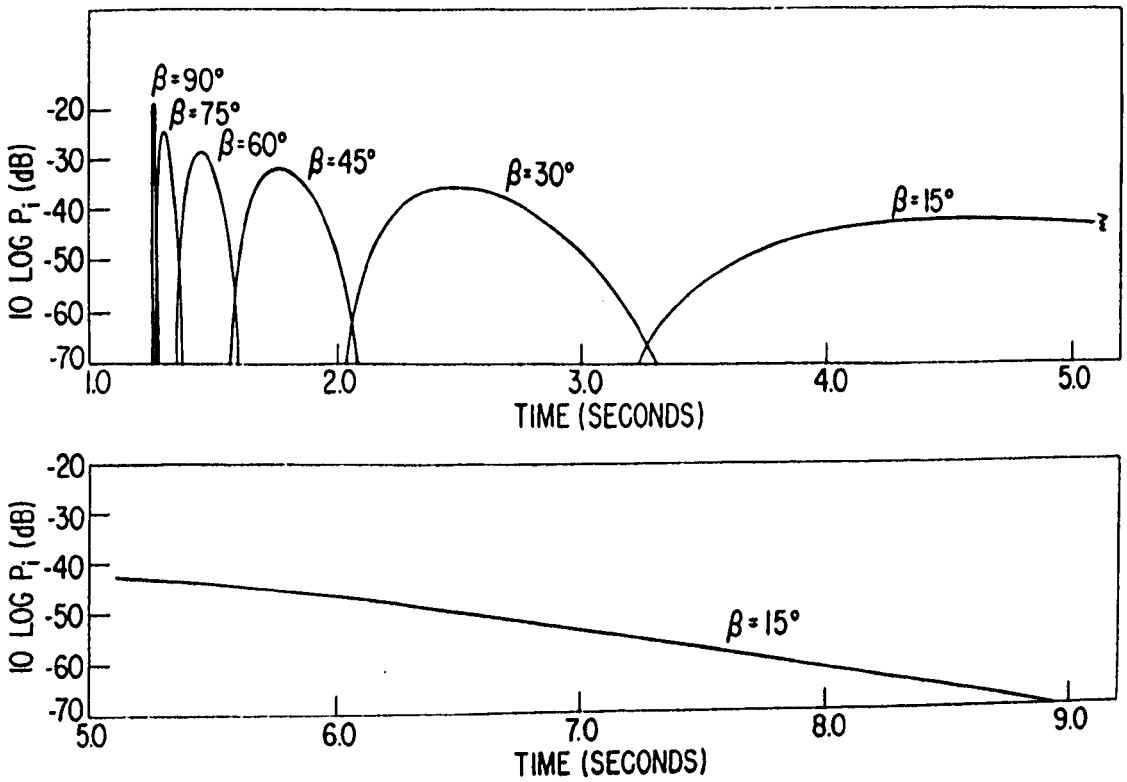

Fig. 5. Normalized incident power as a function of time for various depression angles with the pulse length τ constant (0.01 sec) and with d = 0.9 km and C = 1460 m/sec.

$$S = E - M - G - L - 20\log i + 2D + 20\log d + 20\log(\csc\beta) + 2Kd(\csc\beta) - 10\log p_i \quad (10)$$

EXPERIMENTAL MEASUREMENTS

To compare the predicted envelope of the scattered 19.5kHz signals with those of measured returns from the ocean bottom, an experiment was conducted in the Blake Plateau. Photographs of the bottom show small sand ripples with random direction. The instrumentation and procedures used are discussed in Criss et al. (1967) and in Appendix A (at the end of this work).

A series of runs were made for a series of depression angles, pulse lengths, and speeds. All parameters were held constant for a particular run, while recordings of the monostatic scattered signal were made for 20 to 100 returns. Environmental data were taken periodically during the experiment to enable the computation of refractive effects of the medium in this area. These computations included the sound-speed profile, the average sound speed over the path as a function of the depression angle, the angle of arrival at the bottom as a function of angle, and the pertinent characteristics of the propagation (Appendix 2B).

ANALYSIS OF MEASURED DATA

The amplitude envelope was recorded in analog form (on a decibel scale) as a function of time for each return. The data were then incremented in 10- to 25-msec steps through the duration of the return and converted to digital form with aid of a data reader. Care was taken to retain the time of each reading from the leading edge of the transmitted pulse. The power ratio of each value e_i^2 was averaged over the number of returns recorded for each time increment throughout the return:

$$E_i = 10 \log e_i^2$$

and

$$\langle e^2 \rangle = \frac{1}{n} \sum_{i=1}^{n} e_i^2 \Big|_{t=c}, \quad (11)$$

where n is the number of returns and c is a constant. The mean value of the envelope was then converted to decibels by

$$<E> = 10 \log <e^2>. \tag{12}$$

This makes $<E> \propto <I>$, if the intensity is proportional to pressure squared.

The light line in Fig. 6 illustrates the envelope of a single return as a function of time. The form of the signal envelope, including the large-amplitude fluctuations, is consistent with previous fluctuation studies (Hurdle et al., 1964). The heavy line illustrates the mean envelope $<E>$. Only the first bottom return with a few points from the decaying volume reverberations and part of a second bottom return are included in the average envelope illustrated. Some of the variations in level of the mean envelope at the beginning of the return are caused by variation in the amplitude of the transmitted pulse in that region, caused by the power-supply response of the driver amplifier. The shaded area about the mean envelope is

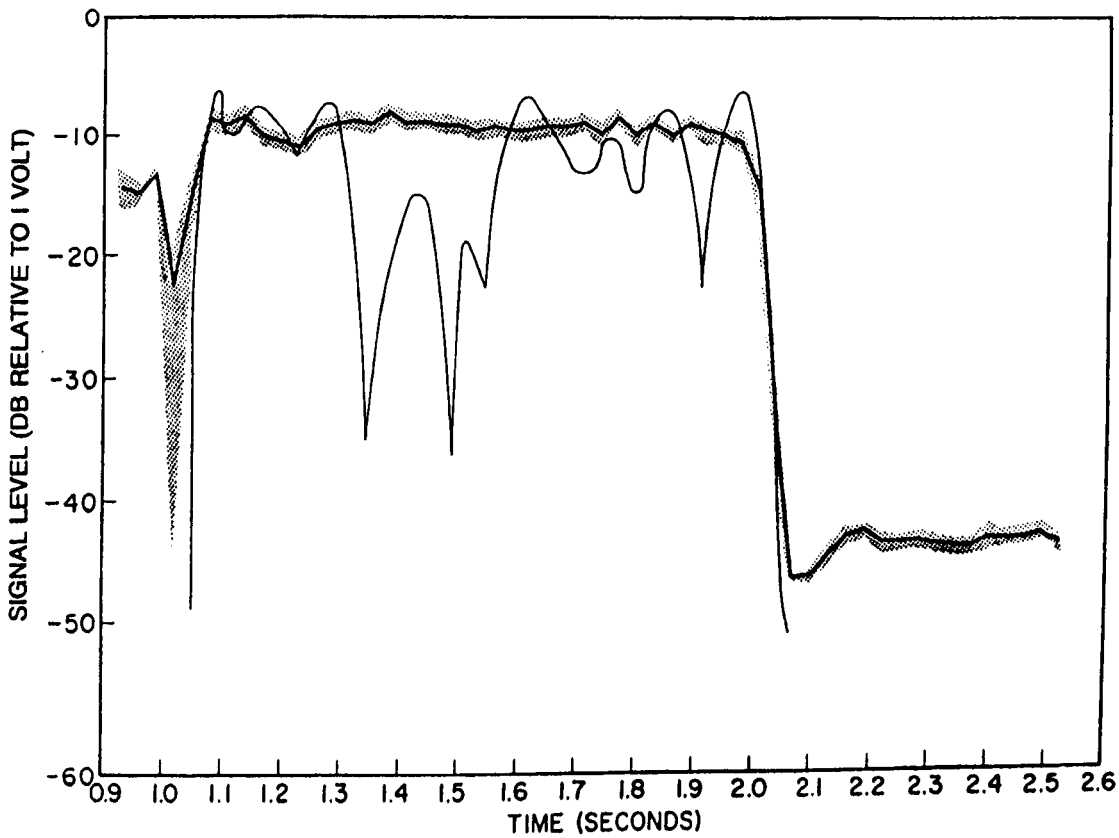

Fig. 6. Envelope of a single return and the mean envelope of the bottom scattered signal as a function of time (Blake Plateau, Sept. 1961; frequency 19.5 Hz; depression angle 90°; pulse length 0.910 sec; depth 805 m, and number of echoes 231).

the 95-percent-confidence interval (Peters and Van Voorhis, 1940). The interval is approximately ± 1 dB about the mean.

INTENSITY AS A FUNCTION OF TIME

Figures 7 through 12 compare the shape of the envelope predicted by the model (solid curve) and the mean intensity from measured data (points). The solid curve in each figure was obtained from the solution of Eq. 6 with the appropriate parameters of pulse length and grazing angle. The points were obtained by using Eqs. 8 and 12 as described. The time scale along the abscissa is the time of the return sequence. Refraction of the medium has been taken into account in the manner described in Appendix 2B.

Some of the volume reverberations can be seen prior to the initiation of the bottom return, particularly at the longer pulse lengths. For the shorter pulse lengths, exemplifield in Fig. 8, the reverberations have decayed to or near the noise level prior to the initiation of the bottom return. For the longer pulse lengths, exemplified by Figs. 7 and 9, a steady state is reached (at approximately 1.15 sec in Fig. 7) when the pulse length is sufficiently long to provide a simultaneous contribution from all of the area defined by the beam. At approximately 1.9 sec in the same figure the return starts to decay as the pulse moves off the area. The noise level is noted at the end of the bottom return, and part of a second bottom return is seen between 2.15 and 2.3 sec. During the steady-state portion of the return the spread of the points about the curve is approximately ± 1.5 dB.

In Figs. 7 through 12 the two scales on the right side of each figure correspond to the curve and the points respectively. The scale on the left side of the line represents power incident on the bottom, and the scale on the right side represents the intensity of the scattered signal 1 yard from the bottom. The curves have been positioned vertically until the best fit was reached. The distance moved (decibels) in fitting the curves corresponds to the scattering strength. The numerical value of scattering strength is obtained by reading the difference between the two dB scales. For example, the scattering strength for the data in Fig. 7 is -17.1dB//yd^2. Note the degree of fit between the measured and predicted envelopes. In

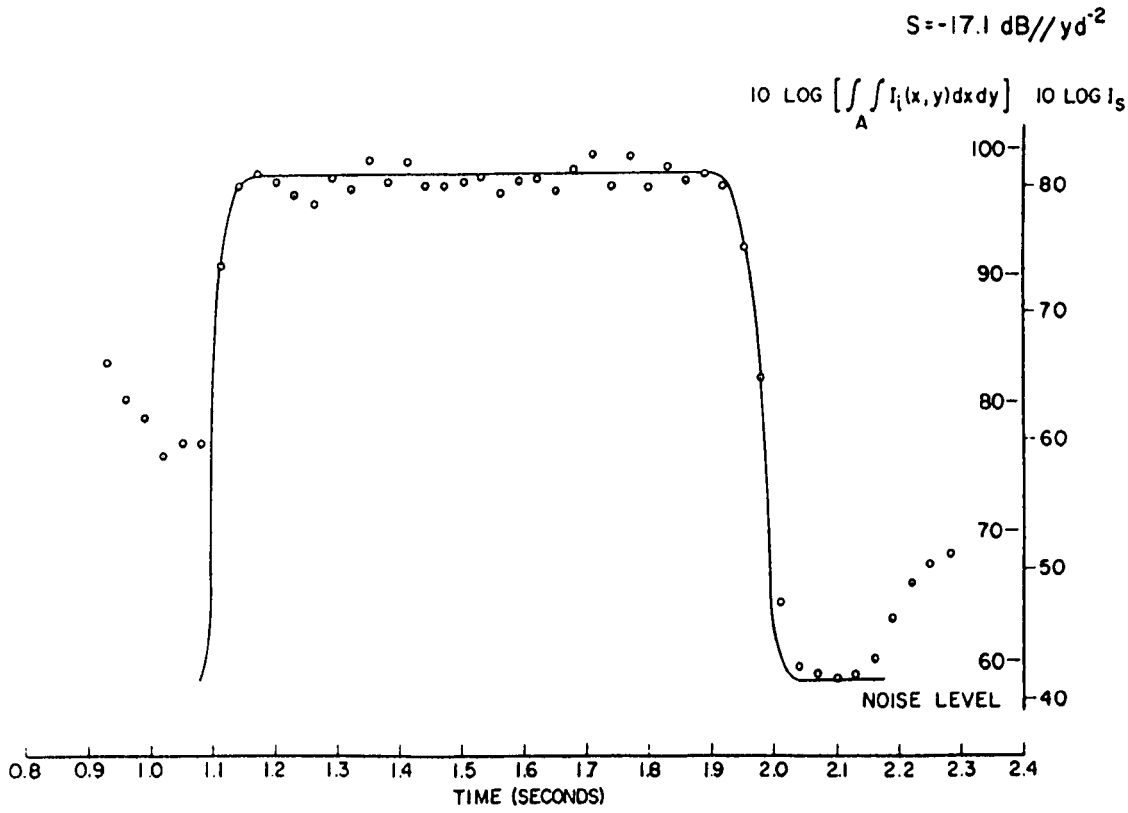

Fig. 7. Measured bottom scattered signals and the predicted envelope as a function of time (frequency 19.5 kHz, pulse length 0.817 sec, depression angle 70°, depth 805 m, echoes averaged 99).

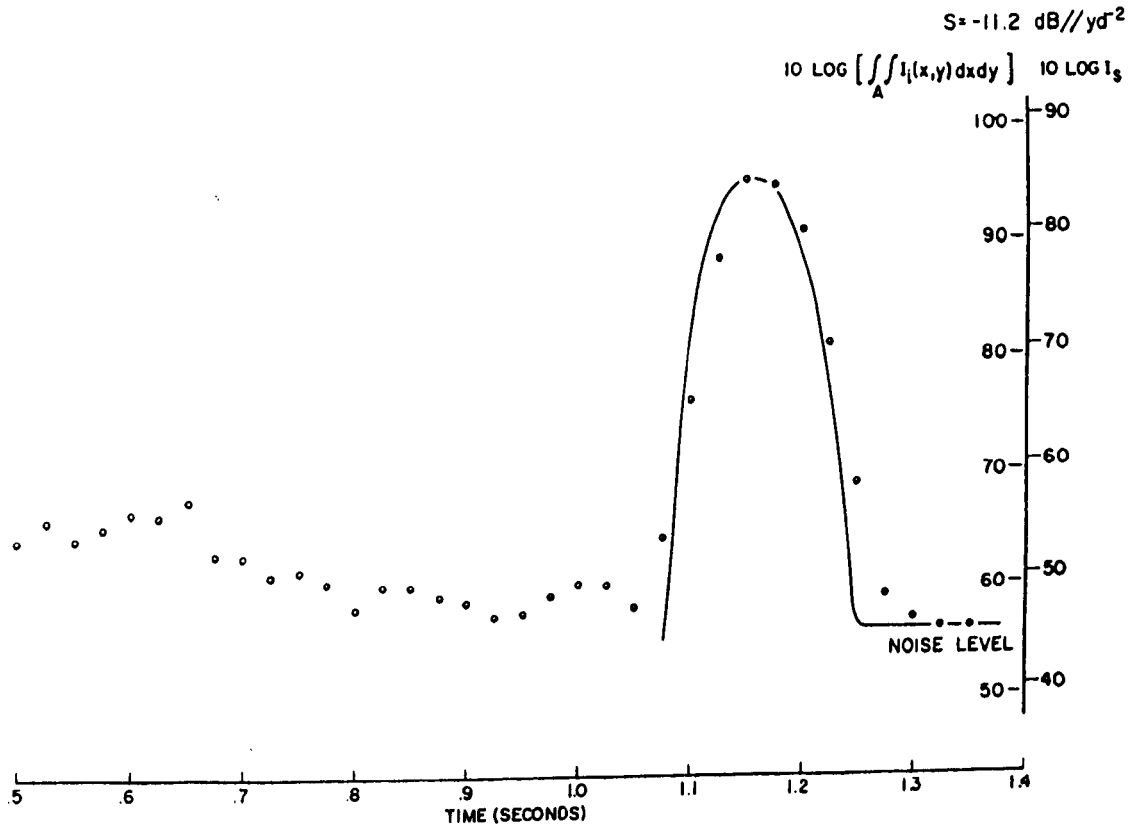

Fig. 8. Measured bottom scattered signals and the predicted envelope as a function of time (frequency 19.5 kHz, pulse length 0.060 sec, depression angle 70°, depth 805 m, echoes averaged 35).

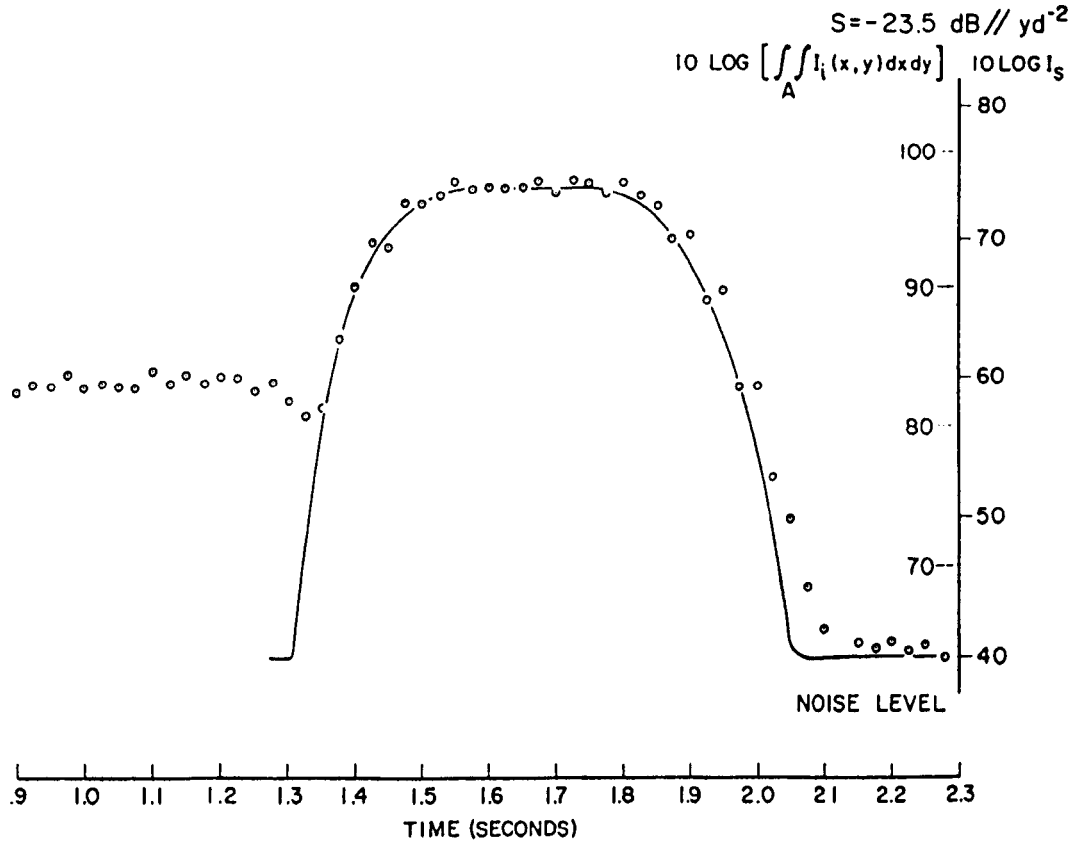

Fig. 9. Measured bottom scattered signals and the predicted envelope as a function of time (frequency 19.5 kHz, pulse length 0.411 sec, depression angle 45°, depth 805 m, echoes averaged 89).

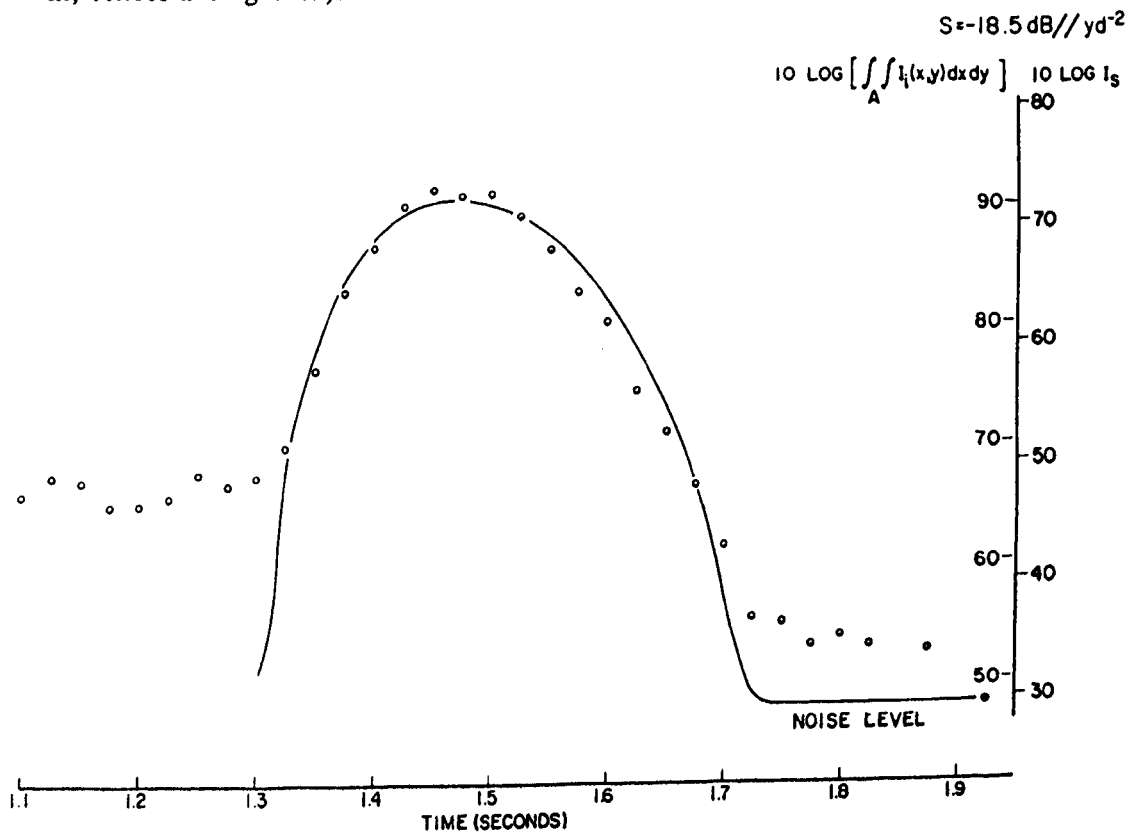

Fig. 10. Measured bottom scattered signals and the predicted envelope as a function of time (frequency 19.5 kHz, pulse length 0.050 sec, depression angle 45°, depth 805 m, echoes averaged 34).

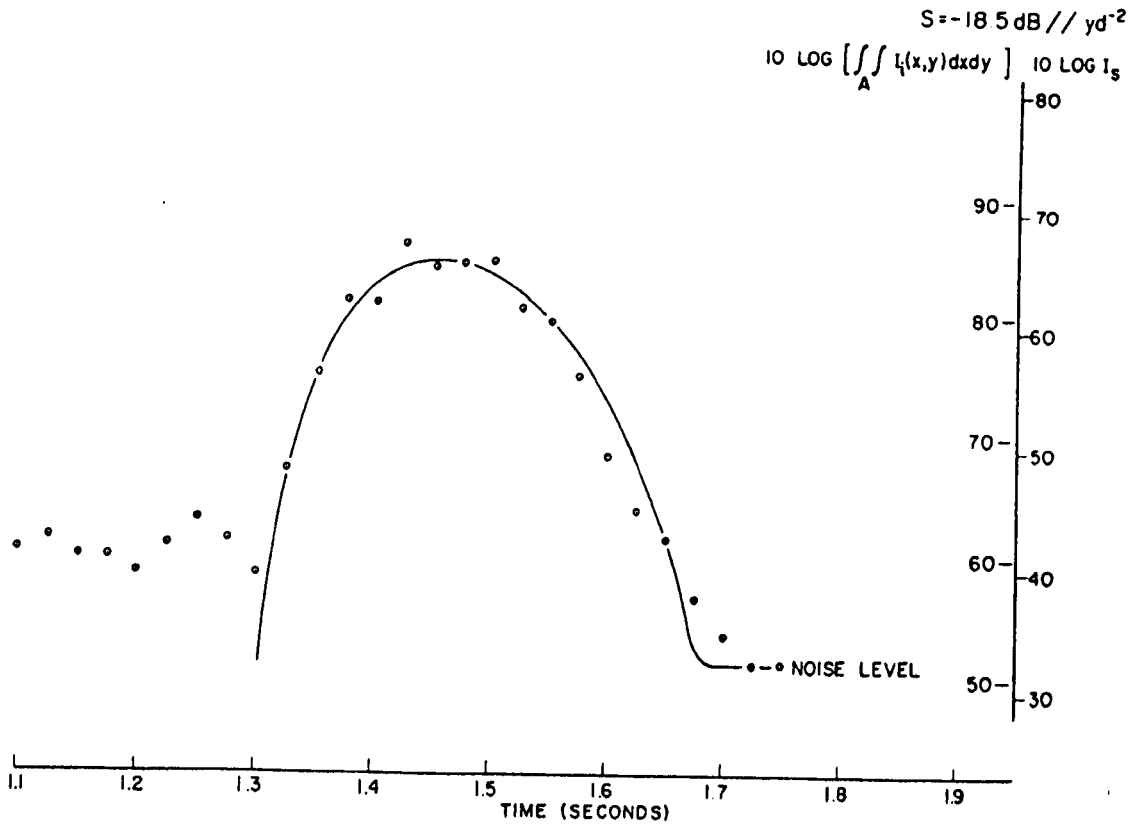

Fig. 11. Measured bottom scattered signals and the predicted envelope as a function of time (frequency 19.5 kHz, pulse length 0.015 sec, depression angle, 45°, depth 805 m, echoes averaged 12).

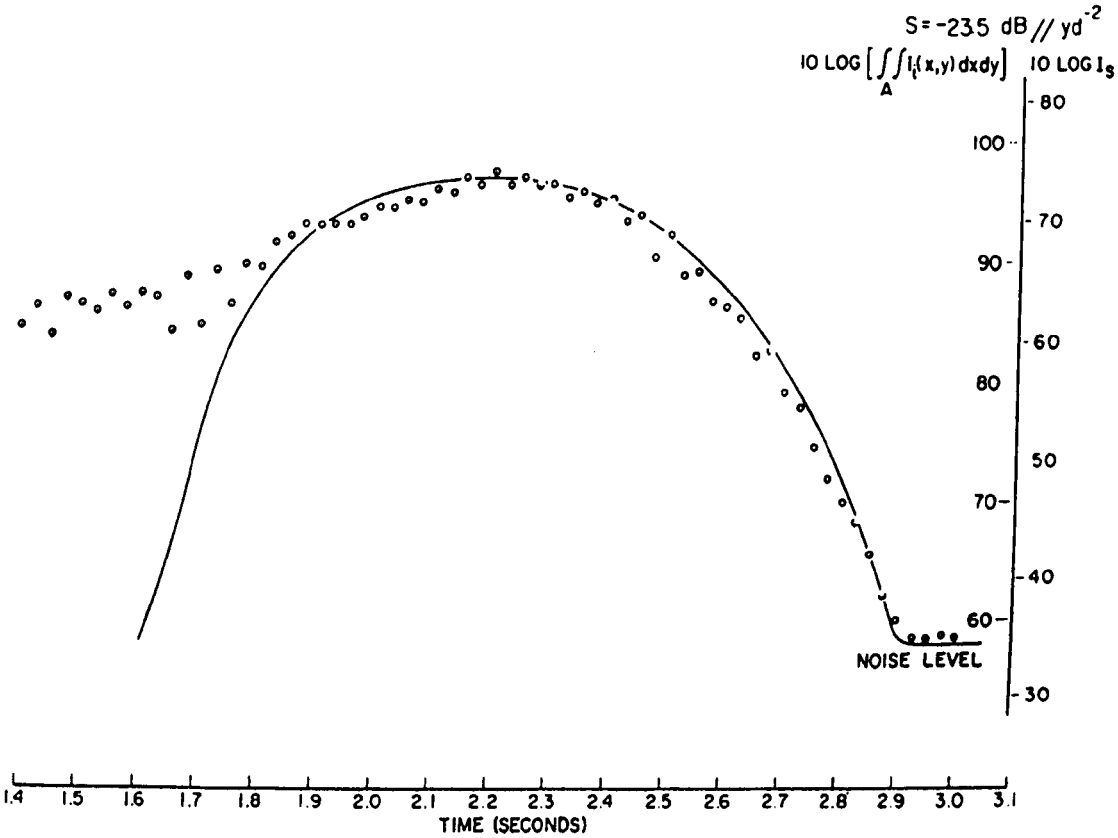

Fig. 12. Measured bottom scattered signals and the predicted envelope as a function of time. (frequency 19.5 KHz, pulse length .510 sec, depression angle 30°, depth 805m, echoes averaged 84)

Fig. 8, for a depression angle of 70 degrees and a pulse length of 60 msec, the major feature is that the pulse length is less than that required for steady state. Note the 2-to-1 expansion of the time scale in this figure as compared with Fig. 7.

Figures 7 through 12 are six sets from among approximately 70 sets of data analyzed and represent the envelope forms experienced and type of agreement obtained between predicted and measured envelope forms of the scattered signals.

SCATTERING STRENGTH AS A FUNCTION OF GRAZING ANGLE AND PULSE LENGTH

If the scattering from the boundary is isotropic, the scattering strength should be independent of pulse length or the dimensions of the insonified area, all other conditions remaining constant. To test this hypothesis, a series of data sets were taken for depression angles between 30° and 90° with pulse lengths varying between 2 msec and 1000 msec. Inspection of the shape of the echoes showed no detectable penetration in the bottom, as indicated previously. With no change in echo shape due to bottom penetration, a number of echoes could be averaged when other conditions are held constant (depression angle, pulse length, and frequency), thus removing the instantaneous fluctuations of the scattered field. Average echoes were obtained in this way for a variety of conditions.

Runs were made in various directions over the bottom in the operating area (Fig. 8 in the Appendix at the end of this work) and analyzed for variations in scatter strength with geographical orientation. No dependence on orientation could be detected in the scattering strength. Refraction of the medium has been taken into account in the manner described in Appendix 2B of this chapter.

It is assumed for short pulses that the changes of the scattering strength, $s(\beta)$ (Eq. 5) are small over the scattering region R (Fig. 2) when the range intercept is approximately 1/10 of the area defined by the beam (0.4° in vertical angle and the lateral intercept approximately ±4°). This allowed the scattering strength to be removed from the integral as S (Eq. 9). For a particular setting of the depression angle β the angle of scattering from the bottom is a

function of time as the insonified area moves across the area defined by the beam. Thus knowledge of the incident intensity as a function of time within the return made possible the deconvolution of the pulse in terms of scattering strength as a function of angle within the beam. That is, the mean curve for each experimental set of echoes is determined for a range of angles centered at the depression angle β. For a frequency of 19.5 kHz the range is approximately $\beta + 10° < \beta < \beta - 10°$. By combining the results over the range of β, the scattering strength as a function of β is obtained as illustrated in Fig. 13.

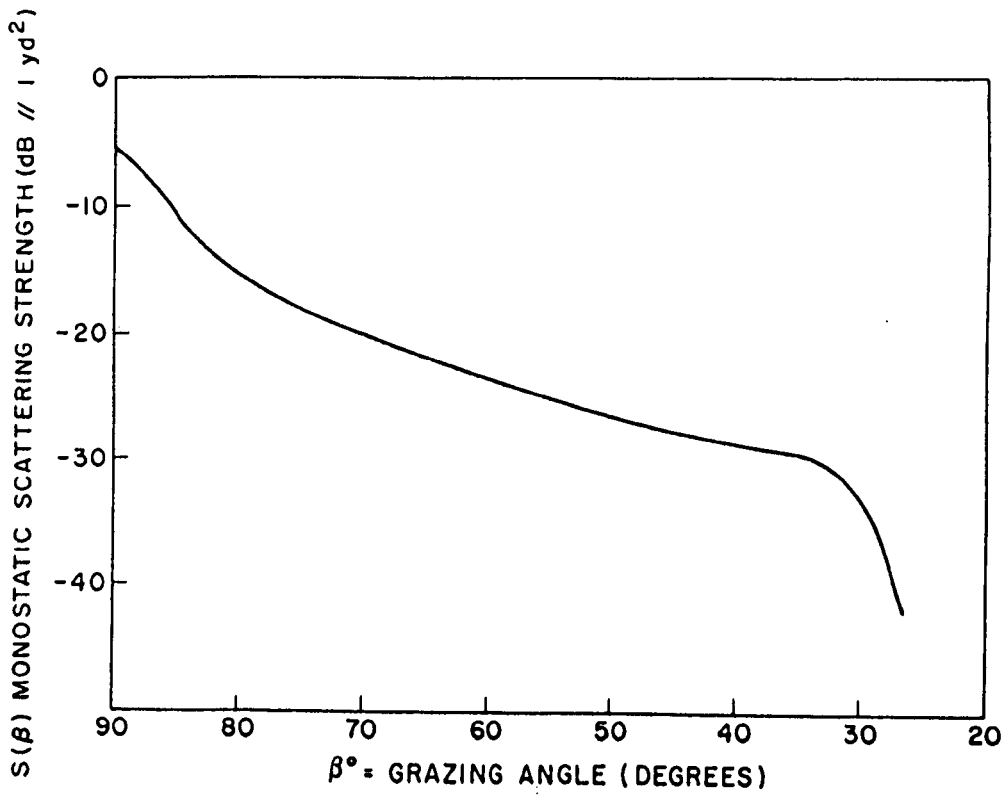

Fig. 13. Monostatic scattering strength curve for 19.5 kHz determined from short pulselength data.

With the scattering strength curve determined as a function of β from short-pulse-length data, the curve can then be numerically integrated over the appropriate increment of angles to obtain the scattered intensity for any pulse length. This integration was done for pulses long enough to receive contributions from all parts of the area simultaneously. The computed intensity curve for long pulses is illustrated in Fig. 14 for $I_0 = 1$. The observed $I_s(\beta)$ for long pulses are plotted as circles in Fig. 14.

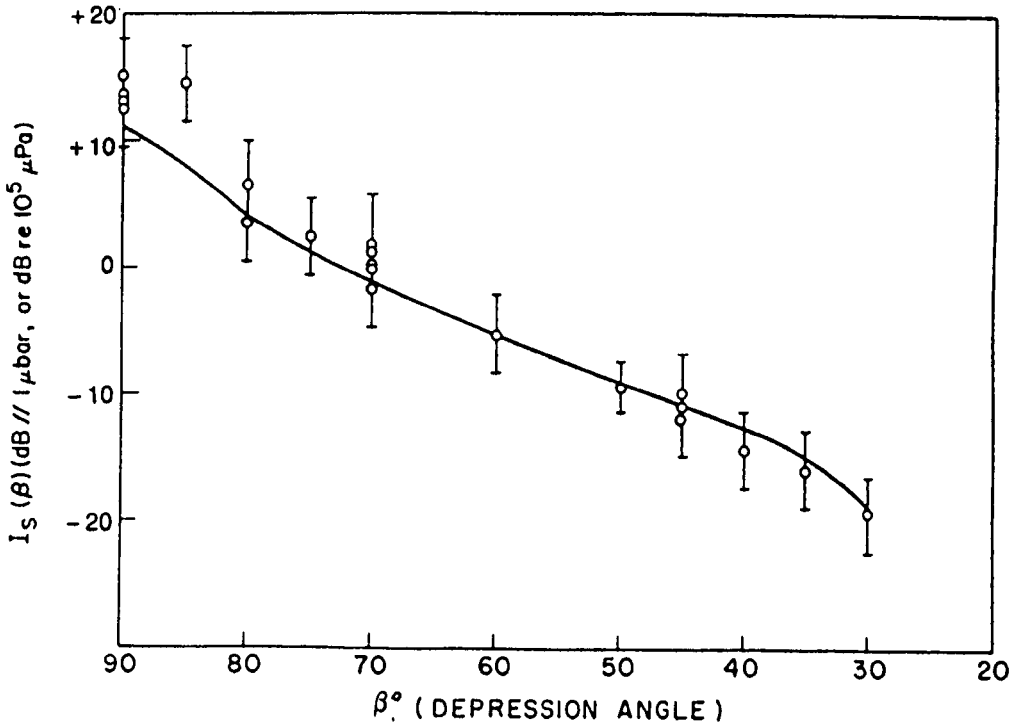

Fig. 14. Measured scattered average intensities of long pulses at 19.5 kHz (circles) versus depression angle. The solid line represents a numerical evaluation of $I_s(\beta)$ using the scattering strength curve of Fig. 13. The bars represent the extreme range of ±1.0 LSD about all of the observations. Note: $I_0 = 1$.

The bars represent the extreme range of ±1.0 LSD about all of the observations, where LSD is the logarithmic standard deviation (defined as 10 log [1 + (σ/m)], in which σ is the standard deviation of the observation and m is the mean). The data point at 85°, being higher than predicted, may be the result of including some specular component. The beamwidth of the source (8° to the half-power points) when coupled with slight variations in the stability of the source platform would bias the point upward.

The agreement obtained indicates no dependence of scattering strength on pulse length in this data. This is the expected result but is at variance with data by Patterson (1969).

A set of 39.0-kHz monostatic scattering data was taken in the same operating area using the same procedures. The 39.0-kHz data was obtained with a transducer having a source and receiving beamwidth of 4° at half-power points, which is half that of the 19.5-kHz data.

Instrumentation characteristics, absorption, and the ambient-noise level did not allow data to be obtained for short pulses at 39.0 kHz. However, if the scattering-strength ($I_s(\beta)$)

curve obtained for 19.5 kHz is used as if it were the 39.0-kHz curve, predicted scattered intensities for long pulses can be computed. The results of these computations are represented as the solid line in Fig. 15. The circles represent experimental 39.0-kHz scattered-intensity measurements for long pulses. The close agreement here implies that the scattering-strength curve for 39.0 kHz is essentially the same as the 19.5-kHz curve for this particular rough bottom, at least up to fairly steep angles. This indicates that the scattering has approached a condition of saturation such that the roughness is large relative to the wavelength of the 19.5-kHz and 39.0-kHz (7.6-cm and 3.8-cm respectively) incident signals.

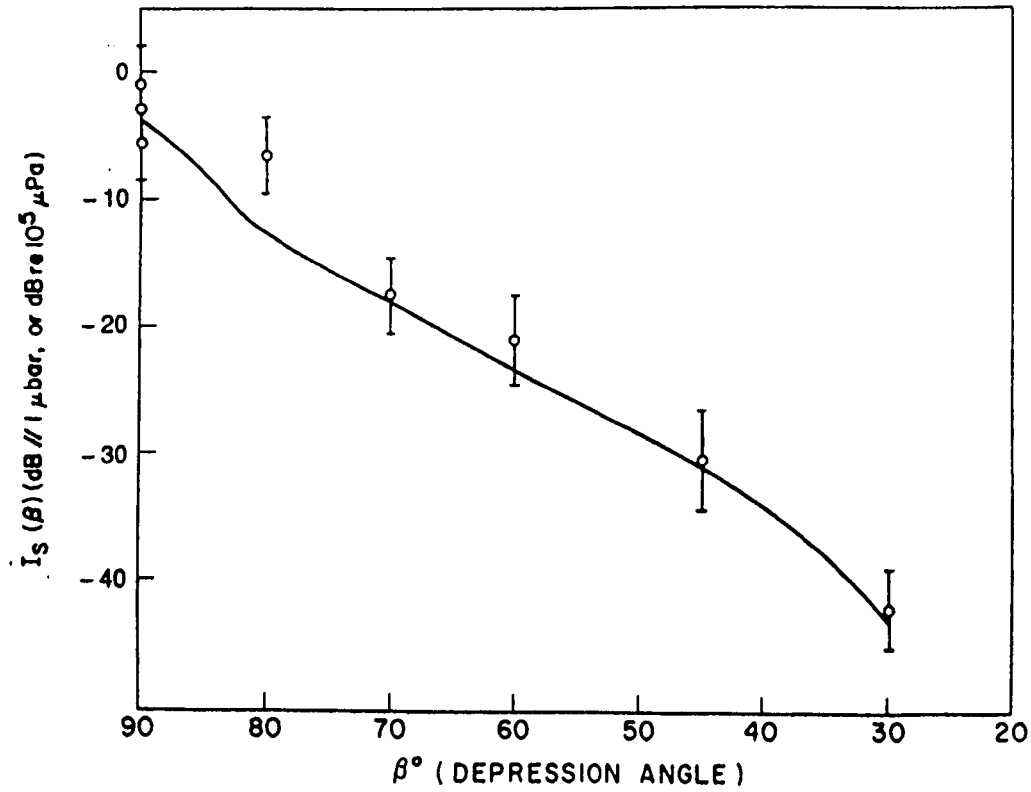

Fig. 15. Measured scattered average intensities of long pulses at 39.0 kHz using the 19.5-kHz scattering strength curve of Fig. 2. The bars represent the extreme range of ±1.0 LSD about all of the observations. Note: $I_0 = 1$.

DISCUSSION

Scattering from a random rough surface continues to be an important area of research, because many practical applications require increased theoretical and experimental knowledge from this research. Some of the pressing applications are electromagnetic scatterometry from satellites, radar scattering from the sea and land surfaces, and underwater acoustic scattering

from the sea surface and bottom. Some of the theoretical advances have been by Zipfel and DeSanto (1972), Trinkaus (1973), DeSanto (1973), DeSanto and Shisha (1974), Zipfel (1974), and Harper and Labianca (1975). Some of the experimental contributions have been by Welton et al. (1972), Boyd and Davenport (1973), Zorning and McDonald (1974), Zorning et al. (1977), and Tuteur et al. (1977). Schuetz and Zipfel (1974) developed a method for programming a computer to generate a description of a three-dimensional rough surface that satisfies a Gaussian distribution in height, slopes, curvature, etc., with this description to be used in instructing a numerical milling machine to make this known statistical rough surface. This surface could then be used in controlled experiments. Numrich (1976, 1978, 1979) used this method in generating a two-dimensional Gaussian surface for laboratory scattering experiments. These experiments also involved a schlieren method by Neubauer (1986) for visualizing the scattered field.

CONCLUSIONS

The temporal character of the signal envelope for monostatic scattered signals have been measured as a function of the acoustic geometry and pulse length. Calculations in which the shape of the return was obtained by numerical integration have been compared with the measured values. The good comparison obtained indicates that the returns are from the scattering boundary and not from the volume below. Monostatic scattering-strength as a function of grazing angle has been obtained for the Blake Plateau at 19.5 kHz for short pulses. Using this curve the scattered intensity for long pulses at 39.0 kHz were predicted having good agreement with measured values.

REFERENCES

M.L. Boyd and R.L. Deavenport, "Forward and Specular Scattering from a Rough Surface," J. Acoust. Soc. Am. **53**, 791 (1973).

H.U. Criss, K.D. Flowers, B.G. Hurdle, R.M. Lee, and K.P. Thompson, "Procedures for a Series of Experiments in Acoustic Scattering from the Ocean Bottom and Volume in the Blake Plateau Area," NRL Memo. Rept. 1767, April 1967.

J.A. DeSanto, "Scattering from a Random Rough Surface: Diagram Methods for Elastic Media," J. Math. Phys. **14**, 1566-1573 (1973).

J.A. DeSanto and O. Shisha, "Numerical Solution of a Singular Integral Equation in Random Rough Scattering Theory," J. Comp. Phys. **15**, 286 (1974).

C. Eckart, "Principles and Applications of Underwater Sound," NDRC Summary Technical Reports, Division 6, Vol. 7, Washington, D.C., 1946.

E.Y. Harper and F.M. Labianca, "Perturbation Theory for Scattering of Sound from a Point Source by a Moving Rough Surface in the Presence of Refraction," J. Acoust. Soc. Am. **57**, 1044-1051 (1975).

B.G. Hurdle, R.H. Ferris, and K.D. Flowers, "Effect of Transducer Velocity on the Structure of Signals Scattered from the Ocean Bottom," J. Acoust. Soc. Am. 36:1936 (1964).

B.G. Hurdle and K.D. Flowers, "Effect of Geometry on Monostatic Scattering from the Ocean Bottom," J. Acoust. Soc. Am. **36**, 1993 (1964).

B.G. Hurdle and K.D. Flowers, "Effect of Geometry on Acoustic Monostatic Scattering from the Ocean Bottom," NRL Rept. 6517, 1967.

W.G. Neubauer, "Acoustic Reflection from Surfaces and Shapes," Naval Research Laboratory, 1986.

S.K. Numrich, "Measurement of the Acoustic Field Scattered at the Liquid-Solid Interface of an Echelette Grating," J. Acoust. Soc. Am. **60**, S56(A) (1976).

S.K. Numrich, "Scattering of Acoustic Waves from Randomly Rough Surfaces," J. Acoust. Soc. Am. **64**, S131(A) (1978).

S.K. Numrich, "Scattering of Acoustic Waves from Randomly Rough Surfaces," University Microfilms, Ann Arbor, Mich., 1979.

C.C. Peters and W.R. Van Voorhis, *Statistical Procedures and Their Mathematical Bases*, McGraw-Hill, New York, 1940.

L.S. Scheutz and G.G. Zipfel, "Theory and Construction of Multivariate Gaussian Surfaces," J. Acoust. Soc. Am. **56**, 99-109 (1974).

L.S. Scheutz and G.G. Zipfel, "Theory and Construction of Multivariate Gaussian Surfaces," J. Acoust. Soc. Am. **56**, 99-109 (1974).

H. Trinkaus, "Fundamental Approximations for the Scattering of Acoustic Waves from a Rough Surface," SACLANTCEN Memo. SM-15, 1973.

F.B. Tuteur, J.G. Zornig, and H. Tung, "Scattering of Underwater Acoustic Signals from a Rough, Moving Surface," S and IS Rept. 7705, Dept. of Engineering and Applied Science, Yale Univ., 1977.

R.J. Urick, "The Backscattering of Sound from a Harbor Bottom," J. Acoust, Soc. Am. **26**, 231 (1954).

P.J. Welton, H.G. Frey, and P. Moore, "Experimental Measurements of the Scattering of Acoustic Waves by Rough Surfaces," J. Acoust. Soc. Am. **52**, 1553-1563 (1972).

G.G. Zipfel, "Scattering of Scalar Waves from a Random Irregular Interface," J. Math. Phys. **15**, 101 (1974).

G.G. Zipfel and J.A. DeSanto, "Scattering of a Scalar Wave from a Random Rough Surface: A Diagrammatic Approach," J. Math. Phys. **13**, 1903 (1972).

J.G. Zornig and J.F. McDonald, "Direct Measurement of Surface-Scatter Channel Coherence By Impulse Probing," J. Acoust. Soc. Am. **55**, 1205-1211 (1974).

J.G. Zornig, P.M. Schultheiss, and J. Snyder, "Bistatic Surface Scattering Strength at Short Wavelengths," Technical Rept. CS-9, Dept. of Engineering and Applied Science, Yale Univ., 1977.

APPENDIX 2A: EVALUATION OF THE NORMALIZED INCIDENT POWER

In Eq. 6 of the text, which is

$$NP_i = \int_R \int I_i(r,\delta,\theta)\, dR\,, \tag{2A1}$$

P_i, the normalized incident power on the bottom boundary, is the integral of the incident intensity over the insonified area. Thus P_i is independent of distance, except for attenuation, and of orientation of the insonified area. That is, there is no power loss in transit to the bottom except for attenuation losses. The method used then will be to evaluate P_i at unit distance from the source/receiver.

As shown in Fig. 2A1, the surface region R_j' is that portion of the sphere of unit radius contained between the cone of vertex angle a_j and the cone of vertex angle $2(90° - \phi)$. When R_j' is projected on the xy plane, the region R_j is obtained. The area of R_j' is

$$A_j = \int_{R_j'} \int dR_j' = \int_{R_j} \int \sec \gamma \, dR_j \, , \tag{2A2}$$

where γ is the angle between the tangent plane of a surface element on the spherical cap and the xy plane. The spherical cap is that portion of the surface of the sphere of unit radius contained within the cone of vertex angle a_j.

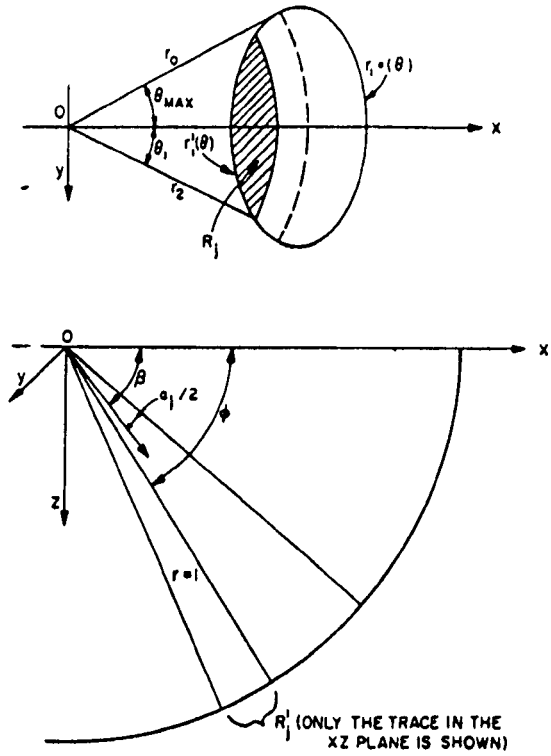

Fig. 2A1. Geometry for calculating the normalized incident power at unit distance.

The beam function, which is directly proportional to $I_i(r,\delta,\theta)$, is a characteristic of the source/receiver. Most beam functions are sufficiently complicated to make the necessary integrations intractable. Thus, we increment the beam function to enable the numerical integration of P_i. This means that we have a finite sum of area-intensity products, as illustrated in Fig. 2A2.

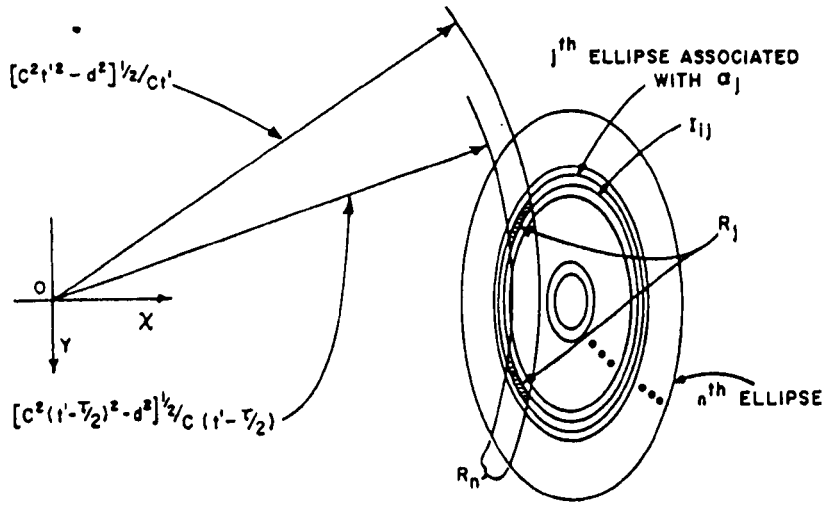

Fig. 2A2. Geometry of the finite sum of area-intensity products.

If

R_n = total insonified area,

R_j = total insonified area contained in the jth ellipse (or ellipse j),

$A_j(t')$ = area bounded by ellipse j and the circle of radius $[C^2t'_2 - d^2]^{1/2}/Ct'$, and

$A_j(t' - \frac{\tau}{2})$ = area bounded by ellipse j and the circle of radius

$$\left[C^2\left(t' - \frac{\tau}{2}\right)^2 - d^2\right]^{1/2}/C\left(t' - \frac{\tau}{2}\right),$$

then

$$P_i(t') = \int_{R_n}\int I_i(r,\delta,\theta)dR_n \approx \sum_{j=1}^{n} I_{ij}(R_j - R_{j-1}) \tag{2A3}$$

$$= \sum_{j=1}^{n} I_{ij}\left\{\left[A_j(t') - A_j\left(t' - \frac{\tau}{2}\right)\right] - \left[A_{j-1}(t') - A_{j-1}\left(t' - \frac{\tau}{2}\right)\right]\right. \tag{2A4}$$

and

$$P_i(t) = \sum_{j=1}^{n} I_{ij}\left\{\left[A_j\left(\frac{t}{2}\right) - A_j\left(\frac{t}{2} - \frac{\tau}{2}\right)\right]\right.$$

$$\left. - \left[A_{j-1}\left(\frac{t}{2}\right) - A_{j-1}\left(\frac{t}{2} - \frac{\tau}{2}\right)\right]\right\}, \tag{2A5}$$

where prior to the arrival of the wave on the boundary

$$A_0(t') = A_0\left[t' - \frac{\tau}{2}\right] = 0,$$

in which

$t' = d/c \sin \phi$ = transit time to the bottom via the path associated with ϕ,

τ = pulse duration,

d = water depth,

C = sound speed (assumed constant), and

$t = 2t'$ = *time* $P_i(t')$ is contributing to the signal received at the source point.

It remains to express $A_j(t)$ explicitly. This is done by letting $u = t/2$ or $u = (t - \tau)/2$ and expressing $A_j(u)$ explicitly. The expression for $A_j(u)$ is then converted to be expression for $A_j(t)$. It is convenient to consider three cases, as determined by the tilt angle β or by both the tilt angle β and the angle a_j:

In case 1, $\beta = \frac{\pi}{2}$ (Fig. 2A3). In this case

$$A_j(u) = 0, \quad u \leq u_0, \tag{2A6}$$

$$A_j(u) = 2\pi[1 - (\frac{d}{cu})], \quad u_0 < u < u_2, \tag{2A7}$$

and

$$A_j(u) = 2\pi[1 - \cos(a_j/2)], \quad u_2 \leq u. \tag{2A8}$$

In case 2, $\beta + (a_j/2) = \frac{\pi}{2}$ (Fig. 2A4). In this case

$$A_j(u) = 0, \quad u \leq u_1, \tag{2A9}$$

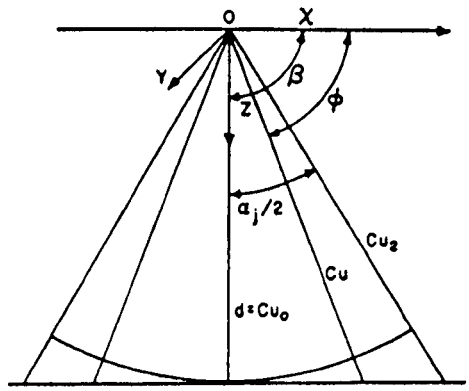

Fig. 2A3. Geometry for case 1

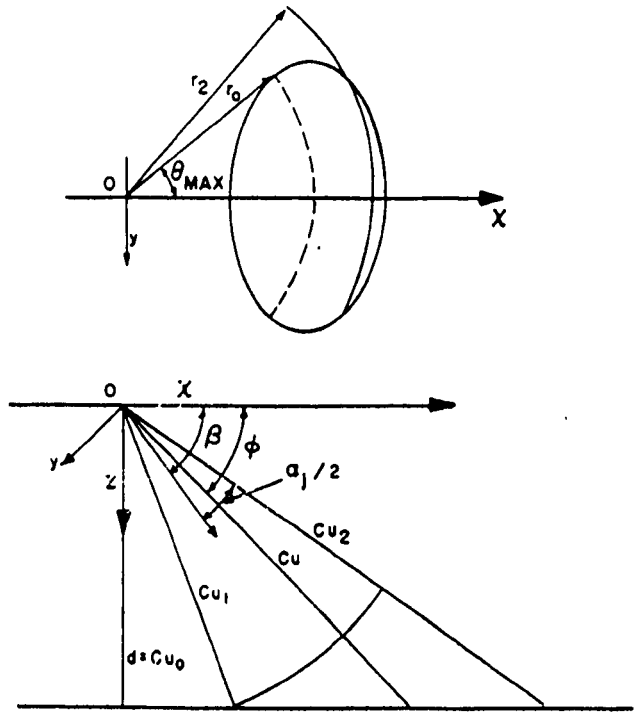

Fig. 2A4. Geometry for case 2

$$A_j(u) = \pi[1 - \cos(a_j/2)] - 2\theta_1\frac{d}{cu} + 2\cos(a_j/2)\cos^{-1}\left[\frac{\cos\theta_1}{(1 - \cos^2\beta\sin^2\theta_1)^{1/2}}\right]$$

$$\pm 2\left\{\cos^{-1}[\cos\beta\csc(a_j/2)\sin\theta_1]\right.$$

$$-\cos(a_j/2)\cos^{-1}\left[\frac{\cot(a_j/2)\cos\beta\sin\theta_1}{(1 - \cos^2\beta\sin^2\theta_1)^{1/2}}\right]$$

$$u_1 < u < u_2, \tag{2A10}$$

and

$$A_j(u) = 2\pi[1 - \cos(a_j/2)], \quad u_2 \leq u, \tag{2A11}$$

where "$\pm$" in Eq. 2A10 is + for $r_2 > r_0$ and − for $r_2 \leq r_0$.

In case 3, $\beta + (a_j/2) > \pi/2$ (Fig. 2A5). In this case

$$A_j(u) = 0, \quad u \leq u_0, \tag{2A12}$$

$$A_j(u) = 2\pi[1 - (\frac{d}{cu})], \quad u_0 < u < u_1 \tag{2A13}$$

$$A_j(u) = \pi[1 - \cos(a_j/2)] - \frac{2\theta_1 d}{cu} + 2\cos(a_j/2)\cos^{-1}\left[\frac{\cos\theta_1}{(1 - \cos^2\beta\sin^2\theta_1)^{1/2}}\right]$$

$$+ 2\cos^{-1}[\cos\beta\csc(a_j/2)\sin\theta_1]$$

$$- 2\cos(a_j/2)\cos{-1}\left[\frac{\cot(a_j/2)\cos\beta\sin\theta_1}{(1 - \cos^2\beta\sin^2\theta_1)^{1/2}}\right],$$

$$u_1 < u < u_2, \tag{2A14}$$

and

$$A_j(u) = 2\pi[1 - \cos(a_j/2)], \quad u = u_2. \tag{2A15}$$

In all three cases

$$u_0 = \frac{d}{c},$$

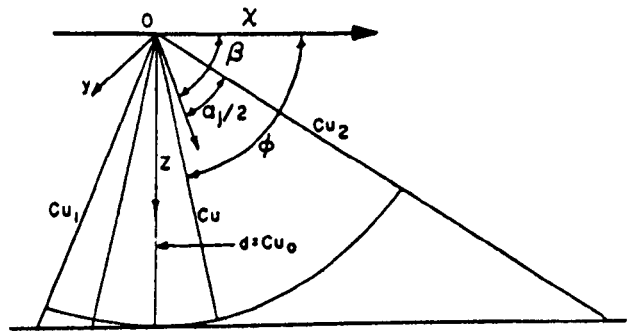

Fig. 2A5. Geometry for case 3

$$u_1 = \frac{d}{c \sin [\beta + (a_j/2)]},$$

$$u_2 = \frac{d}{c \sin [\beta - (a_j/2)]},$$

$$\cos \theta_1 \cos \beta = \frac{\cos (a_j/2) - \sin \beta \sin \phi}{\cos \phi} = \frac{cu \cos (a_j/2) - d \sin \beta}{(c^2u^2 - d^2)^{1/2}}, \quad cu > d,$$

$$\sin \phi = \frac{d}{cu}$$

$$r_2 = \cos \phi = \frac{(c^2u^2 - d^2)^{1/2}}{cu},$$

and

$$r_0 = [1 - \sec^2(a_j/2) \sin^2\beta]^{1/2}.$$

We now express $A_j(u)$ explicitly. As shown in Fig. 2A1, $r(\theta) = r_1'(\theta) \cup r_1(\theta)$ is a projection of the boundary of a spherical cap on the xy plane. It is then an ellipse of the form

$$\frac{(x - h)^2}{a^2} + \frac{y^2}{b^2} = 1, \quad a \geq b.$$

It is easy to verify that

$$a = \sin (a_j/2),$$

$$b = \sin (a_j/2),$$

and

$$h = \cos \beta \cos (a_j/2).$$

Letting $x = r \cos \theta$ and $y = r \sin \theta$, we get

$$r(\theta) = \frac{\cos \theta \cos \beta \cos (a_j/2) \pm \sin \beta[\sin^2(a_j/2) - \sin^2\theta \cos^2\beta]^{1/2}}{1 - \sin^2\theta \cos^2\beta},$$

where $r(\theta) \equiv r_1^i(\theta)$ when the $\pm$ term is $-$ and where $r(\theta) \equiv r_1(\theta)$ when the $\pm$ term is $+$.

Also,

$$r_2 = \cos\theta = \frac{(c^2u^2 - d^2)^{1/2}}{cu},$$

$$\cos\theta_1 \cos\beta = \frac{\cos(a_j/2) - \sin\beta\sin\phi}{\cos\phi} = \frac{cu\cos(a_j/2) - d\sin\beta}{(c^2u^2 - d^2)^{1/2}}, \quad cu > d,$$

$$r_0 = [1 - \sec^2(a_j/2)\sin^2\beta]^{1/2},$$

and

$$\cos\theta_{max} = [1 - \sec^2\beta\sin^2(a_j/2)]^{1/2}.$$

Then for case 1

$$\beta = \frac{\pi}{2} \text{ and } \cos(a_j/2) \leq \sin\phi$$

or

$$\beta + (a_j/2) > \frac{\pi}{2} \text{ and } \cos(a_j/2) \leq \sin\theta \leq -\cos[\beta + (a_j/2)].$$

The area is merely the area of a spherical cap, which is given by

$$A_j(u) = 2\pi[1 - \cos(90° - \phi)] = 2\pi\left[1 - \frac{d}{cu}\right] \tag{2A16}$$

or with respect to time t

$$A_j(t) = 2\pi\left[1 - \frac{2d}{ct}\right] \text{ and } A_j(t - \tau) = 2\pi\left[1 - \frac{2d}{c(t - \tau)}\right] \tag{2A17}$$

For case 2

$$\beta + (a_j/2) \leq \frac{\pi}{2} \text{ and } r_2 \leq r_0.$$

Then (Fig. 2A2)

$$A_j(u)=2\int_0^{\theta_1}\int_{r_1(\theta)}^{r_2} r\sec\gamma\, dr d\theta$$

$$=2\int_0^{\theta_1} d\theta\int_{r'_1(\theta)}^{r_2}\frac{rdr}{\sqrt{1-r^2}}=-2\int_0^{\theta_1}[(1-r^2)^{1/2}]_{r'_1(\theta)}^{r_2}\,d\theta.$$

Since $r_2=\cos\phi$,

$$A_j(u)=-2\theta_1\sin\phi+2\int_0^{\theta_1}(1-[r'_1(\theta)]^2)^{1/2}d\theta$$

$$=-2\theta_1\sin\phi+2\int_0^{\theta_1}\left[1-\left\{\frac{\cos\theta\cos\beta\cos(a_j/2)-\sin\beta[\sin^2(a_j/2)-\sin^2\theta\cos^2\beta]^{1/2}}{1-\sin^2\theta\cos^2\beta}\right\}^2\right]^{1/2}d\theta$$

$$=-2\theta_1\sin\phi+2\int_0^{\theta_1}\left\{\frac{\cos\beta\cos\theta[\sin^2(a_j/2)-\sin^2\theta\cos^2\beta]^{1/2}+\cos(a_j/2)\sin\beta}{1-\sin^2\theta\cos^2\beta}\right\}d\theta$$

$$=-2\theta_1\sin\phi+2\cos(a_j/2)\int_0^{\theta_1}\frac{\sin\beta d\theta}{1-\sin^2\theta\cos^2\beta}+2\int_0^{\theta_1}\frac{\cos\beta\cos\theta[\sin^2(a_j/2)-\sin^2\theta\cos^2\beta]^{1/2}}{1-\sin^2\theta\cos^2\beta}d\theta.$$

The first integral above is of the form #231 in Burington*, and after making the substitution

$$\cos\zeta=\cos\beta\csc(a_j/2)\sin\theta$$

the second integral reduces to form #228. Therefore

$$A_j(u)=-2\theta_1\sin\phi+2\cos(a_j/2)\tan^{-1}(\sin\beta\tan\theta_1)+\pi[1-\cos(a_j/2)]$$

$$-2\cos^{-1}[\cos\beta\csc(a_j/2)\sin\theta_1]+2\cos(a_j/2)\tan^{-1}\left[\frac{\tan\{\cos^{-1}[\cos\beta\csc(a_j/2)\sin\theta_1]\}}{\cos(a_j/2)}\right]$$

or

$$A_j(u)=\pi[1-\cos(a_j/2)]-\frac{2\theta_1 d}{cu}+2\cos(a_j/2)\cos^{-1}\left[\frac{\cos\theta_1}{(1-\cos^2\beta\sin^2\theta_1)^{1/2}}\right]$$

$$-2\cos^{-1}[\cos\beta\csc(a_j/2)\sin\theta_1]+2\cos(a_j/2)\cos^{-1}\left[\frac{\cot(a_j/2)\cos\beta\sin\theta_1}{1-\cos^2\beta\sin^2\theta_1)^{1/2}}\right]. \quad (2A18)$$

*R.S. Burington, *Handbook of Mathematical Tables and Formulas*, Handbook Publishers, Sandusky, 1948.

Equation 2A18 can then be converted to $A_j(t)$ and $A_j(t - \tau)$ as in case 1 (Eq. 2A17) for use in Eq. 2A5.

For case 3

$$\beta + (a_j/2) \leq \frac{\pi}{2} \text{ and } r_2 \geq r_0$$

or

$$\beta + (a_j/2) > \frac{\pi}{2} \text{ and } \sin\phi \geq -\cos[\beta + (a_j/2)].$$

Then

$$A_j(u) = 2\pi[1 - \cos(a_j/2)] - 2\int_0^{\theta_1}\int_{r_2}^{r_1(\theta)} r \sec\gamma \, dr d\theta.$$

As in case 2

$$A_j(u) = 2\pi[1 - \cos(a_j/2)] + 2\int_0^{\theta_1}(1 - r_2)^{1/2}\int_{r_2}^{r_1(\theta)} d\theta$$

$$= 2\pi[1 - \cos(a_j/2)] - 2\theta_1 \sin\phi + 2\int_0^{\theta_1}(1 - [r_1(\theta)]^2)^{1/2} d\theta$$

$$= 2\pi[1 - \cos(a_j/2)] - 2\theta_1 \sin\phi$$

$$+ 2\int_0^{\theta_1}\left[1 - \left\{\frac{\cos\theta_1 \cos\beta \cos(a_j/2) + \sin\beta[\sin^2(a_j/2) - \sin^2\theta\cos^2\beta]^{1/2}}{1 - \sin^2\theta\cos^2\beta}\right\}^2\right]^{1/2} d\theta$$

$$= 2\pi[1 - \cos(a_j/2)] - 2\theta_1\sin\phi$$

$$+ 2\int_0^{\theta_1}\left\{\frac{\cos(a_j/2)\sin\beta - \cos\beta\cos\theta[\sin^2(a_j/2) - \sin^2\theta\cos^2\beta]^{1/2}}{1 - \sin^2\theta\cos^2\beta}\right\} d\theta.$$

As in case 2

$$A_j(u) = \pi[1 - \cos(a_j/2)] - \frac{2\theta_1 d}{cu} + 2\cos(a_j/2)\cos^{-1}\left[\frac{\cos\theta_1}{(1 - \cos^2\beta\sin^2\theta_1)^{1/2}}\right]$$

$$+ 2\cos^{-1}[\cos\beta\csc(a_j/2)\sin\theta_1]$$

$$- 2\cos(a_j/2)\cos^{-1}\left[\frac{\cot(a_j/2)\cos\beta\sin\theta_1}{(1 - \cos^2\beta\sin^2\theta_1)^{1/2}}\right]. \qquad \text{(2A19)}$$

Finally, similar to cases 1 and 2, Eq. 2A19 is converted to terms of $A_j(t)$ and $A_j(t - \tau)$ for use in Eq. 2A5.

APPENDIX 2B: EFFECTS OF REFRACTION IN DETERMINING SCATTERING STRENGTH

If the medium is isotropic or if the velocity gradient in the medium is sufficiently small, Eq. 9 or Eq. 10 of the text is directly applicable. They are not applicable for the medium in which data were taken. Therefore the equations were modified to accommodate the refraction.

Equation 9 from the text is

$$S = (E - M - G + 20 \log r + Kr + D) - (L + 20 \log i - D - Kr + 10 \log P_i). \quad (2B1)$$

Rearranging terms gives

$$S = E - M - G - L - 20 \log i + 2D + 20 \log r + 2Kr - 10 \log P_i. \quad (2B2)$$

The last three terms are sensitive to the effects of the anisotropic medium.

To take into account the refractive nature of the medium, it is convenient to make a series of ray acoustic computations of the propagational factors required. A set of such computations was made for the analysis of the Blake Plateau data. The factors computed (Fig. 2B1) were the following:

θ_0 Angle of the ray with respect to the horizontal at the source (degrees),

θ_b Angle of the ray with respect to the horizontal at the bottom (degrees),

d Depth of the bottom below the source (m),

r_c Distance over the curved path (m),

x_c Horizontal distance from the source to the point where the ray intersects the bottom (m),

r_s Distance over the straight path from the source to the bottom (m),

x_s Horizontal distance from the source to the bottom for the straight path r_s (m),

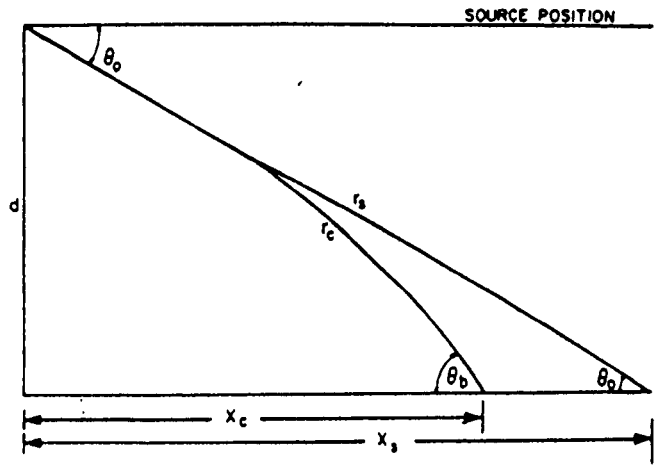

Fig. 2B1. Geometry of the propagational factors

C_v Vertex velocity,

t Travel time from the source to the bottom over the r_c path,

$< C >$ Average sound speed over the r_c path (m/sec),

δd Spreading loss over the r_c path in the downward direction (dB), and

δu Spreading loss over the r_c path in the upward direction (dB).

Computation of these quantities followed Horton's* equations using the conventional method of dividing the sound-speed profile into a number of layers of constant-gradient or linear sound-speed segments. Computations were made with a digital computer, with the depression angle θ being incremented through the angles of interest for the depths employed.

It was found that the variation of the average sound speed over the path as a function of angle was less than 1 m/sec for angles between 15° and 90°. This enabled the use of a constant average sound speed of 1523.9 m/sec for the analysis, having an error of less than 1 part in 3000. Since all measurements were made as a function of time, they were converted to distance using the average sound speed. This applies to Eqs. 2A17, 2A18, and 2A19 in the evaluation of P_i in Appendix 2A.

In evaluating the spreading loss over the return path, indicated by the term 20 log r of Eq. 2B2, it was most convenient to substitute the spreading loss over the upgoing path δ_u

*J.W. Horton, *Fundamentals of Sonar*, U.S. Naval Institute, NavShips 92719, 1957.

Table 2B1. Transducer characteristics.

Transducer Depth (m)	Receiving Sensitivity M (dB re 1 volt/μbar)	Transmitting Response L (dB re 1 μbar) at 1 yard/ampere)
16.5	−74.2	106.4
30.2	−75	105.6

obtained from the computation of propagation factors discussed above. This included both the distance over the curved path and the deviation from inverse square law caused by the refraction. The straight-line distance r in the term $2Kr$ of Eq. 2B2 was replaced by the curved path distance r_c that was computed.

To obtain the average attenuation coefficient K over the path, a numerical integration over the depth divided by the total depth was made:

$$<K> = \frac{1}{d} \int_0^d K(z)\, dz \tag{2B3}$$

and

$$K = 10 \log <K>, \tag{2B4}$$

where $K(z)$ is the function relating absorption and depth. The effects of pressure and change of salinity with depth were considered. The absorption versus depth was obtained by combining the temperature-versus-depth curve (also employed in the propagation computations) and the salinity profiles, using DelGrosso's† tabulation of absorption for various values of temperature and salinity. The Schulkin and Marsh‡ equation was used in taking account of pressure. The value of $<K>$ used in the analysis was 2.48×10^{-3} dB/m.

Pertinent constants of the system and the environment used in the analysis were the following: the fixed gain in the receiving system was $G = 30.6$ dB, the water depth was $d =$

†V.A. DelGrosso, "Dependence of Sound Absorption on Concentration, Frequency, and Temperature in $MgSo_4$ Solutions Equivalent to Sea Water-Graphs from Calculations Based on a Review," NRL Rept. 4279, June 1954.
‡M. Schulkin and H.W. Marsh, "Sound Absorption in Sea Water," J. Acoust. Soc. Am. 34, 864 (1962).

805 m, the transducer characteristics, which are pressure and temperature sensitive, were as given in Table 2B1 at the temperature and depth used, and the source levels for the experiment were in the range of 117.6 to 121.0 dB.

The conversion from depression angle β to grazing angle δ at the bottom is obtained from the computation of the propagation factors, making the scattering-strength measurements independent of the medium refraction.

Chapter 3

AMPLITUDE DISTRIBUTIONS OF MONOSTATIC BOTTOM-SCATTERED SIGNALS*

INTRODUCTION

The purpose of this chapter is to determine the statistical nature of acoustic fields scattered from the ocean bottom for various directions of scatter. Results will be presented as histograms of the amplitude density functions (Fisz, 1963).

THE EXPERIMENT

This experiment was conducted using the monostatic geometry illustrated in Fig. 1. The platform is moving at a velocity of approximately 2 knots with the piston transducer depressed at an angle θ.

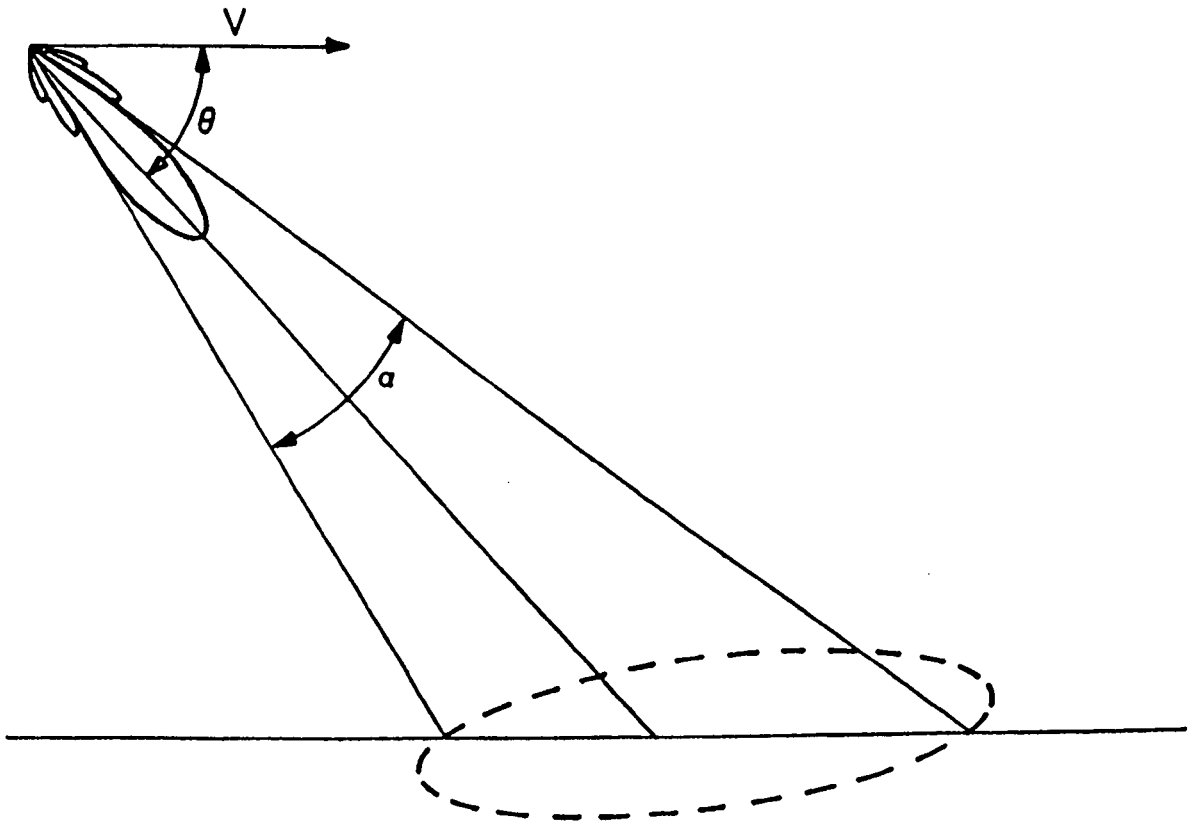

Fig. 1. Geometry of the monostatic scattering experiment.

*Some of this material was presented earlier (Hurdle et al., 1968).

As in the previous discussion, the transducer had a beamwidth α of approximately 8° at the half power points, with all sidelobes being down 17 dB or more. The transducer was driven with a 19.5-kHz pulsed CW signal with pulse lengths between 0.170 and 1.000 sec. In all cases the pulse length was long compared to the transient contribution from the scatter area. This gave a steady-state portion of the return that continues as long as a simultaneous contribution from all of the area defined by the incident beam exists. The received scattered signal envelope was sampled during this steady-state portion at a 2-kHz rate and recorded in digital form on magnetic tape. Instrumentation also provided for amplitude calibration.

The bottom in the experimental area is geographically flat, with essentially constant water depth. Corings indicate the bottom material to be a uniform calcareous ($CaCO_3$-containing) sediment. Photographs of the bottom show small sand ripples with random directions. Previous measurements of scattering strength in the area indicates the bottom to be statistically uniform over the area investigated.

Runs were made with depression angles between 30° and 90°. Table 1 gives the influence of the refraction on the depression angle. For a single run, all parameters were maintained constant, and the data were recorded for a number of scatter returns. Individual returns displayed a large amplitude variation as the interference field produced by the bottom scattering was traversed. The average ratio of scatter signal to ambient noise was 40 dB or greater for all runs.

Table 1. Influence of refraction on the depression angle.

Depression Angle (degrees)	Incident Grazing Angle (degrees)
15	19.7
30	32.4
45	46.4
60	60.8
70	70.5
90	90.0

EXPERIMENTAL RESULTS

The results are presented as histograms such as in Fig. 2. The abscissa is in units of the standard deviation σ for the data sample. The value of the mean μ and the value of the standard deviation σ are stated in each illustration.

The histograms are shown for each depression angle as the depression angle is increased. Figure 2 is for an angle of 45° and displays a good fit to a Rayleigh density function shown as the smooth curve. The Rayleigh density function is the expected function for completely random scattering.

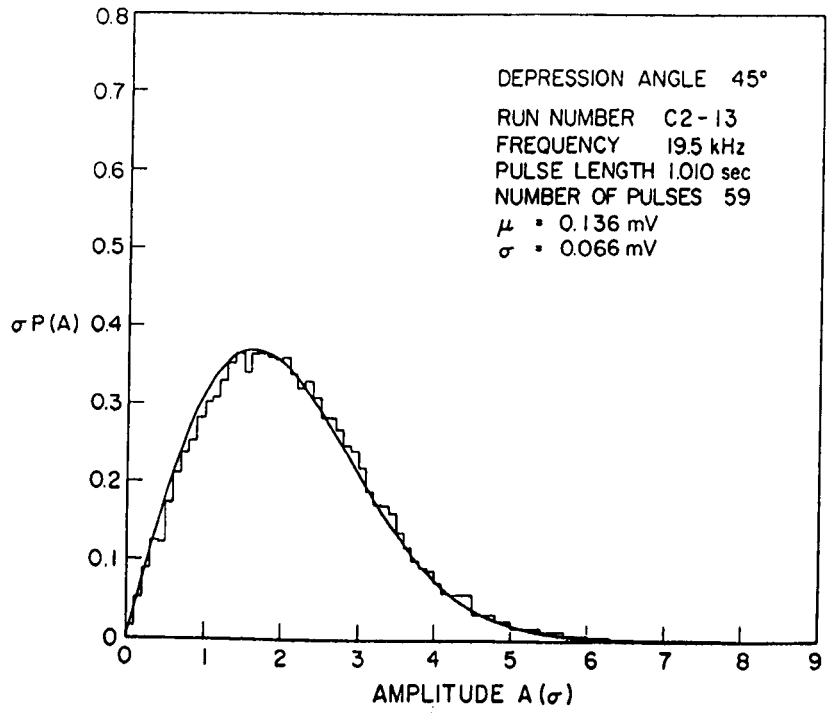

Fig. 2. Histogram for a 45° depression angle with a Rayleigh density function.

Figure 3 is the histogram for 50°. The fit with the Rayleigh curve is not as good at this angle.

Figure 4 is for a 60° depression angle. The correspondence with the Rayleigh distribution is decreasing. A much better fit can be made if an arbitrary Rayleigh parameter is used, but when the sample standard deviation is used to obtain the parameter, as was done here, the disagreement is significant.

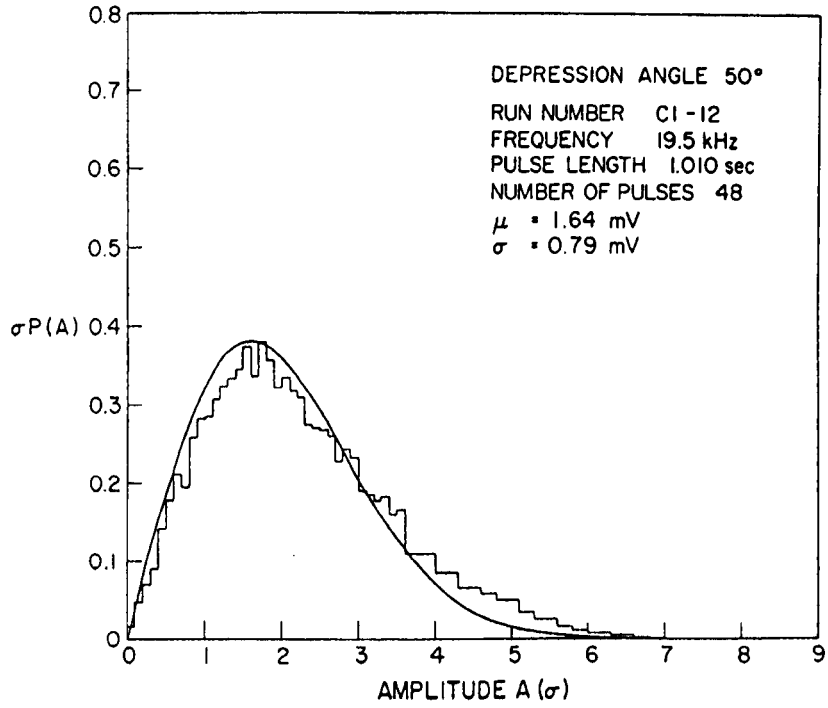

Fig. 3. Histogram for a 50° depression angle with a Rayleigh density function.

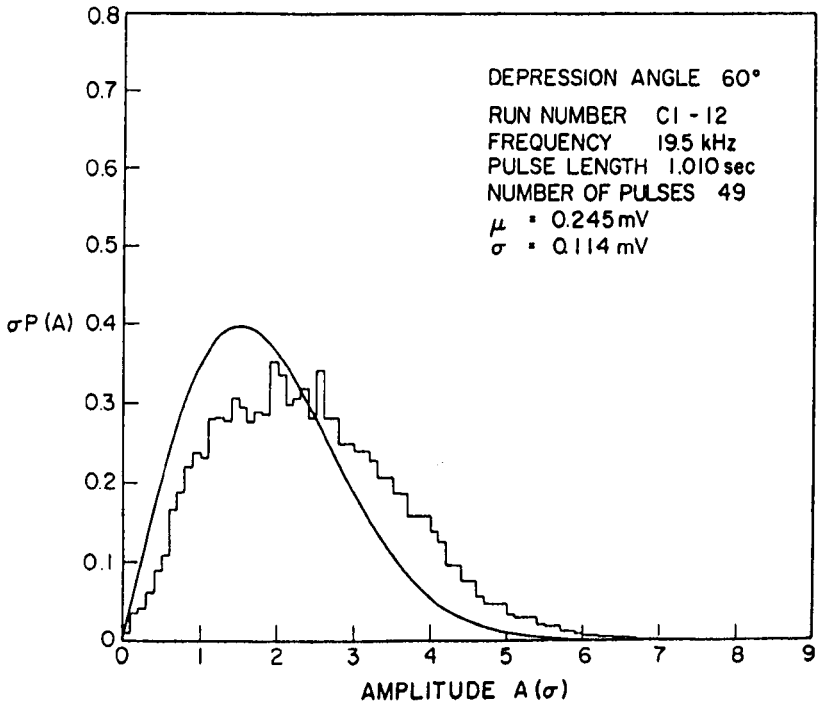

Fig. 4. Histogram for a 60° depression angle with a Rayleigh density function.

In Fig. 5, a closer approach to 90° than the preceding figures, the histograms have progressively deviated from Rayleigh and have begun to evolve into a multipeaked structure. For Figs. 6, 7, 8, and 9 for 75°, 80°, 85°, and 90° respectively, and for the remaining figures, the Rayleigh curve has been eliminated. Two peaks are well defined in each of Figs. 7, 8, and 9, showing an evolution of bimodal peaks as depression angle increases.

Figure 10 is another 90° sample obtained from a completely independent run on a different day. It illustrates the repeatability of the histogram structure at the 90° angle. The data from a run was also divided into four consecutive quarters, and histograms were obtained for each quarter. The structure remains the same, indicating that the bottom was statistically uniform over the run.

Figure 11 illustrates an ensemble histogram that was obtained by selecting one value for each return at a constant time after transmission. This was chosen from the same data used in Fig. 10. Although there were only 186 points, the form of the two histograms is substantially the same.

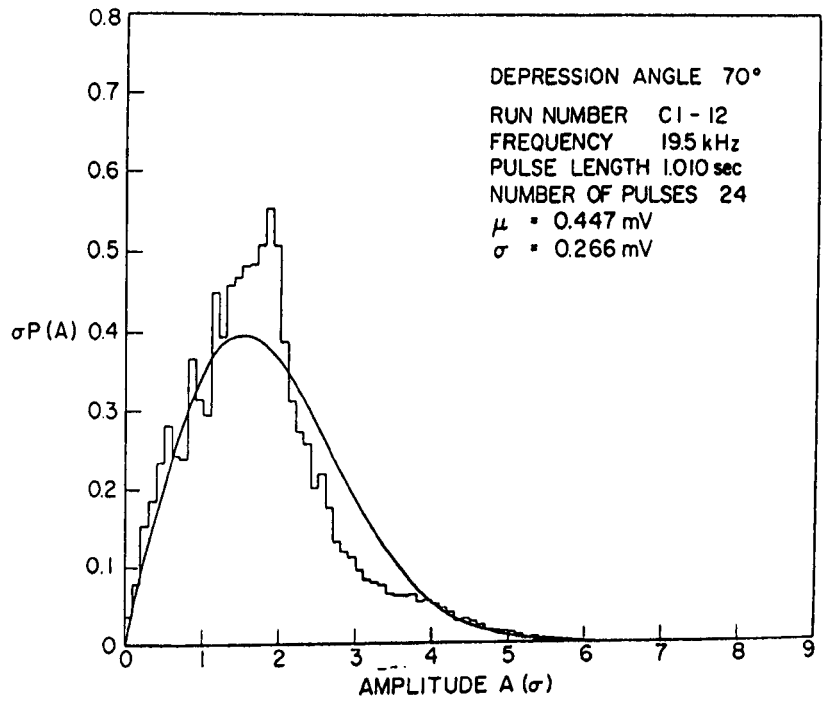

Fig. 5. Histogram for a 70° depression angle with a Rayleigh density function.

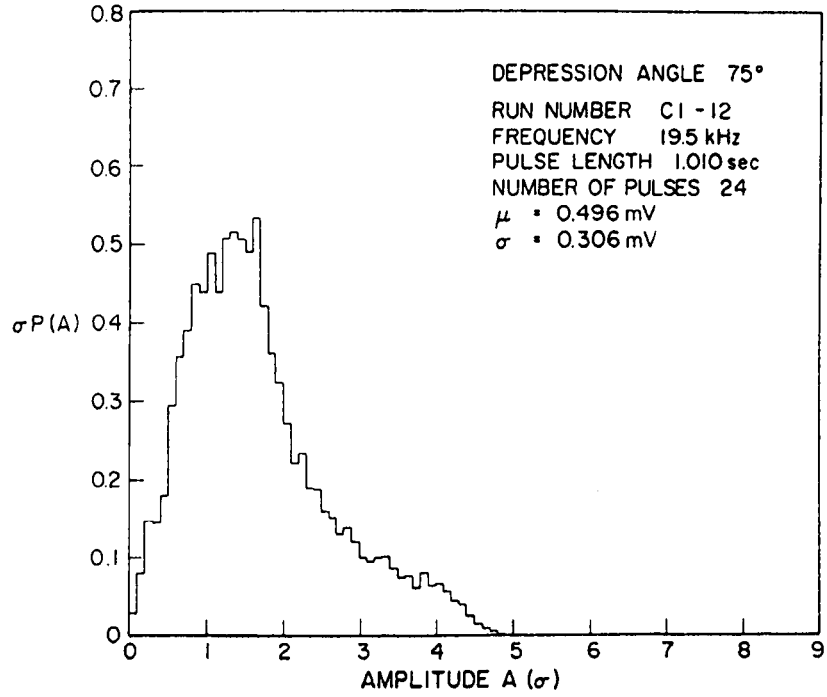

Fig. 6. Histogram for a 75° depression angle.

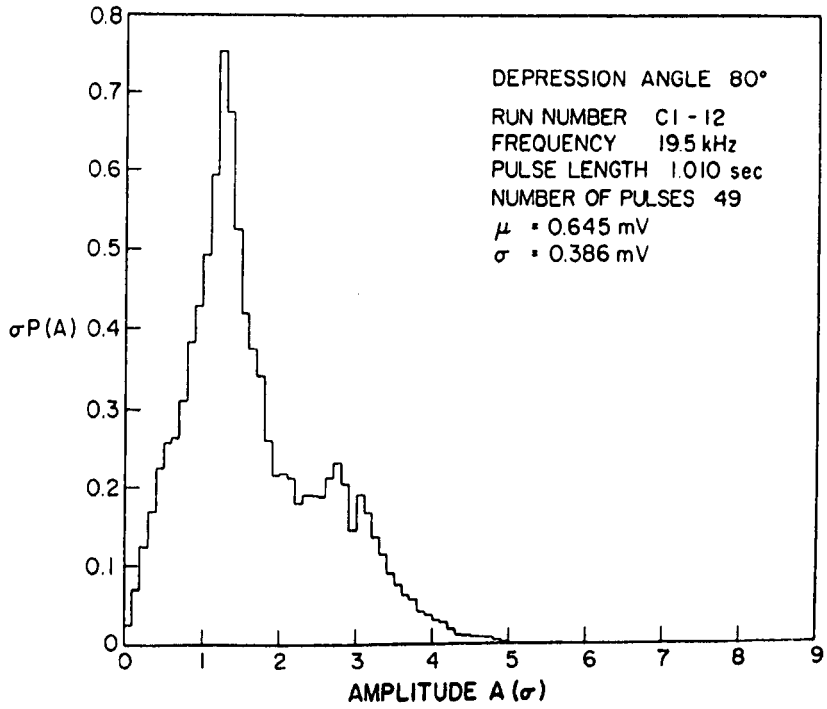

Fig. 7. Histogram for an 80° depression angle.

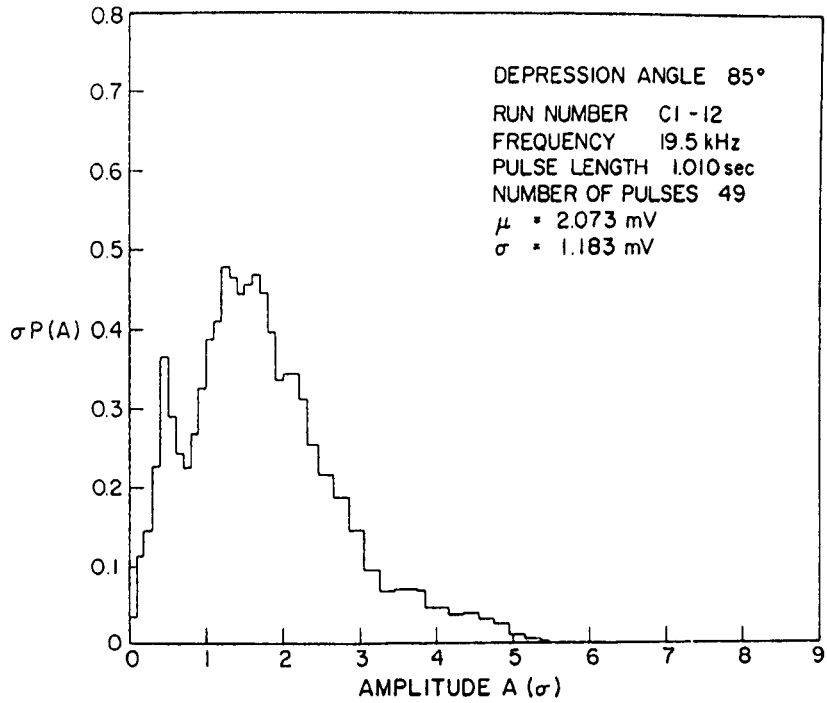

Fig. 8. Histogram for an 85° depression angle.

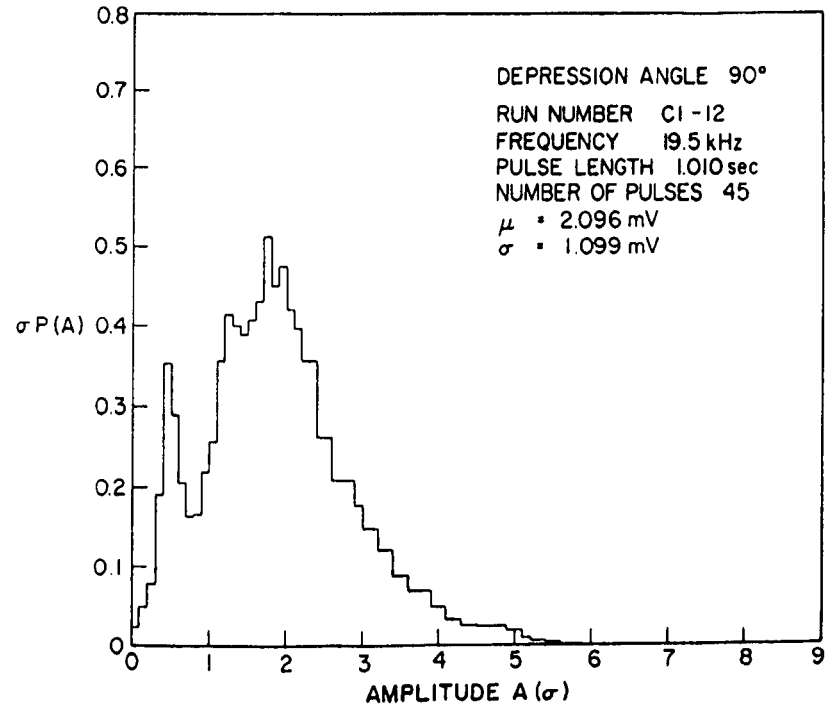

Fig. 9. Histogram for a 90° depression angle.

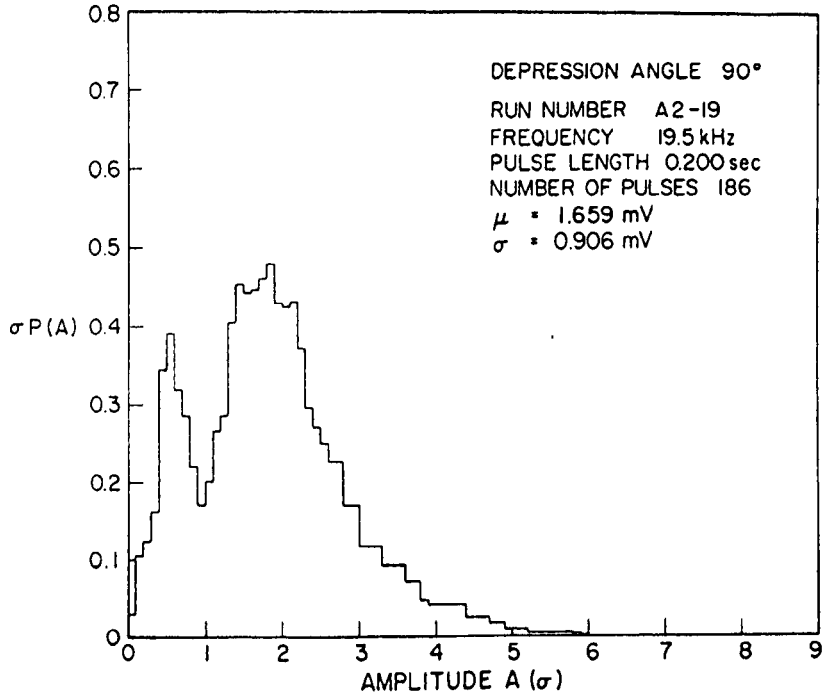

Fig. 10. Histogram for a 90° depression angle (independent sample).

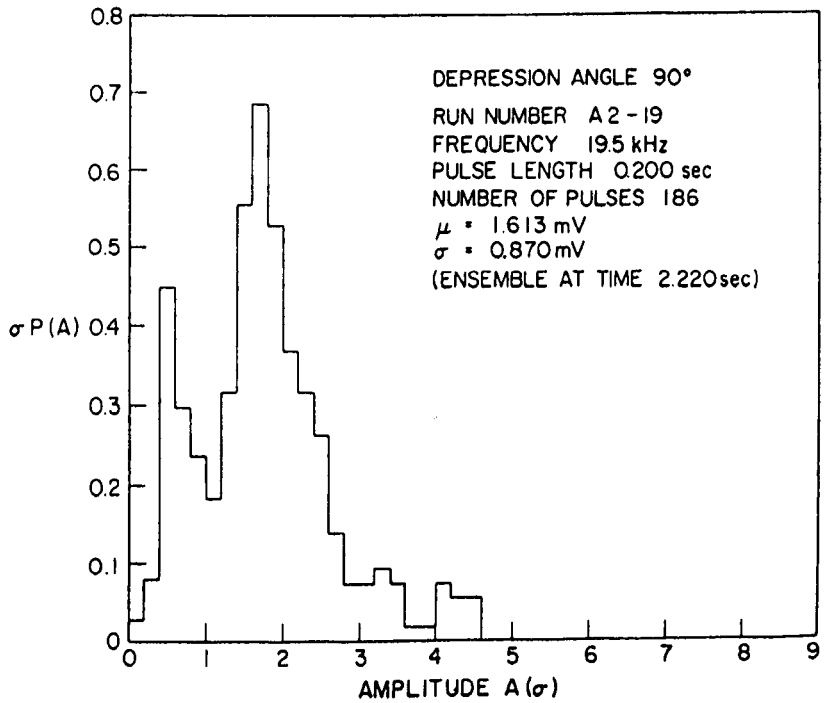

Fig. 11. Histogram for a 90° depression angle (ensemble at time 2.220 sec).

Figure 12 is a histogram of the second bounce, where the signal, transmitted at 90°, has been scattered from the bottom, the surface, and the bottom for the second time. Here the agreement with the Rayleigh density function is again good.

Chapter 1 stated that there is an approximately linear frequency gradient across the insonified area. If one integrates over a signal with a linear frequency gradient, the result is two signals with frequencies corresponding to the frequencies at endpoints of the gradient. The two signals would then combine to form beats. This forming of beats by two signals related in this way to the frequency gradient is confirmed by the fact that the fluctuation or beat rate can be controlled by controlling the rate of change of the transmitted signal frequency and thus the gradient.

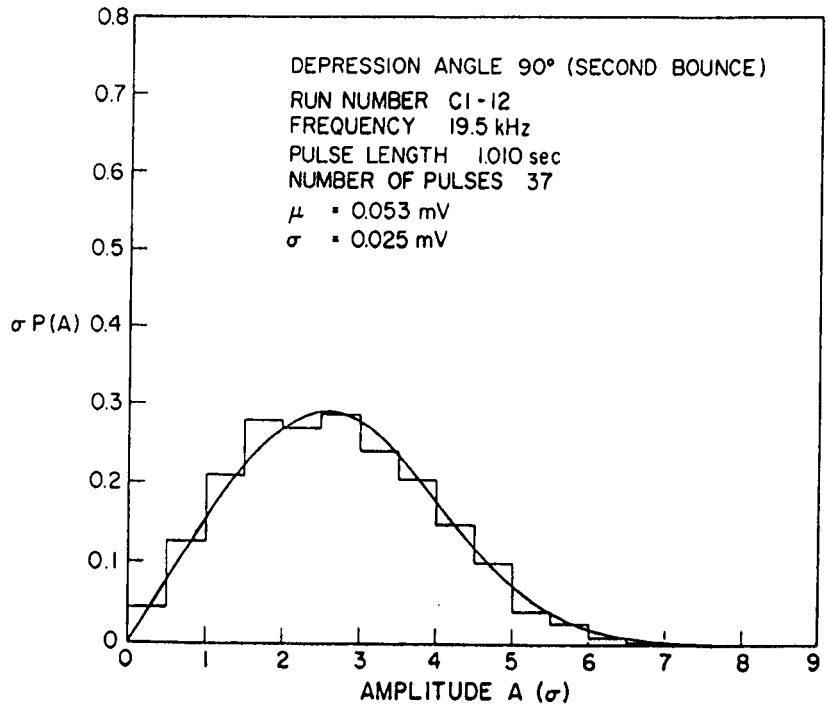

Fig. 12. Histogram for a 90° depression angle with a Rayleigh density function (second bounce).

The amplitude density function of the sum of two signals with random phase and unequal amplitudes will result in a bimodal distribution. Figure 13 is an example of this type of distribution. Although the evolution of the density function from Rayleigh at 45° to the bimodal pattern at 90° is not completely understood, it is clear that the major structure is a result of the Doppler frequency gradient.

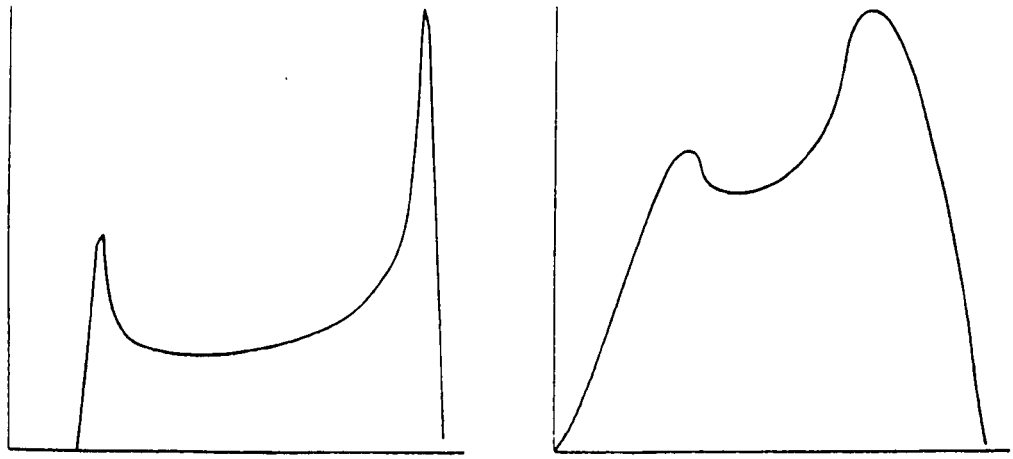

$a_1 = 2, a_2 = 3$; Noise = .05 (σ) $a_1 = 2, a_2 = 3$; Noise = .33 (σ)

Fig. 13. Probability density functions with two components plus noise.

Figure 13 illustrates density functions for two components with amplitudes of 2 and 3 units respectively plus a third component that is a noise or Rayleigh component, with an increase of the noise from Fig. 13a to Fig. 13b. Similarly density functions with three (Fig. 14) and four (Fig. 15) constant-amplitude components have been tried.

Figure 16 is the density function for two components with amplitudes of 1 and 2 units respectively plus a small component of noise, a Rayleigh component with $\sigma = 0.01$. The function's fit to Figs. 9 and 10 shows a correspondence in the major features but not in the details.

Probability density functions for a small number of vectors with random phase and arbitrary amplitudes could become a significant tool in analyzing experimental data when a sum of a small number of vectors is suspected. By varying the parameters until a fit with an experimental distribution is obtained, an interpretation could reveal the number and magnitudes of the contributing vectors. The process needs research to understand and determine the parameters that control the details in the shapes of the distributions that result from these density functions.

CONCLUSIONS

In summary, amplitude histograms of the scattered acoustic field have been obtained in a monostatic experiment. The histograms trend toward a good fit with the Rayleigh density

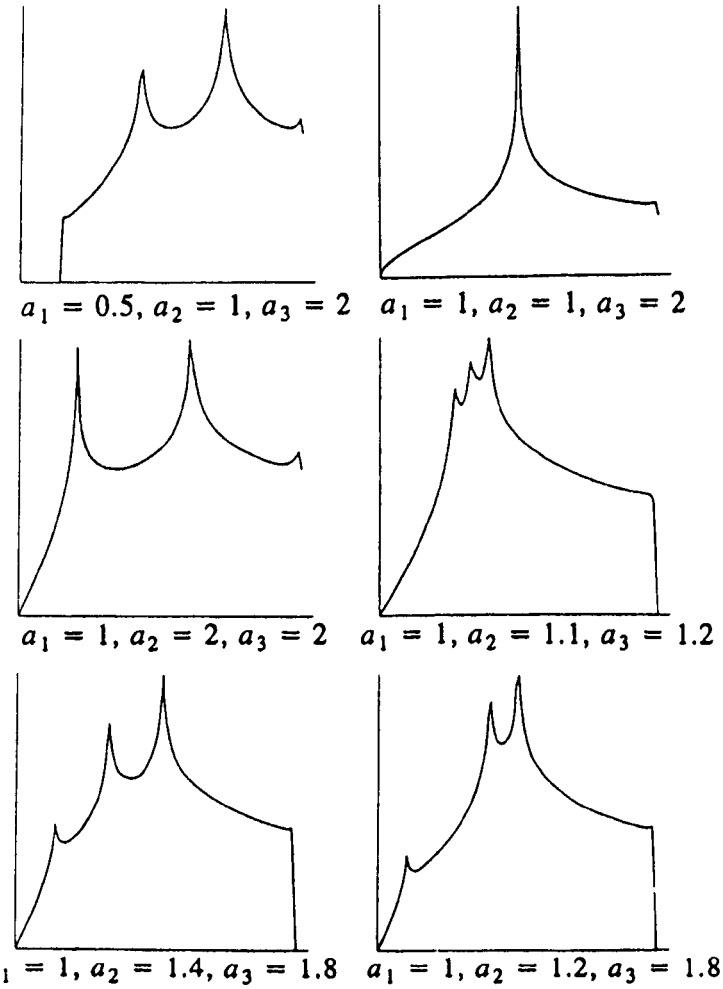

Fig. 14. Probability density functions with three components.

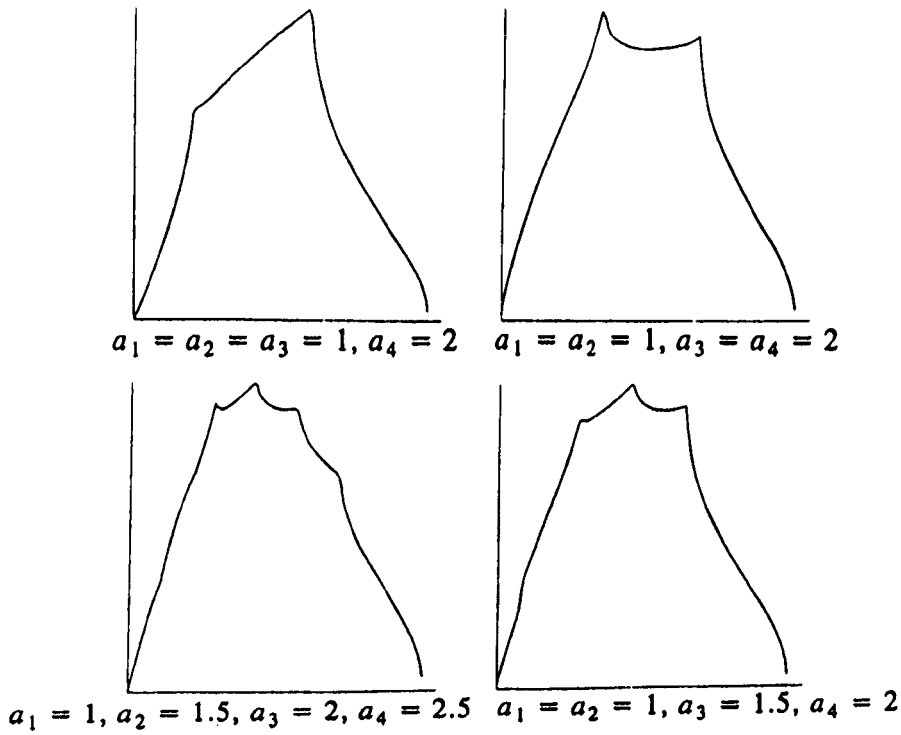

Fig. 15. Probability density functions with four components.

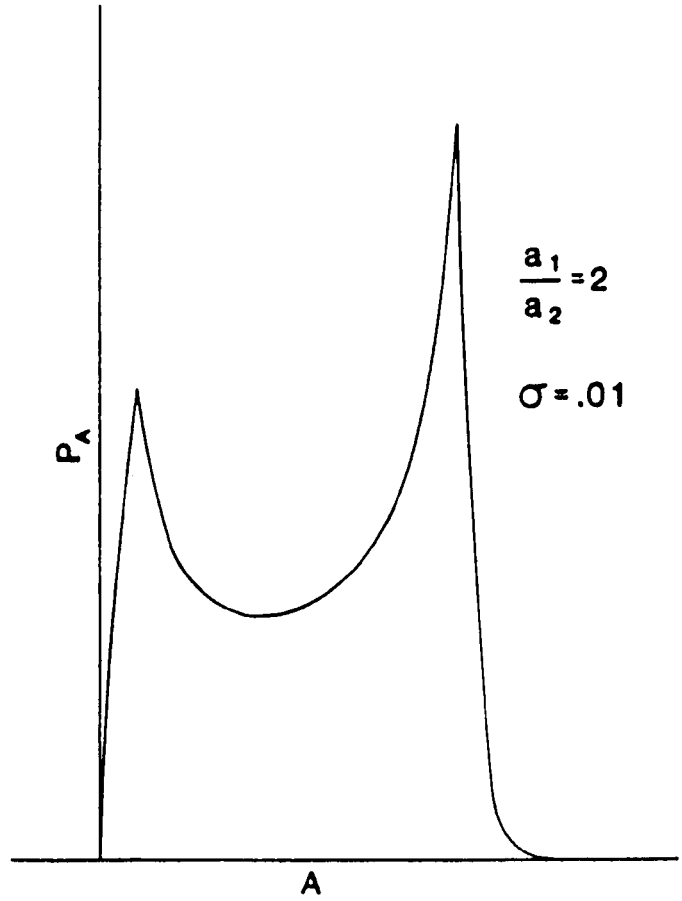

Fig. 16. Probability function with two components (such that $a_1/a_2 = 2$) plus noise (with $\sigma = 0.01$).

function at small depression angles. They progressively deviate from Rayleigh as the angle is increased, taking on a bimodal structure in the vicinity of the specular direction at 90°.

Finally the analyses indicate that the unusual histograms are valid and repeatable statistics of the scatter process, with the bimodal structure originating from the Doppler gradient across the bottom scatter area.

REFERENCES

M. Fisz, *Probability Theory and Mathematical Statistics*, Wiley, New York, 1963.

B.G. Hurdle, K.D. Flowers, and K.P. Thompson, "Amplitude Distributions of Monostatic Bottom-Scattered Signals," J. Acoust. Soc. Am. **44**, 356 (1968).

Edward L. Wright, "Probability Density Functions of n Vectors Added With Random Directions," NRL Rept. 6922, 1969.

Chapter 4

THREE-DIMENSIONAL SCATTERED FIELDS FROM THE OCEAN BOTTOM*

INTRODUCTION

Several models have been developed, generally differing in the approximations and assumptions made, which predict the scattered field. To evaluate these models, it is necessary to have experimentally determined data from a variety of bottom roughnesses and compositions. Data in the specular and monostatic directions, being the easiest to obtain, are available in abundance. Since most models predict essentially the same value in the specular direction, only the monostatic point can be used to discriminate between models. Data in other directions have been obtained by only a few investigators (including Urick (1954), Nolle et al. (1963), Hurdle et al. (1971), and Horton et al. (1967)) over limited regions of the scattered field for a limited number of surface conditions. This chapter presents the most comprehensive set of measurements of the bottom-scattered field yet obtained.

THEORY

The analysis of data for this chapter is based on the isotropic scattering model of Eckart (1946) except that, following Urick (1954), scattering strength is used rather than the scattering coefficient. As in Chapter 2 the model states that

$$I_S = sI_iA \ , \tag{1}$$

where I_S is the intensity of the scattered signal referred to a unit distance (1 yard) from the boundary, s is the scattering strength, I_i is the incident intensity, and A is the insonified area (square yard) contributing to the scattered signal at a particular instant.

*Some of this material was presented earlier (Thompson et al., 1965, and Flowers et al., 1971).

A practical acoustic experiment employing a directive source and receiver requires an integral formulation of the received intensity I_r for a fixed β (Fig. 1), namely,

$$I_r(\psi, \xi) = \int_R \int S(\delta, \psi', \xi') \left[I_0 b(\delta, \theta) \frac{10^{-Kr}}{r^{\gamma}} \right] \left[b_1(\psi', \xi') \frac{10^{-Kr'}}{r'^{\gamma'}} \right] dR , \quad (2)$$

where $s(\delta, \psi', \xi')$ is the scattering strength of dR in the direction (ψ', ξ'),* the first term in brackets is the incident intensity of dR, b and b_1 are the radiation functions of the source and receiver respectively, K (dB / yard) is the average absorption coefficient over the path, γ and γ' are the effective spreading-law coefficients over the paths,** and I_0 is the intensity on the axis at unit distance from the source.†

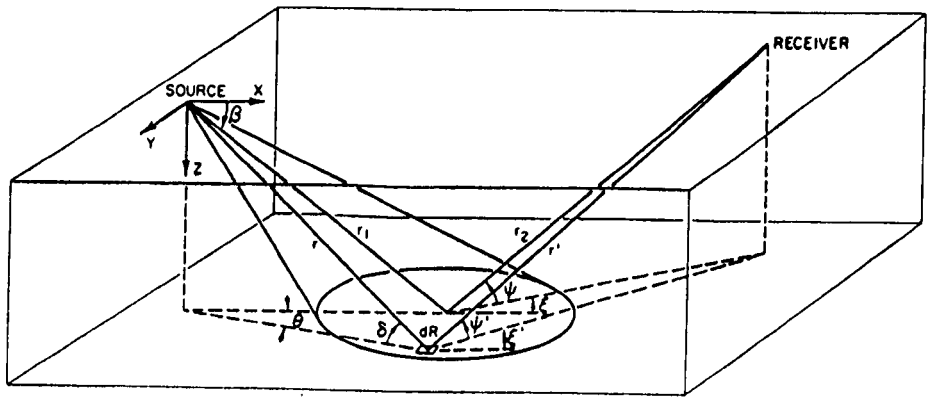

Fig. 1. Scattering geometry.

Now dR contains the factor r^2, so when we make the approximations $\gamma \approx 2$, $r \approx r_1$, and $r' \approx r_2$, Eq. 2 reduces to

$$I_r(\psi, \xi) = \frac{I_0 10^{-K(r_1+r_2)}}{r_2^{\gamma'}} \int_R \int s(\delta, \psi', \xi') b(\delta, \theta) b_1(\psi', \xi') \cot\delta \, d\delta \, d\theta . \quad (3)$$

For the special case of monostatic reception (the receiving transducer the same as the source) Eq. 3 reduces to

$$I_r(\beta) = \frac{I_0 10^{-2kr_1}}{r_1^{\gamma'}} \int_R \int s(\delta) b^2(\delta, \theta) \cot\delta d\delta d\theta . \quad (4)$$

*It is implicitly assumed that the scattering surface is homogeneous.

**The model has allowed for different spreading laws for the different paths. This is due to the dependence of spreading on the initial angle of a ray in the refractive medium. For this experiment the deviations of γ and γ' from 2 were less than ± 0.01.

†I_0 can be determined from the source transmitting response L and the source current i via $I_0 = L + 20 \log i - D$ dB, where D is a loss due to the sonar dome (1 dB in the present experiment).

If the source is directional and the receiver is essentially nondirectional, then $|s(\delta, \psi', \xi') - s(\beta, \psi, \xi)|$, $|\psi' - \psi|$, and $|\xi' - \xi|$ are all small for the ranges of δ and θ considered, so that, as an approximation, $s(\beta, \psi, \xi)$ may be removed from the integral (Chapter 2) and $b_1(\psi', \xi') =$ constant for the solid angle subtended by the insonified area. Then Eqs. 3 and 4 become

$$I_r(\psi, \xi) = \frac{I_0 10^{-K(r_1 + r_2)}}{r_2^{\gamma'}} s(\beta, \psi, \xi) b_1(\psi, \xi) \int\int b(\delta, \theta) \cot \delta \, d\delta \, d\theta \tag{5}$$

and

$$I_r(\beta) = \frac{I_0 10^{-2Kr_1}}{r_1^{\gamma'}} s(\beta) \int\int b^2(\delta, \theta) \cot \delta \, d\delta \, d\theta. \tag{6}$$

For $b(\delta, \theta)$ given in Fig. 2 the integrals in Eqs. 5 and 6 are -16.7 and -19.1 dB as calculated by the method of Appendix A in Hurdle and Flowers (1967) (with steady-state conditions assumed). Thus the scattering strength can be determined from Eqs. 5 and 6 when r_1, r_2, and γ' are determined by ray tracing and K is calculated by the method of Appendix A of this chapter.

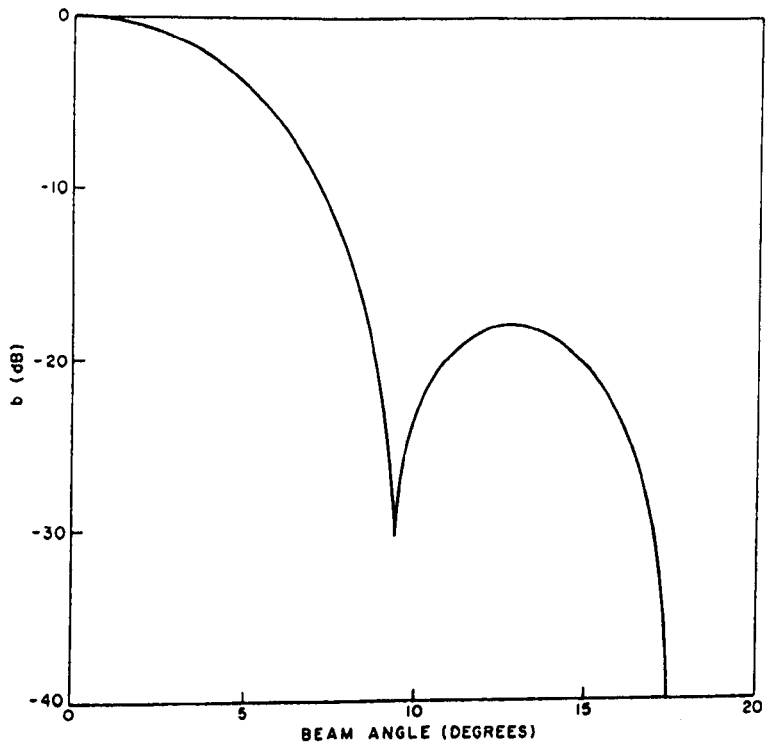

Fig. 2. Source radiation function.

Area of Operations

To obtain the three-dimensional field scattered from the ocean bottom, an experiment was conducted at the Blake Plateau under the conditions as indicated in APPENDIX A ending this work. This area was chosen because of the relative flatness of the bottom, the water depth varying less than ± 2 m over the experimental area, and because of the uniformity of the bottom material, which consisted of a calcareous sediment, as indicated by corings. Photographs of the bottom show small sand ripples with random directions.

Instrumentation

The instrumentation consisted of a special sonar operating at 19.5 kHz (Appendix A) as the acoustic source and a monostatic receiver. Bistatic reception was made on three special sonobuoys with radio links to the ship.

Procedure and Geometry

The return from each scattered pulse was received at the four locations: the transmitting transducer and three buoy-suspended hydrophones. The signals received at the buoy hydrophones were relayed by HF-FM links to a ship. A typical configuration of source, receiving buoys, and ship is illustrated in Fig. 3. The runs were started with the submarine at a range of 3500 to 4500 m from the receiving buoys. As the source progressed along the track, the scatter angles from the center of the insonified area to the receiving buoys increased until the center of the area passed the buoys and then decreased as the range was opened. The run was terminated when the level of the signals dropped to that of the background noise. In general this provided reasonable coverage of the hemisphere with the exception of those elevation angles ψ lying between 0° and 15°. This limitation resulted from the refractive structure of the medium. Each of the runs were made with the depression angle of the source beam held constant throughout the run. The depression angles chosen were 15°, 30°, 45°, 60°, 70°, and 90°. Several runs were made for each depression angle.

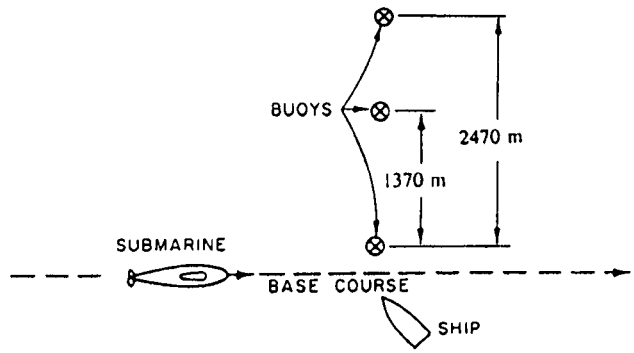

Fig. 3. Geometry of the source and the receivers.

Since the receiving buoys were free floating, it was necessary to monitor their individual positions continuously relative to the source and the insonified area. This monitoring was by an auxiliary acoustic triangulation system consisting of the source, buoys, and ship as described in Appendix 4B.

The entire instrumentation system was synchronized by a crystal clock in each of the two vessels. Both scattering and geometric data were recorded every 10 sec during the runs. Details of the instrumentation system and the characteristics of the runs employed are contained in Criss et al. (1967) and in APPENDIX A, at the end of this work.

Environmental data were taken periodically during the experiment to enable the computation of refractive effects of the medium in this area. These computations included the sound-speed profile, the mean sound speed over the path from the source to the center of the scatter area and from the center of the scatter area to the receiver as a function of the angle, the angle of arrival at the bottom as a function of the depression angle at the surface, the angle of arrival at the receiving points, the spreading loss over the paths as a function of angle, and other pertinant characteristics of the propagation.

ANALYSIS AND RESULTS

Treatment of Measured Data

The received data were analyzed to obtain the scattering strength in its appropriate direction. Values proportional to the received intensity I_r were determined from the received data,

and these values were used in Eqs. 5 and 6 to obtain the scattering strengths $s(\beta, \psi, \xi)$. Since the signals received in the monostatic direction had the same scatter direction throughout each run, it was convenient to treat them as a group. The method of analysis of the data received by the source transducer is contained in Hurdle and Flowers (1967).

For the data received at the buoys, the pressure amplitude envelope was recorded in analog form (on a decibel scale) as a function of time for each of the received scatter pulses. This amplitude-envelope recording was then incremented in 10- to 25-msec steps throughout the steady-state portion of the pulse return, excluding the transient buildup and decay at the leading and trailing edges, and converted from analog to digital form with the aid of a data reader. Each pulse was thus broken down into n increments, and each incremental digital value (designated e_i, $i = 1, \ldots, n$) was then squared to give a power ratio. The power ratios were averaged over the number of increments in each return:

$$< e^2 > = \frac{1}{n} \sum_{i=1}^{n} e_i^2. \tag{7}$$

The mean value of the envelope was then converted to logarithmic form (decibels) by

$$< E > = 10 \log < e^2 >. \tag{8}$$

This makes $< E > \propto < I >$, if the intensity is proportional to pressure squared.

Scattered Field

The mean scattering strength $s(\beta, \psi, \xi)$ for each scattered pulse was then computed using Eqs. 5 and 8. From the symmetry of the experiment to either side of the specular plane, the data in the region $180° \leq \xi \leq 360°$ (Fig. 1) were folded back into the region $0 \leq \xi \leq 180°$. Most of the data were averaged over increments of 10° in azimuth and elevation to provide sufficient quantities for statistical treatment. The only exceptions were the monostatic data points and the data for 90° incidence. The data at 90° are independent of azimuth, as confirmed by inspection. This independence enabled the data to be averaged over 2° increments in elevation.

Thus s is an average value of several mean returns. Along with s the logarithmic standard deviation (LSD) of the mean returns was calculated:

$$\text{LSD} = 10 \log \left[1 + \frac{\sigma}{\mu} \right],$$

where $\sigma = \sigma(< E >)$ and $\mu = \mu(< E >)$.

Figure 4 presents plots of s versus elevation angle of those data falling between 0° and 10° in azimuth for transmitted angles β of about 15°, 30°, 45°, 60°, 70°, and 90°. (The angles incident on the bottom differed somewhat from the depression angles due to refraction.) In all these plots the maximum level of scatter appears in or near the specular direction as expected. Figure 5 is a plot of the LSD corresponding to the data for the 90° incident case shown in Fig. 4f. There appears to be a decrease in variation as the scatter angle is increased.

It can be seen that the maxima of each of the forward-scatter patterns in Figs. 4a through 4d are at or very near (within experimental error) the specular direction. This predominance of specular scattering indicates that most of the energy penetrating the bottom surface is lost from the scatter field, particularly any energy that has penetrated to a significant depth. Such loss reinforces the absence of pulse extension seen in the backscattered returns in Chapter 1 and the high degree of the fit of theoretical and experimental shapes of the monostatic returns in Chapter 2.

THREE-DIMENSIONAL DATA

Average Values of $s(\beta, \psi, \xi)$

The data presented in Figs. 6 through 10 consist of values of $s(\beta\, \psi, \xi)$ for β values of 15°, 30°, 45°, and 75°. Each figure can be considered a top view of half of a hemispherical dome. The elevation angle ψ is divided into nine 10° steps, and the azimuth angle ξ is divided into eighteen 10° steps. The values of $s(\beta, \psi, \xi)$ for $180° \leq \xi \leq 360°$ are assumed to be the same as the reflected values of $s(\beta, \psi, \xi)$ for $0 \leq \xi \leq 180°$, with the axis of symmetry being the (0, 180°) azimuth line.

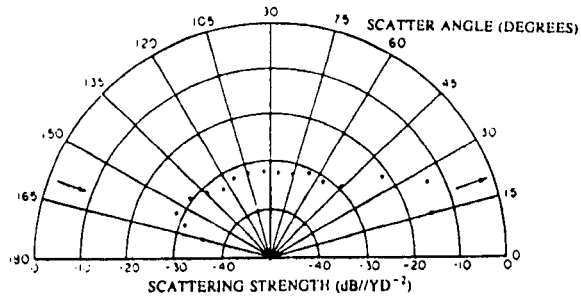

(a) Incident grazing angle 19.7°

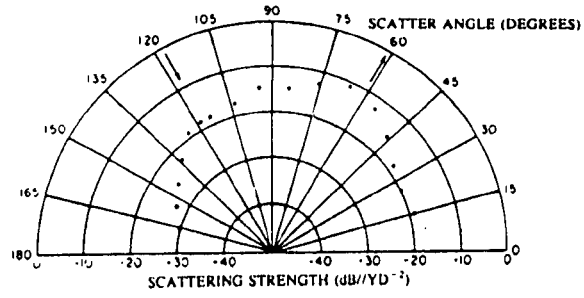

(d) Incident grazing angle 60.8°

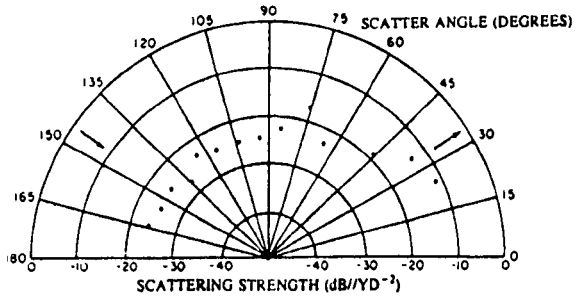

(b) Incident grazing angle 32.4°

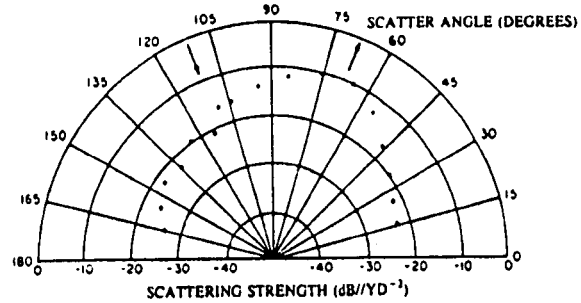

(e) Incident grazing angle 70.5°

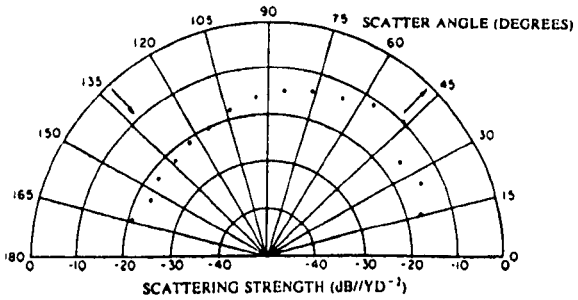

(c) Incident grazing angle 46.4°

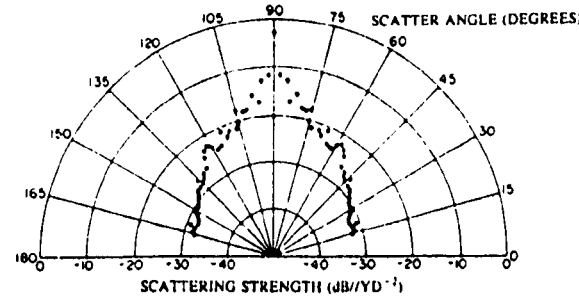

(f) Incident grazing angle 90.0°

Fig. 4. Scattering strength in the specular plane (± 10 ° in azimuth).

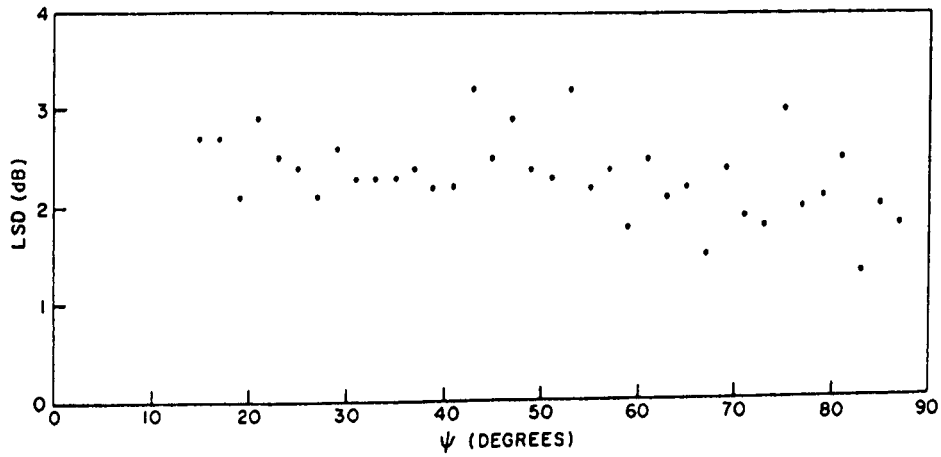

Fig. 5. Logarithmic standard deviation of the average values in Fig. 4f.

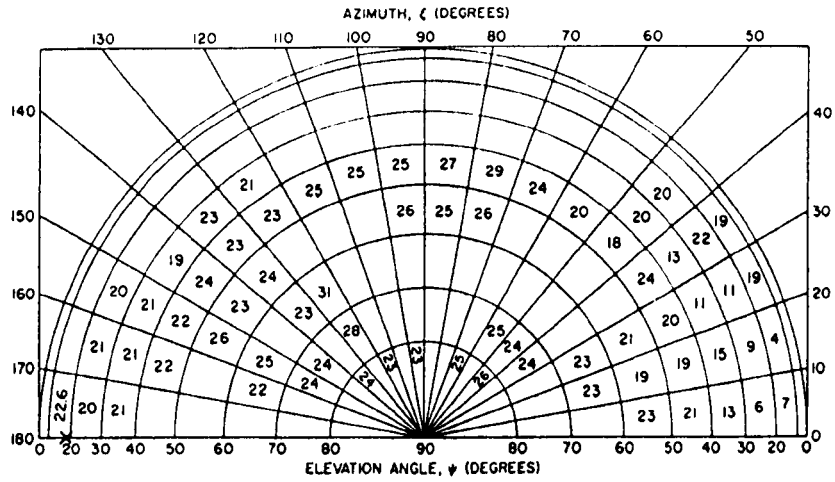

Fig. 6. Scattering strength in the upper half space for an incident grazing angle of 19.7°. The field is assumed symmetrical on either side of the specular plane. (The specular plane is perpendicular to the page along the lower edge of the plot; Fig. 4a is a side view of this plane.) The incident angle is marked with an ×, and the center of the scattering area is directly beneath the pole. The blank 10°-step areas are due to missing values. (Note: All values of scattering strength for Fig. 6-10 are negative.)

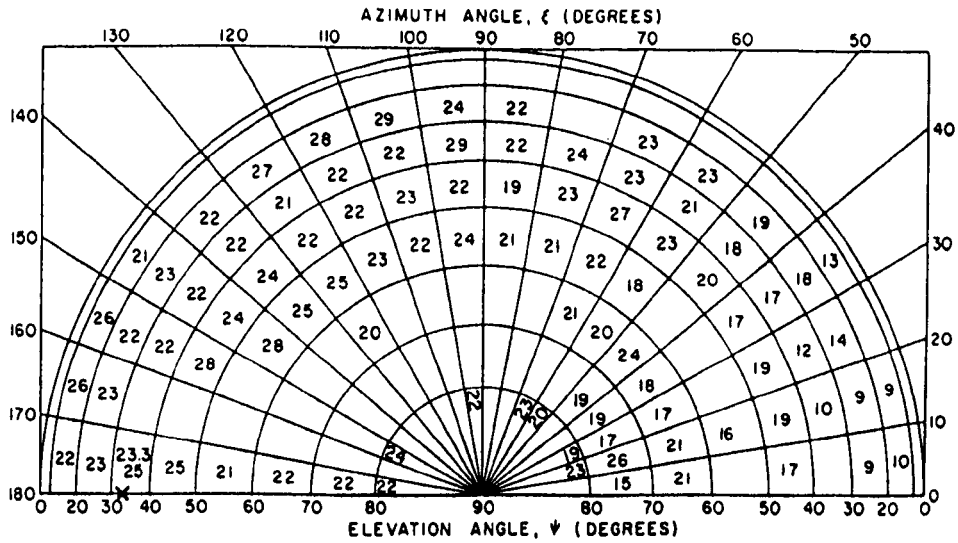

Fig. 7. Scattering strength in the upper half space for an incident grazing angle of 32.4°.

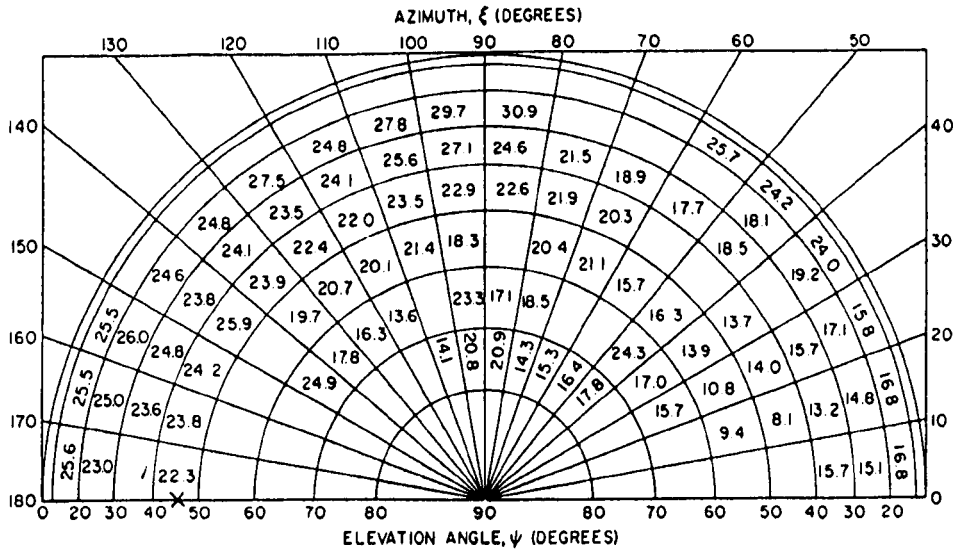

Fig. 8. Scattering strength in the upper half space for an incident grazing angle of 46.4°.

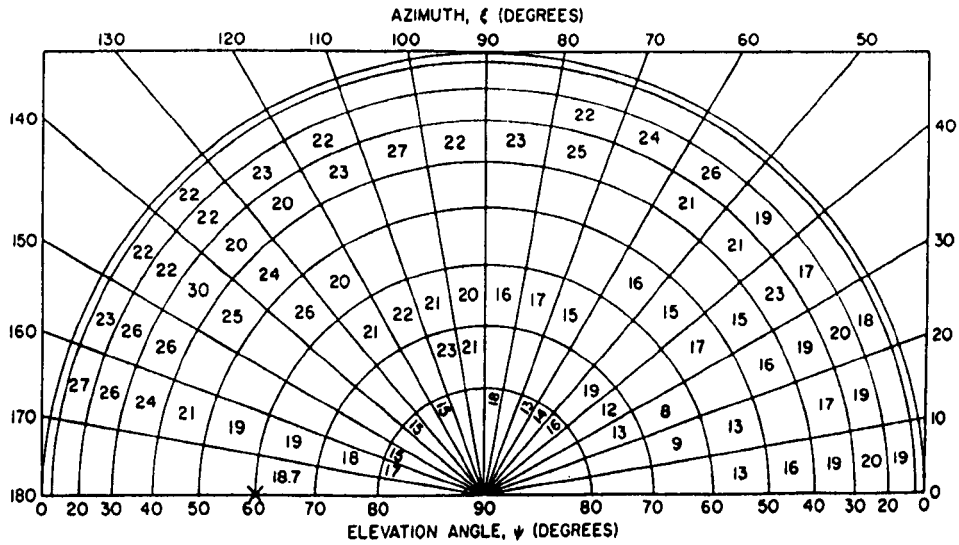

Fig. 9. Scattering strength in the upper half space for an incident grazing angle of 60.8°.

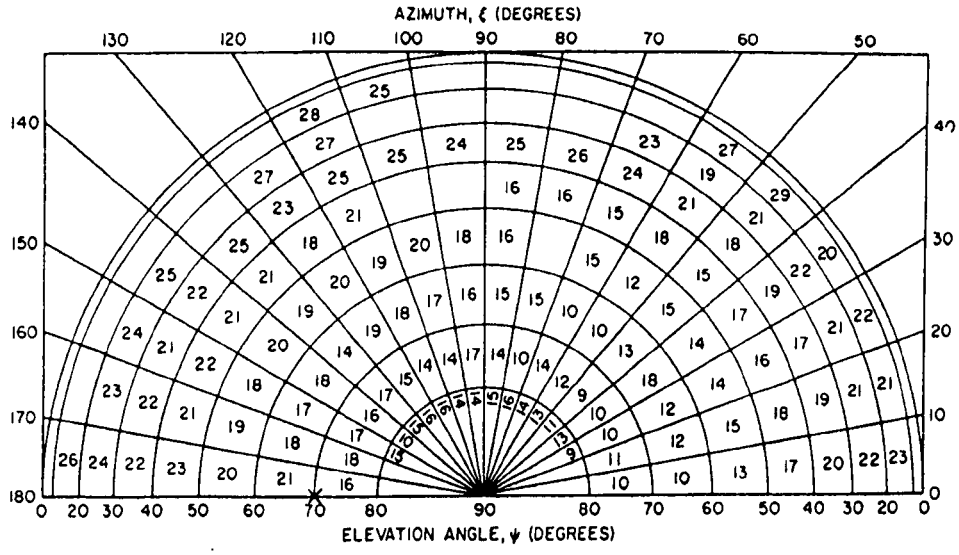

Fig. 10. Scattering strength in the upper half space for an incident grazing angle of 70.5°.

In each figure, the incident angle (or monostatic scatter direction) is marked by an X, and the center of the insonified area is beneath the pole and at the point of convergence of the radial azimuth lines. A number in a 10°-step area is the average value of $s(\beta, \psi, \xi)$ in the directions within that angle. Figures 4a through 4d are plots of the points found between 0° and 90° elevation 0° and 10° azimuth, and 170° and 180° azimuth. In some cases the data in Figs. 6 through 10 were extrapolated from nearby data, as is most noticeable in the case of $\beta = 60°$ (Fig. 9) between 170° and 180° azimuth.

Ratio of Scattered to Incident Power

A numerical integration of $s(\beta, \psi, \xi)$ over a unit hemisphere gives the fraction of the incident power that is scattered from the bottom back into the water. The values of the scattered field were smoothed, interpolated, and extrapolated to obtain a complete coverage of the upper half space. Then the data were numerically integrated as shown in the next subsection. The results are presented in Fig. 11 as the curve labeled Blake Plateau. The curve labeled Bermuda is the result of previous work of this group. The curve labeled Nolle is our integration of data as reported by Nolle et al. (1963) for laboratory experiments on graded sands at 1 MHz. Since the Nolle data were given only for an azimuth angle of 0°, it was necessary to assume symmetry about the specular direction.

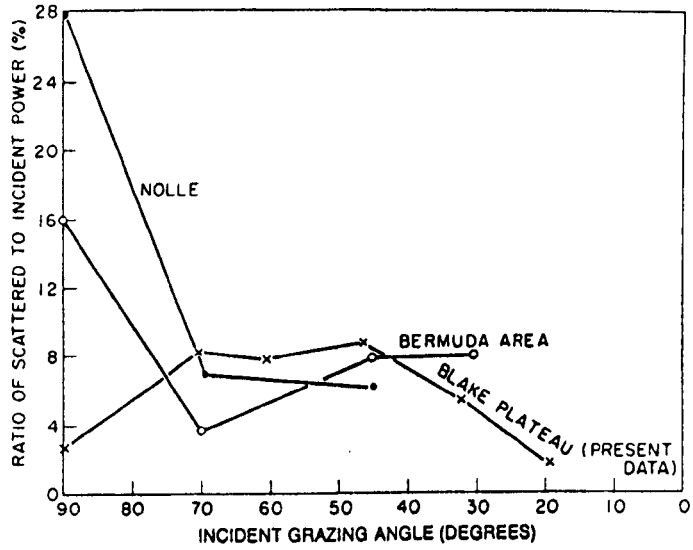

Fig. 11. Computed ratio of scattered to incident power as a function of the incident angle.

An example of the three-dimensional shape of the scattered field is illustrated by the paper model in Fig. 12, which is for 70° incidence and is not logarithmically compressed, as are the other results presented. This model was constructed from data that has been smoothed and interpolated. The line (wire) from the right entering the base indicates the incident angle, and the line to the upper left from the peak indicates the specular direction.

Computation of Scattered Power

The data were interpolated and extrapolated to fill in all the missing areas. The resulting values of $s(\beta, \psi, \xi)$ were then integrated over a unit hemisphere, giving the ratio of the scattered power to the incident power as a function of only β. That is

$$\frac{P(\beta)_{\text{scattered}}}{P_{\text{incident}}} = \int_0^{2\pi} \int_0^{\pi/2} s(\beta, \psi, \xi) \cos\psi \, d\psi d\xi$$

$$= 2 \int_0^{\pi} \int_0^{\pi/2} s(\beta, \psi, \xi) \cos\psi \, d\psi d\xi \, .$$

This integral was numerically evaluated from

$$\frac{P(\beta)_{\text{scattered}}}{P_{\text{incident}}} = 2 \sum_{j=1}^{18} \sum_{i=1}^{9} s(\beta, \bar{\psi}_i, \bar{\xi}_j) (\sin\psi_i - \sin\psi_{i-1}) (\xi_j - \xi_{j-1})$$

$$= \frac{\pi}{9} \sum_{j=1}^{18} \sum_{i=1}^{9} s(\beta, \bar{\psi}_i, \bar{\xi}_j) (\sin\psi_i - \sin\psi_{i-1}) \, ,$$

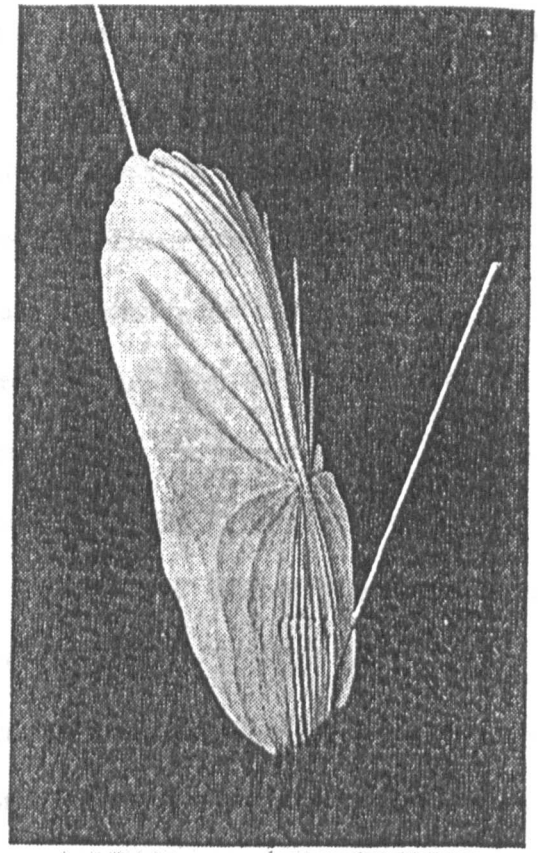

Fig. 12. Three-dimensional model of the scattered field for an incident grazing angle of 70.5°. The incident and specular directions are indicated by the wires.

where

$$\psi_i = i\Delta\psi = i(10°), \qquad i = 1,\ldots, 9,$$

$$\xi_j = j\Delta\xi = j(10°), \qquad j = 1,\ldots, 18,$$

$$\bar{\psi}_i = (\psi_i + \psi_{i-1})/2,$$

and

$$\bar{\xi}_j = (\xi_j + \xi_{j-1})/2.$$

The results of this evaluation are presented in Fig. 11.

CONCLUSIONS

An experiment was performed which gives wide coverage of the three-dimensional scatter field. The scattered field for an incident grazing angle of 90° (Fig. 4), being independent of azimuth angle, is a fairly complete description of the field. The scattered field is

much more directional than the image field from a smooth surface would be: the source was about 8° wide at the 3-dB-down points, but the field was only about 4° wide at the 10-dB-down points. This increased directivity is not present in the scattered fields at other angles of incidence. It is believed that at these other angles the true directivity is not seen because the field was not sampled at a sufficiently fine mesh.

When the scattered fields are integrated over the upper half space, the result is the normalized scattered power (Fig. 11). The amount of power scattered back is small, less than 9% maximum, and the amount of scattered power drops rapidly for both low and high incident grazing angles. The drop for low incident grazing angles would be even less if the hypothesized but unnoticed directivity increase were present. Along with the directivity increase the coincidence of the maxima in the scattered field with the specular direction indicates that the ocean bottom on the Blake Plateau behaves like a scattering surface rather than a scattering volume below the surface.

REFERENCES

H.U. Criss, K.D. Flowers, B.G. Hurdle, R.M. Lee, and K.P. Thompson, "Procedures for a Series of Experiments in Acoustic Scattering from the Ocean Bottom and Volume in the Blake Plateau Area," NRL Memo. Rept. 1767, 1967.

C. Eckart, "Principles and Applications of Underwater Sound," NDRC Summary Technical Reports, Division 6, Vol. 7, Washington, D.C., 1946.

K.D. Flowers, B.G. Hurdle, and K.P. Thompson, "Three-Dimensional Scattered Fields From the Ocean Bottom," NRL Rept. 7325, 1971.

C.W. Horton, S.K. Mitchell, and G.R. Barnard, "Model Studies of the Scattering of Acoustic Waves from a Rough Surface," J. Acoust. Soc. Am. **41**, 635 (1967).

B.G. Hurdle and K.D. Flowers, "Effect of Geometry on Acoustic Monostatic Scattering from the Ocean Bottom," NRL Rept. 6517, 1967.

B.G. Hurdle, K.D. Flowers, and D.P. Thompson, "Bistatic Acoustic Scattering from the Ocean Bottom," NRL Rept. 7285, 1971.

A.W. Nolle, W.A. Hoyer, J.F. Mifsud, W.R. Runyan, and M.B. Ward, "Acoustical Properties of Water Filled Sands," J. Acoust. Soc. Am. **35**, 1394 (1963).

K.P. Thompson, K.D. Flowers, and B.G. Hurdle, "Scattered Fields From The Ocean Bottom" J. Acoust. Soc. Am. **38**, 932 (1965).

R.J. Urick, "The Backscattering of Sound from a Harbor Bottom," J. Acoust. Soc. Am. **26**, 231 (1954).

APPENDIX 4A: EFFECTS OF PROPAGATION

Refractive Effects

The positioning system to be discussed in Appendix 4B fixed the position of all of the receiving sensors with respect to the submarine. Since a sound-velocity structure is present in the medium, positioning with respect to the scattering area becomes more complicated. However, if an initial direction of propagation is given, ray-tracing through the medium locates the position of the insonified area with respect to the submarine. It then remains to determine that unique ray which connects the center of the insonified area and each of the receiving sensors. Also computed are the angles (azimuth and elevation) that the ray makes when leaving the insonified area and when received at the sensor and the spreading losses over these paths. All of the computations were made using Horton's* equations in a ray-trace program in which the sound-speed profile was divided into a number of linear segments.

Absorption

To obtain the average attenuation coefficient K over the path, a numerical integration over the depth divided by the total depth was made. Thus $K = 10\log < K >$, where

$$< K > = \frac{1}{d} \int_0^d k(z)\, dz,$$

in which $k(z)$ is the function relating absorption and depth (Fig. A11 in the APPENDIX A). In determining $k(z)$ the temperature, salinity, and pressure were taken into account. The value of K used in the analysis was 2.268×10^{-3} dB/yard (2.4803×10^{-3} dB/m).**

*J.W. Horton, *Fundamentals of Sonar*, U.S. Naval Institute, 1957.

**B.G. Hurdle, K.D. Flowers, and K.P. Thompson, "Bistatic Acoustic Scattering from the Ocean Bottom," NRL Rept. 7285, 1971.

APPENDIX 4B: MONITORING POSITIONS BY ACOUSTIC MEANS

In measuring the scattering strength at sea with a number of acoustic sensors to obtain the three-dimensional field, it was necessary to know the relative positions of the sensors and source fairly accurately. Then, since the insonified area on the bottom was always fixed with respect to the submarine, the positions of the receiving sensors with respect to the insonified area were known. After the actual spatial positions of the insonified area and the sensors were known, ray paths between them were calculated, and the associated angles were determined. To obtain the relative positions of the sensors and source, an auxiliary acoustic system was developed to measure the geometry illustrated in Fig. 4B1. Ranges R_1 through R_7 and the angle α were recorded simultaneously with each acoustical scattering measurement.

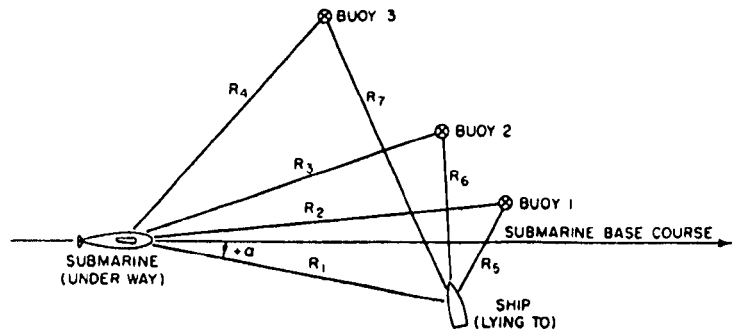

Fig. 4B1. Sonar ranges (obtained automatically every 10 sec) and periscope bearing α to the ship (manually recorded every minute).

The angle α was measured with the periscope of the submarine. To accomplish the range measurements, a 25-kHz source on the submarine transmitted a 1-msec pulse every 10 sec; at the same time a 14-kHz source on the ship transmitted a similar pulse. The buoys received and then retransmitted these signals by HF-FM links to the ship. From knowledge of the speed of the sound in the surface region and the elapsed time over the different paths, ranges R_1 through R_2 were obtained.

The counters, which started to count elapsed time in milliseconds at the same time the pulses originated, were stopped when a received signal level surpassed a preset threshold. The number in the counter was then read out and the counter was zeroed just prior to the beginning of the next 10-sec interval. The count (in milliseconds) was then recorded on

punched paper tape. An example of one run of this type of data is given in Fig. 4B2. Range in time or distance is the ordinate, and the abscissa is the time of transmission. As expected, the ranges R_1 and R_4 are approximate hyperbolas (deviations from exact hyperbolas being caused by submarine course variations and drift of the receiving sensors), and the ranges R_5 through R_7 are approximate straight lines. The range curves R_5 through R_7 are essentially parallel and in this case increase in range with time due to the ship drifting faster than the buoys.

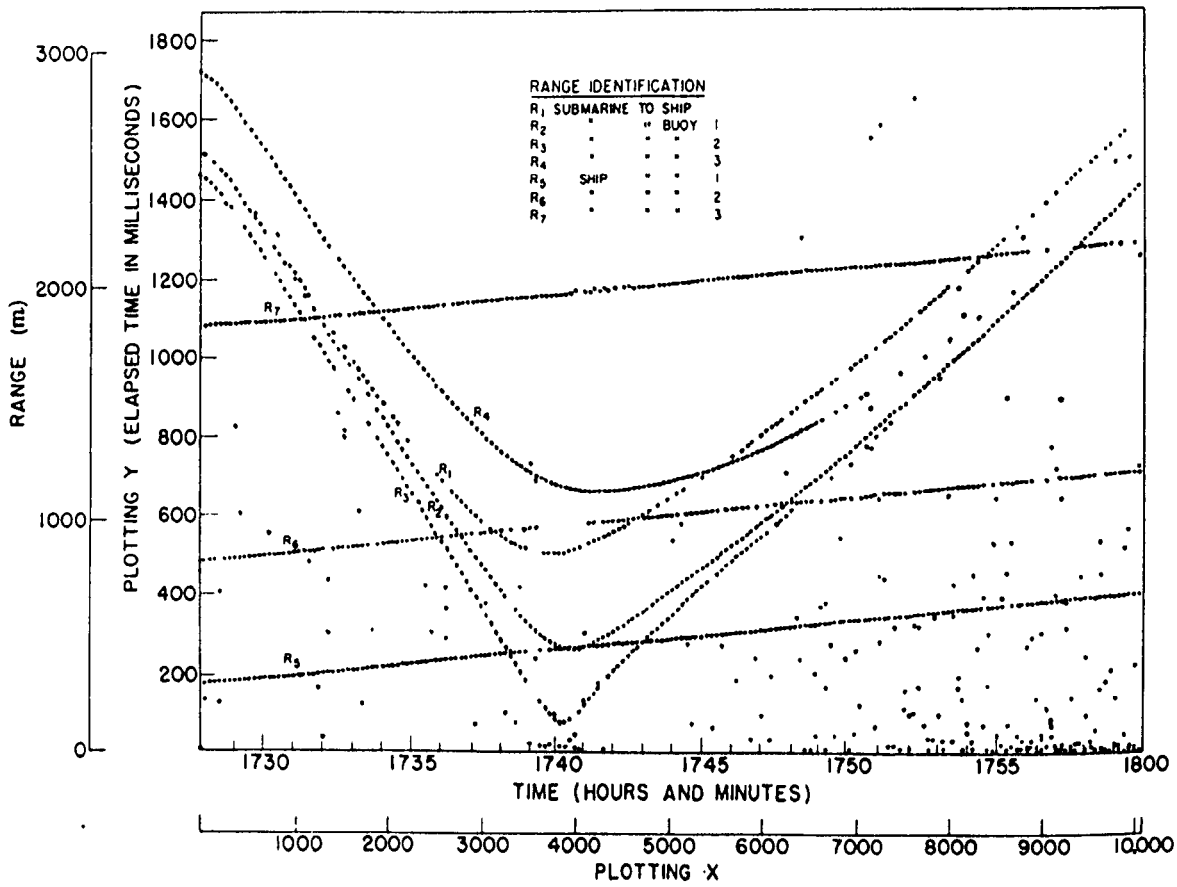

Fig. 4B2. Horizontal ranges (identified in Fig. B1) versus time for run 11. The curves are plotter readouts of the original data on paper tapes, except for some points originally missing and subsequently filled in.

As can be seen, the counters were sometimes stopped by noise bursts, but it was unusual for the counter not to be stopped by the pulse if it was not stopped by noise before the pulse arrives. Missing points were subsequently filled in by linear interpolation for ranges R_5 through R_7 and by hyperbolic interpolation or extrapolation for ranges R_1 through R_4.

Thus for each set of the range measurements, with the depth and location of the scattering area known, the azimuth and elevation of each receiving point with respect to the center of the scattering area were obtained, using the technique of Appendix A in Hurdle and Flowers (1967).

Chapter 5

BISTATIC ACOUSTIC SCATTERING FROM THE OCEAN BOTTOM*

INTRODUCTION

This chapter will be concerned with reflection and bistatic scattering from the ocean bottom. Many authors have dealt with scattering from the ocean bottom in the backward or monostatic case, in which the receiver is at the point of transmission. Chapter 2 discussed rough-surface reflection and scattering. The monostatic case has also been given extensive treatment in the scattering of electromagnetic energy from various boundaries such as the sea surface, various types of terrain, and the ionosphere.

Investigations of reflection and scattering from the ocean bottom in directions other than those of the monostatic case are confined mostly to directions near the specular direction. The BRASS II project has made measurements of bottom loss in and near the specular direction over a limited range of grazing angles.

Urick (1954) made a set of measurements in shallow water at 22 kHz, employing a geometry (Fig. 1) in which the sound was incident on the bottom at grazing angles θ less than 1° with reception over a range of azimuth angles ξ from 30° to 180°, at the same 1° elevation angle ψ. He concluded that the field, for the region investigated, was scattered isotropically.

Nolle et al. (1963) conducted laboratory experiments in a tank on the scattering of sound from water-filled sand surfaces. The shape of the scattered intensity field was obtained in terms of the scattering coefficient for the sound impinging on the bottom at grazing angles θ of 45°, 70°, and 90°. The acoustic field obtained in these measurements is characterized by

*This research was first presented and reported by Hurdle and Flowers (1963), Thompson and Hurdle (1963), and Hurdle et al. (1971).

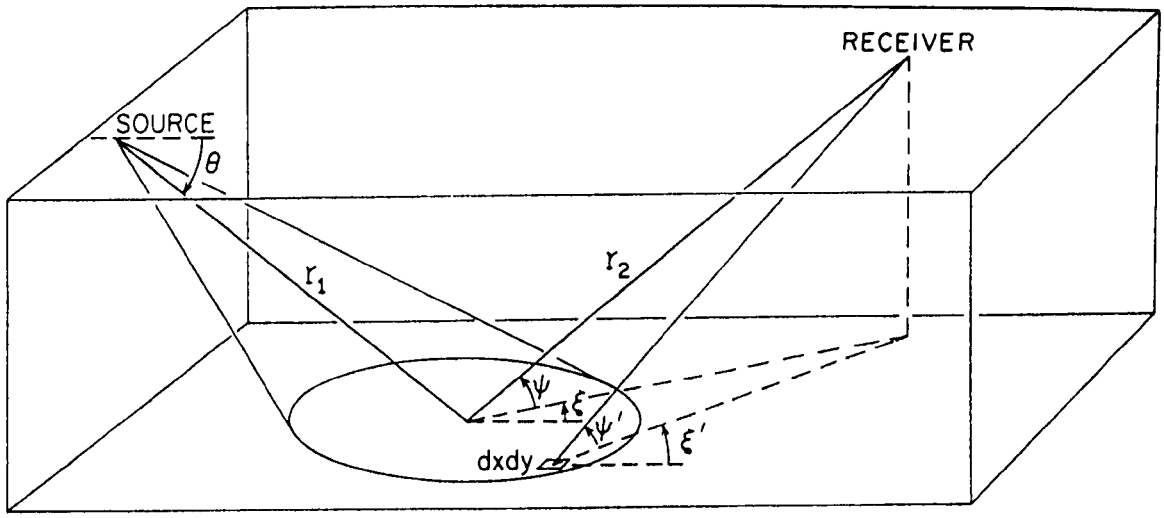

Fig. 1. Bistatic scattering geometry.

a large reflected peak in the specular direction $\psi = \theta$, $\xi = 0°$ and a broad plateau of scattered intensity that decreases as the two scatter angles $\psi = 0°$, $\xi = 0°$ and $\psi = 0°$, $\xi = 180°$ are approached. These data indicate a simple combination of specular reflection and Lambert's law scattering. Lambert's law states that the level of the scattered field will be proportional to the product of the sine of the incident grazing angle θ and the sine of the angle of scatter Ψ. The applications of this empirical law, which seems to fit a number of cases of scattering of electromagnetic waves (optical and longer wavelengths) and elastic waves, are discussed in Urick (1975).

THEORY FOR DATA ANALYSIS

Scattering Strength

The measured data must be considerably reduced for a meaningful presentation of the scattered acoustic field. The approach chosen here is similar to that used in displaying the field of an acoustic source, in which the intensity is plotted radially versus the angle, with the center of the radiator at the pole. The polar plots of the scattered field are similar to the plots in Fig. 4 in Chapter 4.

The scattering strength, a common criterion describing a scattering characteristic of a boundary, is used in this analysis, being displayed as a function of the geometry. Again,

scattering strength is based on the isotropic scatter model of Eckart (1946) except, following Urick (1954), the scattering strength is used rather than the scattering coefficient. Scattering strength s is defined (in units of yard^{-2}) as

$$s = \frac{I_s}{I_i A} , \tag{1}$$

where I_s is the scattered intensity, referred to 1 yard from the center of the insonified area on the bottom, in the direction of observation (dyne sec^{-1} cm $^{-2}$), I_i is the intensity incident on the bottom (dyne sec^{-1} cm^{-2}), and A is the area of insonification on the bottom (yard^2).

For the present case the incident intensity was not a constant over the insonified area due to the directivity of the source. Hence Eq. 1 had to be reformulated. For a fixed depression angle θ

$$I_s(\psi_s, \xi) = \iint_A s(x, y; \psi', \xi') I_i(x, y)\, dxdy , \tag{2}$$

where (Fig. 1) ψ and ξ are respectively the elevation and azimuth angles of the receiver with respect to the center of the insonified area and ψ' and ξ' are respectively the elevation and azimuthal angles of the receiver with respect to $dxdy$. Since s can be considered a constant for the small beamwidth used, that is, $|s(x, y, \psi', \xi') - s(\psi, \xi)|$, $|\psi' - \psi|$, and $|\xi' - \xi|$ are all small for points (x, y) in A, then

$$I_s(\psi, \xi) = s(\psi, \xi) \iint_A I_i(x, y)\, dxdy \tag{3}$$

or

$$s(\psi, \xi) = I_s(\psi, \xi) \left[\iint_A I_i(x, y)\, dxdy \right]^{-1} . \tag{4}$$

Since the intensities incident on and scattered from the bottom are by definition those on and 1 yard from the effective center of the scattering area respectively, the data measured at the surface must be referred to these points. For a directive source with substantially all of

the energy contained in the main beam the double integral in Eq. 4 represents the total power impinging on the bottom. Thus attenuation is the only loss to account for on the downward path. The scattered intensities at the receiver are referred to a point 1 yard from the bottom. This requires accounting for both spreading and attenuation losses over the path from the bottom to the receiver.

Effect of Gradients

Most measurements of acoustic propagation in the ocean are subject to the anisotropic effects of temperature, pressure, and salinity gradients. This experiment was no exception, and significant effects of these gradients were taken into account.

Since all distances were determined from the measurement of acoustic transit time, the average sound speed of propagation over the path through the sound-speed gradient was required. The second effect of the sound-speed gradient accounted for was refraction, which provided the correct geometry. The third effect, associated with the intensity, provided the correct spreading loss, since the sound-speed gradient causes it to deviate from square law. The last effect of the sound-speed gradient accounted for was the average absorption over the path. Each of these effects are discussed in more detail in APPENDIX A.

Working Equations

From Eq. 4 the logarithmic form of the scattering strength is

$$S(\psi, \xi) = 10 \log s(\psi, \xi) = 10 \log [I_s(\psi, \xi)] - 10 \log \left[\iint_A I_i(x, y)\, dxdy \right]. \qquad (5)$$

When propagation is included,

$$10 \log [I_s(\psi, \xi)] = E - M - G + 20 \log r_2 + Kr_2 + B \qquad (6)$$

and

$$10 \log \left[\iint_A I_i(x,y)\, dxdy \right] = L + 20 \log i - D - Kr_1 + 10 \log \left[\iint_A b(x,y)\, dxdy \right], \qquad (7)$$

so that

$$S = E - M - G + 20 \log r_2 + K(r_1 + r_2)$$

$$+ B - L - 20 \log i + D - 10 \log \left[\iint_A b(x, y)\, dxdy \right], \tag{8}$$

where

E = 20 log (scattered-signal amplitude at the receiver),

M = receiving sensitivity,

G = receiver gain,

B = buoy beam-pattern correction,

L = transmitting response,

i = source current,

K = average absorption coefficient,

D = dome loss,

$b(x, y)$ = normalized source radiation function,

r_1 = path length from the source to the scattering area, and

r_2 = path length from the scattering area to the receiver.

Any self-consistent set of units may be used for these quantities.

When the signal was received by the same transducer as used in transmitting (monostatic case), the preceding quantities are the same except $B \rightarrow D$, $r_2 \rightarrow r_1$, and $b(x, y) \rightarrow [b(x, y)]^2$. For the particular source used in this experiment, numerical evaluation gave

$$10 \log \left[\iint_A b(x, y)\, dxdy \right] = -16.7 \text{ dB} \tag{9}$$

and

$$10 \log \left[\iint_A b^2(x, y)\, dxdy \right] = -19.1 \text{ dB} \tag{10}$$

THE EXPERIMENT

Instrumentation

The instrumentation and procedures for conducting this experiment are discussed in Appendix 5B.

Geometry

Data for obtaining the shape of the scatter field were acquired by using a directive source mounted in the USS *Rockville* and a buoy-supported hydrophone with a radio link to the ship. Acoustic pulses were transmitted to the bottom at a depression angle θ. Signals scattered from the elliptical area on the bottom were received bistatically at the buoy hydrophone and monostatically at the source transducer.

The source ship was maneuvered to traverse past the buoy, thus continuously varying ψ and ξ, the bottom scatter angles. This enabled a series of scatter angles to be obtained for each of several depression angles of the source.

Operating Area

The experiment was conducted on the east slope of the Bermuda Rise over areas 1, 2, and 3 indicated in Fig. 2. Areas 1 and 3 have a bottom characterized by the Naval Oceanographic Office as mud-coral. A majority of the data were obtained in area 1, which had an average water depth of 1400 m. Area 3 has the same characteristics as area 1, except for steeper bottom slopes. Area 2 has an ooze bottom and an average water depth of 2300 m.

Results

The results presented in this chapter are for an in-line geometry: $\xi = 0$ or 180°. Polar plots are presented of the mean scattering strength as a function of Ψ. Data obtained in area 1

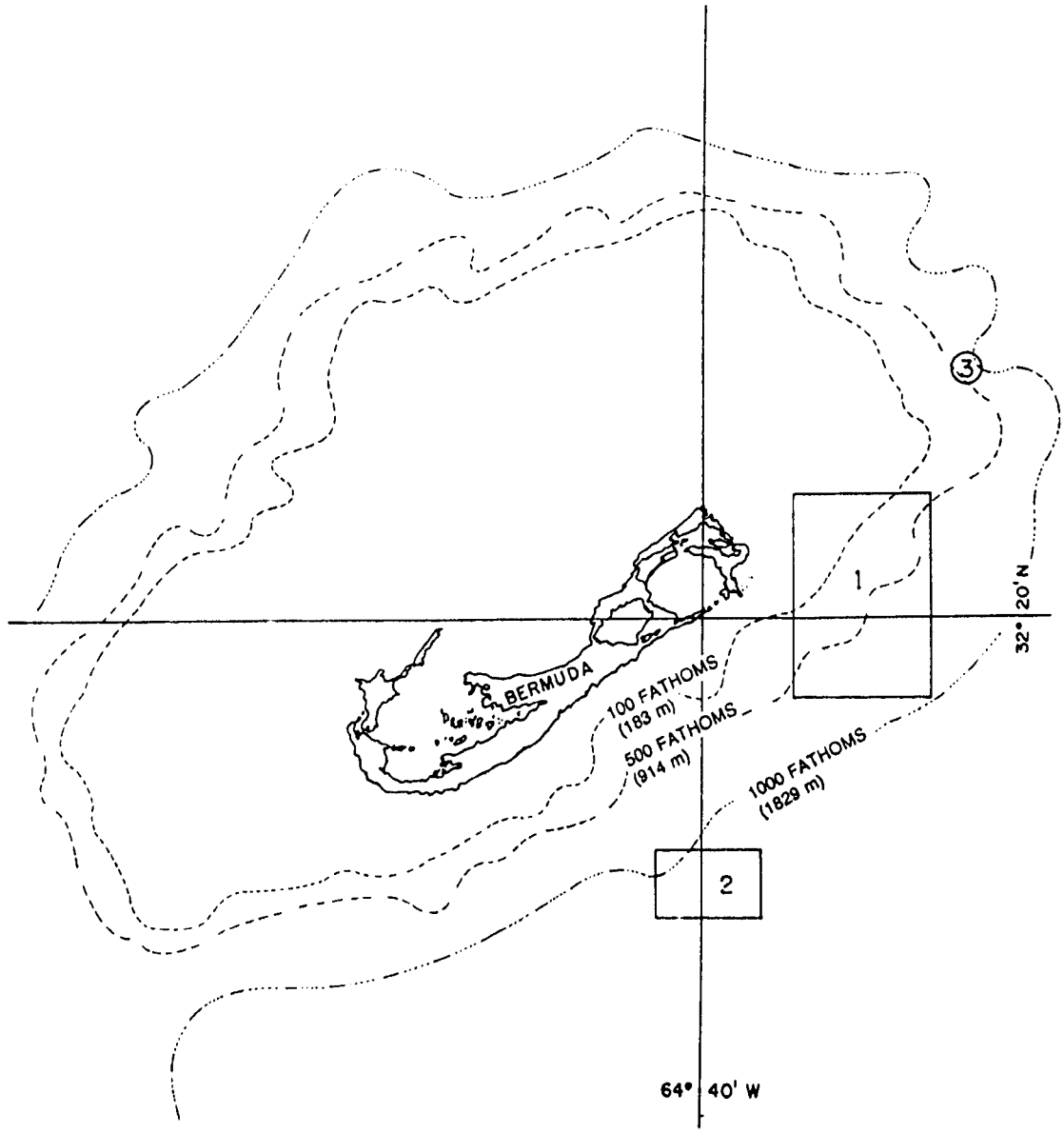

Fig. 2. Operating areas.

are presented in Figs. 3, data obtained in area 2 are presented in Figs. 4, and data obtained in area 3 are presented in Fig. 5. Since in a bistatic experiment of this type complete coverage of the field is difficult, the data points are averages over 10° increments of Ψ and are averages of varying numbers of data points. The error bars at each point indicate $\pm$LSD (logarithmic standard deviation):

$$\text{LSD} = 10 \log \left[1 + \frac{\sigma}{m} \right], \tag{11}$$

in which σ is the sample standard deviation and m is the sample mean.

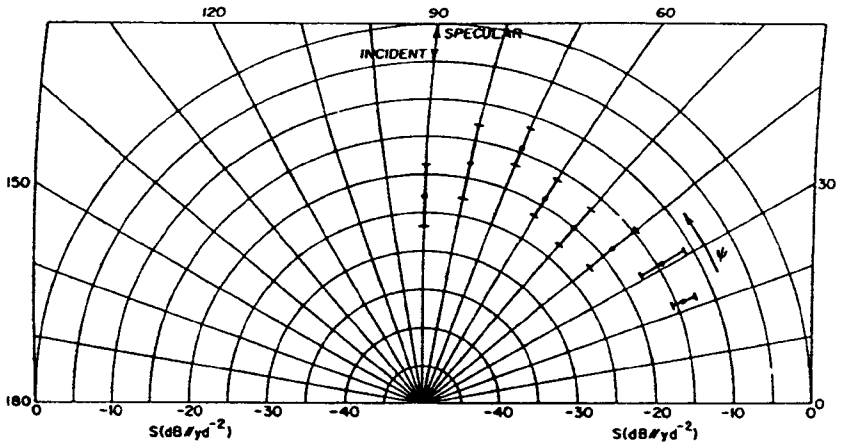

Fig. 3a. Scattering strength S for a depression angle of 90° in operating area 1 (mud-coral bottom).

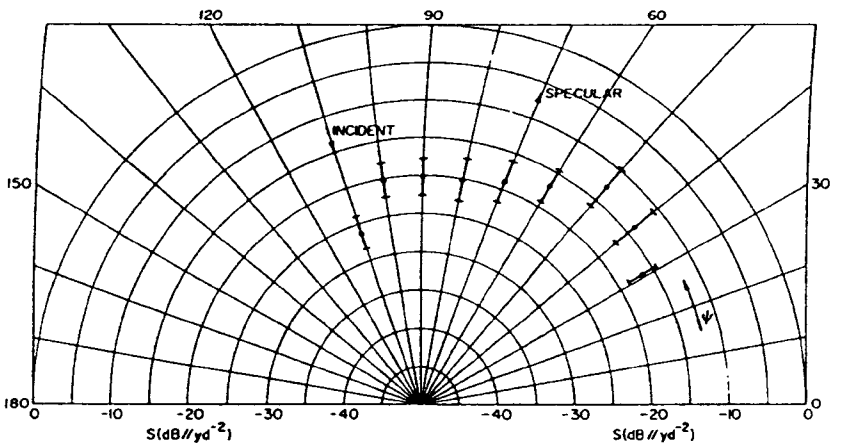

Fig. 3b. Scattering strengths S for a depression angle of 70° in operating area 1 (mud-coral bottom).

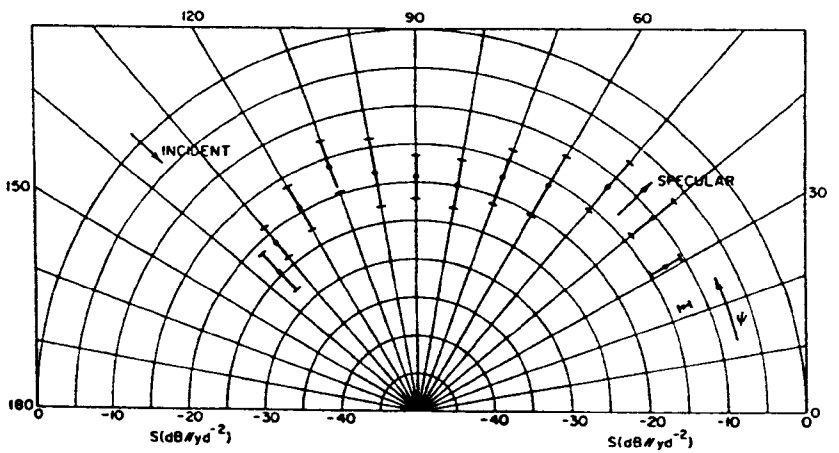

Fig. 3c. Scattering strength S for a depression angle of 45° in operating area 1 (mud-coral bottom).

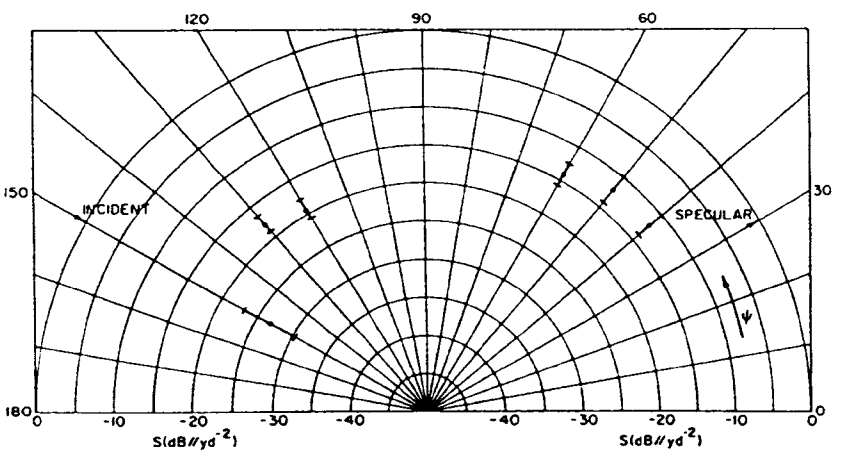

Fig. 3d. Scattering strength S for a depression angle of 30° in operating area 1 (mud-coral bottom).

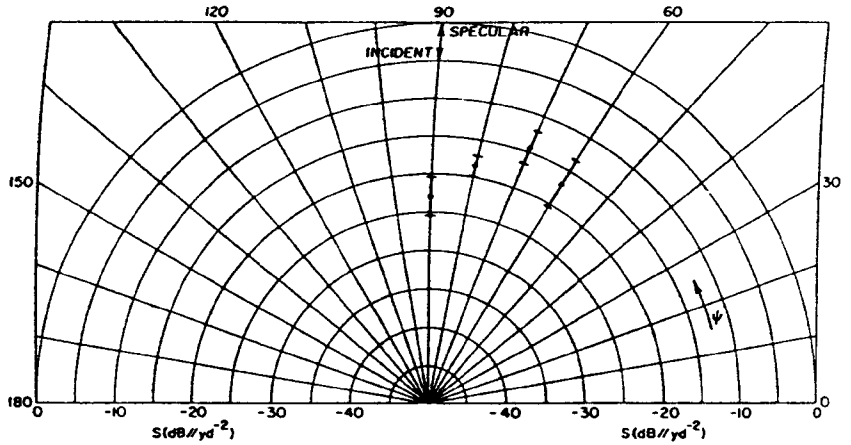

Fig. 4a. Scattering strength S for a depression angle of 90° in operating area 2 (ooze bottom).

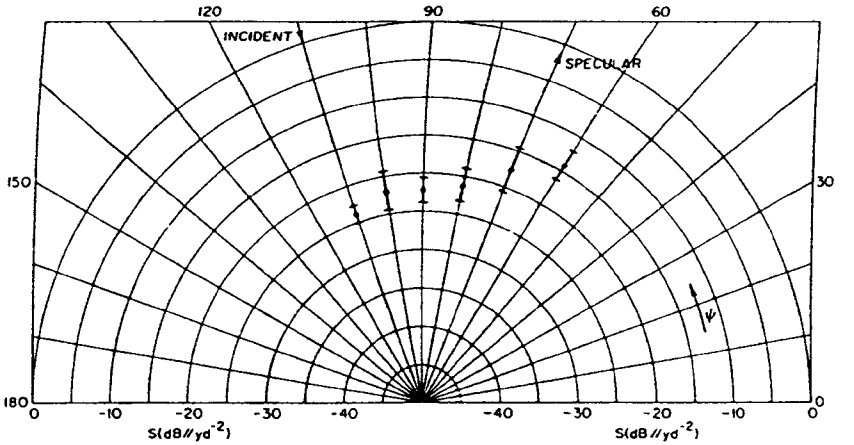

Fig. 4b. Scattering strength S for a depression angle of 70° in operating area 2 (ooze bottom).

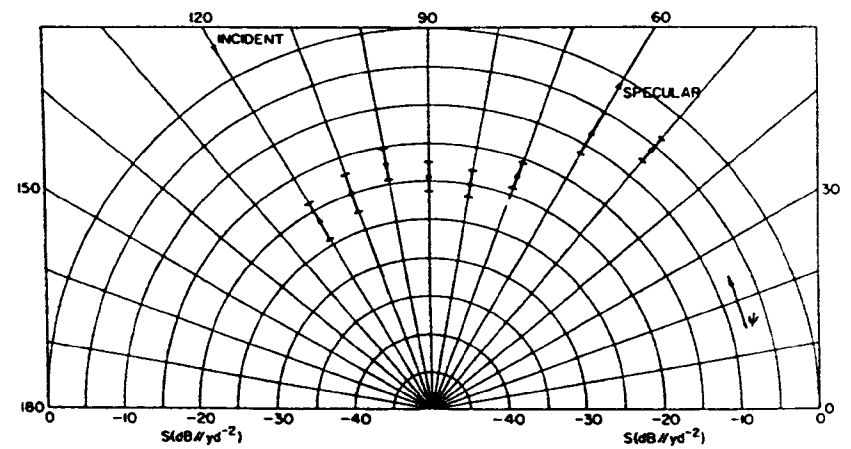

Fig. 4c. Scattering strength S for a depression angle of 60° in operating area 2 (ooze bottom).

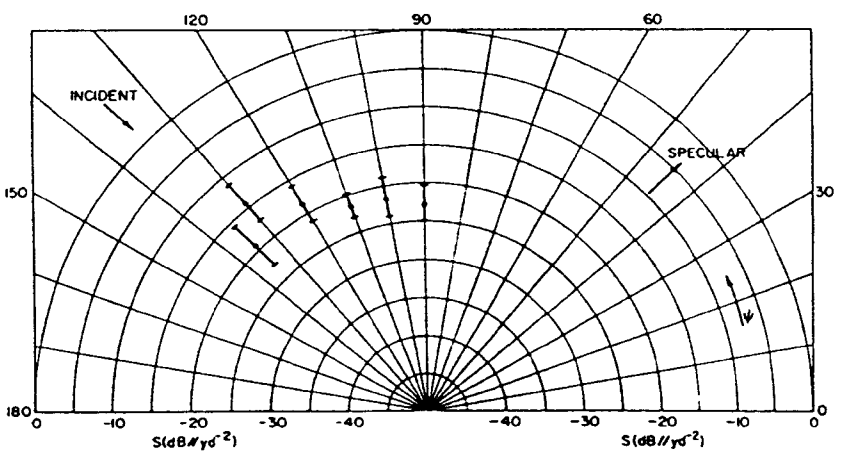

Fig. 4d. Scattering strength S for a depression angle of 45° in operating area 2 (ooze bottom).

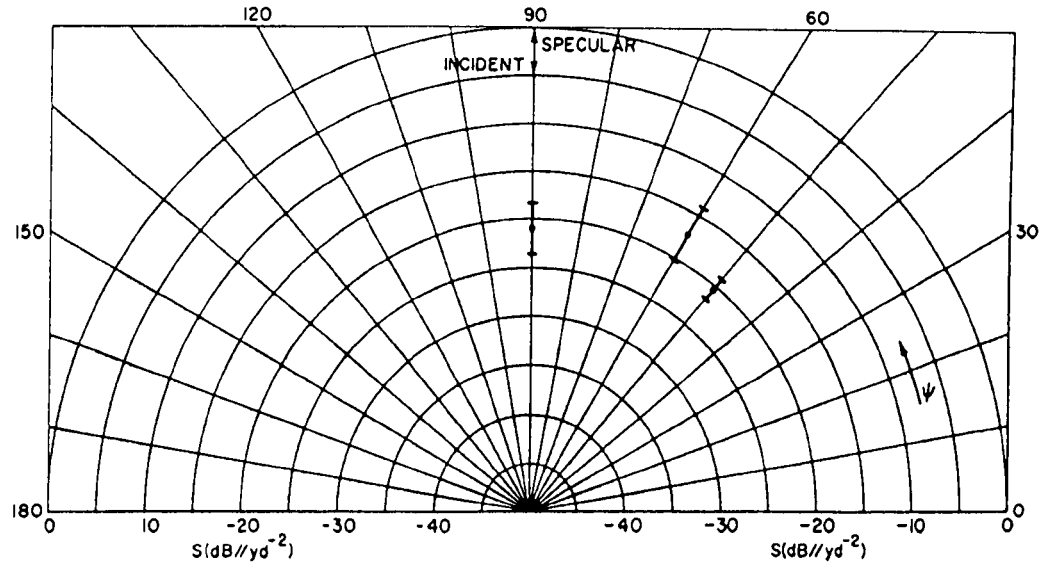

Fig. 5. Scattering strength S for a depression angle of 90° in operating area 3 (mud-coral bottom).

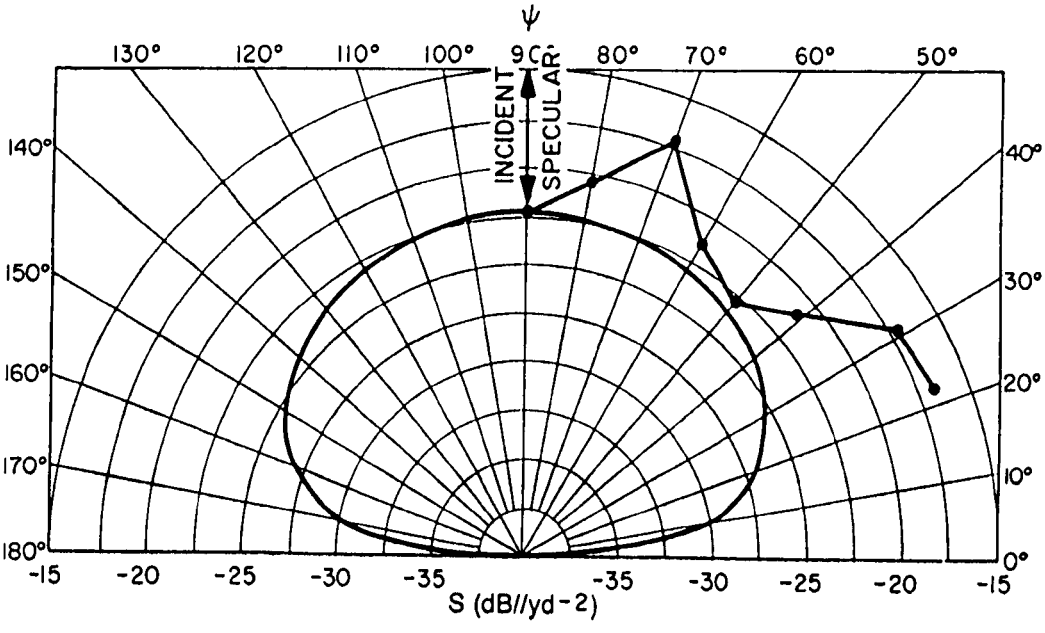

Fig. 6. Lambert's-law fit of the measured scattering strength S of the scatter field (mud and coral bottom), with the fit being made at the normal-incidence (90°) monostatic point.

THE SCATTERED ACOUSTIC FIELD

Discussion

At first glance the form of the measured acoustic fields suggests a combination of reflection and diffuse scattering (Lambert's law). Figure 6 is an example of the fit of the measured scatter field to the Lambert's-law model. The fit is made at the normal-incidence monostatic

point in the field. This fit is not the best or worst. It does indicate that the measured field has little correspondence with the Lambert's-law scattering. When the model is applied at other incident grazing angles, there is no consistent fit as the angle of incidence is changed. That is, the "reflection" component is not in the specular direction and deviates from specular by differing amounts depending on the angle of incidence. Also, the "diffuse scattering" component requires a "constant" multiplier which is a function of the incident angle. In addition the individual scattered pulses were extended in time much more than was expected from geometrical considerations. Therefore the scattered fields are not explained by a combination of reflection and diffuse scattering.

The operation areas were in general undulating with occasional slopes as high as 20°. Obviously a different average bottom slope for each set of data that would explain the difference between the specular direction and the observed maximum is highly unlikely. Also, the average slopes necessary to explain the reflection component still require a nonconstant multiplier for the diffuse component. Finally the maximum slope ($\approx 20°$) encountered does not geometrically extend a pulse sufficiently to explain the observed extension in time. Therefore average bottom slopes do not explain the observed data, although the effect of bottom slope is present in the data to some extent.

Other possible explanations are a subbottom layer or a refraction path through the bottom. The subbottom layer would have to be too far below the bottom to be feasible. A refractive path through the bottom, if attenuation is ignored, can explain the displaced peaks in the results. With the multiple scatter paths associated with this type of bottom, the other discrepancies can be expected.

By use of equations found in Horton (1959) and the known gradient of sound speed with depth in the water column, the gradient in the bottom necessary to refract the center ray such that it arrived at the surface at the apparent angle of maximum scatter was calculated for Figs. 3b and 4b. These were chosen because the direction of maximum scattering strength is better defined. The calculated gradients were 10.2 and 11.0 sec^{-1} respectively.

A gradient with a magnitude of 10.2 sec^{-1} is unusual enough to question its probability of occurrence in this region. Although there are no independent data for this immediate area, Officer and Ewing (1952) reported a layer with a sound speed of 4.51 km/sec obtained from refraction profiling a little east of this area. The calculated vertex sound speed of approximately 4.5 km/sec, corresponding to a gradient of 10.2 sec^{-1}, is in agreement with this layer's sound speed, indicating the possibility of the existence of the gradient.

Figure 7a is a plot of the computed spreading loss as a function of the depression angle θ for a two-layer model (water and bottom) using a gradient of 10.2 sec^{-1} in the lower layer. For $\theta = 70°$ the curve indicates the possibility of a substantial gain over square-law spreading, which is indicated by the line labeled scatter path. Square-law spreading is computed to the point where the refracted ray reaches the surface.

Figure 7b is a plot of horizontal range as a function of the depression angle θ. The dashed curve represents the computed horizontal range from the source to the arrival point of a ray at the surface if specular reflection from the bottom interface was the predominant contributor. The solid curve is the corresponding computed range for rays traversing a refractive path through the bottom. The two points are from the experimental data, representing the peaks of the 70° and 45° mud-coral patterns. The fit of the experimental points to the refractive curve is superior to a fit to the curve based on specular reflection. The other scatter patterns are not complete enough to give a clear indication of where the peak in the pattern occurs. Hence only two experimental points are plotted in this figure. The other patterns do indicate that the points would be above the "specular" curve.

Attenuation in the Bottom

Although a number of factors support a refractive transmission path through the bottom, probably the most important characteristic of the bottom—the acoustic attenuation near 20 kHz—has as yet not been shown to be sufficiently low to make such a path possible.

The material expected in the bottom may be divided into two classes: unconsolidated and consolidated. Attenuation measurements for a number of unconsolidated sediments have been

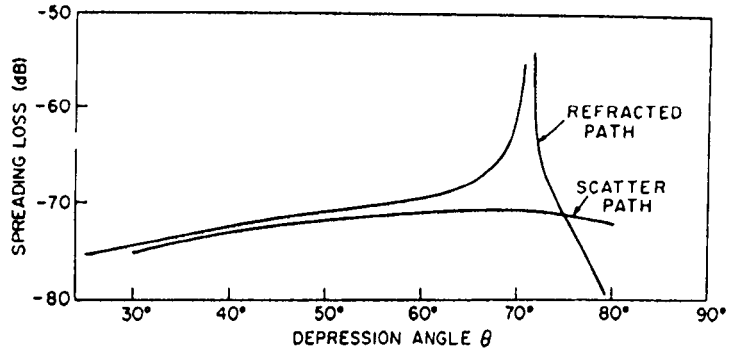

(a) Spreading loss to a surface receiver over the refracted path versus the source depression angle as compared to square-law spreading over the scatter path from the layer boundary.

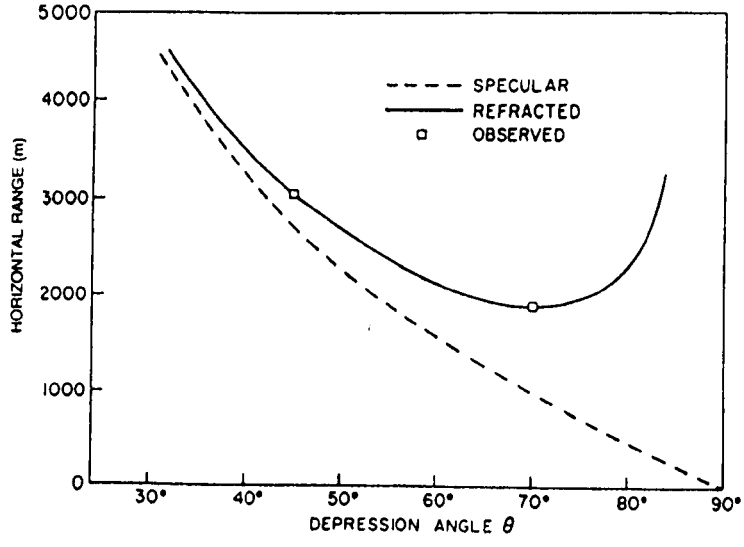

(b) Horizontal range to specular arrival via the refracted path through the bottom (solid curve) and a bottom-interface specular scatter path (dashed curve) versus the source depression angle.

Fig. 7. Results of an analysis of a two-layer model (water and bottom), with a water depth of 1400 m, a water gradient of sound speed with depth of $-0.02\ \text{sec}^{-1}$, and a bottom gradient of sound speed with depth of $+10.2\ \text{sec}^{-1}$.

reported by Shumway (1960) and Hamilton (1974). Generally their values range between 1.5 and 30 dB/m near 20 kHz. If the effective attenuation in the areas investigated here were as much as 1.5 dB/m, a refractive path through the bottom would be impossible. However, if the unconsolidated sediment existed as a thin layer over consolidated material, the losses over

the total refracted path might be sufficiently low to allow a refractive path to predominate over the scattered path. It is believed that the longitudinal compressional wave is the only wave that could have an attenuation sufficiently low to predominate over the scattered field. It is believed that shear and any other type of wave would have much greater attenuation.

A brief review of the literature concerning losses near 20 kHz in consolidated materials yields a wide range of values. Measurements by Struthers (1944) give a range of 0.08 to 0.3 dB/km for pure fused quartz. These values probably represent a lower limit for this class of material under ideal conditions. The measurements reported by Bergmann (1954) also tend to fall in this category. Measurements by Wyllie et al. (1962) give an attenuation of 300 dB/km for marble, and measurements by Born (1941) give values of 850 to 1300 dB/km for sandstone, limestone, and shale. These measurements were made in the laboratory under conditions of atmospheric pressure and no water content.

However, Wyllie et al. (1962) also made loss computations, based on a theory of propagation in porous solids by Biot (1955 and 1956) of the physical properties of rock structures under conditions of compacting pressure and complete liquid saturation. These computations indicated a substantial reduction of attenuation might be expected with respect to that made under laboratory conditions at atmospheric pressure.

Since the mid-1970s interest has greatly increased in low-frequency acoustic interaction with the ocean bottom. The fundamental question has been—how can the attenuation in the ocean bottom be predicted from knowledge of the properties of the bottom, and what properties are the most important in the prediction? Progress has been made, based on Biot (1956, 1962a, 1962b, and 1973), in an understanding of the propagation in fluid-saturated porous media both consolidated and unconsolidated. This includes the nature, shape, and flow properties of the pores, the question of conversion to shear waves, the existence of both slow and fast compressional waves, and the influence of these on the attenuation of low-frequency acoustic waves. The mass of references in this area is too great to be treated here. There are four works, however, that carry most of the important contributions and cite nearly all of

the references. They are Hampton (1973), Kuperman and Jensen (1980), Pace (1983), and Akal and Berkson (1986).

It has been frequently observed that fathograms in the 12-kHz range show returns from layers much deeper than would be possible if the attenuation was as high as that reported by Shumway (1960) and Hamilton (1974). In more recent years in-situ measurements of attenuation in some materials under the conditions of their environments have been reported, such as by Hamilton (1980), Stoll and Houtz (1983), and Jacobson (1987). However, the interpretations have limitations in that these measurements were not made with the source shots as well as the receivers actually on the bottom.

The lengths of the paths required in the bottom are only 0.5 and 0.2 km respectively for depression angles of 70° and 45°. With Struthers' (1944) attenuation values the refractive path would have lower losses than the water path. With reasonable attenuation values (a few tens of decibels per kilometer) these refractive paths could contribute significantly to the scattered field.

Percentage of Power Scattered

It is of interest to determine the ratio of power returned to the water half-space above the bottom to the power incident on the bottom boundary. This enables one to delineate where the power is dissipated. This power ratio P is obtained by integrating the scatter strength (in power-ratio form) over a hemisphere above the region of scatter.

Inspection of the data indicated that $S(\psi)$ was symmetrical about the vertical axis of the hemisphere in the normal-incidence case or was approximately symmetrical about an axis through the peak (the cases of 70°, 45°, and 30° incidence) that could be rotated to coincide with the vertical axis. (Limited data supporting this symmetry were obtained when the ship's heading was not on a line through the source and buoy.) This symmetry enabled the power ratio to be expressed as

$$P = 2\pi \int_0^{\pi/2} S(\psi) \cos \psi \, d\, \psi. \tag{12}$$

The integral was evaluated numerically using symmetry arguments and filling in missing data points.

Computations of P, the ratio of power returned to the water to power incident on the bottom, made for the four mud-coral patterns (Figs. 3) are as follows:

Depression Angle, θ (degrees)	Power Ratio, P
90	0.16
70	0.038
45	0.081
30	0.084

A maximum of approximately 16% of the power is returned to the water for the normal-incidence case. Thus most of the energy was lost in the bottom, implying good energy transmission into the bottom.

CONCLUSIONS

Average scatter fields have been presented in polar plots for various grazing angles. The fields, although not complete, give some idea as to the distribution of energy in the upper half space. They are seen to be complicated and not representable by a simple combination of reflection and diffuse scattering.

Although much evidence indicates the presence of refraction paths through the bottom, it is not conclusive enough to prove their existence. The strongest argument against them is the attenuation that is usually associated with transmission of 20-kHz sound in reasonable bottom-type materials. If indeed the scatter fields do result from bottom transmission, then a conclusion is that the effect must be even larger at lower frequencies.

REFERENCES

T. Akal and J.M. Berkson, editors, *Ocean Seismo-Acoustics*, Plenum, New York, 1986.

L. Bergmann, Table 88, p. 654, in *Ultrasonics*, Springer-Verlag, Zurich, 1954.

M.A. Biot, "Theory of Elasticity and Consolidation for a Porous Anisotropic Solid," J. Appl. Phys. **28**, 168-171 (1956).

M.A. Biot, "Theory of Propagation of Elastic Waves in a Fluid-Saturated Porous Solid," J. Acoust. Soc. Am. **28**, 179-191 (1956).

M.A. Biot, "Mechanics of Deformation and Acoustic Propagation in Porous Media," J. Appl. Phys. **33**, 1482 (1962a).

M.A. Biot, "Generalized Theory of Acoustic Propagation in Porous Dissipative Media," J. Acoust. Soc. Am. **34**, 1254-1264 (1962b).

M.A. Biot, "Nonlinear and Semilinear Rheology of Porous Solids," J. Geophys. Res. **78**, 4924 (1973).

W.T. Born, "The Attenuation Constant of Earth Materials," Geophys. **6**, 132-148 (1941).

C. Eckart, editor, "Principles and Applications of Underwater Sound," NDRC Summary Technical Reports, Division 6, Vol. 7, Washington, D.C., 1946.

E.H. Hamilton, "Geoacoustic Modeling of the Sea Floor," J. Acoust. Soc. Am. **68**, 1313-1339 (1980).

L. Hampton, editor, *Physics of Sound in Marine Sediments*, Plenum, New York, 1973.

J.W. Horton, *Fundamentals of Sonar*, 2nd edition, U.S. Naval Institute, Annapolis, 1959.

B.G. Hurdle and K.D. Flowers, "Discussion of Measured Intensity Fields from Ocean Bottom Returns," J. Acoust. Soc. Am. **35**, (1963).

B.G. Hurdle, K.D. Flowers, and K.P. Thompson, "Bistatic Scattering from the Ocean Bottom," NRL Rept. 7285, 1971.

R.S. Jacobson, "An Investigation into the Fundamental Relationships between Attenuation, Phase Dispersion, and Frequency Using Seismic Refraction Profiles over Sedimentary Structures," Geophys. **52**, 72-87 (1987).

W.A. Kuperman and F.B. Jensen, *Bottom-Interacting Ocean Acoustics*, Plenum, New York, 1980.

A.W. Nolle, W.A. Hoyer, J.F. Mifsud, W.R. Runyan, and M.B. Ward, "Acoustical Properties of Water-Filled Sands," J. Acoust. Soc. Am. **35**, 1394 (1963).

C.B. Officer and M. Ewing, "Seismic Refraction Measurements in the Atlantic Ocean, Part IV, Bermuda, Bermuda Rise, and Nares Basin," Bulletin Geol. Soc. Am. **63**, 779-809 (1952).

N.G. Pace, editor, *Acoustics and the Sea-Bed*, Proceedings of the Institute of Acoustics, Bath Univ. Press, Bath, U.K., 1983.

G. Shumway, "Sound Speed and Absorption Studies of Marine Sidements by a Resonance Method," Geophys. **25**, 451 (1960).

R.D. Stoll and R.E. Houtz, "Attenuation Measurements with Sonobuoys," J. Acoust. Soc. Am. **73**, 163-172 (1983).

F. Struthers, unpublished data from work at NRL on the attenuation in solid quartz rods in a vacuum, 1944.

K.P. Thompson and B.G. Hurdle, "Acoustic Scattering from the Ocean Bottom," J. Acoust. Soc. Am. **35**, 810 (1963).

R.J. Urick, "The Backscattering of Sound from a Harbor Bottom," J. Acoust. Soc. Am. **26**, 231 (1954).

R.J. Urick, *Principles of Underwater Sound*, McGraw-Hill, New York, 1975.

M.R.J. Wyllie et al., "Studies of Elastic Wave Attenuation in Porous Media," Geophys. **27**, 569 (1962).

APPENDIX 5A: REFRACTION AND ABSORPTION

The sound-speed profile illustrated in Fig. 5A1 was constructed from the profile of average temperature versus depth obtained in the operating areas that is shown in the same figure. The profile was constructed using Mackenzie's* equation as modified by Del Grosso's† constant and assuming a constant salinity of 35 °/₀₀. Computation of the absorption is similar to the computations in Chapters 1 and 4.

*K.V. Mackenzie, "Formulas for Computation of Sound Speed in Sea Water," J. Acoust. Soc. Amer. **32**, 100 (1960).
†V.A. Del Grosso, NRL Report 4002 (1952) and NRL Report 4279 (1954).

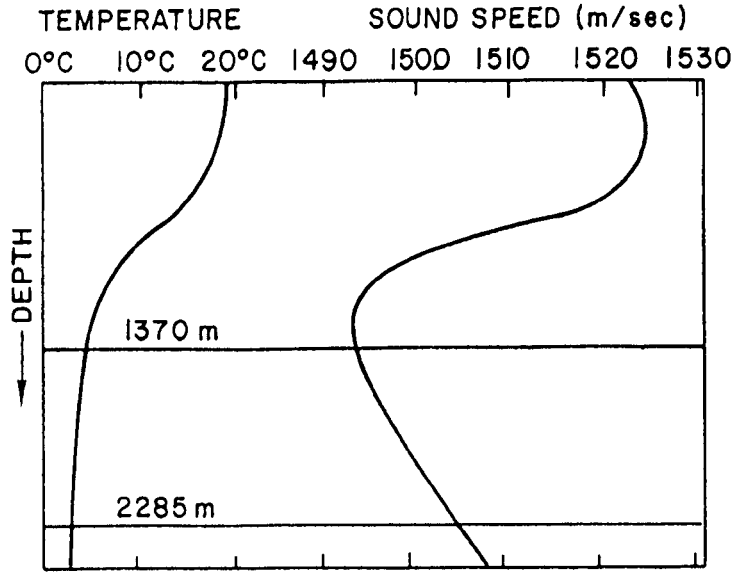

Fig. 5A1. Profile of the average measured temperature (left) and profile of the computed average sound speed (right) for the experiment.

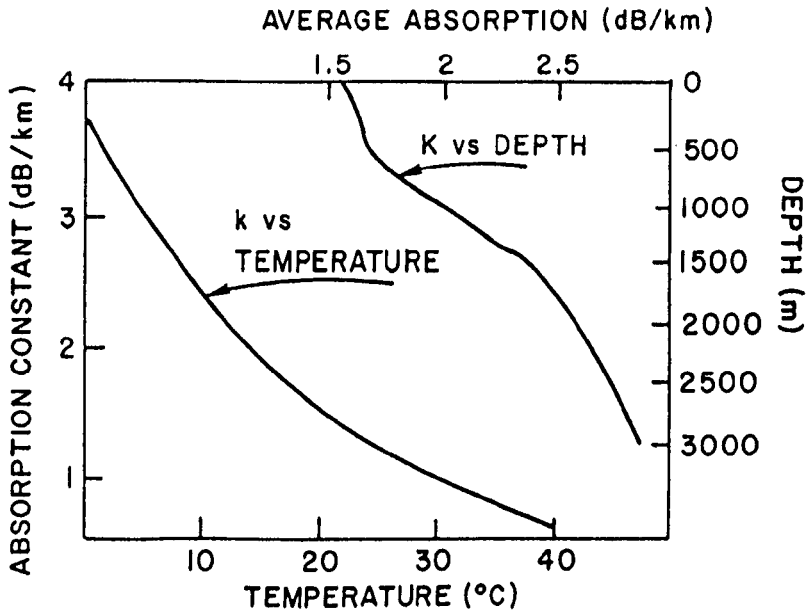

Fig. 5A2. Absorption of 20-kHz sound as a function of water temperature (left) and profile of the average absorption over a path of depth d.

With the relation between absorption and temperature known (left-hand curve in Fig. A2) and the relation between temperature and depth known (left-hand curve in Fig. A1), the absorption is then calculated from

$$K = \frac{1}{d}\int_0^d k(z)\, dz, \tag{A1}$$

where the effects of pressure and salinity changes on $k(z)$ have been ignored. The resulting profile for K (a numerical integration of $k(z)$ over the depth) is presented on the upper right of Fig. A2.

APPENDIX B: INSTRUMENTATION AND PROCEDURES

The transmitted signal originated in a crystal-stabilized oscillator that established the 19.5-kHz frequency of the system. The signal passed through a gate circuit actuated by impulses from the timing control unit, which determined the duration of the signal pulses as well as the interval between them. The pulses so formed then went through an attenuator, which set the signal level, into a 1000-watt power amplifier. The high-level signal pulses were passed through a series inductive matching network, thus matching the driver to the transducer. A transfer relay, also controlled by the timing control unit, switched the transducer from the receiving circuits to the output of the matching network just prior to the initiation of the signal pulse, maintaining connection for the duration of the signal pulse.

The source transducer, designated XDV-1, was a plane circular piston type having a directivity index of -27.1 dB at 19.5 kHz. Its main lobe is approximately 8° wide at the half-power points with all sidelobes down 17 dB or greater. All pertinent characteristics were calibrated by the NRL Underwater Sound Reference Division in their USRL Calibration Reports 1535 and 1968.

The receiving system encompassed those components which received, selected, and amplified the acoustic signals from the water but did not involve the actual recording of data. The following discussion of the receiving system will treat the monostatic system separately from the remote-buoy system.

Monostatic Reception

The acoustic energy in the water scattered back from the insonified area was converted into electrical signals in the XDV-1 transducer used for transmitting. The receiving beam pattern was the same as the transmitting pattern. Signals from the transducer were connected to a constant-gain preamplifier by the normally closed contacts of the transfer relay. As described for the transmitting system, the transfer relay disconnected the transducer from the preamplifier during the transmission. In the normal receiving condition the transducer signals were amplified in the preamplifier and passed through the operate position of the calibrate/operate switch to a decade attenuator, where the system gain was adjusted, before amplification in a tuned, high-gain amplifier, for presentation to the various displays and recording media.

Remote-Buoy System

The principal component of the remote-buoy system was a special radio sonobuoy, constructed to accommodate a wide range of levels and wave forms of underwater acoustic signals. The hydrophone used was a specially designed unit, suspended approximately 4.5 m below the surface. It had a barium titanate cylinder 38 mm in diameter and 38 mm long centrally mounted in a 76-mm-diameter pressure-release cylinder, with the sound exciting the barium titanate through the central cavity, which was open to the sea at the underside of the transducer. This construction provided a transducer with a sensitivity of approximately 97.8 dB below 1 V per microbar and a cardioid-type pattern, which effectively suppresses signals reflected from the surface of the ocean. After the signal from the transducer was amplified in the amplifier section of the sonobuoy, it modulated an FM transmitter, broadcasting in the 162- to 174-MHz frequency band. The amplifier/transmitter combination operated linearly over a signal dynamic range of approximately 60 dB, broadcasting at 0.25 W for approximately 6 hours on a battery load. The radio signal was received aboard ship by a telemetering FM receiver, tuned to the sonobuoy frequency. The output of the FM receiver passed through the operate position of the calibrate/operate switch and thence through a decade

attenuator, in which the system gain was set. It was then amplified in a tuned, high-gain amplifier for presentation to the various displays and recording media.

Measurement System

The measurement system included all components for displaying, recording, and measuring the outputs of the two receiving systems. The signals underwent demodulation and logarithmic amplification for simultaneous recording on the two channels of a Brush two-channel ink recorder. The signals were also displayed on the two beams of a dual-beam cathode-ray oscillograph. A strip-film camera that was focused on the cathode-ray tube was available for additional recording. The camera was provided with a control unit that intermittently started and stopped the film travel, to conserve film during the time between receipt of the echo and initiation of the next outgoing transmitted pulse. In addition a serial time-code generator, which provided sequentially coded values of the time in minutes and seconds, updated every second, controlled an argon-glow-lamp flasher in the camera so as to record the time along the edge of the strip film. This record of time was used for time correlation of the film record with other data.

A single-beam cathode-ray oscilloscope was used in addition to the dual-beam oscilloscope for visually monitoring the signal from the remote-buoy system. A display of a range mark by momentary z-axis brightening of the scope trace assisted in the primary function of this display, which was to facilitate system gain settings and calibrations as well as acoustically tracking the buoy in range and bearing, or tracking the insonified bottom area in tilt.

The location of the buoy had to be known to accurately establish the geometry of the ship/bottom/buoy system. Although the buoy was accurately tracked in bearing by optical means, range had to be determined by measuring the transit time of the direct transmission of sound from the ship-mounted transducer to the buoy hydrophone. Although the direct path is off the main lobe of the ship-mounted transducer, sufficient energy arrived at the buoy hydrophone to provide a good signal for measuring the ship-to-buoy range. This direct signal was fed to the stop channel of a time-interval meter whose timing cycle was initiated simultane-

ously with the 19.5-kHz transmitted pulse. Thus the count displayed on the time-interval meter was proportional to the range from the ship to the buoy. The count was also recorded on paper tape, along with the ping number, on a digital printing recorder. The ping number was necessary for correlating the recorded values of range with the data recorded on the Brush recorder and strip-film camera.

Calibration

The calibration system consisted of those components that were used in establishing the gain and operating levels of the two data receiving channels as well as establishing and measuring the power driving the transducer during the transmitted pulse. For the receiving systems the output of the master 19.5-kHz crystal oscillator went to a voltage-divider potentiometer that was used for accurately establishing a 1-V signal for calibration. The setting of the voltage divider was established and monitored by an AC vacuum-tube voltmeter. The 1-V signal went into a precision attenuator, so that any level of calibration signal could be accurately and readily selected. The output of that attenuator went to the calibrate positions of the calibrate/operate switches of the two receiving systems, thus enabling the substitution of accurately known calibration signals for received signals in the two receiving systems. For measuring the drive into the transducer during the transmitted pulse, an AC vacuum-tube voltmeter was used in conjunction with a cathode-ray oscilloscope. The input to the two instruments could be switched to either the input to the transmitter driver amplifier or across a low-resistance current shunt resistor in the transducer impedance-matching network, providing a direct measurement of transducer current. The voltmeter functioned primarily as a means for calibrating the oscilloscope, whereby a constant signal was used whose amplitude was adjusted to provide the same deflection on the scope as that of the pulses observed during transmission. The reading on the voltmeter was a measurement of the voltage across the current shunt resistor during the transmitted pulse and thus a measurement of transducer current.

System Programming

All timing functions of the complete instrumentation system were accomplished in the timing control unit. This unit provided the gating of the transmitted signal into the driver amplifier as well as the energization of the transmitter-receiver transfer relay for transducer switching. Pulses from the unit were used for synchronizing the sweeps of the oscilloscopes displaying the received signals as well as triggering the camera control unit. For the buoy-range recording system the pulses of the unit's time-base oscillator were used to drive the counters of the time-interval meter, and the unit's time-base oscillator was used for resetting the counters in the time interval meter. One of the variable delay pulses of the unit was used in the z-axis brightening of the monitor scope of the remote-buoy system, providing the variable range mark.

Transducer Positioning

The transducer was positioned by a three-axis stabilized mount, so that any value of bearing and depression below the horizontal could be set for the acoustic-beam axis. The settings could be readily made by handwheels and dials that electrically controlled electromechanical servo drive systems on the transducer mount. To maintain the beam axis in the same vertical plane as that containing the ship and buoy, a target-bearing transmitter, used for optically tracking the buoy, could be switched into the train drive system, substituting for the train control handwheel and dial, so that the transducer bearing was slaved to the optical bearing. To facilitate optical tracking of the buoy, smoke floats were dropped close to the buoy.

Other Instrumentation

In addition to the electronic instrumentation a dead-reckoning tracer was used for maintaining a record of the ship's maneuvers relative to geographic reference points as well as to the buoy location. For measuring the profile of vertical sound speed versus depth, a bathythermograph with a depth capability to 275 m was used periodically. For maintaining a continuous record of the depth of the ocean, a precision depth recorder was employed in conjunction with the ship's sonar sounding set.

Chapter 6

MONOSTATIC ACOUSTIC SCATTERING FROM THE OCEAN VOLUME*

INTRODUCTION

In the study of monostatic acoustic scattering in the ocean, it is expected that the scattering from discontinuities in the volume will approximate the conditions of isotropic scattering. For pure isotropic scattering the location or the phase of the scatterers is required to be random such that statistically there is no preferred direction of the scattered energy. Therefore the scattered power density in any direction is directly proportional to the volume contributing, if the scatterers are of constant strength and density.

A monostatic volume-scattering experiment was conducted to determine the degree of correspondence between scattering from the ocean volume and that indicated by isotropic scattering theory. The question asked was whether the intensity scattered in the monostatic direction would be directly proportional to the volume insonified. Experimental measurements were made for different geometrical conditions, which were controlled by combinations of pulse length and direction of the source from the scattering volume. This experiment also provided volume-scattering profiles from two areas in the Atlantic.

THEORY

The analysis for this experiment is based on the isotropic scattering model by Eckart et al. (1946), except, in accordance with Urick (1954), the concept of scattering strength is used rather than scattering coefficient. This is stated by

$$dI_s = S_v I_i \, dV , \tag{1}$$

where dI_s is the elemental scattered intensity at unit distance from the element of scattering.

*Some of this research was presented earlier (Flowers and Hurdle, 1965, and Hurdle and Flowers, 1967).

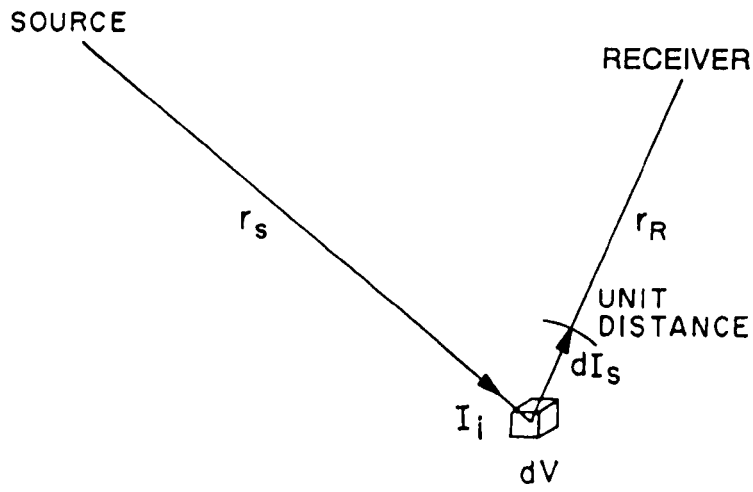

Fig. 1. General geometry for volume scattering.

Figure 1 illustrates the general geometry for volume scattering. From Eq. 1,

$$I_s = \int_V S_v I_i \, dV. \tag{2}$$

If the characteristics of the source, located a distance r_s from the elemental volume, are included, that is, when spherical spreading is assumed over r_s with the energy distributed according to the beam function of the source, and if the absorption is taken into account, I_s becomes

$$I_s = p \int_V \frac{S_v A(r_s) b_s(\theta,\phi)}{r_s^2} \, dV, \tag{3}$$

where p is the source level (which can be considered a constant), $b_s(\theta,\phi)$ is the beam function, and $A(r_s)$ is the absorption over the path r_s.

When the scattered intensity is accounted for at the receiving point, it is further selected by the beam function of the receiver and decreased by spherical spreading and absorption losses over the distance r_R. The scattered intensity at the receiver is

$$I_R = pq \int_V S_v A(r_s) A(r_R) \frac{b_s(\theta,\phi)}{r_s^2} \frac{b_R(\theta,\phi)}{r_R^2} dV, \tag{4}$$

where q is the sensitivity of the receiver and $b_R(\theta,\phi)$ is the beam function of the receiver.

At this point the following restrictions are made:

- The monostatic case is considered; that is, the source and receiving points are coincident: $r_s = r_R = r$.
- The beam function of the source and the beam function of the receiver are identical: $b_s(\theta,\phi) = b_R(\theta,\phi) = b(\theta,\phi)$.
- The beam function possesses circular symmetry about its axis, that is, is independent of θ.

It is assumed that S_v is a constant over volume V and that differential absorption over the volume can be neglected. These assumptions require that the contributing volume be kept small by employing a narrow beamwidth and short pulses. When these restrictions and assumptions are made,

$$I_r = pqS_v e^{-2k\bar{r}} \int_V \frac{b^2(\phi)}{r^4}\, dV, \tag{5}$$

where k is the absorption coefficient for intensity and $\bar{r}$ is the distance from the source/receiving point to the midpoint of the volume. Figure 2 indicates the volume of integration. Therefore, in polar coordinates,

$$I_r = pqS_v e^{-2k\bar{r}} \int_0^{2\pi} \int_{r_1}^{r_2} \int_0^{\pi} \frac{b^2(\phi) r^2 \sin\phi}{r^4}\, d\phi dr d\theta. \tag{6}$$

Integration over θ and r gives

$$I_r = pqS_v e^{-2k\bar{r}} \left(\frac{1}{r_1} - \frac{1}{r_2} \right) 2\pi \int_0^{\pi} b^2(\phi) \sin\phi\, d\phi. \tag{7}$$

For an ideal piston transducer whose beam function is a Bessel function of the first kind divided by its argument, $(J_1(\Psi))/\Psi$, a rigorous solution of the preceding integral was obtained by McLachlan (1934). In solving the integral for a transducer beam function that is employed in obtaining experimental data, it is most often found that the measured function is not exactly

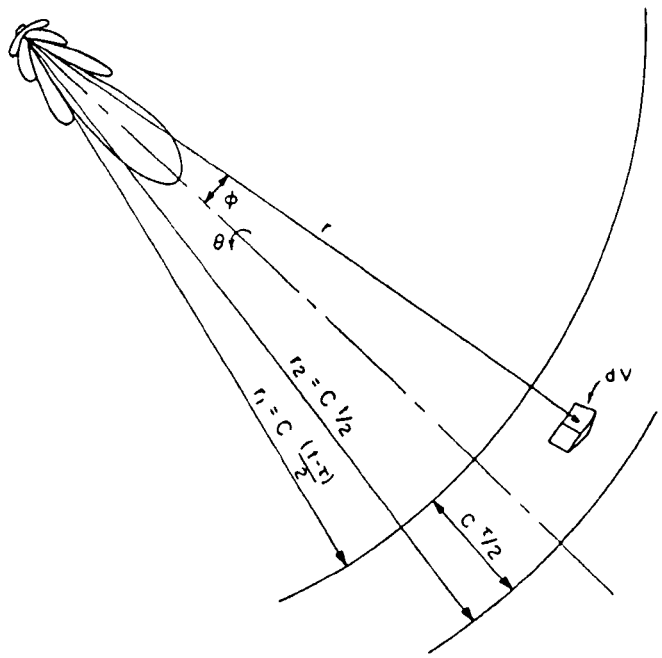

Fig. 2. Volume of integration for monostatic scattering.

analytic. Thus a numerical integration is more appropriate. In this analysis the square of the measured beam function was integrated numerically. Letting

$$b^2 = \left[2\pi\int_0^{\pi} b^2(\phi) \sin\phi \, d\phi\right]^2 \tag{8}$$

results in Eq. 7 becoming

$$I_r = pqbS_v e^{-2k\bar{r}} \left[\frac{1}{r_1} - \frac{1}{r_2}\right]. \tag{9}$$

In practice it is more convenient to write the variable in terms of time t of reception at the receiving point, with the initiation of the transmitted signal being $t_0 = 0$ and the pulse length or duration being τ. Then

$$\bar{r} = \frac{C}{2}\left[t - \frac{\tau}{2}\right], \tag{10}$$

$$r_1 = \frac{C}{2}(t - \tau), \tag{11}$$

and

$$r_2 = \frac{C}{2}t, \tag{12}$$

where C is the sound speed.

Substituting Eqs. 10, 11, and 12 into Eq. 9 gives

$$I_t = pqbS_v \left[\frac{2\tau}{Ct(t - \tau)} \right] e^{-kC[t - (\tau/2)]}. \tag{13}$$

Equation 13 expresses the variation of received intensity with time for a nonrefractive medium, with the pulse length being a parameter and the instrumentation parameters being constant.

EXPERIMENTAL MEASUREMENTS

Data for the experiment were obtained in two areas of the Atlantic, the first in the Blake Plateau (30°10′N, 78°20′W) (Fig. A8 in the Appendix, at the end of this work) about 150 nmi east of Jacksonville, Florida, and the second about 90 nmi southeast of Cape Hatteras (33°57.5′N, 74°45′W).

The instrumentation consisted of a special sonar operating at 19.5 kHz. Special features of the sonar included a piston transducer that was mounted in the bow of a submarine and that could be directed throughout the forward hemisphere. The sonar's beamwidth was approximately 8° to the half-power point with all sidelobes being down 17 dB or more (Fig. 3). This was the same transducer used in experiments discussed in Chapters 1 through 5. Figure 3 illustrates the square of the beam function plotted in the interval between the axis and the second sidelobe. The square of the beam function, $b^2(\phi)$, is shown because the same function is employed in both transmission and reception, as indicated in the previous section. Constant-amplitude sinusoidal pulses were transmitted, with the pulse length controlled by a digital programmer in 1-msec increments. Pulse lengths from 2 to 3000 msec were available. The instrumentation also provided for recording the volume scattered returns with time-base

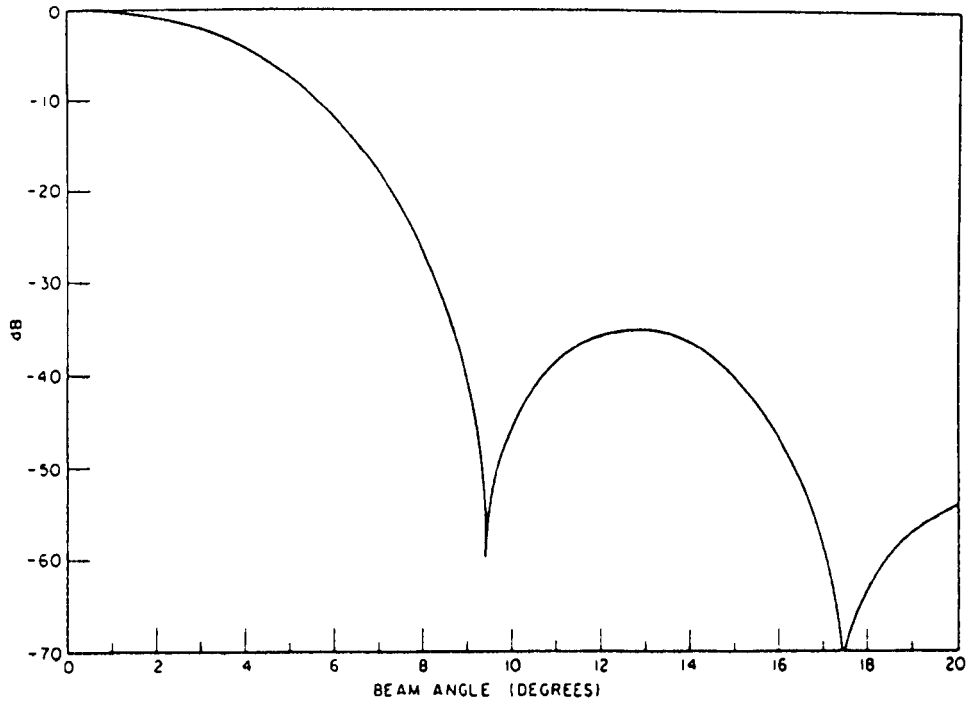

Fig. 3. Measured beam function squared, at 19.5 kHz.

and amplitude calibration. Details of the instrumentation system are contained in the Appendix.

A series of runs was made for a range of depression and elevation angles, pulse lengths, and speeds. All parameters were held constant for a particular run while 20 to 100 returns of the scattered signal were recorded. Environmental data were taken periodically during the experiment to enable the evaluation of the refractive effect of the medium.

ANALYSIS OF MEASURED DATA

The amplitude envelope of the volume-scattered signal as a function of time was recorded in analog form (on a decibel scale) for each return. The data were then incremented in 10- to 25-msec steps throughout the duration of the return and converted to digital form with the aid of a data reader. Care was taken to retain the time of each reading from t_0, the leading edge of the transmitted pulse. The power ratio e_i^2 of each value read was averaged over the number of returns recorded for each time increment throughout the return:

$$E_i = 10 \log e_i^2 \tag{14}$$

and

$$<e^2> = \frac{1}{n} \sum_{i=1}^{n} e_i^2 |_{t=c}, \tag{15}$$

where n is the number of returns and c is a constant.

The mean value of the power ratio was then converted to decibels by

$$<E> = 10 \log <e^2>. \tag{16}$$

Then $<E> \propto <I>$, if the intensity is proportional to pressure squared. Since the data are obtained as a function of time, $<E>$ at each instant represents the return from a volume situated about a particular point in range. Figure 4 illustrates a single return of the volume-scatter signal in which the relative intensity is plotted as a function of time. Also shown, by the dashed curve, is the mean intensity for 30 returns. The individual return is included in the mean of 30 returns. Employing Eq. 13 and making the conventional conversion to the decibel form gives

$$<E(t)> = L + 20 \log i - D + M + G - D + B + S_v(t) - KC\left[t - \frac{\tau}{2}\right] + 10 \log \left[\frac{2\tau}{Ct(t - \tau)}\right], \tag{17}$$

where $S_v(t)$ is the scattering strength at time t, L is the transmitting response of the transducer, i is the source current, D is the dome loss, M is the receiving sensitivity of the transducer, G is the receiver gain (fixed), K is the absorption coefficient, B is $10 \log b$, and $<E(t)>$ is the average of the received signal at time t. In terms of scattering strength Eq. 17 is written

$$S_v(t) = <E(t)> - M - G - L - 20 \log i - B + 2D + KC\left[t - \frac{\tau}{2}\right] - 10 \log \left[\frac{2\tau}{Ct(t - \tau)}\right]. \tag{18}$$

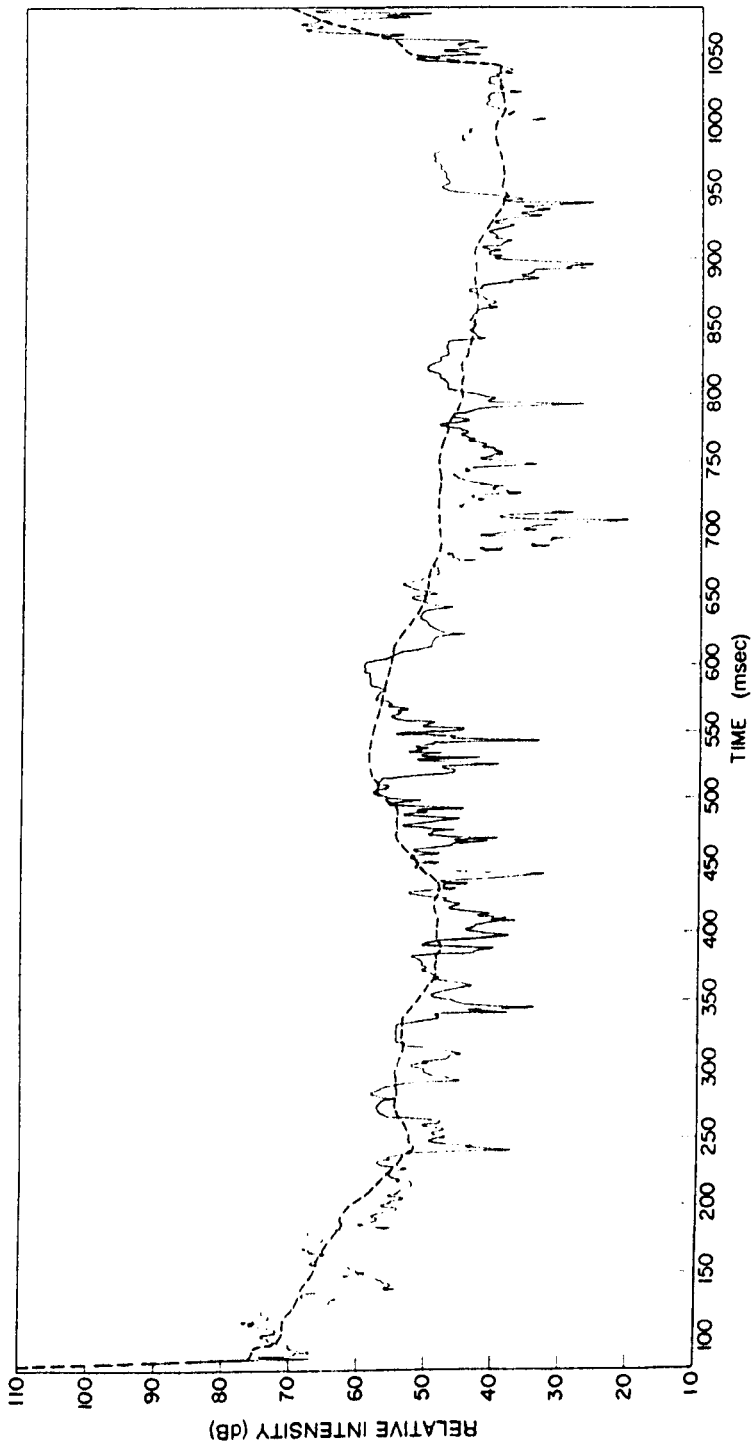

Fig. 4. Received intensity as a function of time.

To obtain the scattering-strength profile, that is, the scattering strength as a function of depth for a nonrefractive medium, the center of the scattering volume (Fig. 5) is positioned in depth by

$$d = d_0 + \frac{Ct \sin \beta}{2} \quad , \tag{19}$$

where d is the depth, d_0 is the depth of the source/receiver, and β is the depression angle (with the sign of β being plus for depression and minus for elevation).

SCATTERING-STRENGTH PROFILE

Figure 6 is a typical scattering-strength profile. Depth is in meters along the ordinate, and scattering strength is in decibels, increasing along the abscissa. This profile was made with the transducer at a depth of 23 m and directed downward at an angle of 45° with respect to the horizontal. The measurements were made in the early morning between 0200 and 0300. The profile shows a steep decrease of scattering strength between the 100- and 200-m depths, a minimum in the region just below 200 m, and a scattering layer at about 455 m.

The effects of refraction on the scattering-strength profile were investigated and found to be negligible for the parameters employed, with the exception of sound speed. The average sound speed over the path, obtained from the computation of propagation factors in the Appendix was employed.

SCATTERING STRENGTH AS A FUNCTION OF PULSE LENGTH

Figure 7 is a composite illustration of six scattering-strength profiles in the Blake Plateau area including the 30-msec profile of Fig. 6. All of the profiles are made with a 45°-depression angle. The pulse lengths for the profiles are 15, 20, 30, 40, 50, and 60 msec. It is not intended that the reader resolve each of the profiles but rather observe how similar the profiles remain as the pulse length is varied by a factor of 4 to 1. Except for the fine structure all of the profiles are the same.

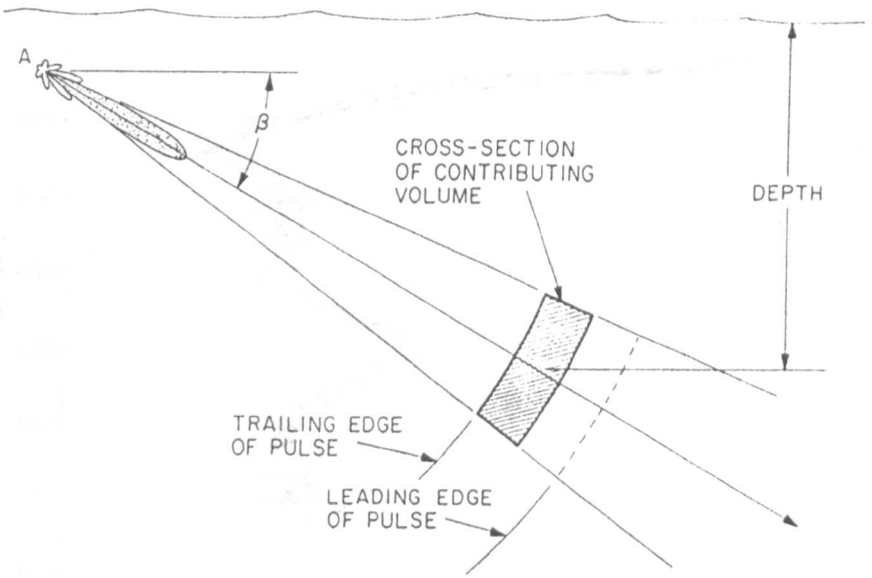

Fig. 5. Location of the scatter volume.

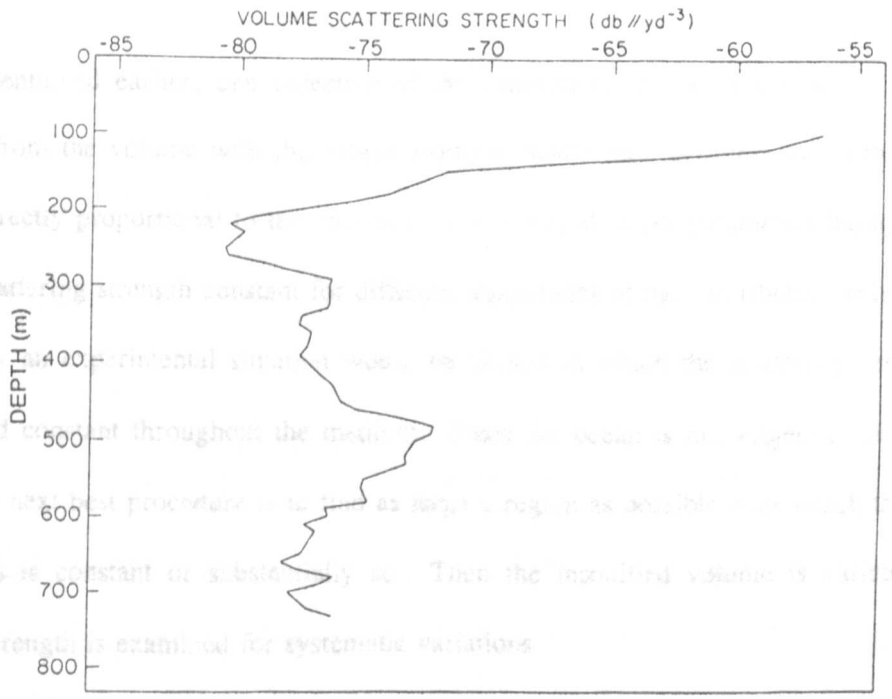

Fig. 6. Typical scattering-strength profile. This profile was obtained at 0222 hours in the Blake Plateau area with $\beta = 45°$ and pulse length $\tau = 30$ msec.

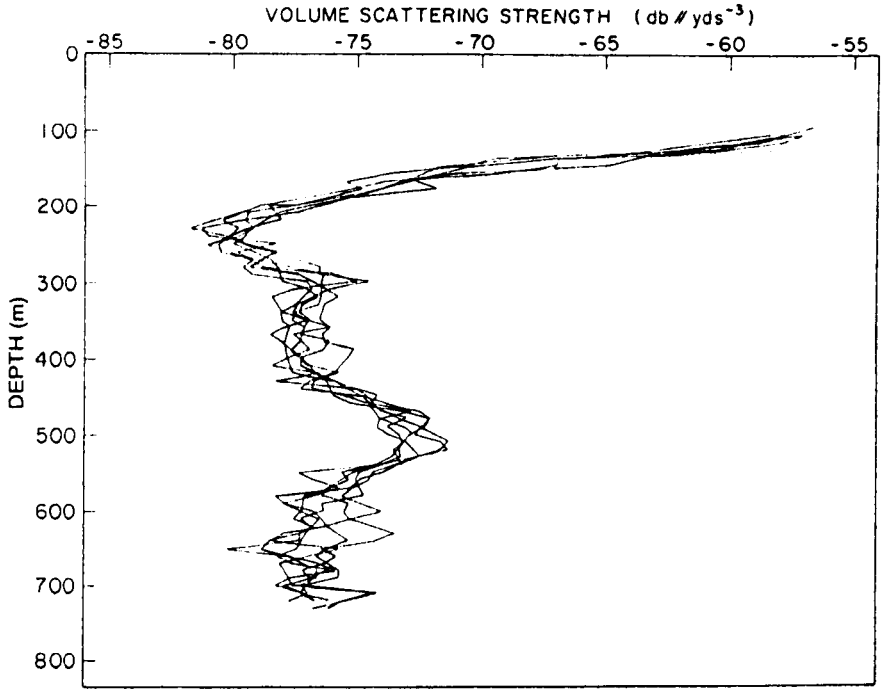

Fig. 7. Composite of six scattering-strength profiles. These profiles were obtained at 0220 to 0225 hours in the Blake Plateau area with $\beta = 45°$ and pulse lengths τ from 15 to 60 msec.

As mentioned earlier, one objective of the experiment was a comparison of measured scattering from the volume with theoretical isotropic scattering. Specifically, is the received intensity directly proportional to the contributing volume, all other parameters being constant, or is the scattering strength constant for different magnitudes of the contributing volume?

Ideally an experimental situation would be chosen in which the scattering strength was uniform and constant throughout the medium. Since the ocean is not subject to this kind of control, the next best procedure is to find as large a region as possible over which the scattering strength is constant or substantially so. Then the insonified volume is varied and the scattering strength is examined for systematic variations.

In this experiment the volume was varied by the control of pulse length. When a short pulse was employed, a region of constant scattering strength, to approximately ± 1 dB, was found between the 300-m depth and the 425-m depth of the scattering-strength profiles of Fig. 7. As the insonified volume was increased by increasing the pulse length, the scattering strength remained constant within approximately ± 1 dB. The size of the region restricted the

maximum pulse length such that a variation in volume of only 4 to 1 was covered. Within the experimental error the scattering strength was constant over the 4-to-1 variation.

Two scattering-strength profiles were taken in the area about 90 nmi south-southeast of Cape Hatteras with the transducer axis directed vertically downward. These profiles are illustrated in Fig. 8. The solid-curve data were obtained with a pulse length of 10 msec, and the dashed-curve data were obtained with a 100-msec pulse length. Both sets of data were obtained between 2300 and 2400 hours. Here good agreement is found between profiles obtained with a factor-of-10 difference in pulse length.

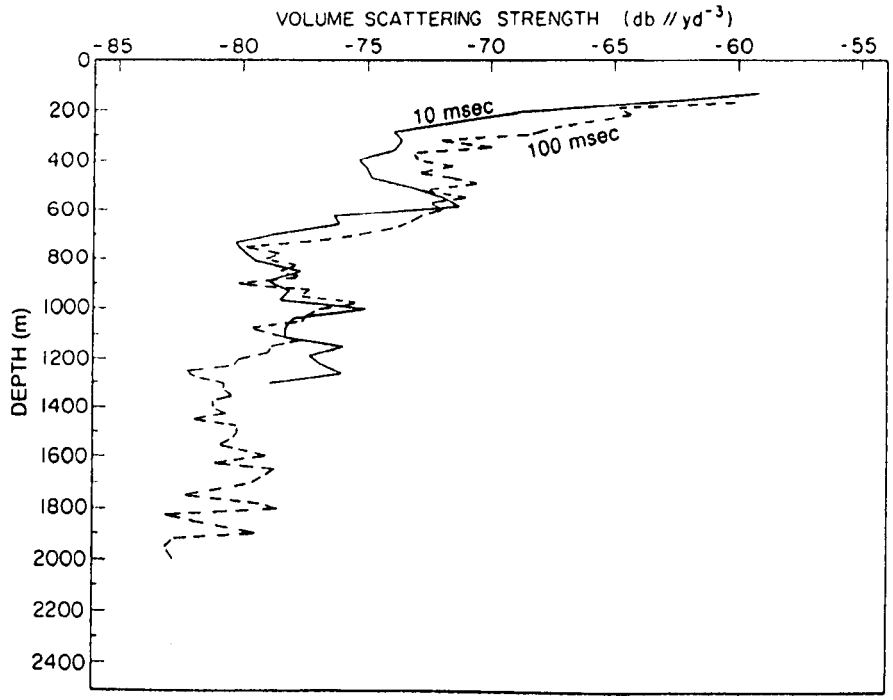

Fig. 8. Scattering-strength profiles obtained at 2330 hours in the Cape Hatteras area with two pulse lengths and $\beta = 90°$.

SCATTERING STRENGTH AS A FUNCTION OF β

A scattering-strength profile was constructed by holding the pulse length constant at 2 msec and varying the elevation of the beam from straight up to straight down in 10° increments. The transducer was at a depth of 55 m for this set of data.

The scattering-strength-versus-time data (Eq. 18) were positioned at the appropriate depths by use of Eq. 19 for each depression or elevation angle. This gave a number of scattering strengths for each depth. Since no systematic variation of scattering strength as a

function of β could be detected, the data were averaged to provide a single profile. The resulting profile is illustrated by the dashed curve in Fig. 9. For comparison, the profiles of Fig. 7 were averaged and illustrated by the solid curve of Fig. 9. Both profiles were made from data taken in the same area of the Blake Plateau, the major difference being the time of day when the measurements were taken. The dashed curve was obtained between 1900 and 2000 hours in the evening, and the solid curve was obtained between 0200 and 0300 hours in the morning. The significant decrease of scattering strength from the dashed curve to the solid curve below the depth of 140 m is attributed to a diurnal change of scatterers in this area. Unfortunately data were not taken that would complete the solid profile near the surface.

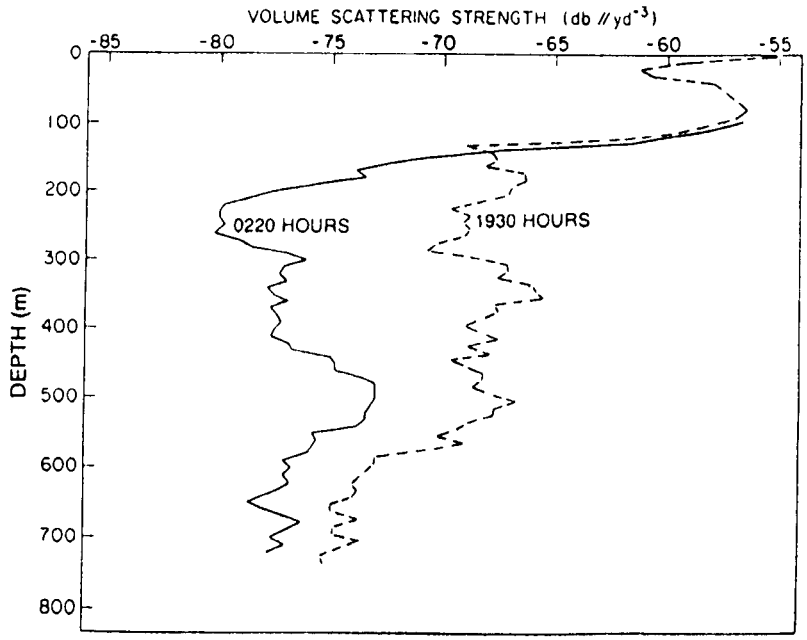

Fig. 9. Comparison of two scattering-strength profiles taken at different times of day in the Blake Plateau area.

SUMMARY

An experiment indicates that the strength of monostatic volume scattering in the ocean is independent of the magnitude of the insonified volume, when the volume is changed by varying the pulse length by a 4-to-1 ratio or more. Thus experimentally measured scattering in the ocean satisfies the isotropic scattering model under the conditions employed.

Scattering-strength profiles measured in two areas of the Atlantic display a decrease of scattering strength of approximately three orders of magnitude from near the surface to a depth of 1800 m.

REFERENCES

H.U. Criss, K.D. Flowers, B.G. Hurdle, R.M. Lee, and K.P. Thompson, "Procedures for a Series of Experiments in Acoustic Scattering from the Ocean Bottom and Volume in the Blake Plateau Area," NRL Memo. Rep. 1767, 1967.

C. Eckart, editor, "Principles of Underwater Sound," NRDC Summary Technical Reports, Division 6, Vol. 7, 1946.

B.G. Hurdle and K.D. Flowers, "Monostatic Scattering from the Ocean Volume," NRL Rep. 6533, 1967.

K.D. Flowers and B.G. Hurdle, "Monostatic Scattering from the Ocean Volume," J. Acoust. Soc. Am. **38**, 932 (1965).

R.J. Urick, "THe Backscattering of Sound from a Harbor Bottom," J. Acoust. Soc. Am. **26**, 231 (1954).

Chapter 7

SPACIAL AND TEMPORAL CHARACTERISTICS OF ACOUSTIC FIELDS IN A DISPERSIVE CHANNEL

INTRODUCTION

During the 1970s a team of scientists in the Propagation Branch at the Naval Research Laboratory conducted a major program in the propagation of low-frequency and very-low-frequency acoustic waves in the ocean. This included both theoretical studies and experiments at sea. Propagation paths totaling more than 5000 nmi in both the Atlantic and Pacific Oceans were traversed with multiple CW sources being towed and impulsive explosive charges being deployed along the tracks. Figure 1 illustrates the nature of the low-frequency propagation experiments. This research resulted in a series of approximately ten papers that comprehensively describe acoustic propagation at frequencies from 5 to 260 Hz in geometrically dispersive ocean channels.

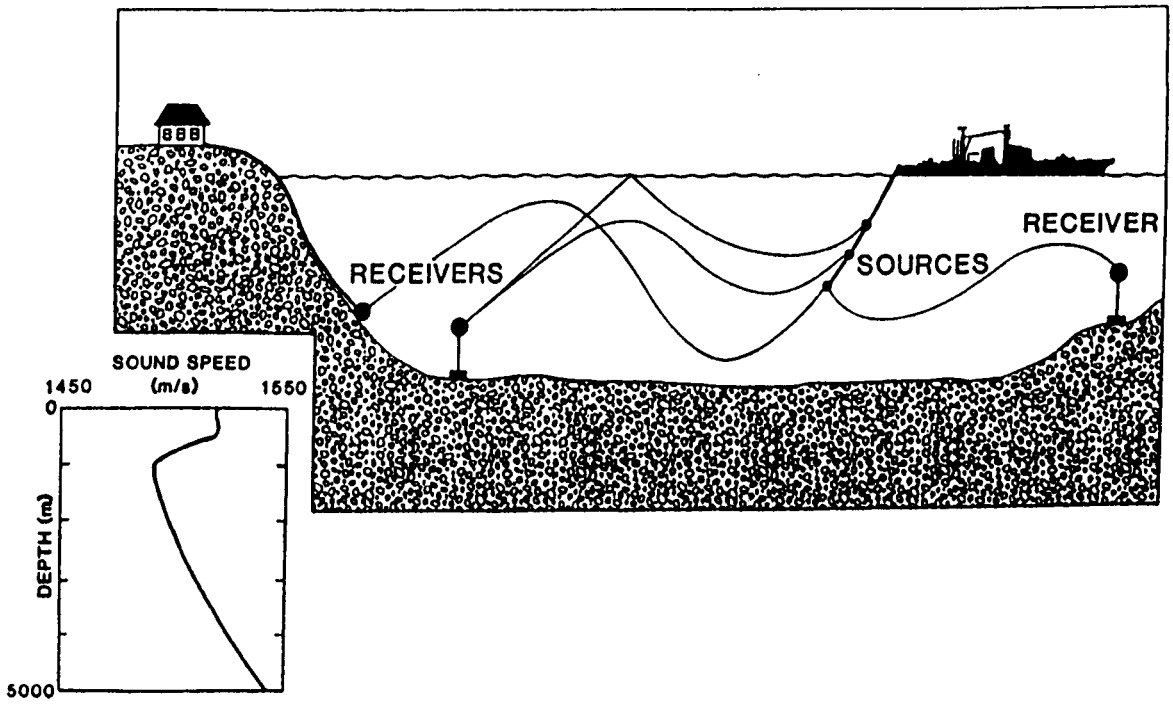

Fig. 1. Low-frequency propagation experiment.

This chapter will begin with a brief review of the nature of and contributions of some experiments to the understanding of propagation of low-frequency and very-low-frequency acoustic waves in the ocean environment. It then continues with a discussion of the nature of the complicated continuous-wave interference field produced by the propagation in both space and time. Emphasis is placed on the fluctuation statistics of the received signal amplitudes and on an imperial model describing them. Also, the phase statistics of the signal and the correlation length of the field are included. A delineation is made between this work, based on a deterministic approach, and propagation through random media, requiring a statistical approach. It will not treat propagation in a random media. The chapter ends with a description and analysis of the propagation and arrival structure of impulsive signals in the channel.

PROPAGATION EXPERIMENTS

Geography

Of the three principal experiments, two were in the North Atlantic Ocean, and one was in the North Pacific Ocean. Figure 2a illustrates the ship's track (and sound-speed-profile regions to be described) for the first experiment, conducted in May 1969 and the first leg of the third experiment, conducted in May 1974. The second experiment was conducted northeast of Midway Island in August 1970 (Fig. 2). The purpose of those experiments was to provide data for comparison with theory and to provide data for analysis of propagation parameters where there was a shortage or incompleteness of existing data. Analysis of these experiments has significantly improved our understanding of the physical processes and their dependence on the environment.

Instrumentation

Table 1 indicates the acoustic sources employed with their operating frequencies and tow depths. The charge weight and deployment range along the ship's track is included for the impulsive sources. The Mark VI source was phase-locked to a frequency obtained by counting down from a rubidium frequency standard. Frequencies of the EM and Honeywell sources were also derived from the rubidium standard. The bandwidths of these sources were at least an order of magnitude smaller than any processing bandwidth.

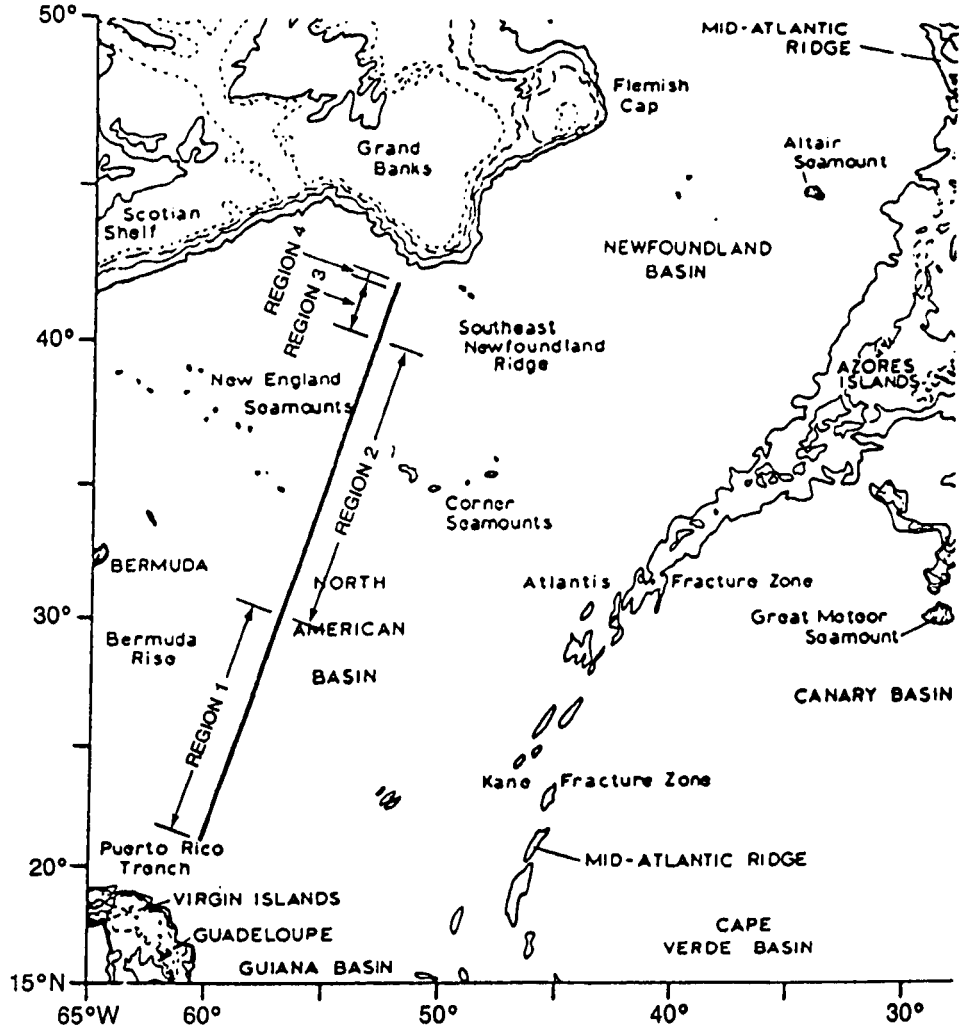

Fig. 2a. Ship's track for the two Atlantic experiments.

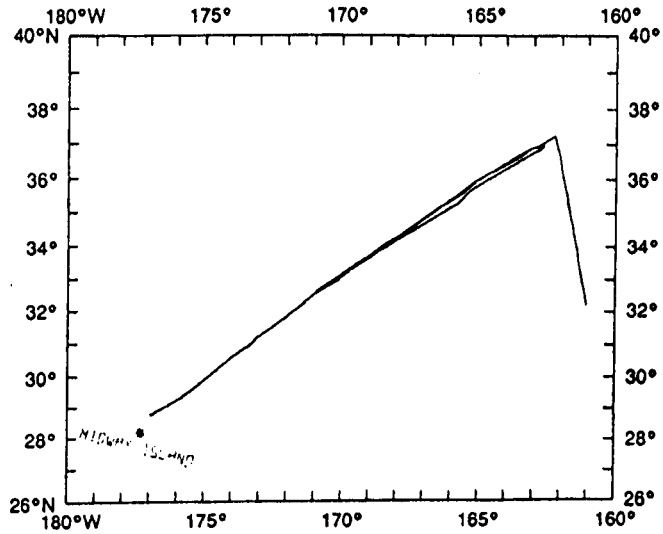

Fig. 2b. Ship's track for the Pacific experiment.

Table 1. Acoustic source data.

Source Type	Atlantic 1969		Pacific 1970		Atlantic 1974	
	Freq. (Hz)	Depth (m)	Freq. (Hz)	Depth (m)	Freq. (Hz)	Depth (m)
Mark VI	13.89	104	15	140	9.807	110
Electromagnetic (EM)	111.1	21	—	—	110	23
Honeywell HX302H	—	—	—	—	262	25
Explosive TNT	15 to 250*	110	15 to 250**	200	—	—

*Passband filtered from the spectrum of frequencies due to a 2.3-kg (5-lb) charge at a range of 6.5 km.

**Passband filtered from the spectrum of frequencies due to a 1.4-kg (3-lb) charge at a range of 13 km.

The signals were received both on deep-sound-channel hydrophones and on bottomed hydrophones. The CW signals were narrowband filtered (Q = 20 for the 1969 and 1970 data and Q = 50 for the 1974 data) at the signal frequencies and recorded both graphically and on magnetic tape in analog form. Shot signals were bandpass filtered between 15 and 250 Hz and recorded on magnetic tape with separate low-gain and high-gain channels to cover the dynamic range. A highly stable timing signal was recorded on the tape to facilitate the processing and analysis. More details on the instrumentation and procedures of the three experiments are contained in Guthrie et al. (1974), Guthrie et al. (1976), and Shaffer et al. (1976).

Navigation

Special attention was given to providing the best position-fixing possible. Four methods were employed to determine the ship's position in time along the track. The first method was to linearly interpolate between fixes obtained using the Navy Navigation Satellite System (NNSS). For a ship at sea this system is claimed to have a typical accuracy of 0.25 nmi. The second method was to use Loran C. The third method was to multiply shot travel time by the mean sound speed. The fourth method was to measure the Doppler shift. The agreement between methods in determining the position was well within 1 km.

Environmental Data

In addition to historical data obtained from many sources, a continuous bathymetric record was made along the entire path of tow using a precision fathometer. Expendable

bathythermograph casts were made every 2 hours to a depth of 760 m. From these casts 52 were used to obtain the sound-speed profile as a function of range. A computer-oriented method (Nutile, 1976) using Leroy's second equation and water-mass identification was employed to convert the temperature profiles to sound-speed profiles. The archival data were used to extend the profiles to the ocean bottom.

The sound-speed profiles fell into four categories over the track (Guthrie et al., 1974). Figure 3 is a plot of the profiles in each region. The profiles are typical for these areas of the Atlantic. In Fig. 4 the depths of the sound-speed maxima and minima are plotted as a function of range along the first leg of the track (Fig. 2a). Near the hydrophone (0-km range) the axis of the SOFAR channel (C) is at the relatively shallow depth of 900 m. As range increases, the axis depth increases to about 1200 m. Beyond about 1800 km the axis depth decreases and, near the Grand Banks, rapidly approaches the surface. Between 1150 and 2450 km, in region 2, there is a secondary sound channel above the SOFAR channel. From 1150 to 2040 km, the secondary channel exists as a subsurface channel with an average axial depth of 108 m (A) and a maximum sound speed at an average of 358 m (B). From 2040 to 2440 km, the secondary channel exists as a surface channel with a subsurface maximum sound speed at 371 m. Between ranges 2230 and 2290 km, within region 2, three profiles (Fig. 3) exhibit characteristics of the third (region-3) class, so that (Fig. 4) the subsurface channel has a discontinuity.

The sound-speed-profile characteristics reflect the water masses encountered along the track (Fenner and Bucca, 1971). The near-surface sound channel in region 2 is produced by a water mass called "18° water." Formed in winter, west of the mid-Atlantic Ridge near 35°N, this water at a temperature of about 18°C sinks to a maximum depth of 400 m and flows south. Because this water mass is isothermal, the pressure effect produces a positive velocity gradient in its presence. South of about 30°N (region 1) the diluted 18° water is responsible for the slight change in the sound-speed gradient between 200 and 400 m deep. Between about 20°N and 35°40'N, the 18° water produces a subsurface sound channel. From 35°40'N north to the Gulf Stream, the temperature of the surface layers above the 18°

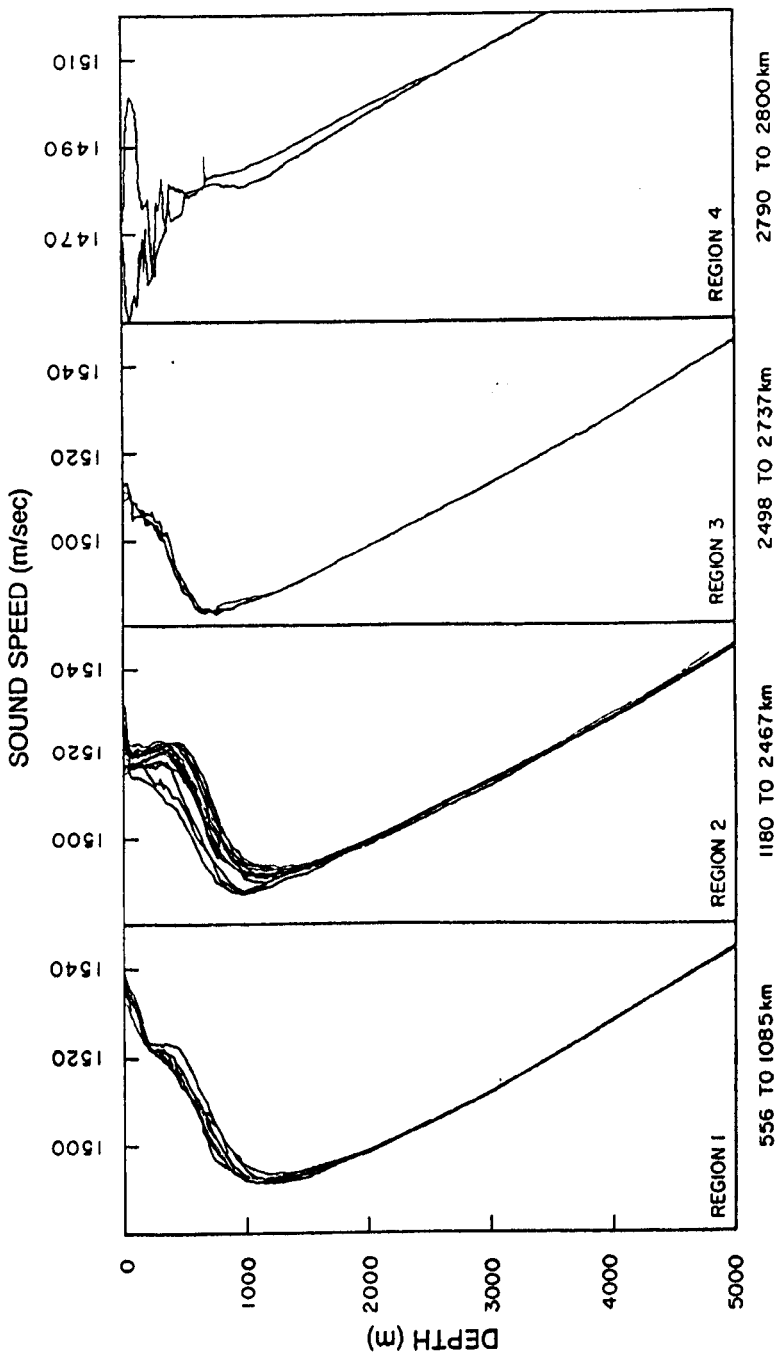

Fig. 3. Four classes of sound-speed profiles found (Guthrie et al., 1974).

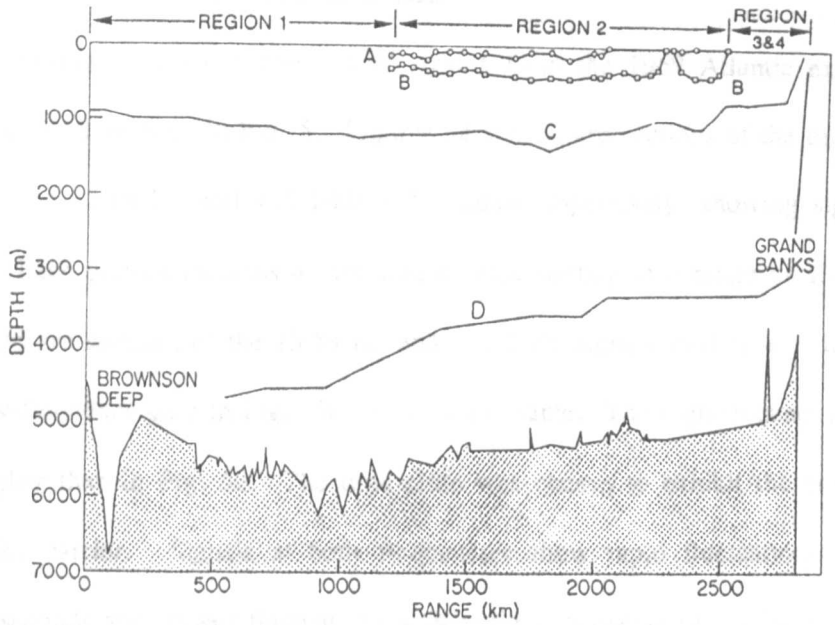

Fig. 4. Bathymetry and sound channels, where A is the subsurface-channel axis, B is the bottom of the subsurface channel, C is the SOFAR-channel axis, and D is the limit of the depth excess (Guthrie et al., 1974).

water is lowered by winter cooling, which results in a surface sound channel. The northern extent of the 18° water and of the upper channel is marked by the Gulf Stream. The average depth of the SOFAR axis for the class-2 profiles exceeds that of the class-1 profiles because of the presence (region 2) of saline Mediterranean Intermediate Water. The class-3 profiles reflect the properties of the cold Slope Water Current. This current is formed on the continental shelf and flows eastward. The class-4 profiles are produced by the Labrador Current. This cold surface flow displaces the thermocline and brings the SOFAR axis near to the surface.

Figure 4 also shows the bathymetry along the ship's track. For ranges to 400 km the depth was taken from bathymetric charts. At greater ranges the depth was determined from the precision-fathometer records. Sound speeds, densities, and gradients in the ocean bottom were taken from Hamilton (1974).

CONTINUOUS-WAVE ACOUSTIC SIGNALS

Typical examples of the received CW signals from the 1969 Atlantic experiment that were analyzed are illustrated in Fig. 5. Figures 5a and 5b are sections of the original graphic recordings of the 13.89-Hz and 111.1-Hz CW signals respectively, showing signal pressure versus time. Each section includes 43 minutes of data starting at a range of 1394 km. Figures 5c and 5d are sections of the 13.89-Hz and 111.1-Hz signals starting at a range of 2744 km. The low-frequency gain in Figs. 5a and 5c is the same. The high-frequency gain in Fig. 5b is 8% higher than in Fig. 5d. The time scale was chosen to exhibit the envelope at the expense of the carrier. Signals at both frequencies show rapid fluctuations with periods under a few seconds and slower fluctuations with periods in excess of 1 minute. The signals from the other two experiments are equally well represented by those of Fig. 5, except that somewhat higher and lower beat rates were observed.

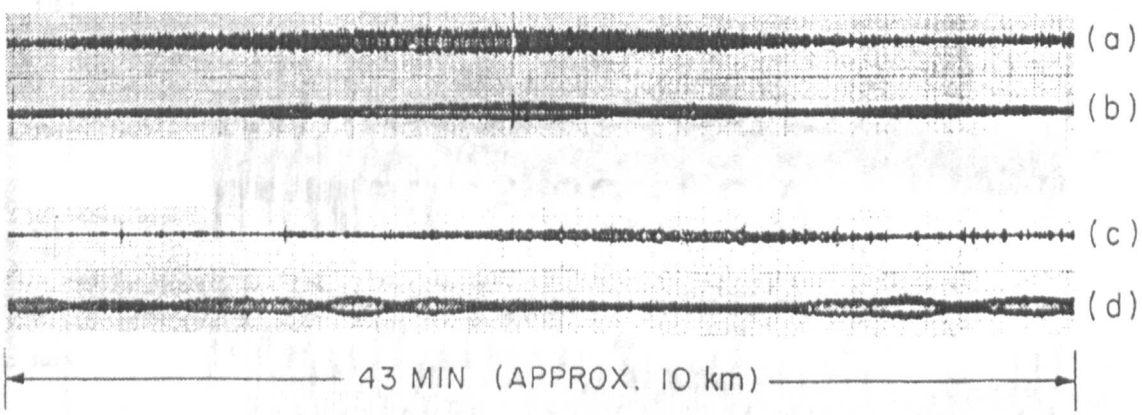

Fig. 5. Graphic recordings of the received CW acoustic pressure (Guthrie et al., 1974): (a) 13.89-Hz signal starting at 1394 km, (b) 111.1-Hz signal starting at 1394 km, (c) 13.89-Hz signal starting at 2744 km, and (d) 111.1-Hz signal starting at 2744 km.

Transmission Loss

Transmission Loss ($TL = 10 \log_{10} I_R/I_0$, where I_0 is the acoustic intensity of the source at 1 yard and I_R is the intensity of the received signal, expressed in dB re 1 yard), is one of the most useful parameters in underwater acoustics. When TL is plotted versus the variables such as range, depth, and frequency, it can be used to enable a greater understanding of the underlying physical processes.

Figure 6a is a plot of the 13.89-Hz TL with samples spaced every 0.43 km. Figure 6c shows the 111.1-Hz TL sampled every 0.215 km. To obtain these TL curves, the 111.1-Hz signal envelope was sampled every minute, and the 13.89-Hz signal envelope was sampled every 2 minutes. These samples were obtained from the graphic recording as 1-minute-long visual averages of the signal. This averaging eliminated those fluctuations with periods much less than a minute. The sample rate then exceeded the Nyquist frequency for the remaining fluctuations. The quantization of the TL levels of Figs. 6a and 6c reflects the coarse digitization employed.

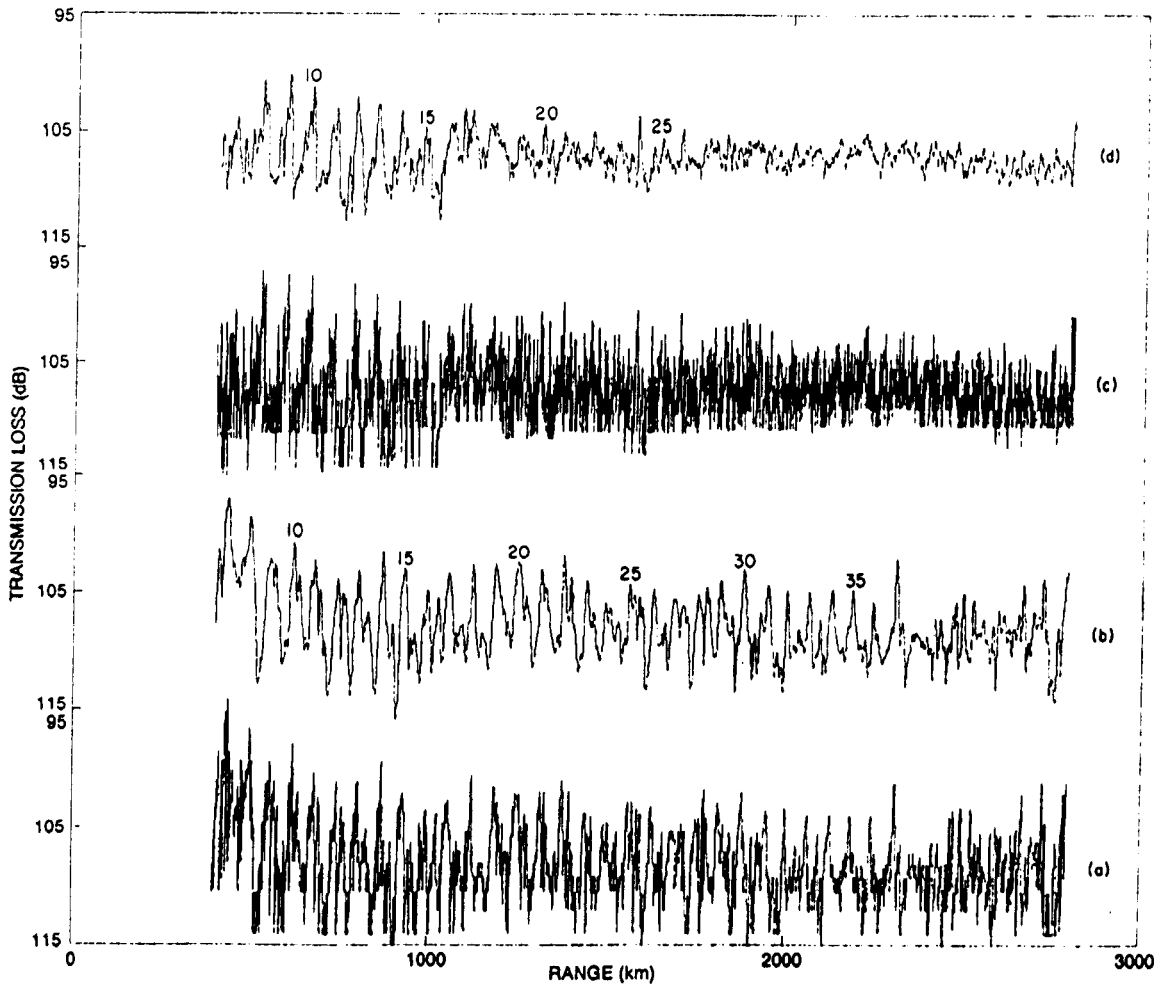

Fig. 6. Acoustic transmissiom loss (TL) versus range (Guthrie et al., 1974): (a) 13.89-Hz TL, (b) 13.89-Hz TL for the received intensity averaged over 7 km, (c) 111.1-Hz TL, and (d) 111.1-Hz TL for the received intensity averaged over 7 km.

Inspection of the 13.89-Hz TL curve (Fig. 6a) shows a fluctuation rate less than that of the 111.1-Hz curve (Fig. 6c). This smaller rate results from the smaller number of propagating modes at the lower frequency. At intervals of about 60 km there appear, for both frequencies, regions of higher average signal level: the convergence zones. To emphasize the convergence zones more clearly, a 7-km moving average of pressure squared is shown in Figs. 6b and 6d for the low and high frequencies respectively. The low-frequency and high-frequency convergence zones appear at different ranges. The 13.89-Hz signal has a convergence-zone spacing of 61.7 km, and the 111.1-Hz signal has a convergence-zone spacing of 65.0 km. The zone numbering, using these zone spacings, is shown above the peaks in Figs. 6b and 6d. The low frequency Convergence Zone shortening results from the increase of the sound-speed gradient over the wave length must be vanishingly small) for the SOFAR modes.

Figure 7 is an expanded portion of the TL curves of Fig. 6 covering the range interval 400 to 1000 km. The location of each high-frequency zone is marked by a vertical line. The shift in range of each high-frequency zone relative to the corresponding low-frequency zone is indicated by an arrow. The analysis indicates that the convergence spacings are 61.7 km for 13.89 Hz and 65.0 km for 111.1 Hz, giving a 3.3-km difference in the zone spacing for the two frequencies. This difference results in the high frequency gaining one full convergence zone over the low frequency at the 20th and 21st zones respectively.

Interference Wavenumber

As previously indicated, the fluctuations of the signal are of two types: spacial and temporal. The spacial fluctuations are produced by the change in range between the source and sensors in the field. Temporal variations are the result of the time variations of the medium. In all data sets in which the sensors are moving, the two types of fluctuation are inseparably mixed. As the frequency is decreased, the increasing wavelength is less influenced by the smaller variations in the medium. Hence, for example, the 13.89-Hz signals were not trapped by the near-surface duct in region 2 of the 1969 experiment. Also, the very-low-frequency fields remain stable over longer times in ocean channels.

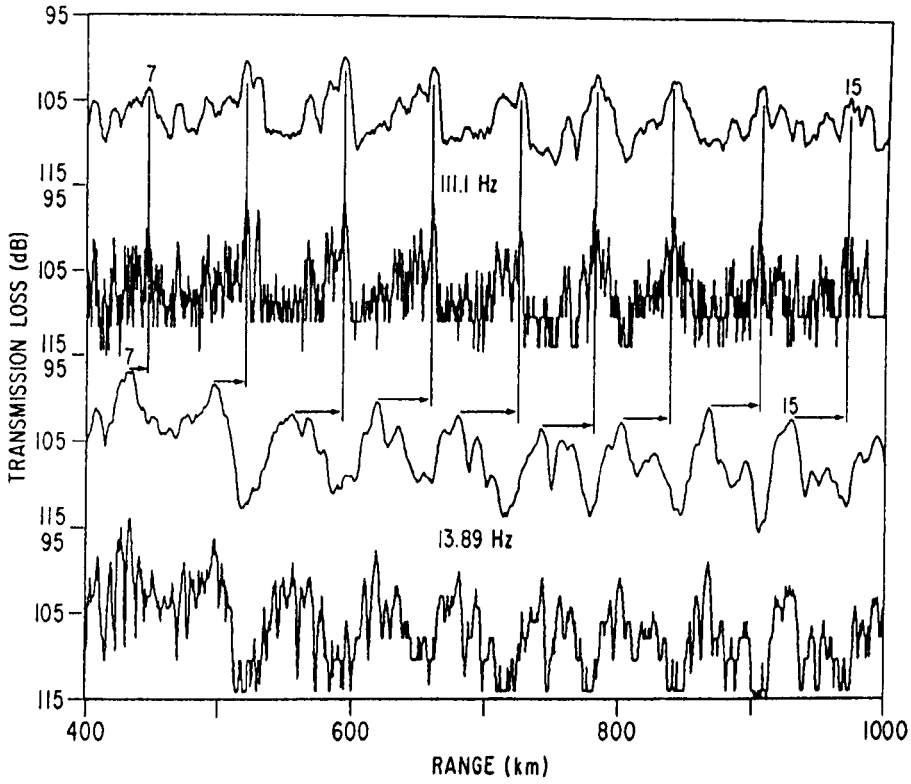

Fig. 7. Acoustic transmission loss versus range. This figure is the section of Fig. 6 between 400 and 1000 km plotted on an expanded range scale. The arrows show the shift in range between corresponding high- and low-frequency convergence zones.

An analysis of the interference-wavenumber or interference-wavelength spectra provides an additional tool in understanding the physics of acoustic propagation in a channel. The CW data were spectrum analyzed in the wavenumber domain. The envelope was squared, and the cylindrical spreading factor was removed by multiplying by range. The power spectrum of the resulting function gave the interference wavenumbers. Signal envelopes in the different sound-speed-profile regions were analyzed separately. Figure 8 is an example of an interference-wavelength spectrum of signal powers for a range interval of 500 km in region 1.

A prominent feature of the spectrum is the large peak at $\Lambda = 62$ km, which corresponds to the convergence-zone spacing. Equispaced peaks are seen to the right of the 62-km peak. In terms of normal modes the convergence-zone phenomenon is a result of the distribution of wavenumbers of the propagating modes.

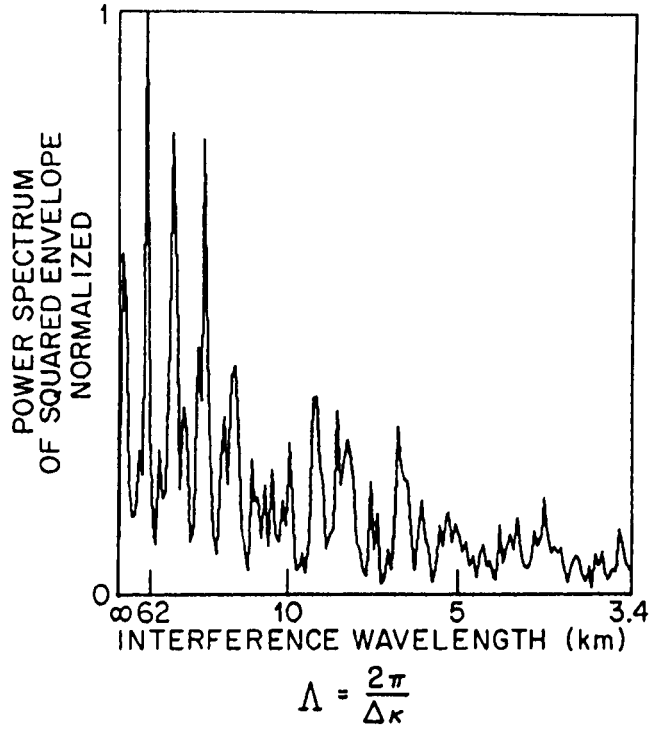

Fig. 8. Interference-wavelength spectrum of signal powers.

A certain subset of these wavenumbers has the property that its members are approximately equally spaced along the kappa axis at intervals $\Delta\kappa$. The members of this subset, the RSR and a few higher SOFAR modes, have phase velocities which lie between the speed of sound near the surface and that at the bottom. The wavenumbers in this subset are spaced such that spectral lines appear at $\Delta\kappa = 2\pi/\Lambda$ and at multiples of this value. The interference wavelengths at less than approximately 5 km are a result of random, relatively weak fluctuations.

CONTINUOUS-WAVE-FIELD STATISTICS

This section will discuss the statistics of the CW field in the ocean channel. The statistics of received signals in the field provide a powerful tool in analyzing and understanding the physical process of propagation in a dispersive channel.

Fluctuation Statistics

The major source of statistical data on the fluctuation of propagated signals in a channel was obtained during the experiment in May 1974. In this experiment three CW acoustic

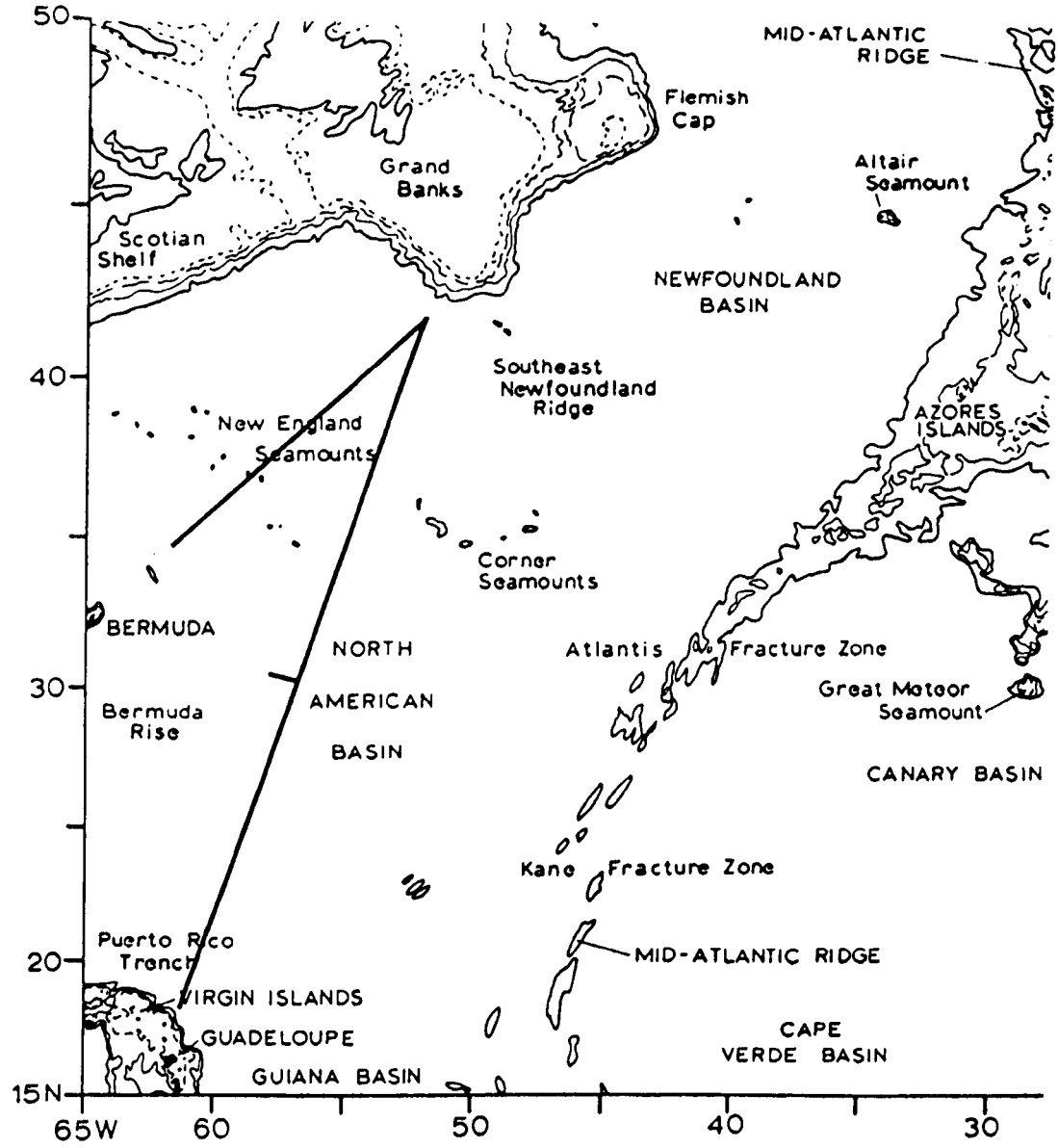

Fig. 9. Ship's track in May 1974.

sources were towed along the track (two legs, with a jog along the first leg) indicated in Fig. 9. The primary frequencies of the three sources were 9.807, 110, and 262 Hz. On short portions of the track the Mark 6 source was operated at 8, 6, and 5 Hz.

Table 1 provides the details of the sources used during the experiment. All three source frequencies were derived from a rubidium frequency standard which locked each source to its frequency with a deviation of less than one part in 10^8.

The signals from each of the sources were received on both suspended and bottomed hydrophones on the western slopes of the Atlantic Basin. Signals were recorded in analog

form on multichannel analog tape. In addition to the received signals a crystal-controlled reference frequency and a coded time signal were simultaneously recorded.

Data clocks were synchronized to WWV Fort Collins, Colo. Two NNSS receivers were employed. One provided a continuous visual display and the other produced a hard-copy-output navigational fix and all input parameters automatically. Loran C and DECCA receivers were interfaced with a printer which automatically recorded a fix every 5 minutes. Details of the shipboard data are contained in Shaffer et al. (1976).

Data Analysis

The trends of the data were analyzed. The data were converted from analog to digital form and organized for the analysis as indicated in Appendix 7A.

The data exhibited the normal characteristics associated with acoustic propagation in the ocean, including convergence zones and other specific geometry-related characteristics such as bathymetric shadowing. These gross characteristics of the data as a function of range significantly change the average received-signal amplitude. This nonstationarity in the data necessitates its removal so that the remainder of the signal amplitude, consisting of the fluctuations about the mean, can be statistically analyzed. One is then confronted with the question as to how much of the amplitude is to be considered mean level and how much is to be considered fluctuation.

The data were examined for a range of moving-average times of 30 to 180 minutes corresponding to spatial averaging of 6 to 36 km. Preliminary plots revealed the presence of slowly varying, long-term trends in the data. It was decided to separate out these effects, so that the autocorrelation and density functions could be estimated for an essentially-zero-mean residual process. Separation would also facilitate comparison of the mean amplitude levels with model predictions. The long-term component was obtained by smoothing the amplitude series with a moving average along its entire length. The smoothed series was then subtracted point by point from the amplitude series to obtain the residual series.

A residual series was determined for both a 3-hour and a 1-hour moving average. The 3-hour smoothing was estimated to be long enough to adequately remove long-term trends. The 1-hour smoothing was used so that the smoothed series would better represent convergence zone amplitudes at the shorter ranges. The number of points in a segment and the moving average size for each frequency, are given in Table 2.

Table 2 — Parameters for statistical analysis.

Frequency (Hz)	Sampling Increment (minutes)	No. of Points in Statistical Segment	No. of Points in Moving Average	
			3 Hours	1 Hour
262	1.0	384	181	61
110	1.0	384	181	61
9.807	4.26667	90	43	15

After the smoothed and residual series were generated, a computer program made the statistical computations. Both time series were inserted and broken sequentially into segments. There were no gaps between segments, and comparable segments for different frequencies and locations had the same starting and ending times. For each segment, an example of which is shown in Fig. 10, the program output included plots of five functions: the smoothed amplitude versus time, the residual amplitude versus time, the cumulative probability distribution function for the standardized residual, the probability-density histogram for the standardized residual, and the autocorrelation function for the standardized residual. The mean m and standard deviation s were calculated over the segment for the residual amplitude series $X(t)$. The standardized residual was then defined as the time series $X'(t) = [X(t) - \bar{X}(t)]/s$ which has zero mean and unity standard deviation. Of the five functions plotted the last three (the cumulative probability distribution function, the probability-density histogram, and the autocorrelation function) were calculated using the standardized residual in order to facilitate comparison of results for different frequencies, receivers, and segments.

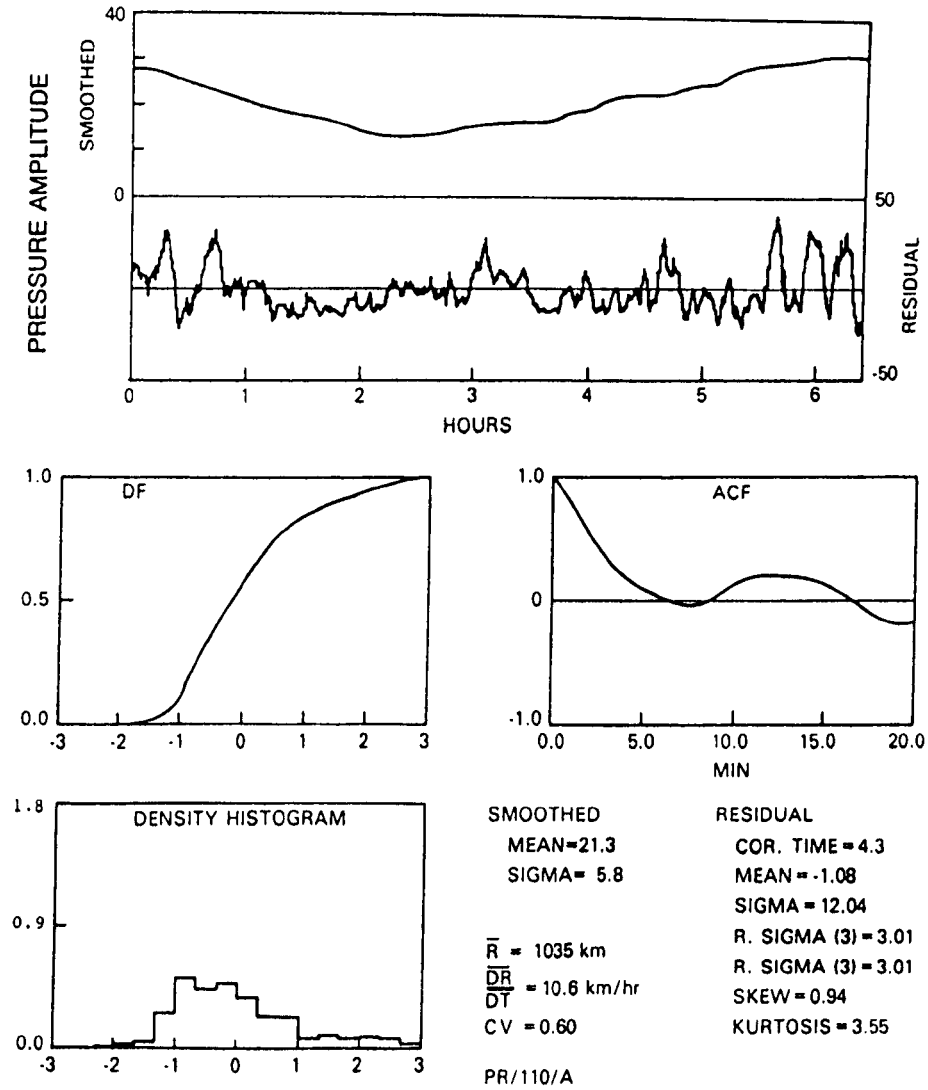

Fig. 10. Sample segment of data showing the smoothed and residual pressure amplitude curves, the residual distribution function (DF), the density histogram, the autocorrelation functions (ACF), and the sample statistics.

The following quantities were computed for each segment:

M - Mean value for the smoothed amplitude,

S - Standard deviation for the smoothed amplitude,

m - Mean value for the residual amplitude,

s - Standard deviation for the residual amplitude,

R - Average receiver-to-source range,

$\overline{(dR/dt)}$ - Average time rate of change in the receiver-to-source range,

CV - Coefficient of variation,

tau - Correlation time of the residual amplitude,

skew - Skew for standardized residual,

kurtosis - Kurtosis for the standardized residual, and

ν - Parameter for fitting Pearson's system of density curves.

In this notation the coefficient of variation is defined as CV $= s / (M + m)$. The correlation time is the time required for the autocorrelation to fall below 1/e (= 0.36789). It was estimated by a linear interpolation of lag times, corresponding to the observed autocorrelation values about 1/e. The use of the term "random component" in defining R. sigma (N) and R. sigma (3) requires some elaboration. The residual amplitude time series is assumed to be essentially the sum of a deterministic series and a purely random series. Further the deterministic component is assumed to be locally a polynomial. Estimates for both the degree of the polynomial and the variance of the random component were obtained by using a variate difference method.

The skew of a probability density function is a measure of its degree of asymmetry about the mean. The kurtosis is a measure of the peakedness of the density function. For standardized samples the skew and kurtosis are estimated by calculating the third and fourth moments about the mean respectively.

Preliminary examination of probability densities for selected segments indicated that they could be adequately fitted by Pearson's system of curves, to be found in Elderton and Johnson (1969). The parameter ν determines which of six types of curves will best fit the density function for the segment. The coefficients for making the fit are functions of the first four moments about the mean.

For each receiver and each frequency those segment statistics were plotted which were thought to be range or range-rate dependent. Samples of these plots are presented in Figs. 11 and 12, with Fig. 11 being for the 1-hour smoothing time and Fig. 12 being for the 3-hour smoothing times. The plots consist of the coefficient of variation (CV), the standard deviation

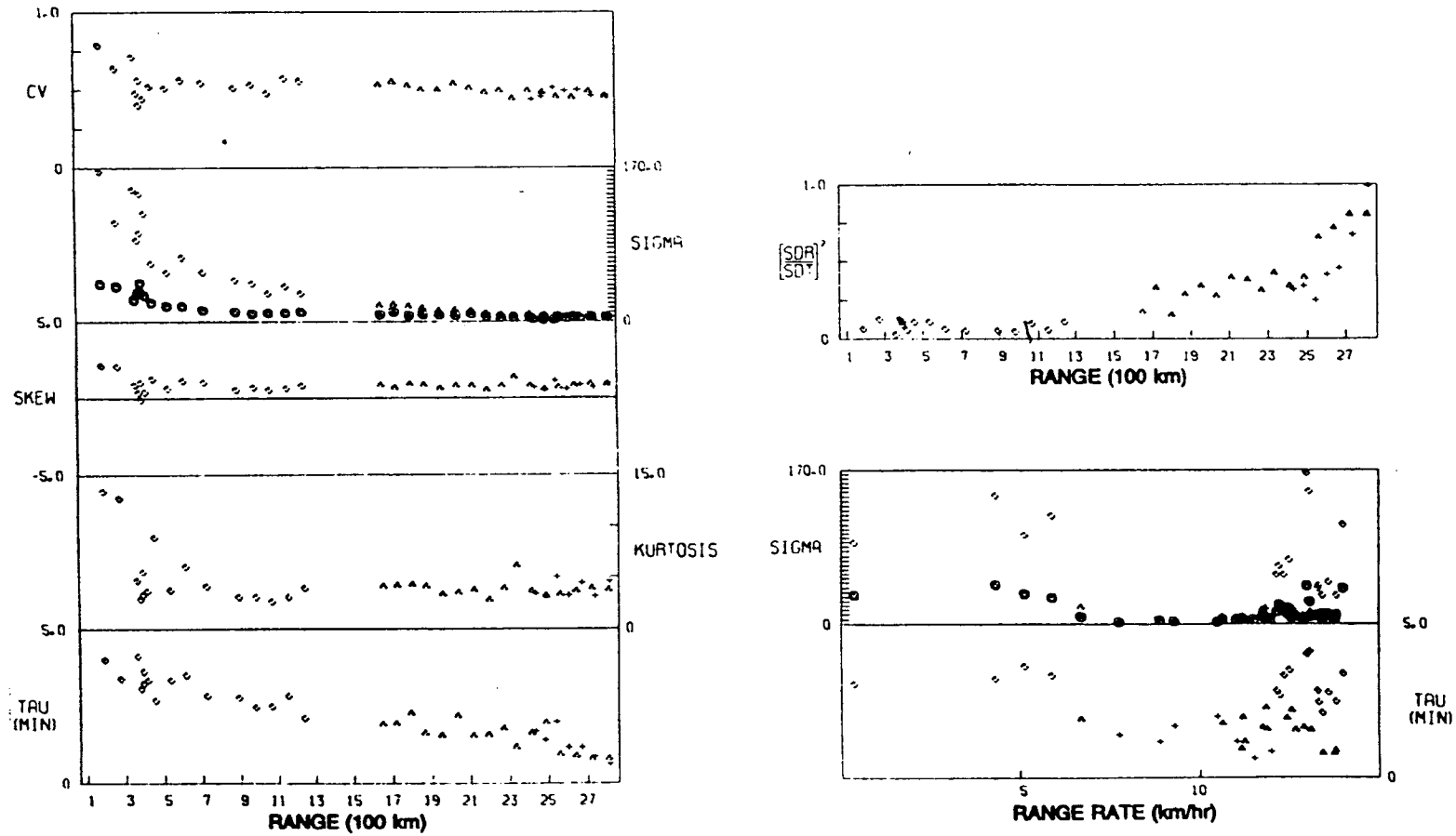

Fig. 11. Various statistics as a function of range or range rate, for a 1-hour smoothing time.

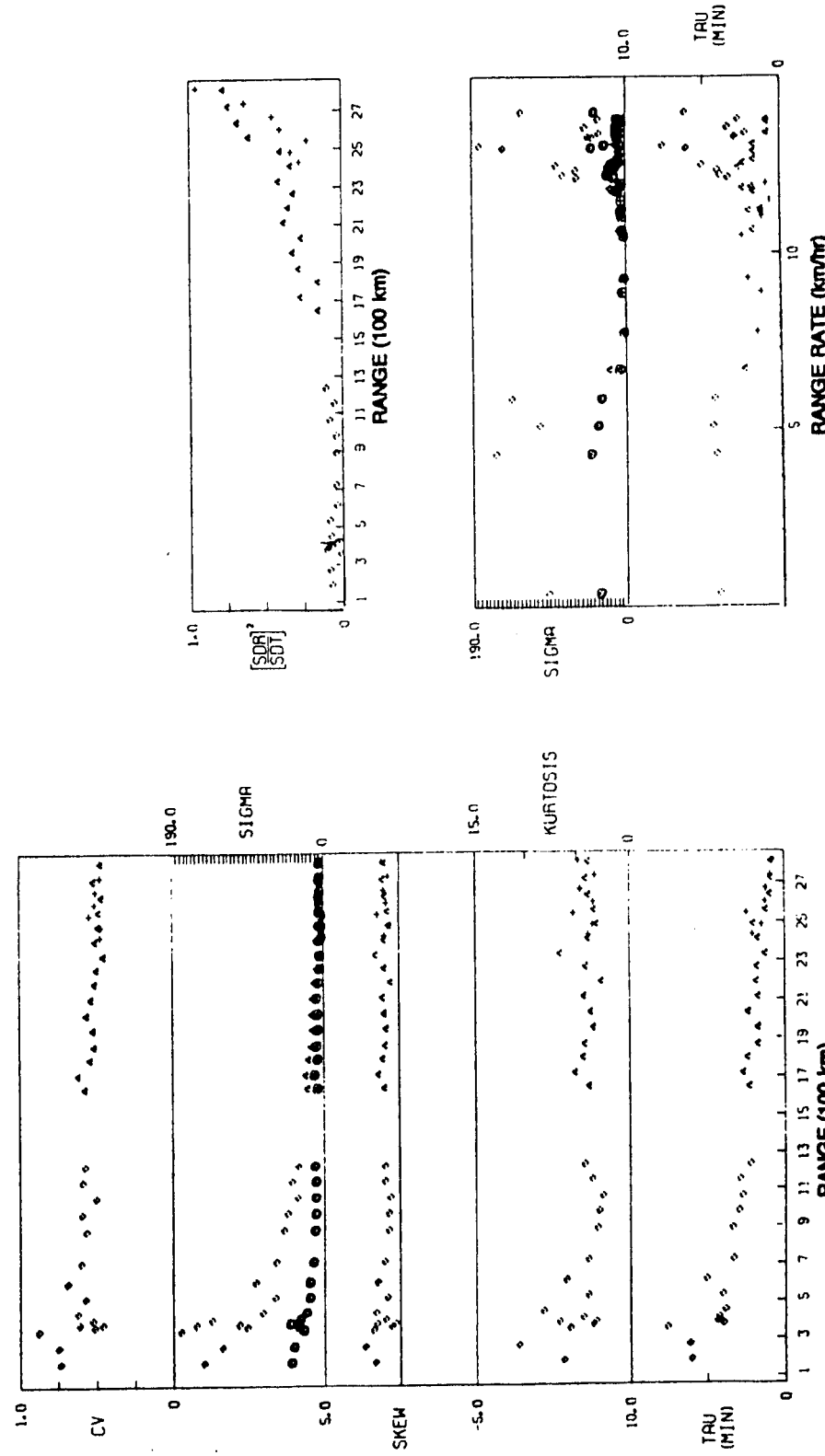

Fig. 12. Various statistics as a function of range or range rate, for a 3-hour smoothing time.

(sigma), the skew, the kurtosis, the correlation time (tau), and the ratio of the random estimate of the residual power to the total residual power $(SDR/SDT)^2$, all plotted as a function of range. The standard deviation (sigma) and correlation time (tau) are also plotted as a function of range rate. The circled values in the sigma plots are the estimates of the standard deviation of the random part of the residual signal. The three symbols used indicate the portion of the track from which the data originates: the diamonds denote data from that portion of the track south of Bermuda, the triangles denote data from the portion of the northward-going track north of Bermuda, and the crosses denote data from the southward-going track north of Bermuda.

After each data set had been analyzed in this manner, plots were made of the coefficient of variation, skew, kurtosis, and spacial-correlation length as a function of range for each set. It was observed that with the exception of the correlation lengths for the low frequency, each of these statistical descriptors exhibited a weak linear dependence on range, independent of the receiving site, whether bottom mounted or suspended. It was also observed that the descriptors for the two higher frequencies (110 and 262 Hz) were not statistically different. Thus, the data were grouped as either high-frequency data or low-frequency data, and the best linear fit (in the least-squares sense) to the plot of each statistical descriptor as a function of range was calculated.

These linear trends in the data, shown in Fig. 13 and listed in Table 3, were then removed, and histograms of the variation about these trends were determined. These distributions, shown in Figs. 14 and 15, include the distribution of spatial-correlation lengths for the high frequency. The correlation lengths for the low frequency will be discussed later. The zero value of the abscissa in the distribution for each statistic corresponds to the location of the linear trend, which was removed. The mean and standard deviation (sigma) about the mean are listed below the distribution of each statistic along with the skew and kurtosis of the corresponding standardized data, which have zero mean and unity variance. These values of mean, standard deviation, skew, and kurtosis may be inserted into the Pearson system of equations to provide a mathematical approximation for the density function of each statistic.

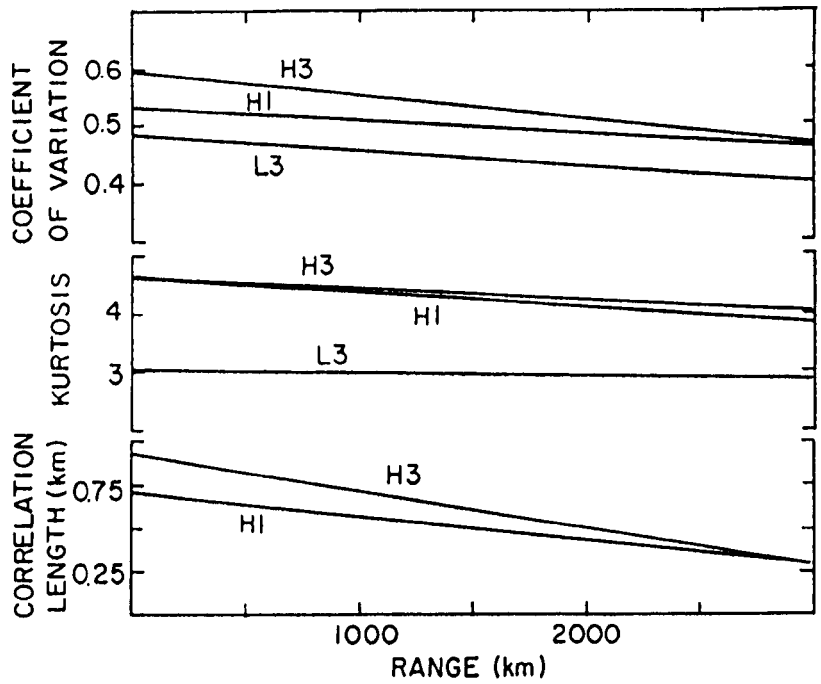

Fig. 13. Linear trends in the statistics as a function of range for the high-frequency 3-hour smoothing (H3), the high-frequency 1-hour smoothing (H1), and the low-frequency 3-hour smoothing (L3).

Table 3. Slope and intercept values for the linear fits to the coefficient of variation, skew, kurtosis, and correlation length (Fig. 13).

Function	3-Hour Smoothing, Low Frequency		3-Hour Smoothing, High Frequency		1-Hour Smoothing, High Frequency	
	Slope*	Intercept	Slope*	Intercept	Slope*	Intercept
Coefficient of variation	−0.0278	0.486	−0.0432	0.599	−0.0239	0.535
Skew	−0.0925	0.657	−0.0713	1.10	0.0259	0.751
Kurtosis	−0.0438	3.01	−0.211	4.67	−0.256	4.64
Correlation length (km)	—	—	−0.215	0.937	−0.137	0.714

*Slopes require the range to be in thousands of kilometers.

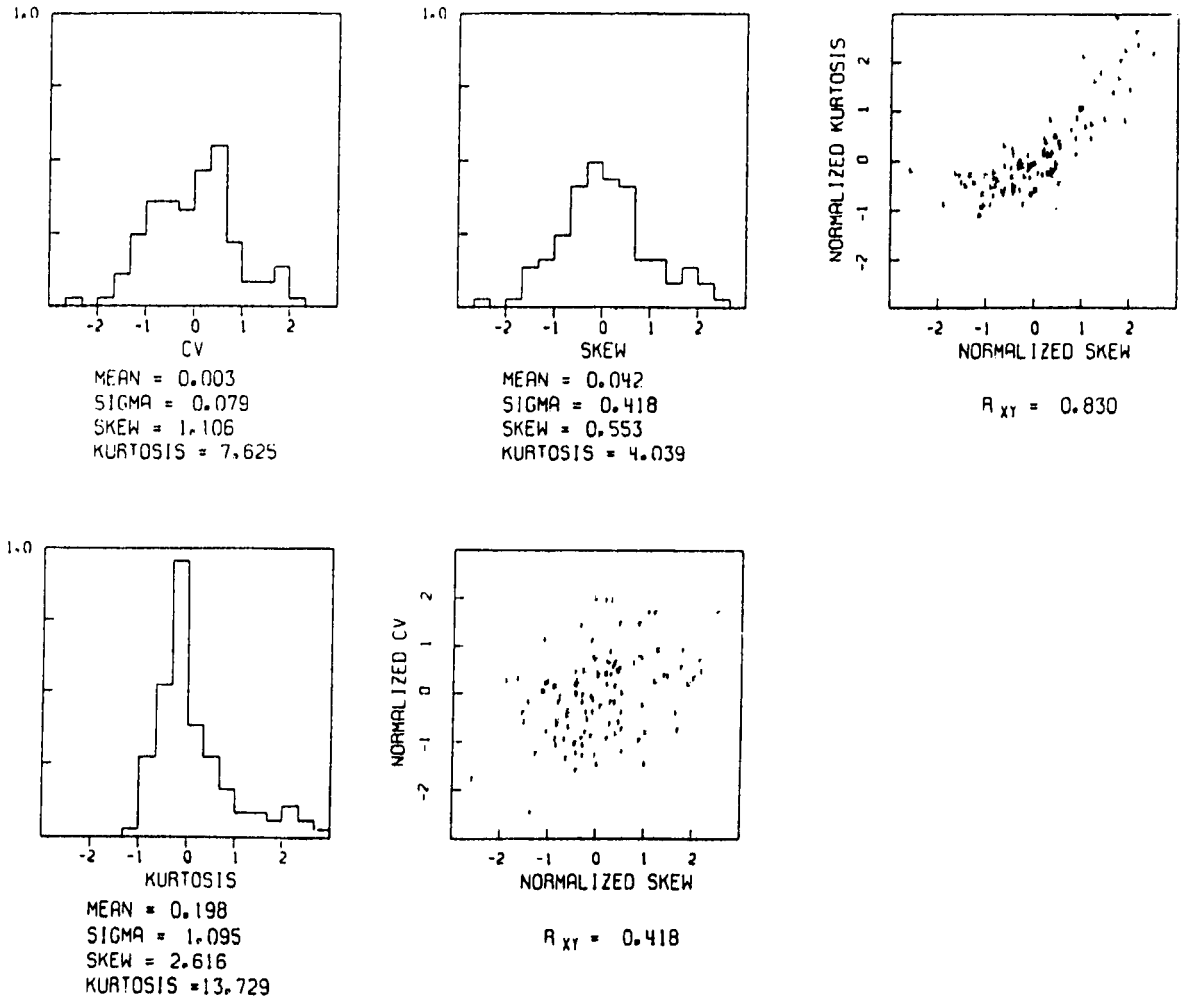

Fig. 14. Normalized density functions and correlation plots of the statistics for the low-frequency 3-hour smoothing

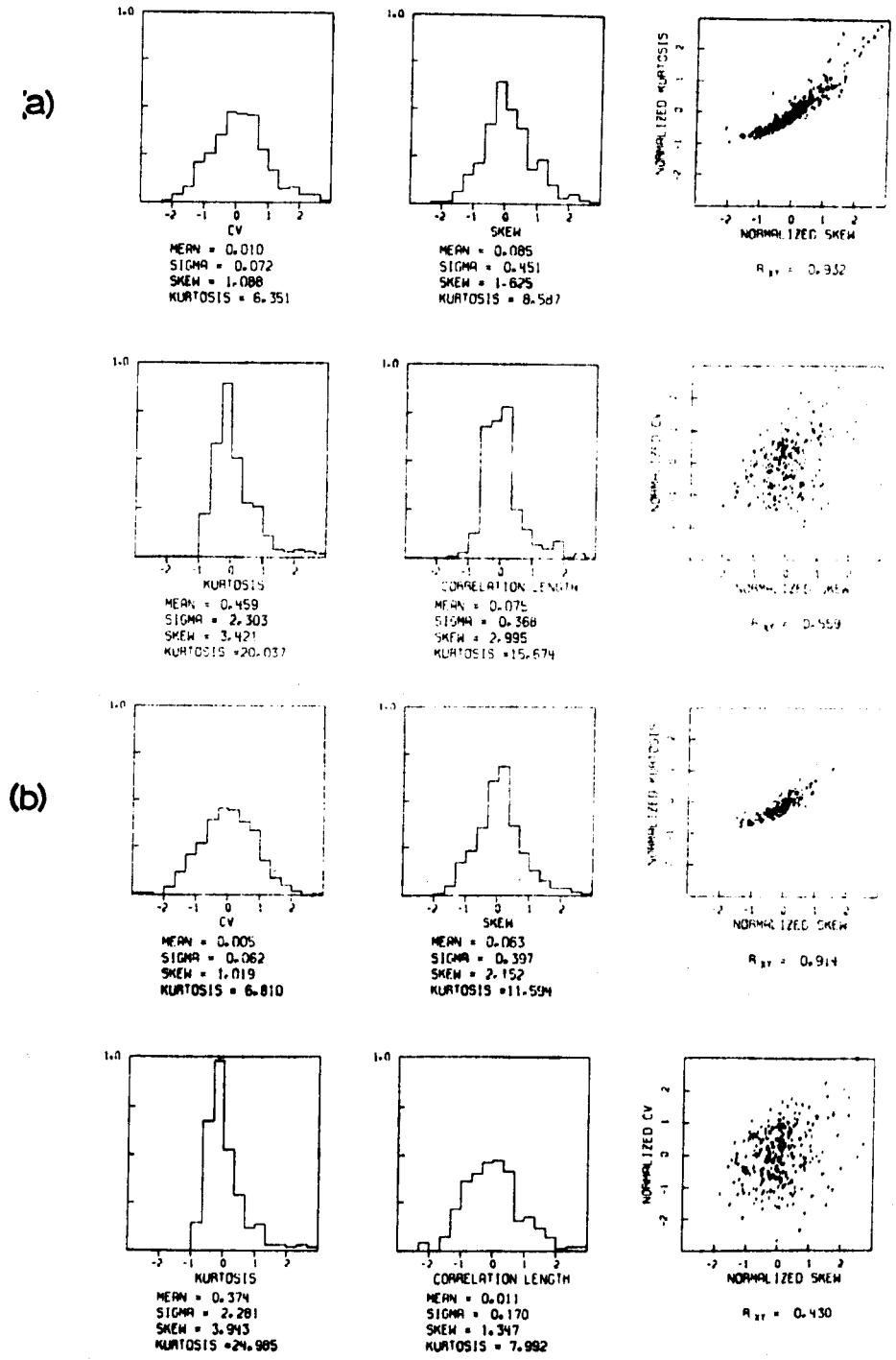

Fig. 15. Normalized density functions and correlation plots of the statistics for high-frequency (a) 3-hour smoothing and (b) 1-hour smoothing.

Also included in Figs. 14 and 15 are plots of the normalized skew as related to normalized kurtosis and the normalized skew as related to the normalized coefficient of variation. The normalization in each case is with respect to the corresponding sigma. These plots essentially allow one to test the correlation between these variables. It is clear that the normalized skew and kurtosis are highly correlated, the only deviation from unity correlation coming at the low end, where there appears to be an absolute minimum of the kurtosis. If one simply equates the normalized skew and kurtosis, then one can express the skew as skew $= a_0$ kurtosis $+ a_1 r + a_2$, where r is the range and the a_j are constants. The appropriate values for these constants are given in Table 4. One could relate the normalized skew and kurtosis with an exponential or power law, which of course would produce a different relation between the skew and kurtosis. A linear fit is chosen here because of its simplicity and the fact that it does fit the data within plus or minus one standard deviation quite well. The plot of the normalized skew versus the normalized coefficient of variation shows a negligible correlation between the two.

Table 4. Parameters relating skew and kurtosis
(skew $= a_0$kurtosis $+ a_1 r + a_2$)*

Constant	3-Hour Smoothing, Low Frequency	3-Hour Smoothing, High Frequency	1-Hour Smoothing, High Frequency
a_0	0.382	0.196	0.174
a_1	−0.0758	−0.0299	0.0704
a_2	−0.493	0.185	−0.0564

*The range r should be in thousands of kilometers.

Model

The linear trends (Fig. 13) and the associated distributions (Figs 14 and 15) about them constitute the empirical fluctuation model of low-frequency propagation in the deep ocean. With the constraint that the skew and kurtosis are linearly related, this model gives a complete statistical description of the second, third, and fourth moments of the received acoustic-amplitude probability density function. The average amplitude may be supplied from a variety of sources, such as data banks or models. An average over 12 km for the 1-hour model or

over 36 km for the 3-hour model is recommended. At longer ranges where convergence-zone structure is not pronounced, averages over larger range increments may suffice.

To use the model, one specifies a low or high frequency, a range, and an average signal amplitude. The second moment is then determined from the coefficient of variation (CV), by use of either the linear trend alone or the linear trend and statistical selection from the distribution of CV. The kurtosis is selected similarly, and the skew is determined using the appropriate constants in Table 4. The result of this process may be sufficient for the user's needs. However, if the user wishes, the first four moments obtained may be used to generate the probability density function of the amplitude, using Pearson's system of fitting density functions (Elderton and Johnson, 1969). With this system the functional forms of the density functions for our model are of the three basic types

$$p(x) = p_0(1 + x/A_1)^{m_1}(1 - x/A_2)^{m_2}, \qquad \text{(typeI)}$$

$$p(x) = p_0\left[1 + \left(\frac{x}{a} - \frac{\nu}{r}\right)^2\right]^{-m} \exp\left[-\nu \tan^{-1}\left(\frac{x}{a} - \frac{\nu}{r}\right)\right], \qquad \text{(typeII)}$$

and

$$p(x) = p_0(1 + x/A_1)^{-q_1}(1 - x/A_2)^{q_2}, \qquad \text{(typeIII)}$$

where all of the densities have their origin at the average amplitude and all constants are functions of the first four moments. A complete description of these densities and how to calculate them is contained in Appendix 7B. The 3-hour model is confined to types (I) and (III) with the bulk of the data being described by (type I). The 1-hour model spans all three types of the functional forms, with the bulk of the data being described by (type II). In general the model predicts, by use of the three types, a skewed, Rayleigh-shaped type of density function as illustrated in Fig. 16a, but it may yield a shape as illustrated in Fig. 16b.

Spacial-Correlation Lengths

The spacial-correlation lengths of the residual signal amplitudes are markedly different from low to high frequency. For the high frequencies the correlation lengths (computed from

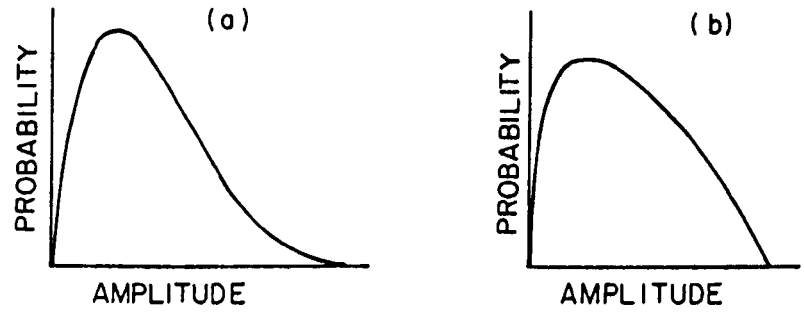

Fig. 16. Density functions for the residual signal amplitude as predicted using the fluctuation model. These functions are most often Rayleigh shaped (a) but may have a "cocked hat" appearance (b).

the 1/e point) are independent of the receiver and decrease linearly with range. They tend to diverge from linearity at the close ranges, where the correlation lengths tend to increase more rapidly with decreasing range. The 1-hour smoothed data tend to fit the linear model better for the shorter ranges but also, as expected, decrease the overall correlation length. The linear trends for the high frequencies are exhibited in Fig. 13, and their associated distributions are presented in Fig. 15.

The low-frequency correlation lengths show a horizontal directional dependency as well as a complicated range dependency. The correlation length increases with range, tends to level off, and then in general decreases with increasing range. The mean correlation length at 100 km is approximately 7 wavelengths, increasing to 30 wavelengths at 2200 km. The explanation of this behavior is that for short ranges the increase of correlation length with range can be attributed to the increasing loss of bottom-interacting modes with increasing range. The level portion of the curve then represents a stabilization of the number of paths contributing to the received signal in a stable environment, and the decrease with range past 2200 km is probably the result of loss of coherence among these paths from changes in the sound-speed profile and bathymetry.

Shaffer et al. (1974) estimated coherence lengths along the track on the basis of a near-constant amplitude and near-linear phase. They estimated lengths of 30 wavelengths at 90

km, 857 wavelengths at 1000 km and 42 wavelengths at 2700 km. Fitzgerald et al. (1976) reported a crossrange coherence length of 11 wavelengths at a range of 65 km using the same criteria. At first glance these lengths appear to be inconsistant with the correlation lengths. However, the coherence lengths were based on the occurrences of maximum lengths in the field and thus would fall on the tail at the maximum end of the distributions. The correlation lengths increase by a factor of 2 to 3 when placed in the tails of the distributions. Also, the criterion for the correlation-lengths determination is probably more stringent than the criterion for the coherence determination.

Comparison of Amplitude-Fluctuation Observations With Theory

No general theory exists yet which allows one to compute the statistics of amplitude fluctuations observed on a stationary hydrophone when the signal is from a steady CW source moving relative to the receiver. The difficulty is that the fluctuations are the result of both changes in the medium and the motion of the source in the complex interference field. On the basis of previous calculations (Ramsdale, 1977) it was decided to ignore the effects of the medium fluctuations and to generate a set of amplitude values which would fluctuate solely due to the sampling of the complex interference field. The plan was to treat these values in the same way as the experimental data and compare the two sets of values for the coefficients of variation, the skew, the kurtosis, and the spacial-correlation length.

Due to the preliminary nature of the investigation, a simple normal-mode model was used to generate the acoustic amplitudes, and investigation was restricted to the 9.8-Hz data only. At the outset, again for simplicity, the only values generated were for a radial run from the source to the receiver, which offered a one-to-one correspondence between time and range. In particular, amplitude values were generated for a section of track from 690 to 1630 km in range during which the data were of excellent quality and exhibited 15 well-defined convergence zones.

The normal-mode amplitudes were generated using a standard NRL model (SOLID) (Miller and Ingenito, 1975). Values for sound speed in the water column were taken to be an

average of typical values occurring over the propagation path. Sound speeds, densities, and gradients in the bottom were taken from Hamilton (1974).

To simulate the amplitude data, the amplitude was computed every 4.27 minutes (every 94 m) as the ship moved along the track at 7.1 knots. The number of modes used corresponded to the quotient of twice the receiver depth and the wavelength of the source frequency. The resulting amplitude time series was then processed in a manner identical to the measured data.

Comparison of the smoothed-amplitude time series (3-hour running average) generated using the normal-mode model with that from the experimental data showed that the number of convergence zones was the same and that their height and width agreed well but that they did not occur at exactly the same range values. This disagreement in absolute position is a result of using a slightly incorrect average sound-speed profile and could probably be corrected if one did a more precise calculation, such as using a parabolic equation with range-dependent profiles. This disagreement should not bias the comparison of amplitude-fluctuation statistics, since the interval over which it was computed is slightly larger than the convergence-zone spacing, so that each such interval will contain a full range of amplitude values.

The amplitude statistics for both the model-generated values and the measured values are plotted against range in Fig. 17. Considering the statistical scatter in the data, the agreement between the two sets of values is quite good. However, the model-generated values of the coefficient of variation, the skew, and the kurtosis are consistently smaller than the comparable values obtained from the experimental data, whereas the model-generated correlation lengths are slightly larger. These preliminary calculations indicate that for this case one can generate reasonably good amplitude-fluctuation statistics by ignoring the effects of the fluctuating medium and generating the amplitude values in accordance with a moving source sampling the complex interference field.

To test the general validity of this technique, amplitude values were generated for the same portion of the track but for receivers that were not radial to the tow. The acoustic field was then being sampled more densely in space than for the radial tow. The results showed

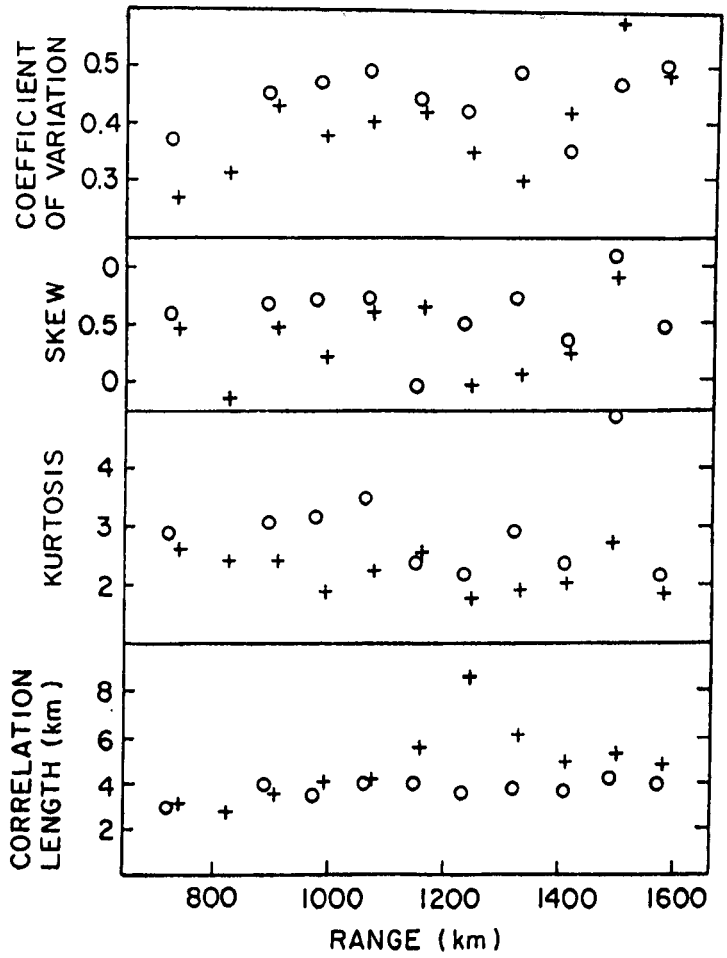

Fig. 17. Statistics for a 9.8-Hz signal. The open circles represent measured data, and the crosses represent values generated using a normal-mode-propagation model. (For this range segment the coefficient of variation appears to be increasing with range. When the coefficient is plotted for the complete range, a decrease with range is clear.)

that the coefficients of variation were approximately half the experimental values and that the correlation lengths were approximately twice the experimental values. These results indicate an additional cause of fluctuations in the measured data when the tow was not radial. One cause may be that for each small change in range the sound is traversing a completely different section of the ocean, whereas in the radial tow the section of the ocean is only incrementally different. Another cause may be variations in the interaction of the received signal with the rough bottom in the vicinity of the receiver due to the changing bearings of the source.

The simple normal-mode calculations presented here represent only a preliminary but nevertheless encouraging attempt to explain the source of the observed amplitude-fluctuation statistics.

Phase Characteristic

An important property of the signals propagated in the deep ocean channel is the phase of a the signal as a function of frequency and range. In an ideal isotropic medium the phase of the signal rotates uniformally through a 2π radians (360°) for each wavelength of the signal traversed in range. If the source is in motion, only the Doppler shift has to be taken into account to correlate the received signal with its transmitted replica. When the signal traverses the interference field of a dispersive channel, it experiences large phase excursions (up to π) at the deep null points and lesser variations at other interference points as exemplified in beat signals. The phase variations are the least in the broader region of the in-phase sums. The statistics of the variation of the phase in a dispersive channel are important not only in communications but many other applications.

One could approach this problem of phase excursions by comparing the received signal with the transmitted replica. Another experimental approach is to determine the degree of crosscorrelation obtained when two signals with different frequencies are propagated from the same source to the same receiver through the channel. The two signals will not correlate directly, but require an appropriate transformation. If the two signals were propagated in the ideal isotropic medium, when transformed should provide a unity correlation coefficient. In the channel the correlation will be degraded. The question is: How will the correlation coefficient vary as a function of frequency, frequency ratio between the two signals, and range of propagation through the channel? An important advantage in propagating pairs of signals through the channel is that the ratio of the two signals is invariant with the frequency, since the Doppler shifts are proportional.

Significant contributions to the understanding of phase dispersive processes and to the quantification of the correlation statistics have been made by Gerlach et al. (1983), Flowers

and Gerlach (1983), and Flowers (1983, 1985). Reported in this set of papers are theoretical studies, simulation studies, and experimental measurements in determining the statistical deviation of the frequency ratio of two signals transmitted through a channel relative to the correct ratio. These studies and measurements were done for frequencies between 10 and 100 Hz, frequency ratios between 1 and 10, and ranges up to 1000 km. The influence of various signal-to-noise ratios was included.

It was found that the RMS deviation in observed ratios was directly proportional to the ratio q and the range rate $\dot{R}$. (As q approaches 1, a measure of single-frequency dispersion is obtained.) This led to a spectral dispersion distribution of the observed ratio in which 90% of the values fell within $(5 \times 10^{-6})\, q\dot{R}$ of the true ratio. There was essentially no frequency influence in the deviation and only a weak dependence on range, increasing slightly (20 to 25%) with ranges to 900 km. A deep-ocean model of the acoustic dispersion is developed and compared with experimental data. Excellent correspondence was observed.

Discussion

It has long been recognized that there are two major aspects of propagation in an ocean channel dominated by refraction as a result of the sound-speed profile. The first is the predictable complexity of the field that is produced as the predominant features of the channel and boundary refract and reflect the waves to produce the interference field. This aspect is viewed primarily as a deterministic process. The second is the complex distortion of the wave fronts, produced by features that are unknown in detail, as they propagate along a path through a medium varying in space and time. Primarily, the variations, in the body of the medium are produced by fluctuation about the average sound-speed structure. This is treated as a statistical process and referred to as propagation through random media.

Early work on propagation through random media was started by Pekeris (1942) during World War II and followed by Bergman (1946) and Mintzer (1953) immediately after the war. Their work was undertaken to explain the effect of temperature fluctuations in the ocean on acoustic propagation, based on the theory of single scatterers. The Russian monographs

by Chernov (1960) and Tartaski (1961) provided a complete review of random media research on scattering of acoustic and electromagnetic waves conducted in the Soviet Union at that time. They emphasized the importance of turbulence spectrum as the primary description of the scatter mechanism. They introduced the Rytov approximation to Western researchers with the claim that it is the correct approximation to account for multiple scattering. However, Tatarski's (1971) second monograph tended to move away from the use of the Rytov approximation that he had stressed earlier. Most of the effort during the 1960s was directed toward the electromagnetic propagation problem (Bourret, 1962, Keller, 1962, Beran and Parrent, 1964, Beran, 1966, and Frisch, 1968).

Increased attention was given to the ocean acoustic application in the 1970s. The emphasis of the research shifted to differences in the mechanism that produced the perturbations in the medium, different scales of perturbations and acoustic wavelengths, and the anisotropy of the acoustic medium. In addition, the ocean's basic sound-speed profile gives rise to special problems. There were three groups of researchers with somewhat different but complementary approaches.

Beran and McCoy working with a group at the Naval Research Laboratory used the transport equations to study the propagation of the mutual coherence function, particularly the second- and fourth-order moments of the field (Beran and McCoy, 1974a, 1974b, 1976, 1977, and McCoy and Beran, 1976, 1979). Baer et al. 1984 provide a parabolic-approximation approach to the problem.

The JASON group stressed the mechanism of the source of the perturbations: the fluctuating continuum in the ocean (with emphasis on internal waves) (Munk and Zachariasen, 1976). This model provided a range at which the randomness of the field is completely saturated for increasing scattering out of the path from the source to the saturation range. One technique introduced was the Feyman path integral formalism (Dashen, 1979). Predictions by the JASON model were compared with experimental results (Ellinthorpe et al. 1975-1977, and Ewart, 1976). At the higher frequencies of these experiments the comparisons were reasonably good, but at the lower frequencies the magnitude of the scattering was too

large. For example, the JASON model would have predicted that the 37th-convergence zone peak of Fig. 6 would have been greatly degraded. The JASON research is summarized in Flatte et al. (1979).

A small group centered around Tappert at New York University contributed to theoretical techniques in relating the quantized motion of a particle in a perturbed potential field with the ocean acoustic problem (Besieris and Tappert, 1973, 1976), in using the Monte Carlo method (Wilson and Tappert, 1979), in using model expansion in formulating the scatter problems (Dozier and Tappert, 1978a, 1978b), and in the advancing the parabolic approximation method (Tappert and Hardin, 1974, and Tappert, 1977).

In the early 1980s Uscinski (1980, 1982) contributed to the solution of the parabolic fourth-moment equation. Advances were made in the understanding of intensity fluctuations in the ocean by employing numerical simulation of a sound wave propagating through a region of ocean containing internal waves (Macaskill and Ewart, 1984a, and Uscinski, 1986). Intensitities measured in the ocean have been compared with those predicted analytically (Uscinski et al., 1983, Ewart et al., 1983, Ewart and Reynolds, 1984, and Macaskill and Ewart, 1984b).

Almost all of these approaches to the problem of propagation in random media are tied to a path or geometric acoustics. Also in all cases the basic equations are intractable, requiring major assumptions to obtain practical solutions. Thus the approaches to the problem have not gone beyond evaluation of the assumptions.

IMPULSIVE ACOUSTIC SIGNALS

Experiments

As stated previously, in the Atlantic experiments charges equivalent to 2.3 kg (5 lb) of TNT were detonated every half hour at approximately 110 m deep. The signals were received on the same hydrophones as the CW signals. The impulsive signals were filtered through a 15 to 250-Hz passband and then rectified and tape recorded in analog form.

In the Pacific experiment the impulsive sources were 1.4-kg (3-lb) TNT charges detonated at 200 m deep with a range spacing of 13 km over the track. In this experiment the track was traversed three times in a ten-day interval, twice outgoing in range and once incoming. The same recording procedure was used as for the Atlantic experiments.

Arrival Structure

Fitzgerald et al. (1974), Nutile (1976), and Nutile and Guthrie (1979) provide a detailed analysis of the structure of the propagation path and the arrival timing of the impulsive signals. The paths and arrival structure were compared with computations using ray theory.

The rectified impulsive signals were displayed on a graphic recorder with a linear response. Each shot signature consists of a series of pulses or arrivals due to the dispersive or multipath propagation. For shots spaced at small range intervals, successive signatures resemble one another, permitting alignment in a systematic manner. Figure 18 is such an arrangement for all the shot signatures in the experiment. Figure 19 is an abstract of Fig. 18, showing the presence or absence of signals above a threshold but not the magnitude. Figures 20, 21, and 22 show details in the data of Fig. 18 for region 1 (Figs. 2a and 4), region 2, and regions 3 and 4 respectively.

The arrivals in the shot signatures of Fig. 18 divide visually into three groups. The intense arrivals resembling echelons along an undrawn positive-slope line are produced primarily by RSR rays. The arrivals above and to the left of this line are produced by leakage rays. These leakage rays are trapped for part of their propagation time in the subsurface sound channel of region 2. At some point in region 2 the rays leak out of the subsurface sound channel and travel under the influence of the SOFAR channel. The arrivals below and to the right of the RSR arrivals in Fig. 18 are produced by rays which follow SOFAR paths near the receiver.

Alignment of the shot signatures to produce Fig. 18 was initiated by arranging the leakage arrivals along vertical lines (Fitzgerald et al. 1974). After the alignment had been completed, analyzed, and compared with ray-tracing results, the abscissa labels of Fig. 18, 19,

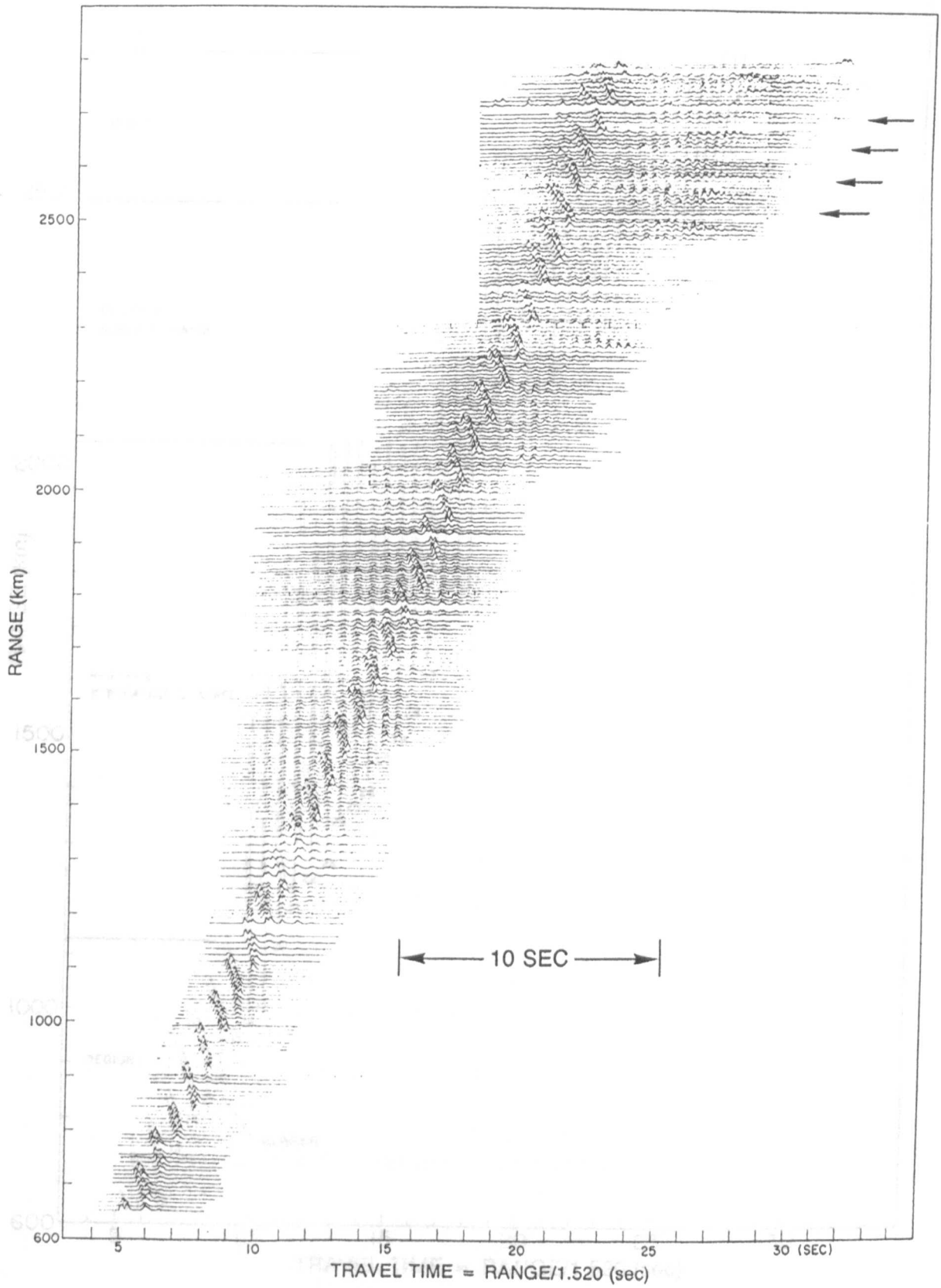

Fig. 18. Aligned shot signatures (Fitzgerald et al. 1974).

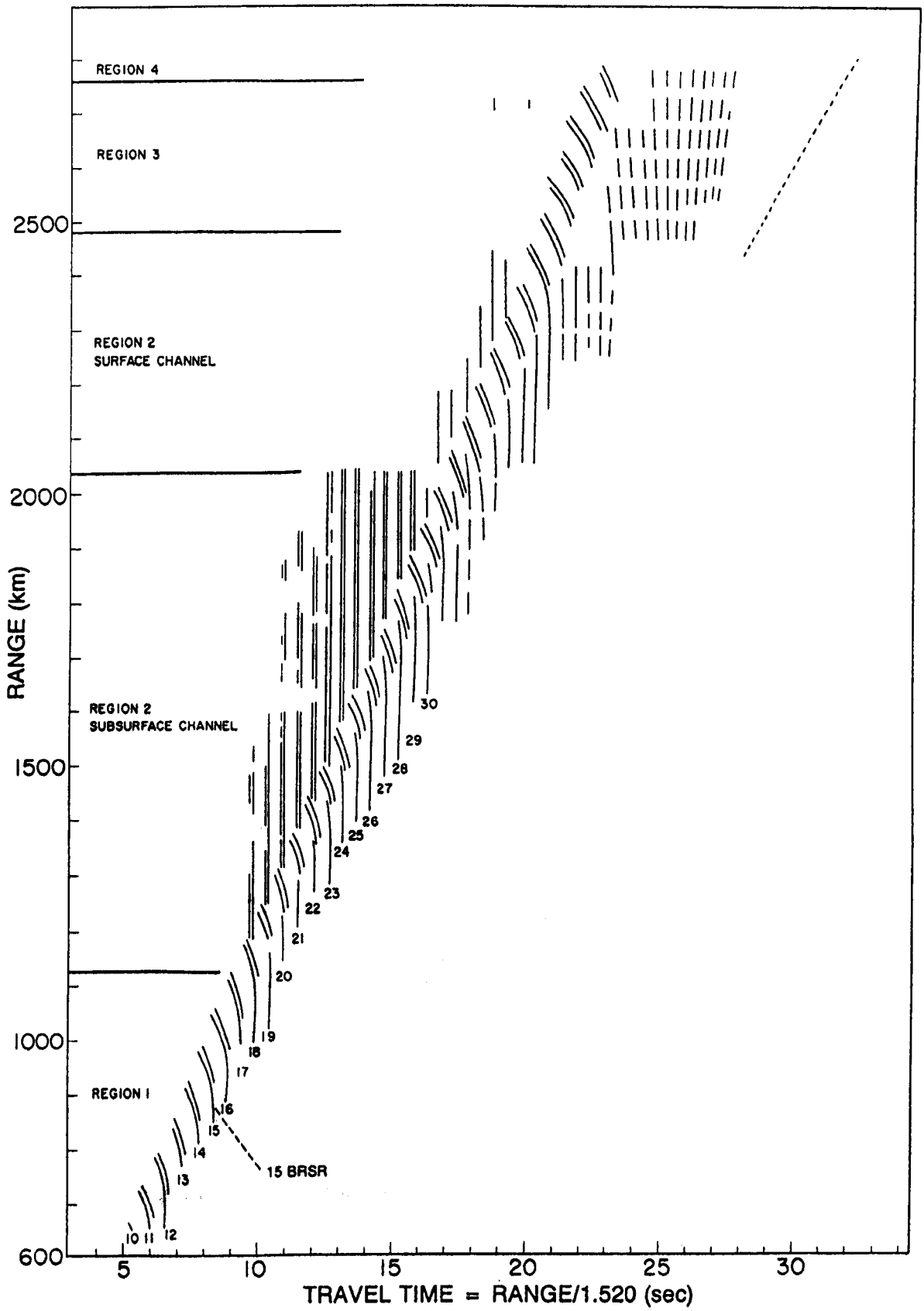

Fig. 19. Abstract of aligned shot signatures (Fitzgerald et al. 1974).

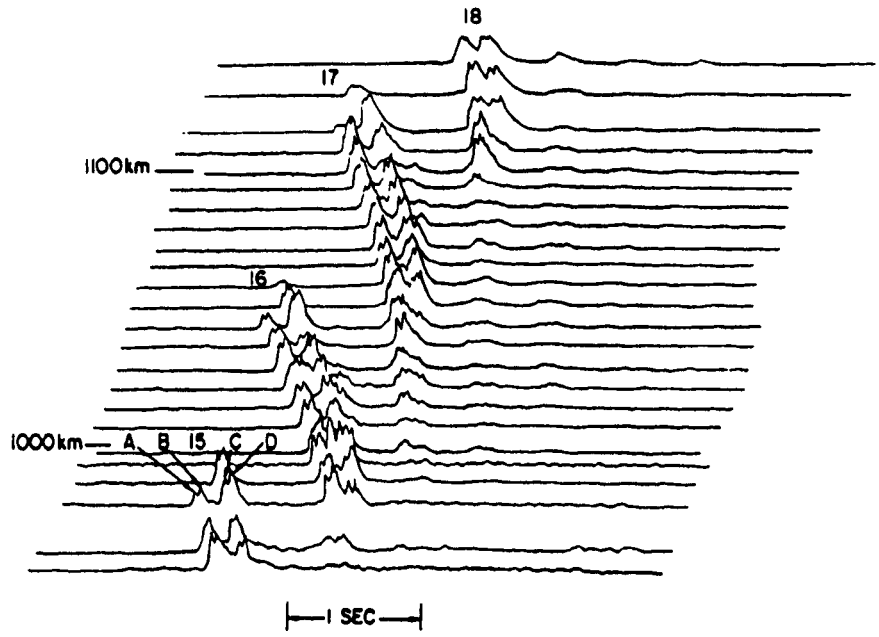

Fig. 20. Details of shot signatures in region 1.
Arrival classes are numbered (Fitzgerald et al. 1974).

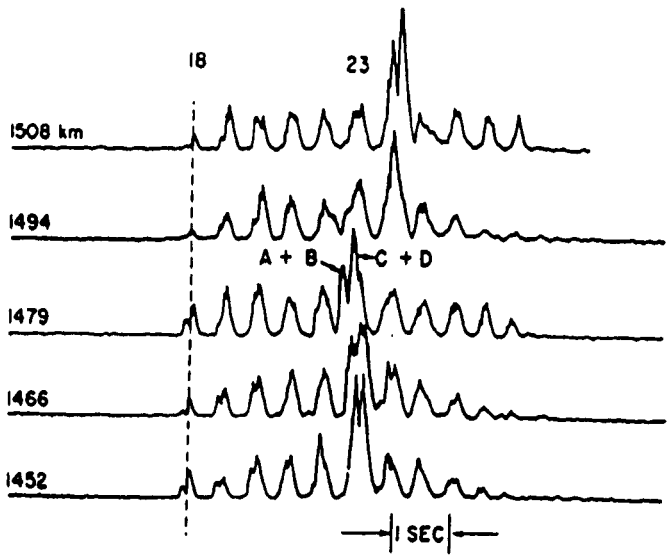

Fig. 21. Details of shot signatures in region 2 (Fitzgerald et al. 1974).

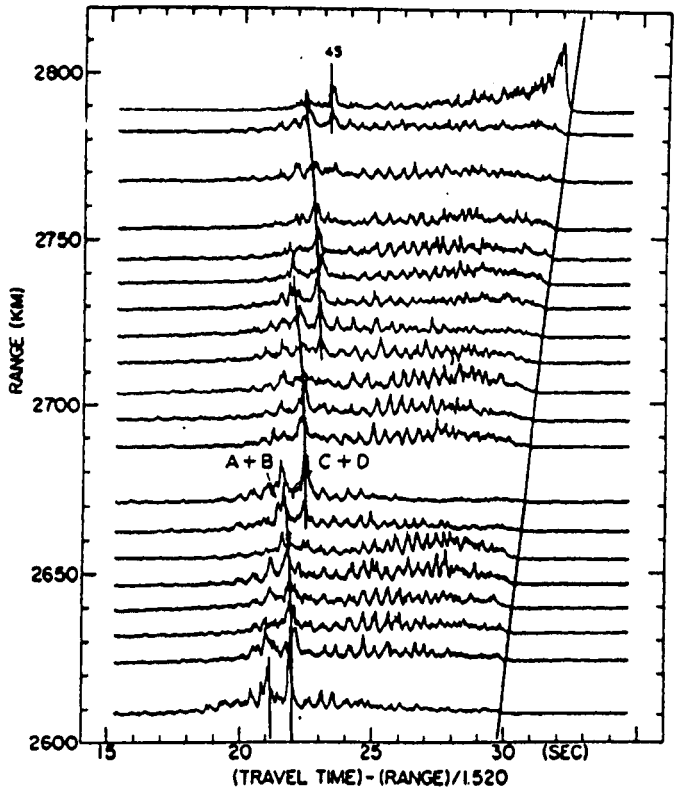

Fig. 22. Details of shot signatures in regions 3 and 4 (Fitzgerald et al. 1974).

and 22 were added as interpretive approximations. These abscissa labels arise from the vertical alignment of leakage arrivals, each of which travels for some range interval in the subsurface sound channel at an average horizontal speed of 1.520 km/sec.

Arrival Classes

Consider a class of arrivals which constitutes a continuous line segment in Fig. 19. In particular, consider the line segment marked 15. As explained in Fitzgerald et al. (1974), the rays which produce the arrivals in this class refract upward 15 times while below the SOFAR axis (are said to turn under the axis 15 times, or have 15 turn-unders). At 900 km the arrivals are produced by SOFAR rays, at 1000 km they are produced by RSR rays, and ranges longer than 1000 km no ray turning under 15 times can connect the source and the receiver, so that the class terminates. In Fig. 19 the class of arrivals having 18 deep turn-unders does not terminate with the RSR arrival at 1180 km. The class is continued at longer ranges by those leakage arrivals which turn under 18 times after leaving the subsurface sound channel.

Description of Data by Oceanographic Region

In all four oceanographic regions there is a depth excess. In region 1 the expected RSR and SOFAR rays are observed. Bottom interacting rays (BRSR) are not in evidence. If they were present then, as a ray tracing program indicates, the classes of BRSR rays would lie along line segments similar to the dashed line marked 15 BRSR in Fig. 19.

Figure 20 shows the shot signatures of region 1 in greater detail. The class of arrivals with 15 deep turn-unders can be further analyzed into arrivals A + B and C + D which correspond to upgoing and downgoing arrivals at the receiver respectively. The set of arrivals A + B which are upgoing at the receiver, contains both arrival A, which is a upgoing at the source and arrival B, which is a ray downgoing at the source. As one would expect, the arrival C + D with one more turn-over persists to a longer range than arrival A + B. Although, as shown in Fig. 20, it is tempting to further analyze the signatures arrivals A, B, C, D, caution is required because a shot's bubble pulse period is approximately equal to the separation between arrivals A and B or C and D.

The oceanography of region 2 differs from that of region 1 by the presence of a strong near-surface sound channel (Figs. 3 and 4). This sound channel permits the source and receiver to be connected by additional paths, the leakage rays. Figure 21 shows the shot signatures of shots in region 2 in greater detail. Arrivals lying along the vertical dashed line marked 18 are produced by rays which are trapped in the subsurface sound channel until they reach region 1, where they become SOFAR rays and turn under 18 times before they reach the receiver. The class of arrivals which is noted as having 23 deep turn-unders is produced by RSR and SOFAR rays for ranges less than 1479 km. At larger ranges the rays of this class are trapped in the subsurface sound channel and leak out of the channel at approximately the 1479-km range. Figure 19 indicates that the number of observed leakage arrivals decreases markedly with increasing range at about 2040 km. At this range the subsurface channel is replaced by a surface channel. The decrease in number of leakage arrivals is a result either of surface scattering, or of imperfect development of the surface channel. In

region 2 the near-surface channel and the accompanying decrease in surface sound speed make possible additional RSR paths. These paths convert to SOFAR paths on entering region 1 and account for the additional arrivals which follow SOFAR paths near the receiver in Fig. 21 and in region 2 of Fig. 19.

Figure 22 shows the shot signatures of regions 3 and 4 in greater detail. Region 3 is separated from region 2 by the Gulf Stream. Compared with the sound-speed profiles of region 2, those of region 3 show a lower surface temperature, a greater depth excess, and a shallower SOFAR axis. The arrival structure shows the continuing RSR pattern and an increasing number of arrivals which follow SOFAR paths at the receiver. These SOFAR arrivals result from better coupling of the source to the SOFAR channel and from RSR to SOFAR conversion between regions 3 and 2 and regions 2 and 1.

The northern waters of region 4 have a low surface temperature, a weak or absent thermocline, and a near-surface SOFAR axis. The shot signature at maximum range in Fig. 18 and in Fig. 22 shows the characteristic SOFAR signal cutoff. The line marking the termination of the shot signatures in Fig. 22 intersects the RSR diagonal at approximately zero range and zero time. This leads to the conclusion that the line marks the axial ray arrival. In Fig. 19 this asymptote is shown as a dashed line.

Discussion

Consider the pattern of RSR arrivals in Fig. 18. The pattern repeats with a period of about 62 km, which is the convergence-zone interval.

The vertical lines denoting the classes of leakage arrivals in Fig. 19 recur with a period of 0.53 sec. This period is a measure of the average sound speed in the near-surface channel (Fitzgerald et al., 1974).

In the range interval 2500 to 2800 km the arrivals which follow SOFAR paths near the receiver periodically fade in intensity in Fig. 18. Shot signatures with low-amplitude SOFAR arrivals are marked with arrows. The fading period is approximately equal to a convergence-zone interval. The SOFAR arrivals are produced primarily by RSR rays in

region 3 that convert to SOFAR rays at the boundary with region 2. If the RSR rays in region 3 are near the surface as they cross the boundary with region 2, they may be scattered by the Gulf Stream and only weakly convert to SOFAR rays.

The slower traveling SOFAR arrivals of shot signatures at 2261 to 22185 km in Fig. 18 are unusually strong because at that range a localized mass of cold water is present at and below the source depth. This near-surface cold water mass provides better coupling of the source to the SOFAR channel. The existence of such a localized water mass is evident on sound-speed profiles taken at 2230 and 2290 km.

Figure 23 illustrates the evolution in a ray class as the range increases. The BRSR ray c at range R_1 becomes the RSR ray d at the convergence zone, at range R_2. At greater range R_3, it becomes the leakage ray b. Energy may also arrive from R_3 via those previously described SOFAR rays with stretched cycle lengths.

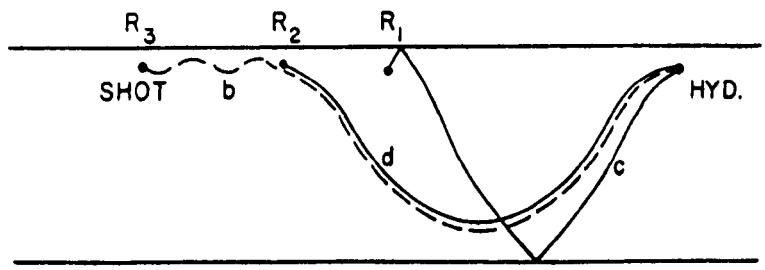

Fig. 23. Evolution of a ray class as the range increases.

Fitzgerald et al. (1974) demonstrated the frequency dependence of signals leaked from a duct. They showed that the amplitude decreases the earlier the leakage arrival and that it decreases faster as the frequency is lowered. This results from the subsurface channel leaking the lower frequency energy at a faster rate. Also it decreases from the lowering of the initial coupling of the energy into the channel as the waelength approaches cutoff.

The evolution in range of a ray class from SOFAR rays to RSR rays is continuous in regions 1 and 3 and discontinuous in region 2. This effect is due to the near-surface sound channel in region 2. The channel traps the rays within a certain vertical angular spread at the source, thereby interrupting the progression from SOFAR rays to RSR rays. Figure 19 also

shows the presence of 36 RSR classes, numbering 10 through 45. In the same interval there appear 37 SOFAR classes. The additional SOFAR line appears in the subsurface-channel area of region 2. This effect is not understood.

Nutile and Guthrie (1979) demonstrated that the Pacific propagation is primarily refraction-refraction (RR), with the axis depth remaining almost constant over the track and the surface sound speed decreasing by approximately 8 m/sec between the southern and northern ends of the track. Because all of the Pacific propagation can be considered in a single region, the shot-signature structure and the multipath-arrival structure are more easily identified with the aid of ray-theory calculations than in the more complicated Atlantic data. Nutile and Guthrie (1979) also showed that the environmental stability of the Pacific data allowed the arrival pattern to remain stable for more than a week.

CONCLUSIONS

The nature of low-frequency acoustic propagation in an Atlantic channel was illustrated by experimental measurements. The transmission is dominated by convergence zones at the 13.90-Hz frequency for essentially the total length of the 2500-km channel. This indicates that the wavelength is sufficiently long so that the sound-speed variations in the channel, such as near surface ducts and other perturbations, have little influence on the propagation. The higher frequency, 111 Hz, is strongly influenced by the near-surface channel, obscuring convergence zones for a large increment of the range by continuous leakage of the energy from the duct.

Clear indication of the frequency dependence of the convergence zone spacing as a function of frequency is seen in comparing the two transmission-loss curves. The convergence zone spacing decreases as the frequency is lowered, resulting in 21 zones for the lower frequency in the same space as 20 zones at the higher frequency. The global spacial structure of the field is illustrated by the power spectrum of the squared signal envelope over a 500-km region of the field. The spectrum is dominated by the convergence zone peak.

The statistics of signals propagating over long distances in an ocean channel were analyzed in detail. Major differences were seen between a low-frequency signal of 9.8 Hz and two higher frequency signals at 110 Hz and 262 Hz. There is no significant difference in the statistical descriptors of the 110-Hz and 262-Hz signals. All of the moments show some decreases as a function of range.

By use of the linear trends and the variability about the trends, a simple empirical model was obtained that describes for each of the frequences the fluctuation of signal amplitude as a function of range. This model should be sufficient for most predictions. However, if a better statistical description is required or it is desired to generate a probability density function of the amplitude, a more involved model using the first four moments of the amplitude in Pearson's system of fitting density functions may be employed.

The correlation lengths (horizontal) in the channel at the two higher frequencies vary from approximately 0.8 km to 0.3 km as range increases to 3,000 km. The low-frequency correlation lengths show both an azimuth dependence and a complicated range dependence.

A simulation used a simple normal mode model in generating signals to match the experimental data. The simulated data were then analyzed in the same manner as the experiment data. The statistics of the simulation and the experiment are in good agreement.

The phase characteristics of the channel were measured by propagating parts of signals at two frequencies in the channel and correlating them at the point of reception. The degree of correlation indicated that the ratio of the low-frequency phase errors is less than 10^{-5} and that the error ratio is directly proportional to the ratio of the two signal frequencies, and to the range rate.

A discussion is made of the relation between this work's determinist approach to propagation in a channel and propagation through random media, which is a statistical approach.

The chapter concludes with the description of the propagation of an impulse in the dispersive channel. The relationship of the complicated multipath arrival patterns to the sound speed properties of the medium are made. The influence of the various scales of the medium characteristics seen in continuous-wave propagation are confirmed by the results of the impulse analysis.

REFERENCES

R.N. Baer, J.S. Perkins, E.B. Wright, and J.J. McCoy, "Stochastic Propagation of the Mutual Coherence Function in the Deep Ocean," J. Acoust. Soc. Am. **75**, 1407-1414 (1984).

M.J. Beran, "Propagation of the Mutual Coherence Function Through Random Media," J. Opt. Soc. Am. **56**, 1475-1480 (1966).

M.J. Beran, *Statistical Continuum Theories*, Interscience, New York, 1968.

M.J. Beran and J.J. McCoy, "Propagation Through an Anisotropic Random Medium," J. Math. Phys. **15**, 1901-1912 (1974a).

M.J. Beran and J.J. McCoy, "Propagation of Radiation From a Finite Beam or Source Through an Anisotropic Random Medium," J. Acoust. Soc. Am. **56**, 1667-1672 (1974b).

M.J. Beran and J.J. McCoy, "Propagation Through an Anisotropic Random Medium: An Integro-differential Formulation," J. Math. Phys. **17**, 1186-1189 (1976).

M.J. Beran and J.J. McCoy, "A Cylindrically Symmetric Coherence Formulation for the Ocean," J. Acoust. Soc. Am. **61**, 596-599 (1977).

M.J. Beran and G.B. Parrent, Jr., *Theory of Partial Coherence*, Prentice-Hall, Englewood Cliffs, N.J., 1964.

P.G. Bergman, "Propagation of Radiation Into a Medium with Random Inhomogeneities," Phys. Rev. **70**, 486-492 (1946).

I.M. Besieris and F. Tappert, "Kinetic Equations for the Quantized Motion of a Particle in a Randomly Perturbed Potential Field," J. Math. Phys. **14**, 1829-1836 (1973).

R.C. Bourret, "Propagation of Randomly Perturbed Fields," Canadian J. Phys. **40**, 782-790 (1962).

L.A. Chernov, *Wave Propagation in a Random Medium*, translated by R.A. Silverman, McGraw-Hill, New York, 1960.

R.J. Dashen, "Path Integrals for Waves in Random Media," J. Math. Phys. **20**, 894-920 (1979).

L.B. Dozier and F.D. Tappert, "Statistics of Normal Mode Amplitudes in a Random Ocean. I. Theory," J. Acoust. Soc. Am. **63**, 353-365 (1978a).

L.B. Dozier and F.D. Tappert, "Statistics of Normal Mode Amplitudes in a Random Ocean. II. Computations," J. Acoust Soc. Am **64**, 533-547 (1978b).

W.P. Elderton and N.L. Johnson, *Systems of Frequency Curves*, Cambridge Univ. Press, New York, 1969.

A.W. Ellinthorpe et al., Naval Underwater Acoustics Center Technical Memorandums associated with the Joint Oceanographic Acoustic Experiment, Naval Underwater Systems Center, New London, Conn. (1975-1977).

T.E. Ewart, "Acoustic Fluctuation in the Open Ocean—A Measurement Using a Fixed Refracted Path," J. Acoust. Soc. Am. **60**, 46-59 (1976).

T.E. Ewart and S. Reynolds, "The Mid-ocean Acoustic Transmission Experiment, MATE," J. Acoust. Soc. Am. **75**, 785-802 (1984).

T.E. Ewart, C. Macaskill, and B.J. Uscinski, "Intensity Fluctuations. Part II: Comparison with the Cobb Experiment," J. Acoust. Soc. Am. **74**, 1484-1499 (1983).

D.F. Fenner and P.J. Bucca, "The Sound Velocity Structure of North Atlantic Ocean," U.S. Naval Oceanographic Office, Informal Rept. 71-13 (unpublished).

R.M. Fitzgerald, A.N. Guthrie, D.A. Nutile, and J.D. Shaffer, "Influence of the Subsurface Sound Channel on Long-Range Propagation Paths and Travel Times," J. Acoust. Soc. Am. **55**, 47-53 (1974).

R.M. Fitzgerald, Guthrie, and J.D. Shaffer, "Low-Frequency Coherence Transverse to the Direction of Propagation," J. Acoust. Soc. Am. **60**, 752-753, (1976).

S.M. Flatte, R. Dashen, W.H. Munk, K.M. Watson, and F. Zachariasen, *Sound Transmission Through a Fluctuating Ocean*, Cambridge Univ. Press, Cambridge, 1979.

K.D. Flowers, "Geometric Dispersion of Acoustic Signals Propagated in a Deep Ocean Channel," J. Acoust. Soc. Am. **73**, 806-809 (1983).

K.D. Flowers, "Modal Dispersion Effects on Coherent Signal Processing Parameters," IEEE Trans. Acoust., Speech, Signal Processing ASSP-33, 1092-1094 (1985).

K.D. Flowers and A.A. Gerlach, "Model Validation of the Geometric Dispersion of Acoustic Signals Propagated in a Deep Ocean Channel," J. Acoust. Soc. Am. 74, 204-209 (1983).

Frisch, U. (1968), "Wave Propagation in Random Media," pp. 76-198 in *Probabilistic Methods in Applied Mathematics*, Vol. 1, A.T. Bharucha-Reid, editor, Academic Press, New York.

A.A. Gerlach, K.D. Flowers, and R.B. Johnson, Jr., "Acoustic Dispersion in a Deep Ocean Channel," J. Acoust. Soc. Am. 74, 196-203 (1983).

A.N. Guthrie, R.M. Fitzgerald, D.A. Nutile, and J.D. Shaffer, "Long-Range Low-Frequency CW Propagation in the Deep Ocean: Antigua-Newfoundland," J. Acoust. Soc. Am. 56, 58-69 (1974).

A.N. Guthrie, J.D. Shaffer, D.A. Nutile, and R.M. Fitzgerald, "Long-Range Propagation Experiment: Procedures and Shipboard Data," NRL Memo. Rept. 3405, 1976.

E.L. Hamilton, "Geoacoustic Models of the Sea Floor," pp 181-221 in *Physics of Sound in Marine Sediments*, L. Hampton, editor, Plenum, New York, 1974.

J.B. Keller, "Wave Propagation in Random Media," Proc. Symp. Appl. Math. 13, 227-246 (1962).

C. Macaskill and T.E. Ewart, "Computer Simulation of Two-Dimensional Random Wave Propagation," IMA J. Appl. Math. 33, (1984).

C. Macaskill and T.E. Ewart, "The Probability Distribution of Intensity for Acoustic Propagation in a Randomly Varying Ocean," J. Acoust. Soc. Am. 76, 1466-1473 (1984).

J.J. McCoy and M.J. Beran, "Propagation of Beamed Signals Through Inhomogeneous Media: A Diffraction Theory," J. Acoust. Soc. Am. 59, 1142-1149 (1976).

J.J. McCoy and M.J. Beran, "Directional Spectral Spreading in Randomly Inhomogeneous Media," J. Acoust. Soc. Am. 66, 1468-1481 (1979).

J.F. Miller and F. Ingenito, "Normal Mode FORTRAN Programs for Calculating Sound Propagation in the Ocean," NRL Memo. Rept. 3071, 1975.

D. Mintzer, "Wave Propagation in a Randomly Inhomogeneous Medium. I," J. Acoust. Soc. Am. 25, 922-927 (1953).

W.H. Munk and F. Zachariasen, "Sound Propagation Through a Fluctuating Stratified Ocean: Theory and Observations," J. Acoust. Soc. Am. 59, 818-838 (1976).

D.A. Nutile "Computer Programs for Obtaining Sound Speeds from Digitized Environmental Data" NRL Rept. 7993, 1976.

D.A. Nutile and A.N. Guthrie, "Propagation Paths to Midway Island," J. Acoust. Soc. Am. 65, 70-74 (1979).

C.L. Pekeris, "Note on the Scattering of Radiation in an Inhomogeneous Medium," Phys. Rev. 71, 268-260 (1942).

J.D. Shaffer, R.M. Fitzgerald, and A.N. Guthrie, "Coherence of Low-Frequency Acoustic signals in the Deep Ocean," J. Acoust. Soc. Am. 56, 1122-1126 (1974).

J.D. Shaffer, R.M. Fitzgerald, and D.A. Nutile, "Long-Range Propagation Experiment: Antigua-Newfoundland, May 1974. Procedures and Shipboard Data NRL Operation 74-16-03," NRL Rept. 7978, 1976.

F.D. Tappert, "The Parabolic Approximation Method," pp. 224-286 in *Wave Propagation and Underwater Acoustics*, Lecture Notes in Physics, Vol. 70, J.B. Keller and J.S. Papadakis, editors, Springer-Verlag, Heidelberg, 1977.

F.D. Tappert and R.H. Hardin, "Computer Simulation of Long-Range Ocean Acoustic Propagation Using the Parabolic Equation Method," p. 452 in *Proceedings of the Eighth International Congress on Acoustics*, Vol. II, Goldcrest, London, 1974.

V.I. Tatarski, *Wave Propagation in a Turbulent Medium*, translation by R.A. Silverman, McGraw-Hill, New York, 1961.

V.I. Tatarski, *The Effects of the Turbulent Atmosphere on Wave Propagation*, translation, National Technical Information Service, Springfield, Va., 1971.

B.J. Uscinski, "Parabolic Moment Equations and Acoustic Propagation Through Internal Waves," Proc. Roy. Soc. London A372, 117 (1980).

B.J. Uscinski, "Intensity Fluctuations in a Multiply Scattering Medium. Solution of the Fourth Moment Equation," Proc. Roy. Soc. London **A380**, 137 (1982).

B.J. Uscinski, "Range and Time Dependence of Acoustic Intensity Fluctuations," pp. 253-267 in *Ocean Seismo-Acoustics*, T. Alcal and J.M. Berkson, editors, Plenum, New York, 1986.

B.J. Uscinski, C. Macaskill, and T.E. Ewart, "Intensity Fluctuations. Part I: Theory," J. Acoust. Soc. Am. **74**, 1474-1483 (1983).

H.L. Wilson and F.D. Tappert, "Acoustic Propagation in Random Oceans Using the Transport Equation," Science Applications Inc., Rept. 78-639-LJ (La Jolla, Calif.), 1978.

APPENDIX 7A: DATA REDUCTION FOR STATISTICAL ANALYSIS

The data reduction consists of the extraction of the signal levels as a function of time from the analog tapes. This was done for each of the frequencies and for each of the receivers. The analysis instrumentation allowed two channels of the data to be converted from analog to digital form simultaneously. Figure A1 illustrates this process.

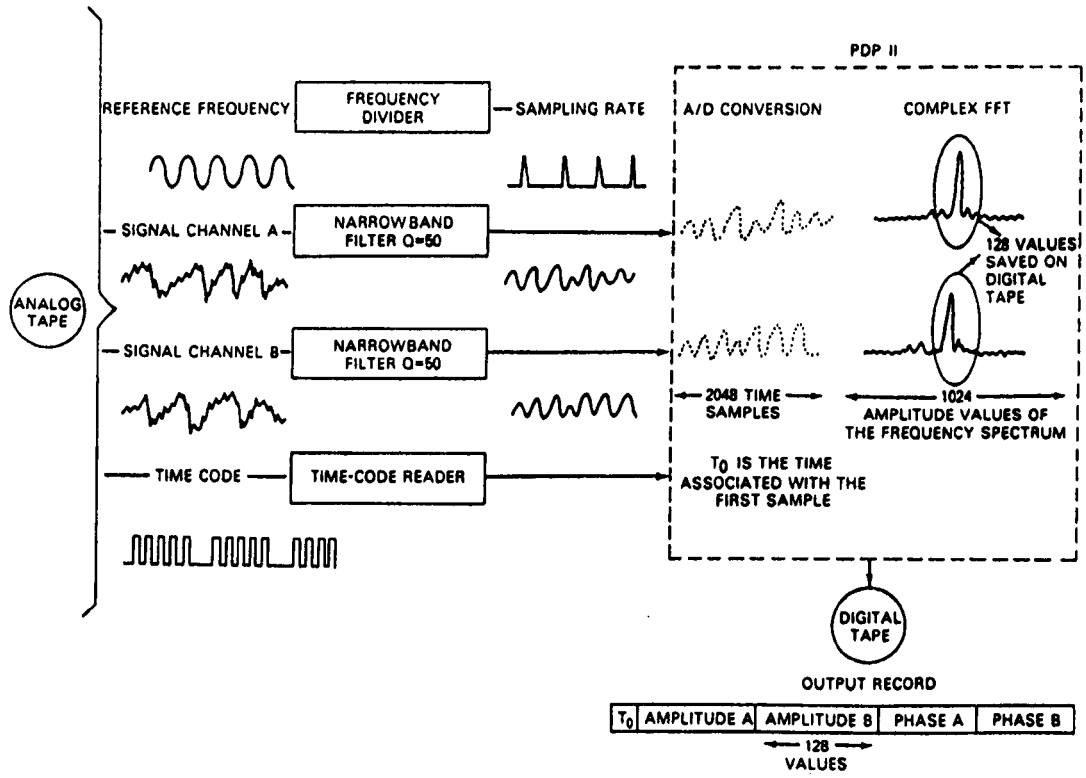

Fig. 7A1—Schematic diagram of data flow in the first stage of reduction

In the extraction of the signal levels as a function of time or range, the sampling rate and associated resolution in the frequency domain are as presented in Table A1. Two facts govern the choice of sampling frequency. One is that the signals being digitized are band-limited signals and thus need to be sampled at only a rate greater than twice the bandwidth. (In practice the signals were sampled from 5 to 20 times as fast as this minimum rate in order to reduce contributions from the aliased noise.) The other fact is that the sampling frequency is adjusted so as to have the source frequency fall near the center of the transform. The sampling frequency was derived by dividing a reference frequency on the analog tape by an

Table 7A1. — Summary of data-reduction parameters.

Source Frequency (Hz)	Sampling Frequency (Hz)	Transform Length (scc)	Data Discarded per Minute (sec)	Frequency Spectrum Output on Tape (Hz)	Line Width (mHz)
9.807	8.0	256	0	9.531-10.31	3.906
110	40	51.2	8.8	108.711-111.211	19.531
262	$\frac{1000}{18} = 55.55$	36.864	23.136	260.200-263.672	27.100

integer. This use of a reference frequency on the tape adjusts the sampling in accordance with any variations which occur in tape-recorder speed, thereby virtually eliminating the effects of wow and flutter.

After the choice of a sampling frequency of 8 Hz for the 9.807 Hz-data, the decision to accumulate $8 \times 256 = 2048$ samples before taking an FFT was based on the observation that the signal-to-noise ratio on occasion was so low that the source signal could often not be observed cleanly on shorter transforms, such as 1024 or 512. At the higher frequencies (110 and 262 Hz), one FFT is taken each minute, but the FFT is based on a time interval of less than 1 minute. Thus some data are discarded.

The width of each bin in the transform was approximately 3.9 mHz for 9.8 Hz, 19.5 mHz for 100 Hz, and 27.2 mHz for 262 Hz. The result of this initial processing is a time series of signal amplitudes for each channel processed. These amplitudes are *not* in decibels, and all subsequent statistical analysis was done using the amplitudes in linear form, not in decibels.

A decision to record 128 values of the transform on digital tape was motivated by the need to save not only enough lines to allow for shifts in frequency due to variations in source Doppler but also enough to observe any surface modulation and have noise samples available for analysis. The phase values for both channels were recorded on the tape along with the amplitude values.

The next step in this initial stage of the reduction was to use the spectral-amplitude-data on digital tape to derive the signal amplitude as a function of time. This step was done sequentially for each set of spectral amplitudes on the tape by first searching a given number of lines centered on the expected signal frequency to find the one with the maximum value. (The number of lines searched depends upon the variable Doppler, induced mainly by varying ship speed and direction.) This maximum amplitude along with those of the adjacent lines are squared and summed and the square root taken to determine the total amplitude of the signal.

At the conclusion of this phase of the processing, there were for each frequency and each location one or more digital tapes containing the signal amplitude for two channels along with the time of each amplitude. The data on these tapes were now processed through software on the computer to determine the statistics of the fluctuations in signal amplitude. The primary goals of the statistical processing were to establish correlation times, to obtain probability-density and distribution information, and to investigate range and frequency-dependent effects.

For each receiver location, the great-circle distance to the ship at the time of each navigational fix was calculated using the navigation data described in Shaffer et al. (1976). A linear interpolation of this information was used to assign a value of the receiver-to-source range for each point of the amplitude time series.

After this processing was completed, the data were in the form of an amplitude time series, covering a time interval of 14 to 16 days, corresponding to three frequencies (262, 110, and 9.8 Hz) and three receiver locations. To have maximum comparability between frequencies and locations, it was decided to compute statistics over time segments of equal length. The length of a time segment should be large enough to ensure good estimation of the probability density function and the autocorrelation function, yet small enough to avoid effects due to large variation in range. These considerations and examination of amplitude-versus-range plots led to the choice of 384 minutes, a number divisible by the sampling increment of each amplitude time series. There are therefore 59 such segments for the entire experiment.

APPENDIX 7B: PEARSON'S THREE MAIN TYPES OF DISTRIBUTIONS

This appendix presents the details of the equations for the three basic types of probability distributions, labeled types I, II, and III in the main text. It then shows how one would use them together with the tabulated signal data to generate probability density functions for the signal amplitude.

Pearson's equations (discussed in Elderton and Johnson (1969)) allow one to compute an approximate probability density function for a set of data by using the first four moments of the data (taken about the mean). The results of this analysis presented in terms of the coefficient of variation, the skew, and the kurtosis. The skew and kurtosis correspond to the third and fourth moments respectively and were computed for a standardized distribution, which is with zero mean and unity variance. One can thus use Pearson's equations with zero mean and with unity variance and skew and kurtosis from the empirical model to compute a corresponding standardized probability density function. After supplying a mean signal level, one can compute the standard deviation by using the coefficient of variation from the signal model. The standardized probability density function should then be translated to this mean level and the amplitudes scaled according to the computed standard deviation.

The first step in the use of Pearson's equations is to decide which of the three main distributions to use. This is done by computing a classification parameter η, given by

$$\eta = \frac{\beta_1(\beta_2 + 3)^2}{4(4\beta_2 - 3\beta_1)(2\beta_2 - 3\beta_1 - 6)}, \tag{7B1}$$

where β_1 is the square of the skew and β_2 is the kurtosis. A negative η indicates type I, a positive η less than 1 indicates type II, and a positive η greater than 1 indicates type III. For all three types the formulae following have the origin at the mean.

Type I

The type-I probability density function $p(x)$ is given by

$$p(x) = p_0(1 + x/A_1)^{m_1}(1 - x/A_2)^{m_2}, \quad -A_1 < x < A_2. \tag{7B2a}$$

The quantities required for the calculation are

$$r = 6(\beta_2 - \beta_1 - 1)/(6 + 3\beta_1 - 2\beta_2)\,, \tag{7B2b}$$

$$c = \frac{1}{2}\left[\beta_1(r+2)^2 + 16(r+1)\right]^{1/2}, \tag{7B2c}$$

$$m_1\,, m_2 = \frac{1}{2}\left[r - 2 \pm r(r+2)\beta_1/2c\right], \tag{7B2d}$$

$$A_1 = \frac{c(m_1+1)}{m_1 + m_2 + 2}\,, \tag{7B2e}$$

and

$$A_2 = \frac{c(m_2+1)}{m_1 + m_2 + 2}\,. \tag{7B2f}$$

When the skew is positive, m_2 in Eq. 7B2d is the positive root. The normalization factor in Eq. 7B2a is a complicated expression containing gamma functions and in practice is most easily determined numerically by computing $p(x)$ with $p_0 = 1$ and requiring the integral of $p(x)dx$ to be unity over the interval $-A_1 \le x \le A_2$.

Type II

The type-II probability density function $p(x)$ is given by

$$p(x) = p_0\left[1 + \left(\frac{x}{a} - \frac{\nu}{r}\right)^2\right]^{-m} \exp\left[-\nu \tan^{-1}\left(\frac{x}{a} - \frac{\nu}{r}\right)\right], -\infty < x < \infty\,, \tag{7B3a}$$

where r is the negative of the value computed in Eq. (7B2b). The other quantities required for the calculation are

$$m = \frac{r+2}{2}\,, \tag{7B3b}$$

$$\nu = -r(r-2)\beta_1 / \left[16(r-1) - \beta_1(r-2)^2\right]^{1/2}, \tag{7B3c}$$

and

$$a = \frac{1}{4}\left[16(r-1) - \beta_1(r-2)^2\right]. \tag{7B3d}$$

Again the normalization is most easily determined in a practical sense by computing $p(x)$ for $p_0 = 1$ and requiring the integral of $p(x)dx$ (over at least five standard deviations from the mean) to be unity.

Type III

The type-III probability density function is given by

$$p(x) = p_0(1 + x/A_1)^{-q_1}(1 + x/A_2)^{q_2}, \quad -A_2 < x < \infty. \tag{7B4}$$

The functional forms for the type-I and type-III distributions are quite similar. When one replaces m_1 by $-q_1$ and m_2 by q_2, the quantities q_1 and q_2 are determined from Eq. 7B2d, A_1 is determined from Eq. 7B2e, and A_2 is the negative of Eq. 7B2f. Normalization is again most easily established via numerical integration.

Chapter 8

THEORY AND ANALYSIS OF PROPAGATION IN A REFRACTIVE CHANNEL

INTRODUCTION

It is extremely difficult to obtain a realistic picture of interference of waves propagating in a duct by employing ray theory or geometric acoustics. The most useful approaches have been based on wave theory, the normal-mode theories and parabolic approximation theories. This chapter discusses the results obtained with normal mode theory for very low frequencies propagated in an ocean channel. It will illustrate how a simple monochromatic signal from a moving source is transformed, in the propagation process, into a set of closely spaced narrowband signals received in the channel. The chapter continues with a description of the two-dimensional structure of the field and the behavior of the field in the presence of a periodically changing environment, (an internal tide) and an arbitrarily changing sound-speed profile. It ends with a discussion of potential improvements in measuring signals in an interference field if a measurement of acoustic particle velocity can be obtained coincidental with the pressure measurement.

To compare observations with theory and analyze the physical nature of propagation in a refractive duct, Guthrie et al. (1974) developed a normal-mode theory for propagation from a moving source in a duct with a bilinear sound-speed profile. Although there are a number of normal-mode models for propagation in layered media, this is the first model including a moving source. Later, Ramsdale (1977) used the Guthrie et al. (1974) moving-source treatment in a propagation model for a duct with a parabolic sound-speed profile.

Both of these theoretical treatments were implemented in computer programs. The theory of Guthrie et al. (1974) was primarily employed in demonstrating the spacial character of propagation in a duct, and the theory of Ramsdale (1977) was employed to demonstrating

the temporal character of fluctuations in the field and in the received signal. The treatment of propagation through a random medium is not included in this work, a random medium being considered only as the limiting factor on the predictability of the field as the frequency is increased.

PROPAGATION

Transmission Loss

The theory of Guthrie et al. (1974) was employed in a computer program to calculate the transmission loss (TL) as a function of range and depth for a near-surface source in a bi-linear duct. A bilinear profile that approximated the Atlantic profile of region 1 was chosen. This profile is illustrated in Fig. 1.

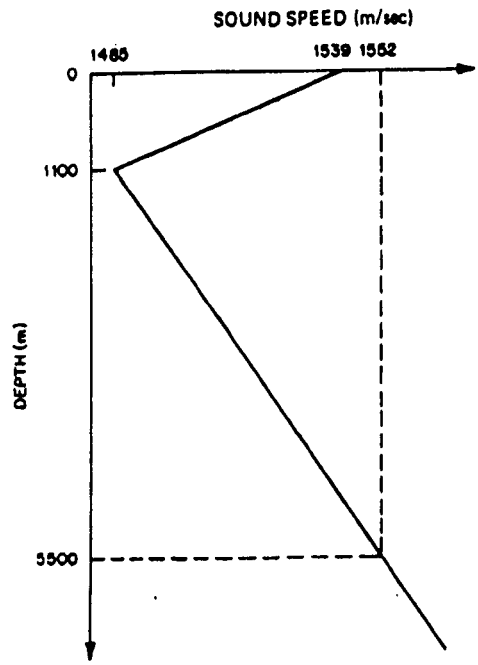

Fig. 1. Sound-speed profile used in ocean model computations.

Calculations of TL for a source 104 m deep and a frequency of 13.89 Hz were made for a receiver depth at the axis of the profile as a function of range. Figure 2 is a plot of TL as a function of range for the sum of the first 20 modes. The second curve is the sum of the RSR modes, and the third curve is the sum of the SOFAR modes.

The TL curve for the sum of all modes displays the normal interference structure seen in low-frequency propagation and is in good agreement with the 13.89-Hz curves of Ch. 7 Figs. 6 and 7. Since the model is not an exact representation of the physical situation, the comparison is not exact.

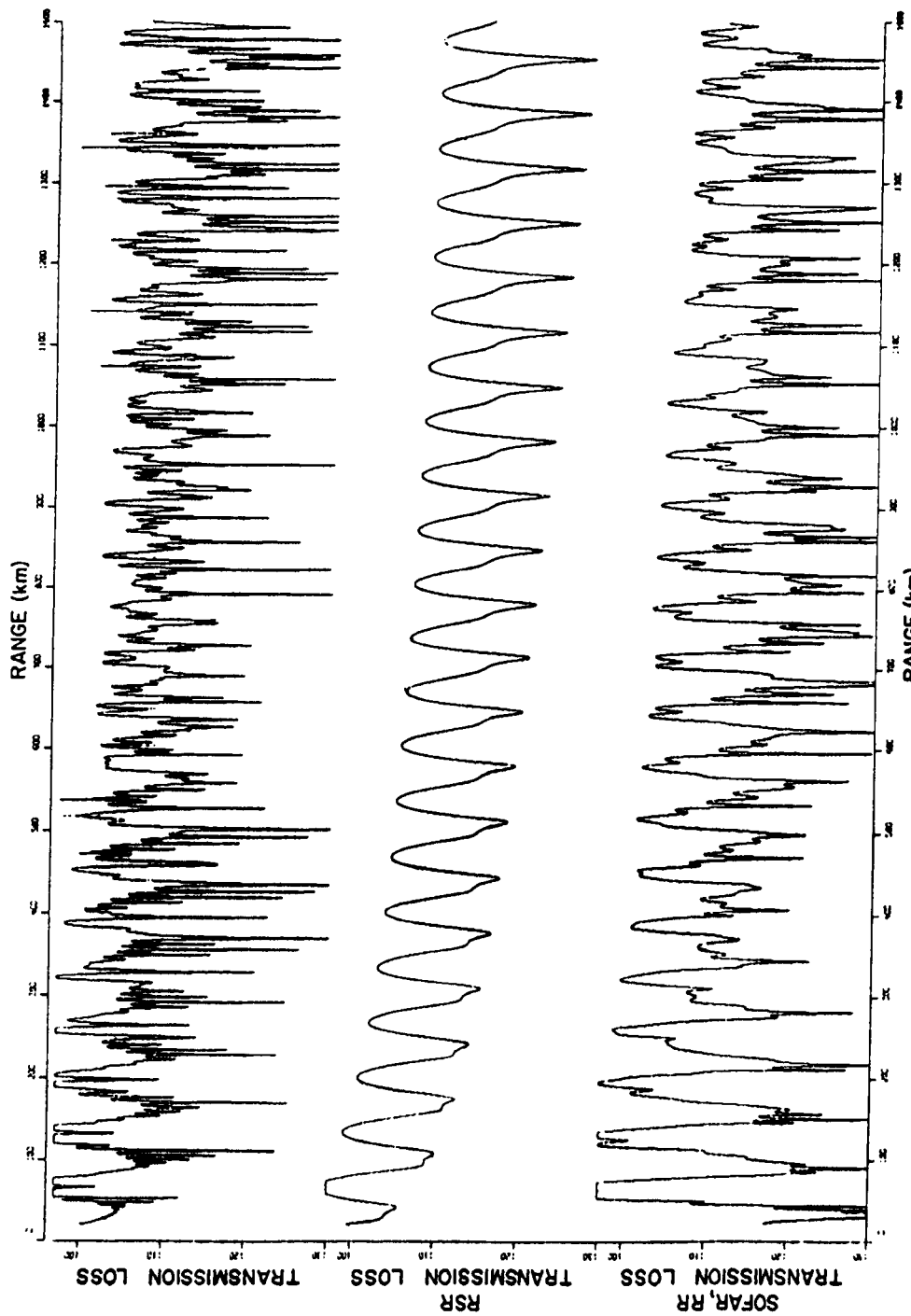

Fig. 2. Transmission loss as a function of range, with the top plot being the sum of the first 20 modes, the middle plot being SOFAR modes 1 through 16, and the bottom plot being RSR modes 17 through 20.

Spectral Spread of Received Signals

Since the source is in motion, each of the modes will have a unique radiating angle from the source and thus a unique frequency produced by the Doppler shift. A source speed of 7 knots (3.60 m/sec), the bilinear profile, and the normal-mode model, were used in calculating the relative amplitudes and frequencies for each of the first 20 modes. Figure 3 illustrates both the relative levels and frequencies for each of the modes. If one visualizes the field produced by all of the modes beating together, one then can appreciate the spacial and temporal complexity of the field near the receiver.

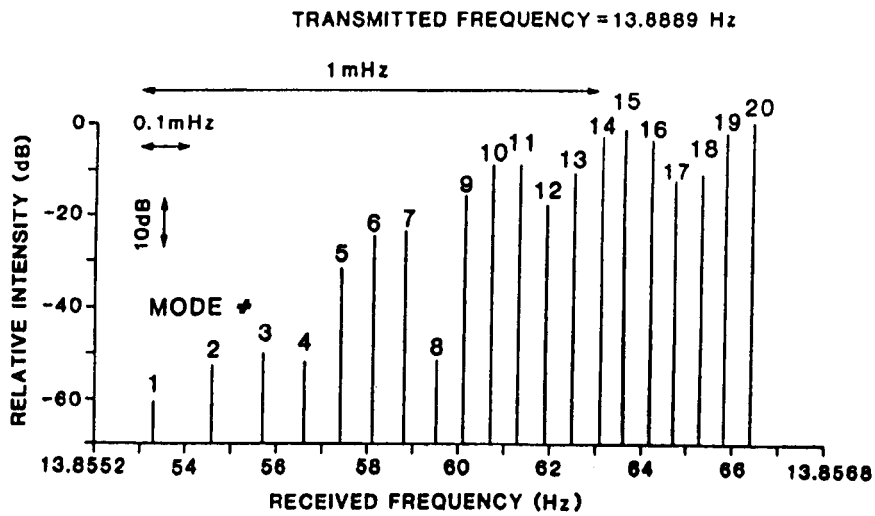

Fig. 3. Calculated amplitudes and beat frequencies of the received signals for the first 20 modes when the transmitted frequency is 13.8889 Hz and the source speed toward the receiver is 3.60 m/sec. Shown at the top left is the frequency-difference scale or beat-frequency scale.

The difference in the frequencies of the 20th and 1st modes, which is the beat frequency, or interference frequency, is 1.3 mHz, or 0.0013 sec^{-1}. This interference frequency corresponds with an interference period of 12.8 min. The difference in the frequencies between the 18th and 19th modes is 5×10^{-5} sec^{-1}, or 1/20 mHz. The corresponding period is 5.56 hours. At present no one has been able to resolve spectral lines with this fineness of spacing from measured data.

Intensity Structure of the Field

If the propagating medium is independent of range, the field moves through the medium at the velocity of the source vector. If the field is frozen at an instant, the complexity of its structure can be seen. With use of the normal-mode model, the contours of isointensity were calculated. Figure 4a illustrates the geometry and the relative positions of two examples of the intensity contours of the field as a function of range and depth. Figure 4b is the intensity or TL contours for a frequency of 13.89 Hz at a range interval between 50 and 100 km and a depth interval of 800 to 1400 m. The plot is centered about the minimum, or axis, of the sound-speed profile. The vertical scale has been exaggerated about 83-to-one. Figure 4c is a plot of the isointensity contours for the field in range and depth, again at 14 Hz, centered about the channel axis and at a range interval of 1200 to 1250 km.

The intensity fields of Figs. 4b and 4c can be considered as frozen in space at an instant in time. However, in all moving source and fixed receiver cases, the field is dynamic, moving through the receiving point at the rate of the ship's velocity vector. The moving source fields as seen by a fixed receiver is approximately the same as the field generated by a fixed source as seen by a moving receiver. The small difference arises from the nonlinear Doppler shift for the moving source. The propagation in the channel is also required to be range independent.

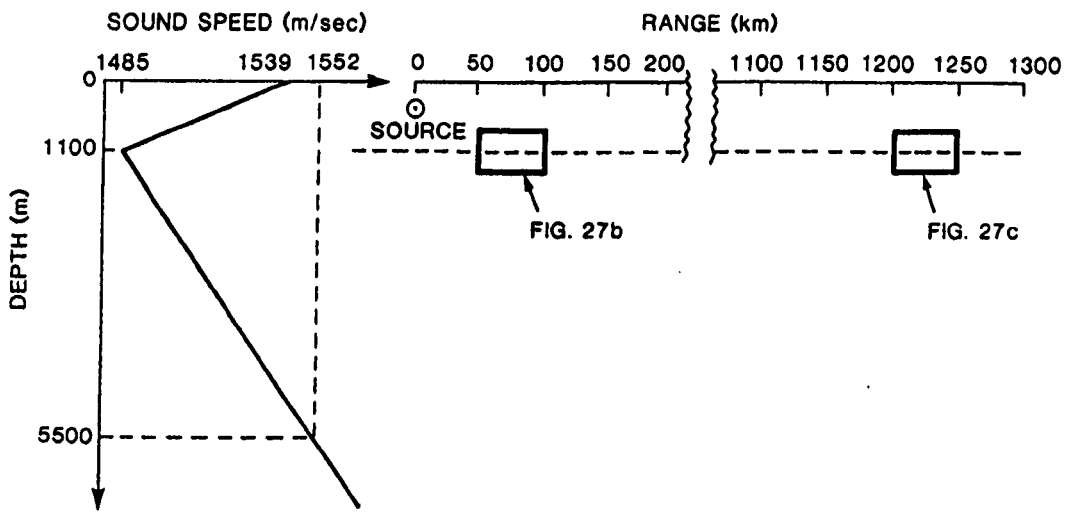

Fig. 4a. Bilinear sound-speed profile and the locations of isointensity calculations of the interference field.

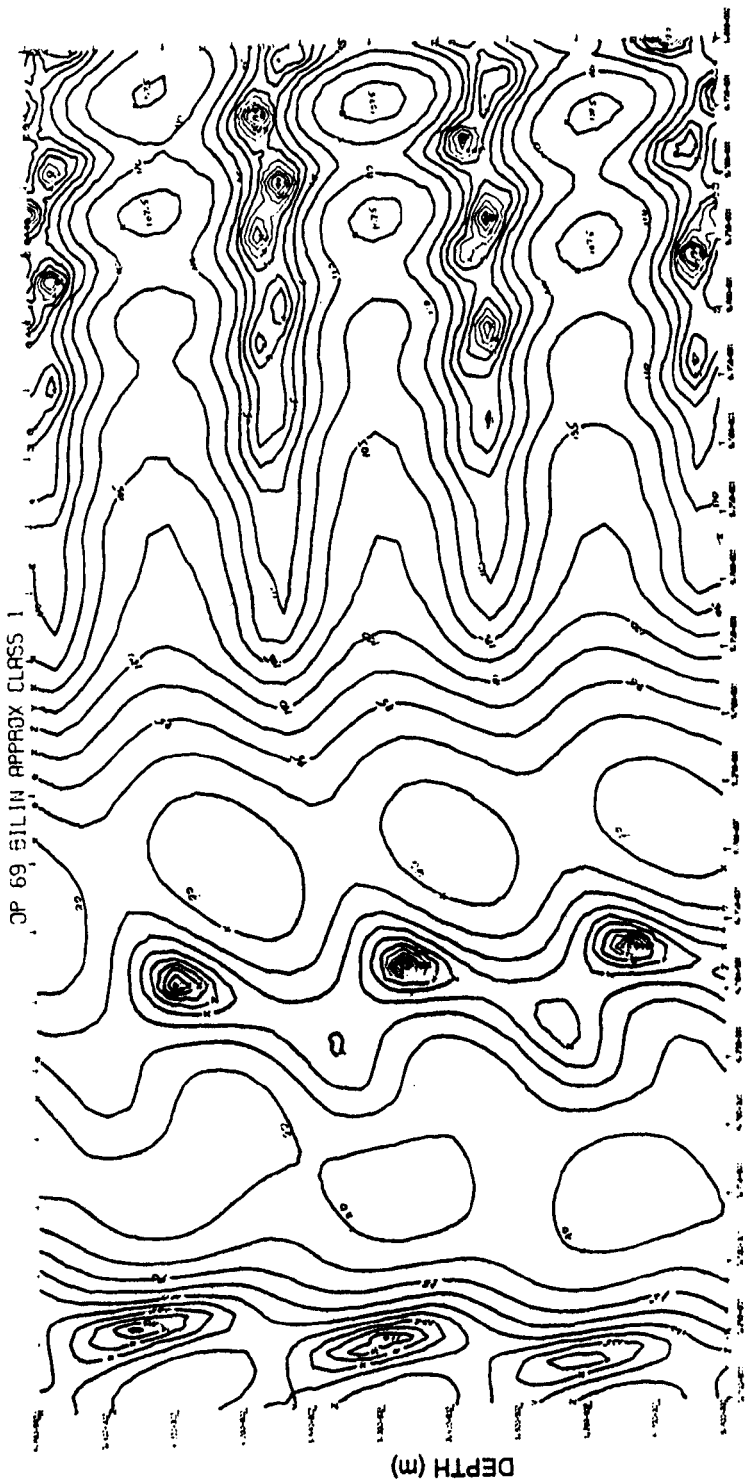

Fig. 4b. Isointensity field for the section in Fig. 4a between 50 and 100 km in range and 800 and 1400 m in depth.

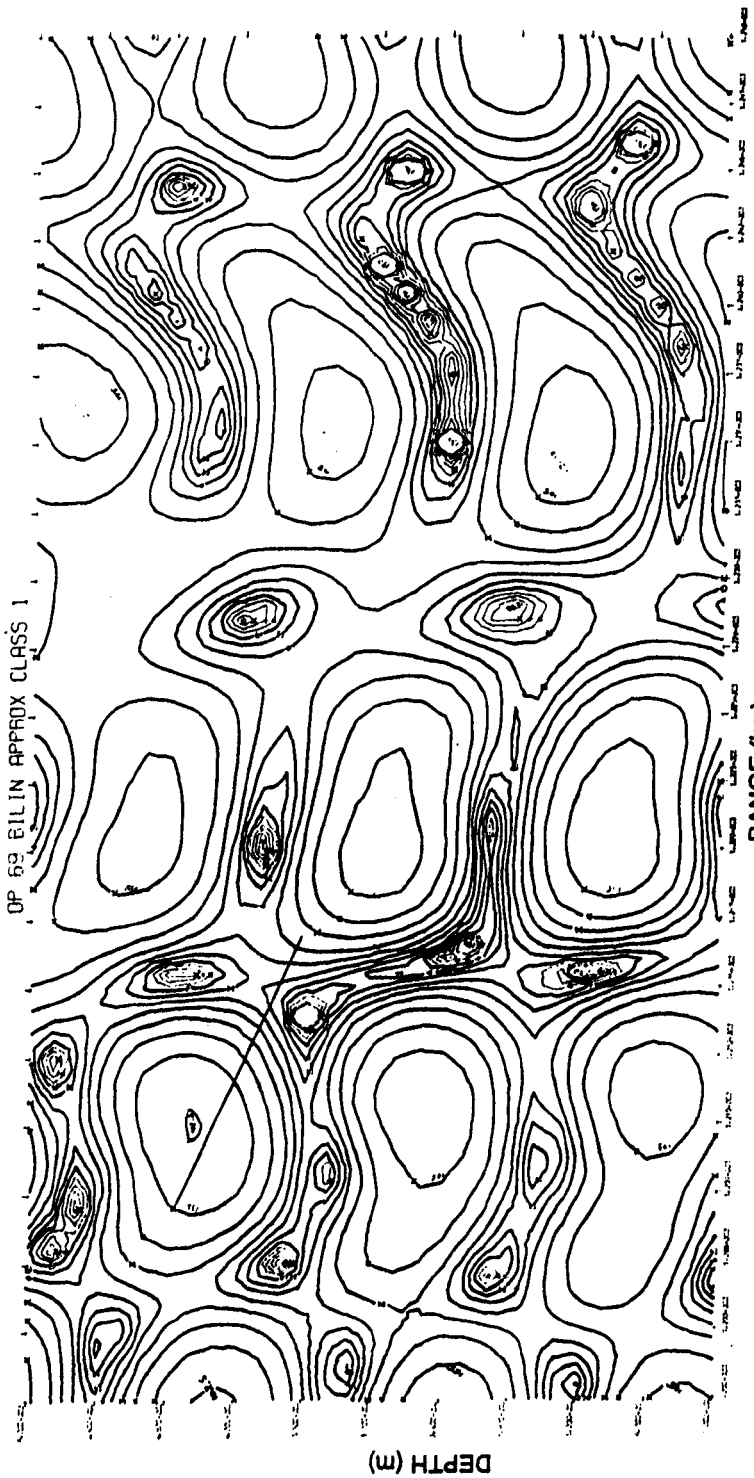

Fig. 4c. Isointensity field for the section between 1200 and 1250 km in range and 800 and 1400 m in depth.

This inverse relation of source and receiver motion is indeed fortuitous, because it would be almost impossible to conduct long-range propagation experiments using fixed sources and moving receivers. The hydrodynamic self-noise generated by the moving receiver would require an increase in the source level well beyond the ability of current technology to achieve the necessary signal to noise ratios.

Interference and Fluctuation

When the source is in motion and the receiver is stationary relative to the medium, the field moves past the receiver. Each mode will have a slightly different frequency as a result of the Doppler spread across the radiating angle. The received signal is the linear sum of the arriving waves and has a varying amplitude in the form of beats.

The simplest case is that of the source moving near to and parallel to a perfectly reflecting boundary that defines an infinite half space, with the boundary here being the sea surface. Figure 5a illustrates the geometry. This is the well-known Lloyd-mirror case, discussed by Wood (1960), where only two rays combine to produce the interference field. Figure 5b illustrates the amplitude fluctuation of the field as the source and receiver move relative to each other. The interference length increases as the angle between the direct path and the surface-reflected path decreases, which is synonymous with the decrease in the Doppler difference in the frequencies of the two arrivals as the angle decreases. The Lloyd-mirror case constitutes the simplest interference field found in the ocean. In Fig. 6 bottom reflection has been introduced in addition to the reflection from the surface. The depth of the source is 2 wavelengths from the surface, and the depth of the bottom is 100 wavelengths. The range is in kilowavelengths. The field is more complicated than in the Lloyd-mirror case, and a higher order of interference exists. The near range is more complicated than the method can follow, and as range increases the complexity decreases. The dynamic range of this illustration is approximately 100 dB.

As the interference field becomes more disordered, the probability density function of the amplitude should approach a Rayleigh distribution. This would be analogous to the case

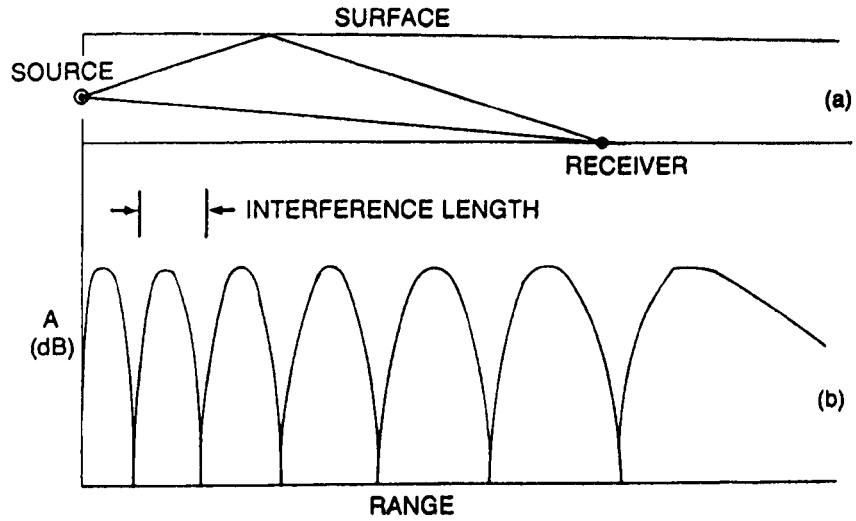

Fig. 5. Amplitude levels of the received signal in the Lloyd-mirror case (source or receiver moving at a fixed depth, with other being deeper) as a function of the source-to-receiver range.

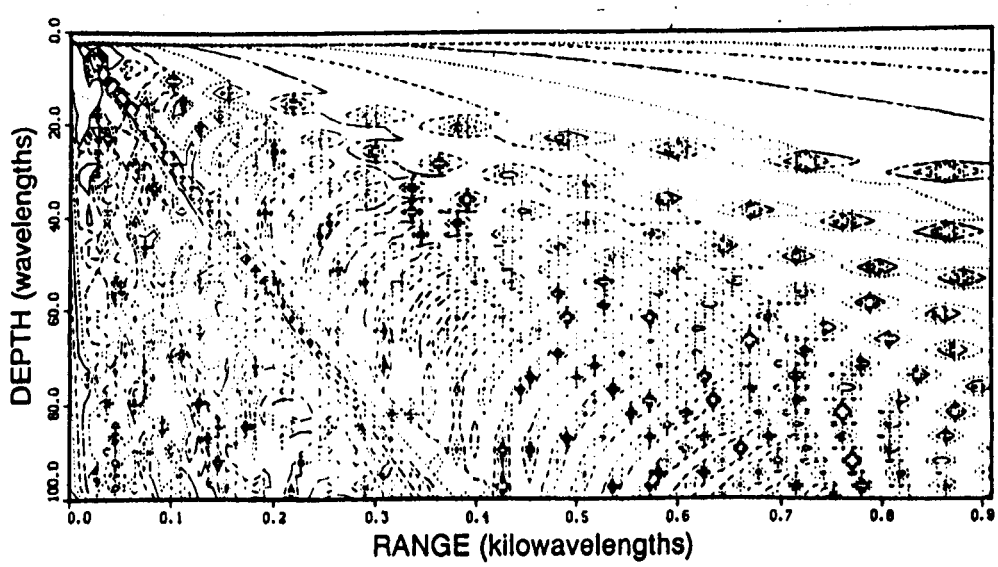

Fig. 6. Isointensity contours of an interference field.

of low-angle scattering from the bottom, illustrated in Fig. 2 of Chapter 3, where the measured density function is compared with a Rayleigh density function.

INFLUENCE OF ENVIRONMENT

Influence of the Sound-Speed Structure on the Intensity Field

The sound-speed profile plays a major part in the structure and position of the interference field in the sound channel. To illustrate this influence, a region of the computed field was chosen in the vicinity of a convergence zone between 500 and 600 km in range and with a depth interval of 200 m centered about the channel axis. Figure 7a indicates the location of

the selected region and the simple bilinear sound-speed profile representing the Atlantic environment in region 1 (Figs. 2, 3, and 4). Figure 7b shows the 14-Hz transmission loss as a function of range along the channel axis between 450 and 625 km. Isointensity contours of the interference field for a range interval of 525 to 550 km and a depth interval from 1000 to 1200 m are plotted in Fig. 7c, which has a 125-to-one magnification of the vertical scale. This illustration has a dynamic range of 30 dB from the broad 100-dB contour in the upper left of the section to the 130-dB contours in several of the deep nulls. This intensity pattern is typical for low-frequency acoustic fields in an ocean channel. The size of the broad, or higher level, features in the vertical direction is of the same order as the 102-m wavelength. The variation in level of areas in the region of nulls in the field is large compared to the wavelength. In the horizontal direction (with a scale 1/125 that of the vertical scale) the variations in the field are very small compared to wavelength, except in the deep nulls.

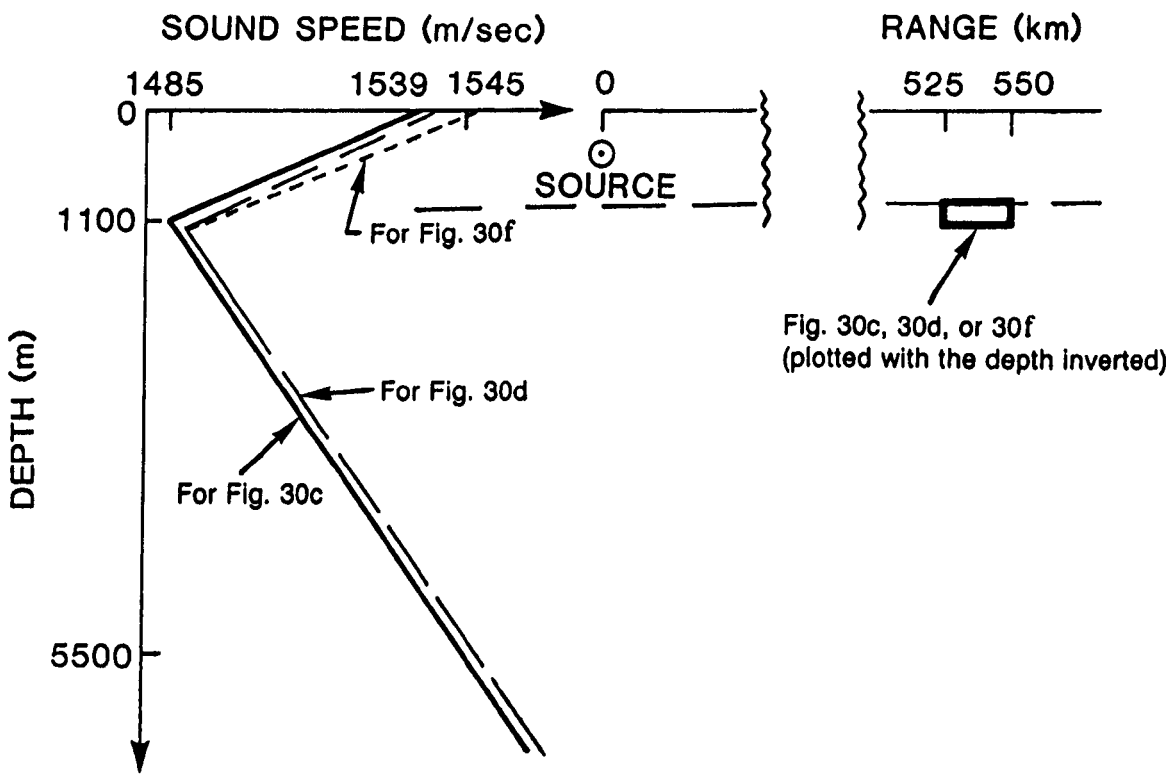

Fig. 7a. Sound-speed profiles and the location of the calculated intensity field.

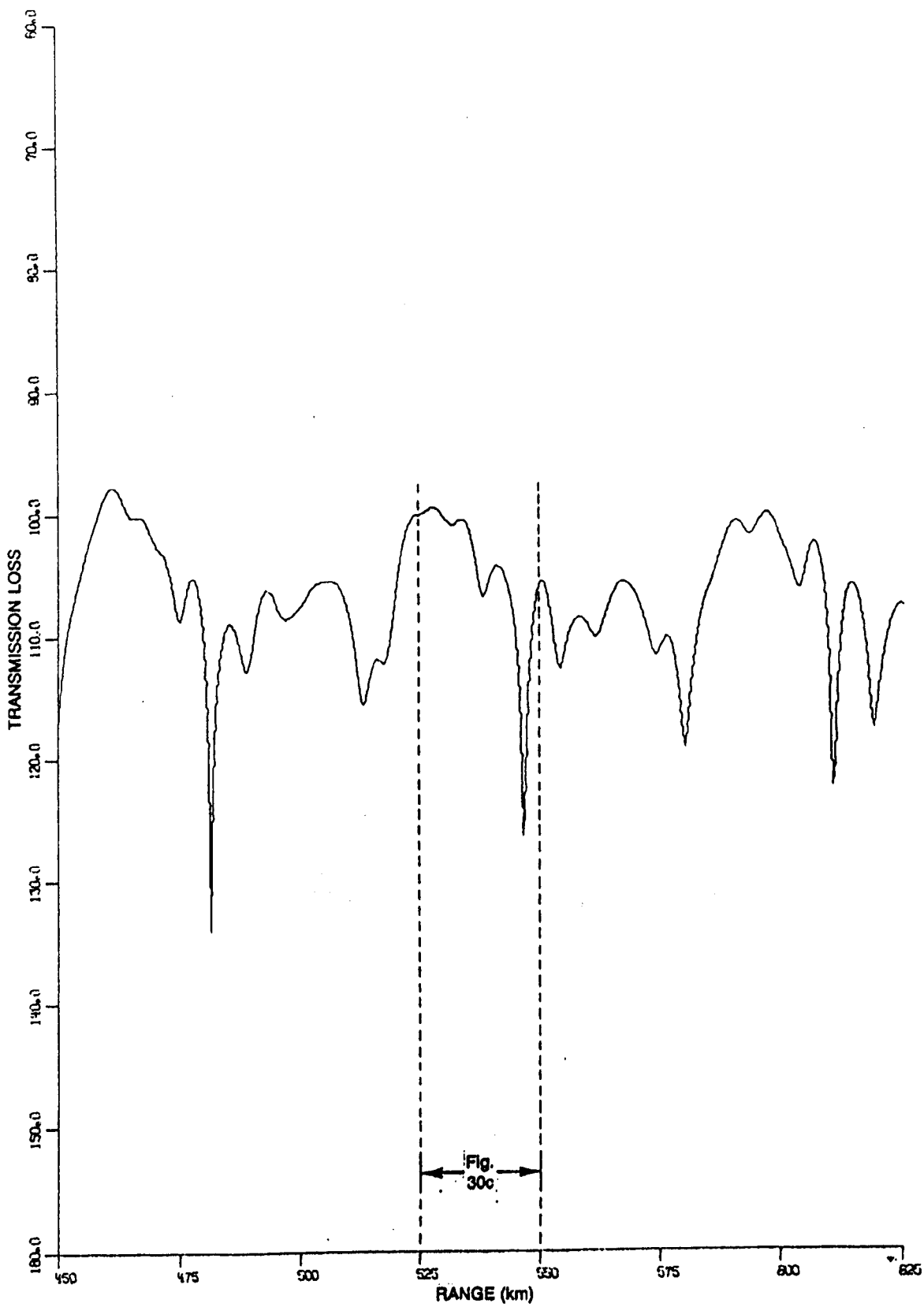

Fig. 7b. Transmission loss between 450 and 625 km at a depth of 1000 m and a frequency of 14 Hz.

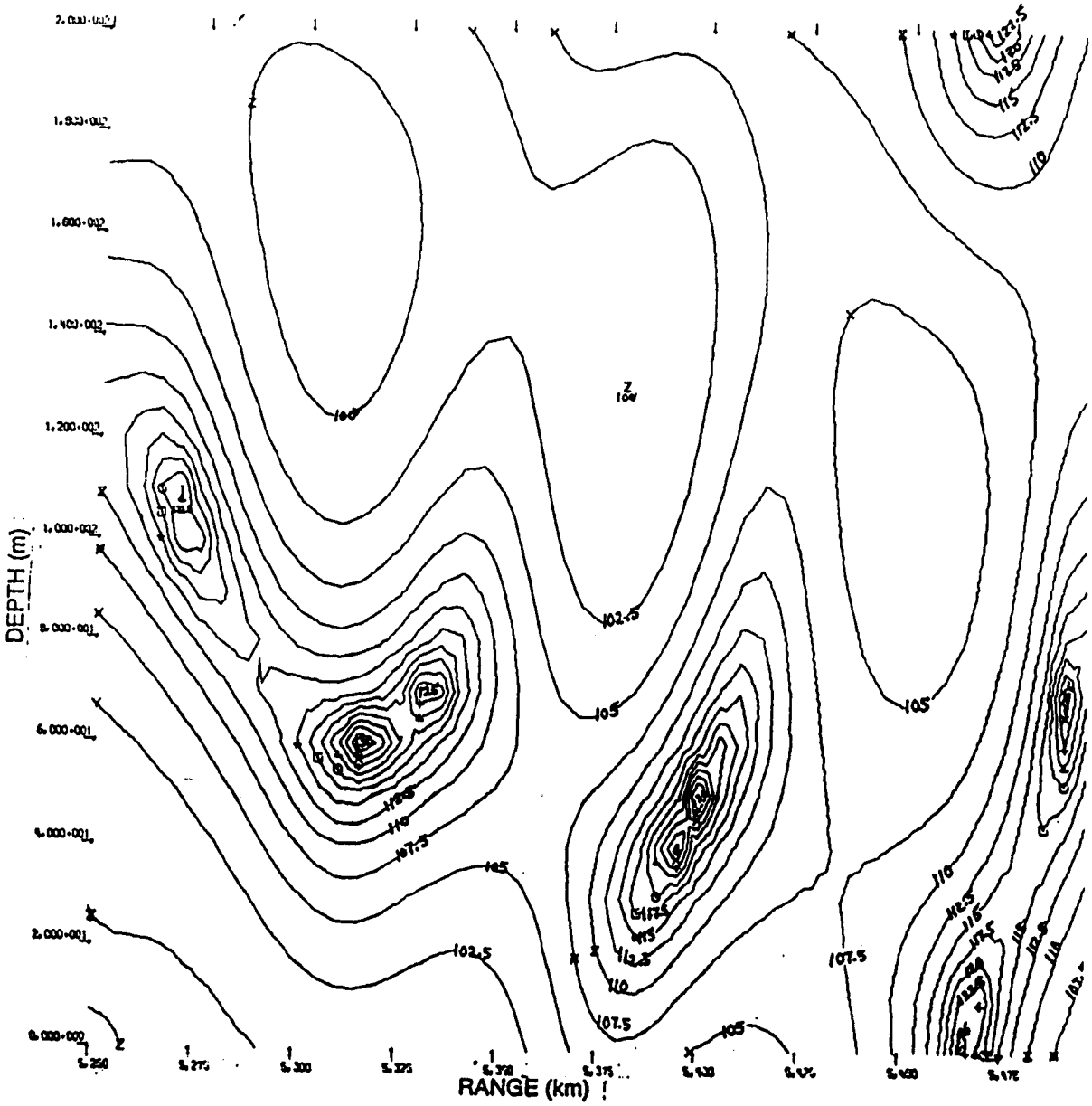

Fig. 7c. Isointensity contours in the section designated in Fig. 7a calculated for 14 Hz using the sound-speed profile indicated.

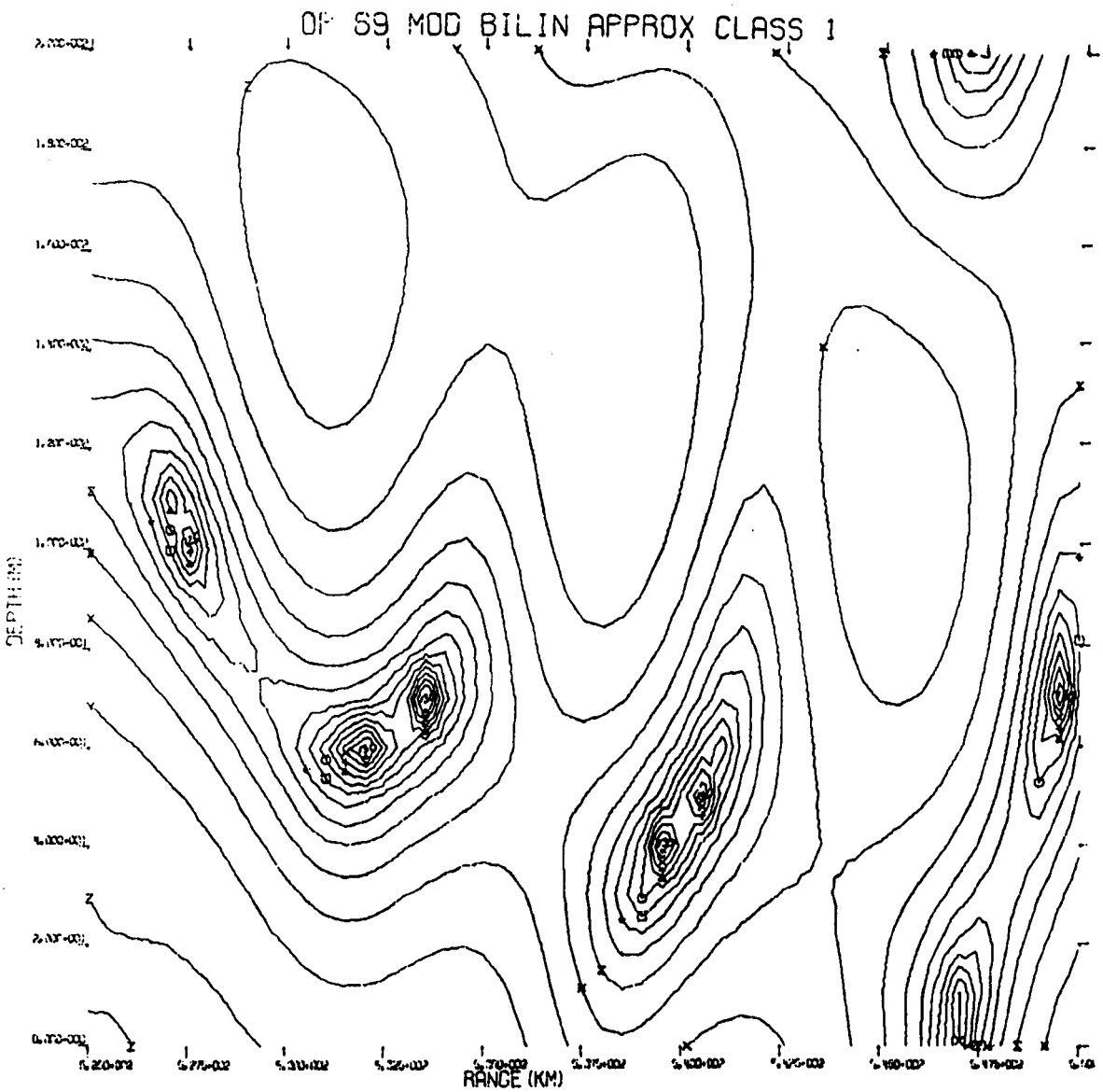

Fig. 7d. Isointensity contours in the section designated in Fig. 7a calculated for 14 Hz using the sound-speed profile indicated.

The sound speed of the profile was then changed by increasing the sound speed by 1 m/sec over the entire profile (Fig. 7a). The intensity field was then recomputed (Fig. 7d). This field appear to be almost identical with that of Fig. 7c. Figure 7e is an overlay of Fig. 7d onto Fig. 7c to show how closely the two fields match. However, to make this match, Fig. 7d had to be shifted to the left on Fig. 7c. The shift in the range-scale arrows at the bottom of Fig. 7e shows that this field computed from the modified profile with the higher sound speed has moved out in range by approximately 350 m. Thus the interference structure of the field is well behaved for small uniform changes in sound speed. If the sound-speed profile

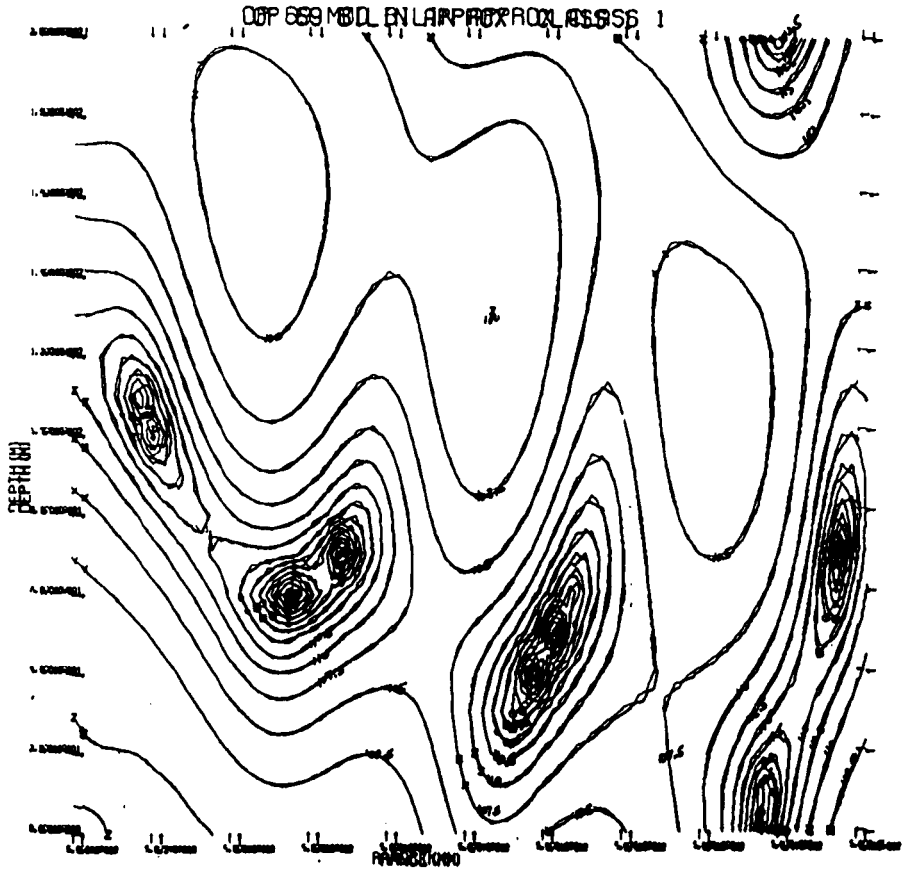

Fig. 7e. Superposition of Figs. 7c and 7d, shifted as indicated by the arrows at the bottom to emphasize the similarity of the patterns.

had been reduced, the field would have moved toward the receiver. More correctly, the field can be visualized as plotted on a stretched rubber sheet, fixed at the origin, for a particular sound-speed profile. When the sound speed of the profile is increased or decreased, the stretch of the rubber sheet is increased or decreased respectively. The small difference (<20 m) across the 25-km interval at 500 km between stretching the plot in going from Fig. 7c to 7d and simply translating the plot in range is less than the plot's resolution.

A second modification of the sound-speed profile was made by increasing the sound speed at the surface by 5 m/sec while retaining the remander of the profile. This modified bilinear profile was then used in calculating a new field (Fig. 7f). Figure 7g is an overlay of this new field onto that of Fig. 7c. The modified-profiles field is somewhat distorted relative to the basic field, being displaced and rotated slightly. However, the structure of the field has not changed much. If a receiver had been placed at almost any fixed point in the basic field,

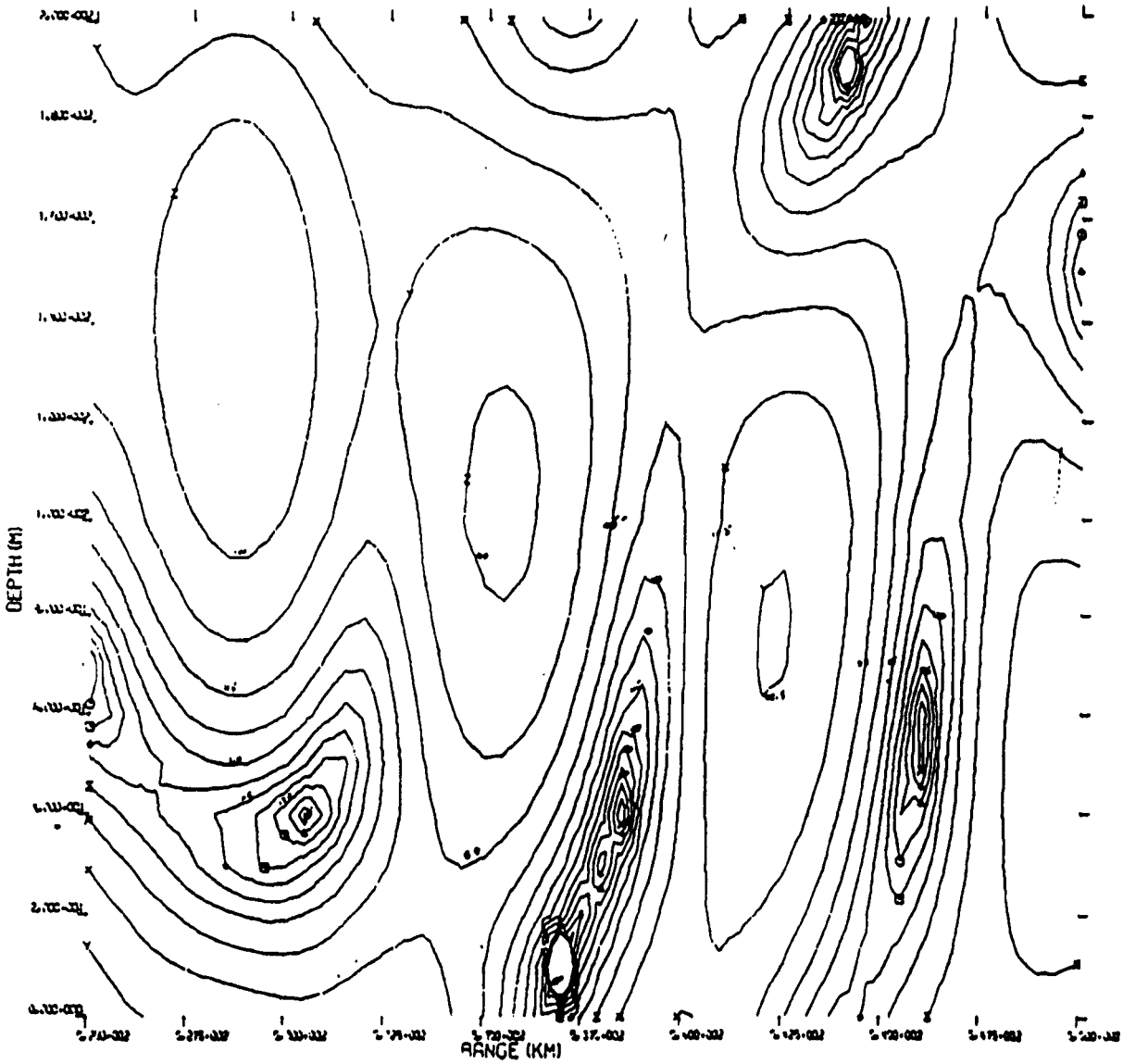

Fig. 7f. Isointensity contours in the section designated in Fig. 7a calculated for 14 Hz using the sound-speed profile indicated.

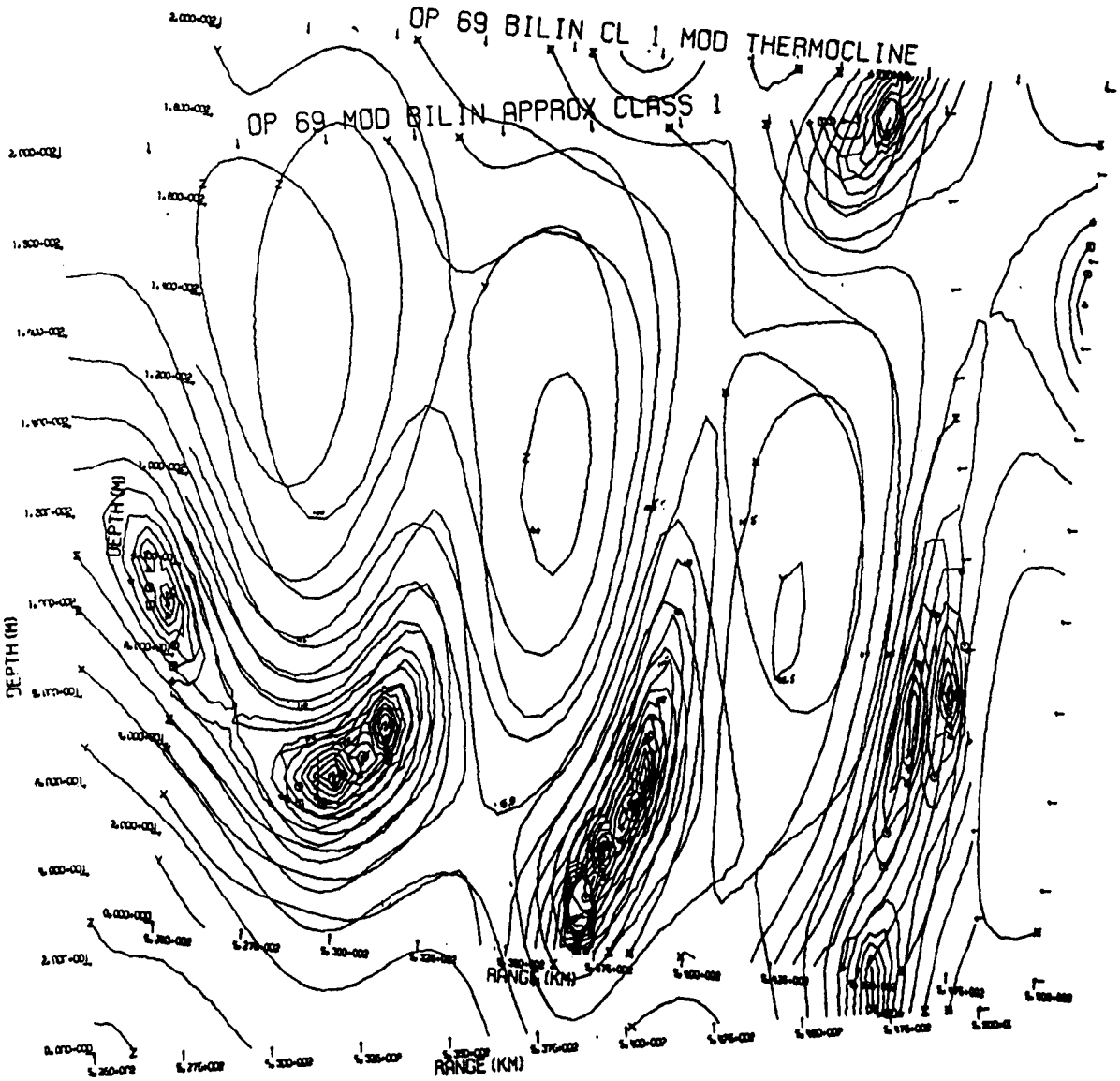

Fig. 7g. Superposition of Figs. 7c and 7f.

it would probably have seen an amplitude and phase change that was almost random with essentially no predictability. This type of change in the sound-speed profile is frequently seen as the surface is heated to a greater or lesser extent by the sun.

Variations in the Field from Internal Tides

One of the most interesting variations in acoustic fields is that generated by the first-mode semidiurnal internal tide in ocean channels. Mooers (1975) has shown that this tide perturbs the sound-speed profile in a sinusoidal manner within the 12.42 hour period. Figure 31 is an example of the variation in the profile envelope for a 100-m-amplitude internal tide.

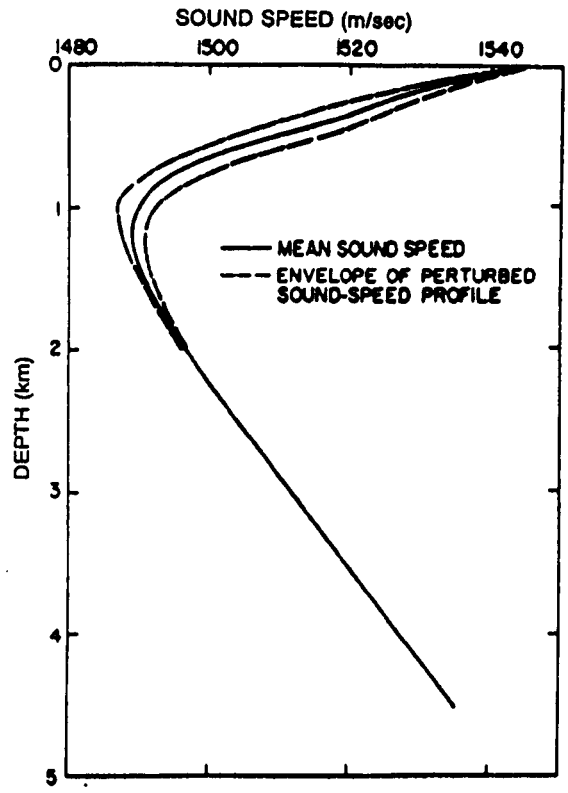

Fig. 8. Mean sound speed and perturbation envelope (from Mooers (1975)) in the case of a 100-m-amplitude internal tide.

Mooers (1975) showed that the greater the amplitude of the internal tide, the greater the variation of the sound speed about the mean profile. Ramsdale (1977) simulated the internal tide by varying the sound speed in a parabolic profile in a sinusoidal manner about its mean position. This work reinforced the concept that the structure of the interference field stretched or contracted with small changes in the sound-speed profile. For natural changes in the profile, such as an internal tide in the ocean, the distortion of the interference field is relatively insignificant. The significant change produced by the sound-speed variation is in its change of position.

Calculations of the amplitude and phase variations of the received signal were made for a typical Atlantic sound channel. The tidal variations and the sound speed were simulated by a perturbed parabolic profile. Figure 9 shows the profile and the geometry of the source and receiver. The variation in the signal level and phase at the receiving hydrophone, at a range of 400 km, over the tidal cycle for a 100-Hz CW signal is shown in Figs. 10a and 10b

respectively. The figures show a symmetry about the first-quarter and third-quarter points of the 12.42-hour period of the semidirurnal internal tide.

An obvious difficulty one has in tracking the behavior of the field with a fixed source and a fixed receiver is that one has no way of perceiving how the field is changing when the observed signals change. It may be moving in or out or it may be distorting as a result of changes in the sound-speed profile.

A possible method for improving the understanding of propagation in ocean sound channels and for tracking the sound-speed changes in the channel would be to change the frequency in small increments. Since the sound speed C is equal to the product of the frequency f and the wavelength λ, a change in f holding C constant will change λ. When C is changed holding f constant, λ is again changed. The structure of the field would remain constant for small changes in frequency. Thus small incremental changes in frequency would walk the interference field past the receiver in an orderly manner. This would be possible only if the natural change in the sound speed in the medium were slower than the rate at which the experiment could be carried out. It is possible that a small continuous change in

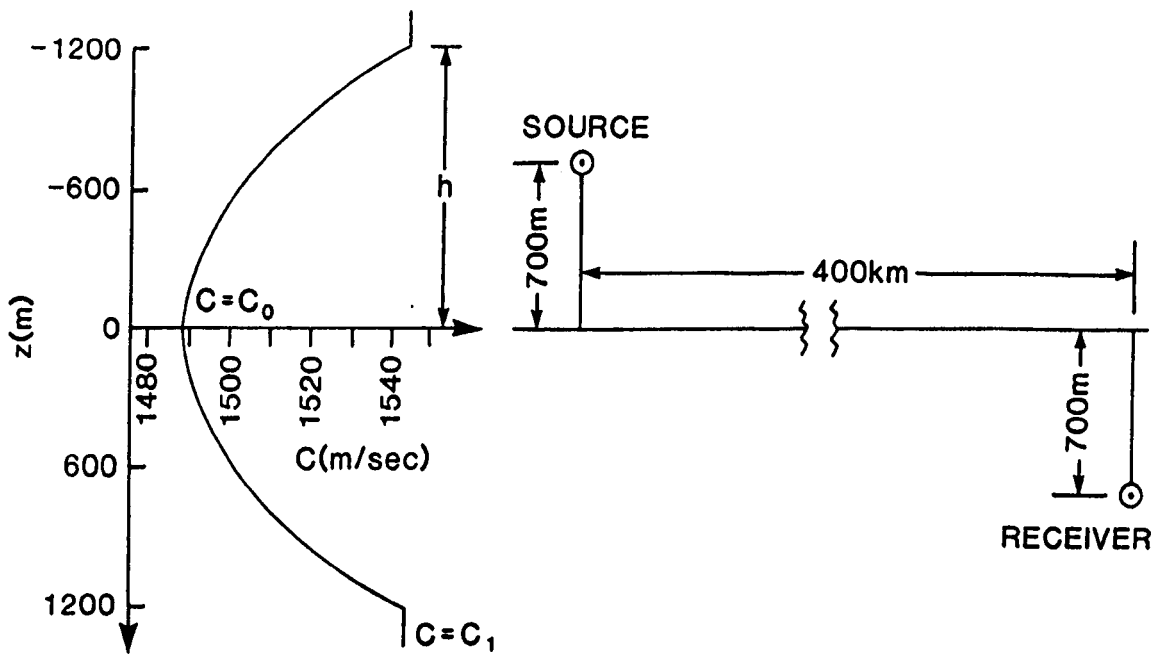

Fig. 9. Truncated parabolic profile used in simulating an Atlantic internal tide, given by: $C(z) = C_0 (1 - \alpha^2 z^2)^{-1/2}$, where $\alpha = h^{-1} [1 - (C_0/C_1)^2]^{1/2}$ and $|z| < h$, and, at the right, the acoustic geometry. The values for the calculations were $h = 1200$ m, $C_1 = 1544.63$ m/sec, $C_0 = 1489.55$ m/sec, and $\Delta C_0 = 0.196$ m/sec.

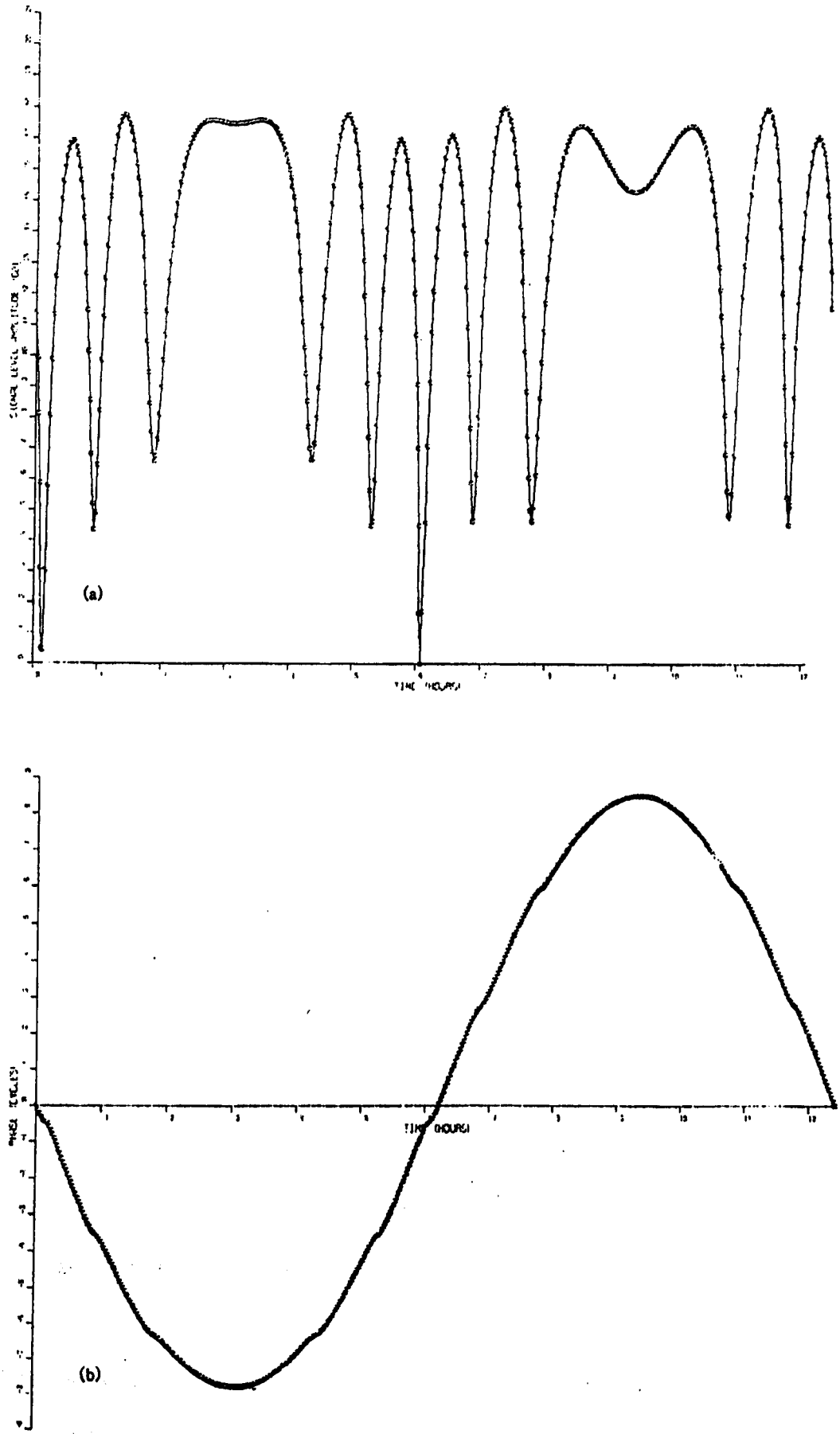

Fig. 10. Variation of the amplitude (b) and phase (c) from calculations simulating an Atlantic internal tide.

frequency could match the natural change in the channel, thus minimizing the fluctuation. This match would essentially stop the motion of the interference field. There is a similarity between reducing the fluctuation by controlling frequency in the backscattered field (Chapter 1) and here in the propagated field. With the availability of current computing capacity and adaptive processing techniques, controlling frequency to minimize fluctuation in the field could be a powerful tool in ocean-basin acoustic tomography at very low frequencies. Such minimizing of fluctuation could be very useful in tracking changes in the environment.

Particle Velocities in Interference Fields

Essentially all of the experimental information and observations that have been obtained on the behavior of acoustic fields in the ocean have been obtained with hydrophones, which are acoustic pressure sensors. Hydrophone technology has reached a high degree of development, providing more than adequate sensitivity and flexibility in underwater sound applications. However, there is no equivalent in the ability to sense particle velocities. This inability does not mean that particle velocity has been overlooked or that there has been no effort to provide a measuring instrument. There has been effort in both areas. Since intensity is proportional to the square of the pressure in a plane wave, and a good approximation at large distances is a spherical wave, the measurement of pressure is sufficient for many applications. In the description of near and interference fields and in complicated fields near elastic boundaries, a true measure of intensity is obtained from the product of the complex pressure and particle velocity. The behavior of the intensity vector would increase this information concerning the behavior of interference fields. The added information in the velocity vector could possibly contribute almost as much as the pressure.

An example would be two plane waves intersecting, one 45^0 up and the other 45^0 down, in a frozen interference pattern. A plot of the pressure field would be represented by Fig. 11a. The corresponding particle-velocity field is illustrated in Fig. 11b. The pressure field illustrates the normal sum and difference pattern of the interference field. However, the

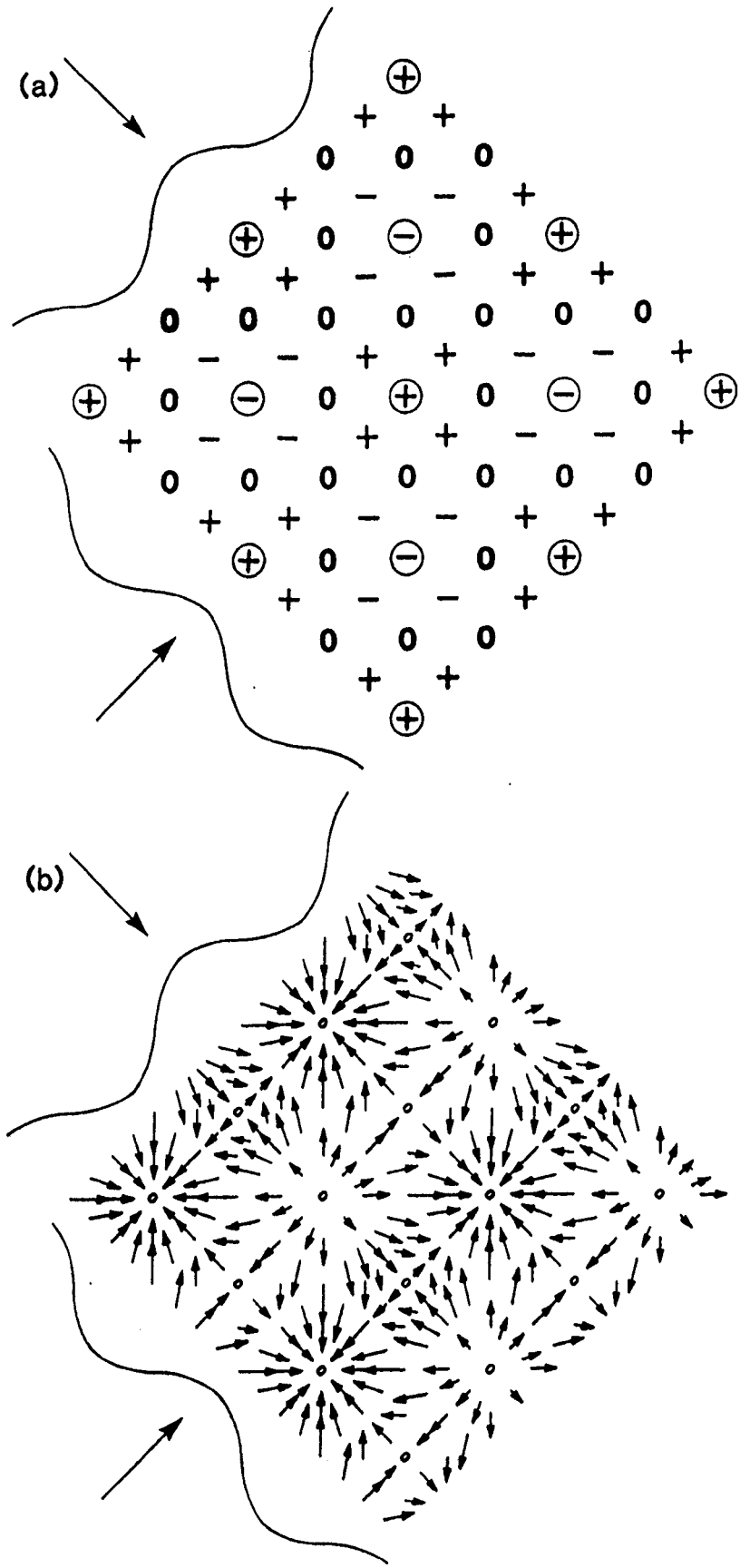

Fig. 11. Pattern of the pressure field (a) and the particle-velocity (b) in an interference field.

particle-velocity field displays a complicated vector pattern. The direction of the velocity vector along an interference line of the field is normal to the direction of propagation, having a maxiumum amplitude when the pressure is a minimum. If one could obtain significant samples of the vector field, the vector field should be extremely useful in analysis.

In practice it is estimated that any experimental particle-velocity measurement in the ocean would be limited to about 100 Hz and below. This limit is due to the small particle displacement, less than 10^{-12} m (1 picometer, or 1 pm), above 100 Hz for a signal level equivalent to sea state zero.

CONCLUSIONS

By use of a normal-mode model, calculations of propagation in a dispersive channel illuminate the transformation of a simple moving monochromatic source to complicated interference fields. The received signals consist of a set of narrowband lines.

The low-frequency transmission-loss curve as a function of range is found to be the sum of two sets of modes: the RSR and SOFAR modes. The transmission-loss curve has a complicated interference structure, dominated by convergence zone peaks. The structure of the calculated transmission loss corresponds quite well with the measured transmission loss of Chapter 7.

Computations of the spacial acoustic field in a channel, in terms of isointensity contours, provide a means of visualizing the complexities of the field in range and depth. This enables one to envision the results of placing a linear array in the field when it is remembered that large phase shifts occur in the vicinity of the intensity nulls.

The sensitivity of the interference field to changes in both time and space of the sound-speed environment is provided by model calculations. These results clearly indicate how a signal will fluctuate as a function of time for a moving source and also for a fixed source in a temporarily changing environment. The simulations also show only minor changes of the field for significant deviations in the sound-speed profile.

REFERENCES

A.N. Guthrie, R.M. Fitzgerald, D.A. Nutile, and J.D. Shaffer, "Long-Range Low-Frequency CW Propagation in the Deep Ocean: Antigua-Newfoundland," J. Acoust. Soc. Am. **56**, 58-69 (1974).

C.N.K. Mooers, "Sound Velocity Perturbations Due to Low Frequency Motions in the Ocean," J. Acoust. Soc. Am. **57**, 1067-1075 (1975).

D.J. Ramsdale, "Acoustic Fluctuations Using the Parabolic Profile," J. Acoust. Soc. Am. **61**, 65-75 (1977).

A.B. Wood, *A Textbook of Sound*, Bell and Son, London, 1960.

Chapter 9

SUMMARY, RECOMMENDATIONS, AND REMARKS

INTRODUCTION

This chapter summarizes the results of the investigation into two phenomena that cause acoustic interference in the ocean: scattering from the ocean floor and propagation in a spacially and temporally varying ocean channel. The summary is followed by a discussion of applications that use the physical understanding of the mechanism and the properties of acoustic fields resulting from this research. A part of this discussion includes observations and suggestions concerning items for future research. The chapter ends with a delineation of the writer's personal involvement in the research covered by this work.

EXECUTIVE SUMMARY

Ocean acoustic experiments were conducted and analysis made for two areas of underwater acoustics: ocean-bottom scattering and the propagation of acoustic waves in a geometrically dispersive sound channel. The objectives of this research were to provide a description and an understanding of the physical properties and their behavior for these two areas. This was done by comparing the analyzed results of the experiments with theoretical computations.

A series of ocean-bottom-scattering experiments were conducted in two field operations. The experiments were designed to test hypotheses of the mechanisms of scattered signal fluctuation, determine the spacial structure of the scattered field, learn more about the acoustic interaction with the sea-bed, and to obtain numerical values of the scattering strength. The analysis of the signal-fluctuation data indicates that source and receiver motion produces a Doppler gradient across the insonified area, resulting in a beat or interference structure in the received signal. The fluctuation rate is a function of the acoustic geometry and is linearly

related to the source and receiver motion and to signal frequency. Spacial structure and dynamic behavior of the scattered field is shown to be related to, and consistent with, the fluctuation of the received signal. Also shown is that the spacially fluctuating structure or lobes of the scattered field correspond to the radiation of a source with the dimensions of the scatter area, rather than the dimensions of an image of the original source. Both fluctuation and field characteristics are shown to agree with simple models. Data from the two ocean areas indicate no subbottom returns in one case and subbottom returns in the second case, with the possibility that energy was transmitted into and refracted out of the bottom. In addition, volume-scattering-strength profiles measured in two ocean areas showed variations of 25 dB as a function of depth. Significant differences were observed between profiles obtained below a depth of 150 m during the day and at night.

Three continuous-wave and impulsive-source experiments covering frequencies from 5 to 260 Hz were conducted over ranges up to 3000 km, with reception on fixed hydrophones. Propagation in the Atlantic is dominated by convergence zones at low (13.9 Hz) frequencies. The higher frequency at 111 Hz is strongly influenced by a natural near-surface ocean duct which leaked energy along the duct, thus obscuring convergence zone peaks over a large increment of the range. The convergence zone spacing at the lower frequency (13.9 Hz) was significantly less than the 111-Hz frequency. This results in 21 zones for the lower frequency occurring in the space of 20 zones at the higher frequency. Propagation of impulsive sources in the channel shows complicated multipath arrival patterns produced by spacial variation in the sound speed. The analysis of impulsive signal experiments provided a complementary picture to the continuous-wave results.

Analysis of the statistics of signals propagating over long distances resulted in significant differences between the 9.8-Hz signal and two higher frequency signals at 110-Hz and 262-Hz. Surprisingly, there was no significant difference in the statistical descriptors of the 110-Hz and 262-Hz signals. A simple empirical model describing the fluctuation of the signal amplitude was obtained by using the linear trends of the moments and the variability about the

trends. Use of these statistical results and a more complicated system of fitting density functions, provides a method of obtaining probability density functions of the signal. The signal correlation distances of 300 to 800 m were found over a range increment of 3,000 km at the two higher frequencies. Of interest is that at the low frequency this correlation distance varied from 750 m to 3200 m, and indicated a strong dependence on range. A simulation was made using a normal-mode model in which signals were generated to match the experimental data. When the simulated data were analyzed in the same manner as the experimental data, gratifyingly good agreement was found in the comparison.

Simulation of interference fields in the channel provides an understanding of the mechanisms that control the transmission loss and the transformation of the simple monochromatic transmitted signal into a set of closely spaced frequency lines at the receiver. The simulation also provides an illustration of the nature of the interference field in range and depth in terms of isointensity contours.

Sensitivity of the field, produced by both time and space changes in the sound-speed environment, was obtained from model calculations. These calculations provide a clear indication of how signals fluctuate in time for a moving source, and how the field is changed as a function of time for a fixed source and changing sound-speed profile. Satisfactory agreement has been found between results of ocean experiments, and both simple and complicated models which define mechanisms and relationships in the interference fields.

These experiments clearly revealed the fascinating relationship between sound in the ocean and factors which control its behavior. Some of these results were occasionally not predicted. However, the results generally conformed to the grand scale of nature's order.

ACOUSTIC APPLICATIONS AND FUTURE RESEARCH

There are two primary reasons for conducting underwater acoustic research in the ocean. The first is to provide information necessary in the design of equipment for detecting and localizing underwater objects, and also for remotely sensing the ocean environment. The

second is to provide knowledge and understanding of the behavior of acoustics in the ocean which are necessary for the efficient operation of these equipments. This section will indicate some of the motivation for conducting underwater acoustic research and will recommend areas of future research.

When this research on ocean-bottom scattering was begun, little was understood about the mechanisms and dynamics of fluctuations of the scattered signals, and about the relationship between this fluctuation and the scattered field. Scattering, or reverberation, originating from the ocean's surface, volume, and bottom, provides the major interference in detecting and localizing objects in the sea. Therefore, it is important to understand the nature of these physical processes. This work provides a significant contribution to the understanding and quantification of acoustic scattering from the ocean bottom.

It is important to extend our knowledge of ocean-bottom scattering to the regions of low acoustic frequencies in order to predict the three-dimensional characteristics of reverberation which is generated at both the bottom interface and within the volume of the ocean bottom. For low-frequency active operation, both monostatic and bistatic, it is required that the propagation in a dispersive channel and the scattering from the bottom, be combined for accurate prediction of the character of a signal from an object, and of the reverberation from the insonified region near the object. Not only is the character of the signal and of the reverberation important, but a knowledge of the signal-to-reverberation ratio is required as well. This knowledge includes the separation of signals reflected from buried objects in the ocean bottom from other acoustic returns.

Another area in which an extension of this research can be fruitful is in providing methods for more precise navigation involving the positioning of a vessel relative to a point over the ocean bottom, enabling the ship to depart and return precisely to that certain point. This capability is also needed for navigation involving submarines operating beneath sea ice. They need the further measure of safety provided by knowledge of the most advantageous direction for emergency surfacing.

One of the most important areas for future research is in the basic understanding of the transitions of the acoustic field reflected from a perfect mirror surface to the field scattered from a rough surface and in the understanding of the consequences that this transition produces.

It is also believed that research concerning probability density functions of the sum of n vectors of arbitrary amplitude and random phase, can provide a unique tool in the analysis of signals which contain a small number of components.

Acoustic propagation in the ocean channel provides the principal means for detecting acoustic sources and underwater targets in the ocean at long ranges. The research thus discussed in this work adds significantly to the understanding of the physical mechanisms and processes involved, particularly in our ability to more readily locate acoustic sources and receivers in the ocean. Acoustic-propagation knowledge also enhances our ability to configure receiving arrays, to choose the best acoustic frequency for an application, and to understand the influence of the ocean environment (temperature, salinity, and depth) on the propagation and structure of acoustic fields in the ocean.

In addition to the urgent need for future research into the behavior of combined low-frequency propagation and scattering, there is a long-term requirement for the remote sensing of the ocean environment itself, (energy, temperature, salinity, and the ways in which they change).

Although this knowledge is of utmost importance for naval activities, it is of even more importance in predicting the weather and the climate, these being the most vital environmental factors of our civilization and directly influencing life on this planet. Currently, the greatest deficiency in long-term weather prediction is the inability to measure and use the influence of the oceans. Satellites are able to provide information concerning the ocean's surface but not the ocean body below the surface. Underwater acoustics provides the only known means of remotely sensing the properties of the ocean volume and bottom. Thus, research should con-

tinue into acquiring knowledge about the behavior of low-frequency acoustic fields, developing the ability to measure the properties of these fields by adding the coincidental measure of particle velocity to that of pressure, and to employing advanced processing such as matched field in a tomographic system. The addition and integration of the acoustic information, with use of the current capabilities of meteorology, satellites, and other sensing systems, should provide significant extensions in the future forecasting of our weather.

Underwater acoustics, specifically with regard to fields of acoustics interference, provides a frontier of scientific challenge, a pursuit rich in implications, and a chance for rewarding endeavor. It is hoped that the future will be witness to more opportunities and the continued efforts of scientists concerning this subject, and to further solutions and applications of underwater acoustics' remaining mysteries.

APPROACH, PROCEDURE, AND RESPONSIBILITY

As indicated in the Preface and Acknowledgments, the experiments contained in this work were carried out by a team of scientists and technicians. This team effort was also true of the analysis of the resulting data. As the leader of this team, I had direct responsibility for the planning, conduct, and coordination of these experiments, the analysis of the data and the reporting of the results. The only exception is the research on Phase Characteristics (a section in Chapter 7) in which I had the indirect responsibility. Care has been taken to reference the portions of this work that have been published by members of the evolving research team, and their contributions are recognized in the Acknowledgments. Also, care has been taken to acknowledge other work that is scientifically related to this research.

The major thrust of this thesis is the integration and interpretation of the mechanisms involved in the behavior of acoustic interference fields. This contribution is completely my own.

Specifically, the research contained in Chapters 1 through 6 involved two major experiments at sea. My responsibility in these experiments was to provide the concepts for the vari-

ous parts of the experiments, plan the conduct of the operations to obtain data to prove or disprove the concepts, and coordinate the conduct of the experiments to ensure the acquisition of quality data. The responsibility of the other members of the team was to prepare and to test the individual pieces of equipment, including the design and construction of a number of the special components, indicated in Appendix A. Incidentally, some of the special instrumentation represented significant advances in electronic digital data recording and calibration technology. It was the responsibility of the team under my supervision to install the instrumentation in the ships, to test the system, and to ensure proper calibration procedures. During the operations it was necessary to monitor the data for quality and completeness. Occasionally, during the operations, because of weather, equipment casualties, or new ideas arising from observations of the data, the operation plans were changed.

On completion of the sea experiments, the first step was the organization of the data into a form for processing and analysis. For example, it was necessary that the signal received on a hydrophone in the three-dimensional experiment (Chapter 4, Appendix 4B) corresponded with the geometric positions of the receiving hydrophone and that the transmitting source be correlated as a function of time. The data was then organized in a time-flow sequence and these sequences were statistically processed and organized in a form to show dependencies on the various parameters. The team provided vital support in the organizational and computational phases of the analysis. Again, it was my responsibility to guide the process to ensure that the analysis supported the initial hypothesis or decided that the hypothesis required alteration to conform to the observed data. Extensive computations were made in order to compare analyzed data with a theoretical hypothesis (for example, the temporal shape of the monostatic scattered signal envelope in Chapter 2). Here again, the team provided support to the research in developing the geometry and carrying out the computations. This was also true for many of the calculations required in modifying the acoustic geometry based on the refractive properties of the medium. Further, in conducting the analysis, I tested the hypotheses or modified them as necessary to comply with the physical observations. It was then necessary

to interpret these hypotheses and observations in terms of physical mechanisms and functional relationships between the various parameters and variables.

On this basis I was responsible for working out the mechanisms and functional relationship of the scattered acoustic signals and the acoustic fields as a function of the dynamics and the acoustic geometry (Chapter 1) and their written descriptions, documenting the research results. This procedure was repeated for the work discussed in each of the scattering chapters (Chapters 1 through 6).

A major part of the research concerning acoustic fields in a dispersive channel was accomplished in three ocean experiments conducted in the 1970s (discussed in Chapter 7). The generic procedure for planning and conducting the experiments was the same as discussed for the scattering experiments, the major difference being the physical scope of the experiments, in which the distances between the acoustic source and the receiver were greater than 1000 nmi. These distances required that the operations be coordinated from a central point with good communications to the acoustic source ship and to each of the acoustic reception and recording points. It also required that the central coordinating point had access to auxiliary information such as weather forecasts for the operating area.

I had direct supervisory responsibility for the research team during these experiments, for the analysis of the data obtained, and for the reporting of all results. I coordinated these experiments from the central point, ensuring the adherence to the operation plans, except when changes were required due to weather equipment casualties, or a change in the nature of the received data.

The material of Chapter 7 is a review and consolidation of information concerning the nature of propagation in a dispersive channel. The section on the statistics of propagated signals is original and represents a significant contribution to the knowledge of signals thus propagated in a channel. The ideas and concepts of Chapter 8 are completely my own, except for computational support in producing the illustrations.

APPENDIX A

PROCEDURES, INSTRUMENTATION, AND ENVIRONMENT FOR THE EXPERIMENTS OF CHAPTERS 1, 2, 3, 4, AND 6

INTRODUCTION

The purpose of this appendix is to describe the instrumentation, procedures, and details of the types of data collected for a series of scattering experiments conducted at sea. These are:

- An experiment to determine the nature of the fluctuation and the field of bottom-scattered signals, plus an experiment in which the transmitted signal was frequency modulated linearly with varying rates to determine the degree of control over the fluctuation rate of the bottom-scattered return.
- A monostatic bottom-scattering experiment to determine the degree of correspondence between measured bottom scattering and an extended isotropic scattering model. The parameters varied were pulse length and beam depression angle. This experiment yielded data for computing bottom-scattering strength as a function of grazing angle (Chapter 2). This experiment also provided the data for the statistic of the probability density function (Chapter 3).
- An experiment to determine the configuration of the acoustic field in three dimensions when scattered from the sea bottom and to determine the fraction of incident power returned to the water or lost in the bottom. The direction of the incident beam on the bottom was the major parameter for this experiment (Chapter 4).
- A monostatic volume-scattering experiment to determine the degree of correspondence between scattering from the ocean volume and that indicated by isotropic scattering theory. Measurements were made for different geometries, which were controlled by combinations of pulse length and direction of the source from the scattering volume.

This experiment also provided data for profiles for volume-scattering strength with depth (Chapter 6).

In the study of acoustic reflection and scattering in the ocean it is convenient to use a submarine as the source platform for the acquisition of experimental data. In fact it is difficult to provide an alternate platform that incorporates the mobility and stability required. By employing directive transducers with good directional control, the same instrumentation can be employed in obtaining data on monostatic scattering from the surface, volume, and bottom. Measurements of bottom-scattered fields in directions other than monostatic require sensors attached to a surface ship or sensors suspended from free-floating buoys, monitored by a surface ship. Free-floating buoys with a radio link to the ship are more convenient as receiving platforms. The major disadvantage of buoys is the necessity of continuously monitoring their positions in the sound field.

Therefore the experiments outlined above were conducted using a submarine as the source platform with buoys and a monitoring ship as receiving platforms. Figure A1 illustrates the geometrical configurations used in measuring the scatter field in three dimensions. In addition to measuring the acoustic pressure of the scattered signal, an acoustic method (involving precise timing of transmissions and receptions, as will be discussed later) also was used for measuring the positions of the receivers in the field.

For experiments involving only monostatic scattering from the bottom, surface, and volume, the submarine source transducer was employed as the receiver, and operations were conducted independent of the surface ship.

INSTRUMENTATION

Instrumentation in the USS *Rockville* (the surface ship) and the USS *Grouper* (the submarine) was divided into two functions: signal data and geometric data. The signal-data function included all the components involved in the measuring bottom-scattered signals. Such components were those that generated, monitored, and projected known levels of signals toward the bottom and received, processed, and displayed the returned signals. The

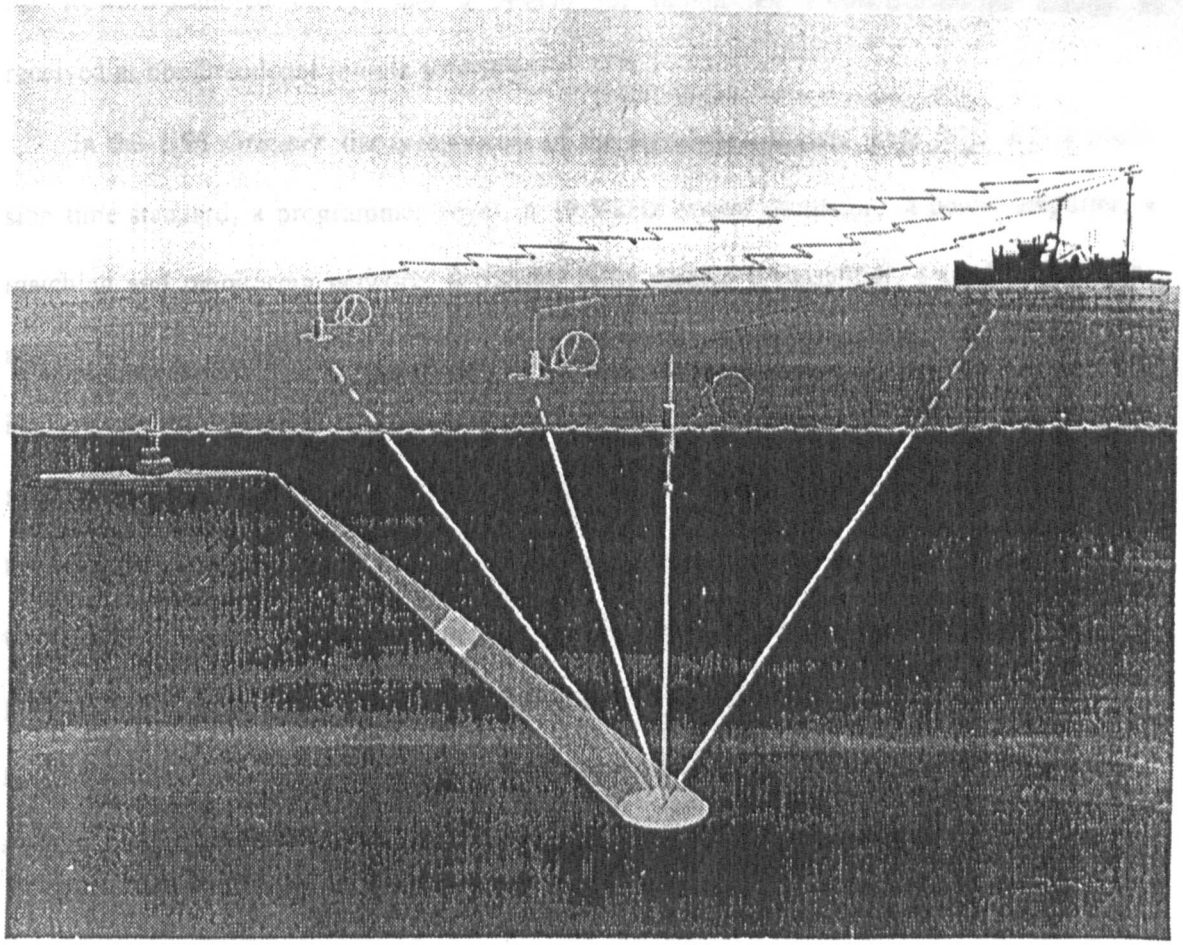

Fig. A1. Platform configuration.

geometric-data function included all the components involved in determining the relative location and orientation of all the signal transducers used in the operation and of the insonified area of the bottom. The components associated with this function were those that maintained accurate time synchronism, generated acoustic ranging pulses, received and processed the pulses, measured time intervals, and digitally recorded the time data, course, bearing, and other appropriate position and environmental data. Some of the components of the total instrumentation system were common to both functions. However, for clarity the particular components will be discussed from the standpoint of contributions to each function.

Signal-Data Instrumentation

The portion of the signal-data instrumentation installed in the USS *Grouper* provided the directional acoustic energy source and the means to measure the backscattered return. The portion installed in the USS *Rockville* provided a directional monitoring system on the ship

for forward-scattered energy and a system for monitoring forward-scattered energy as received at nondirectional remote sonbuoys.

In the USS *Grouper* the components of the signal-data system were (Fig. A2) a precision time standard, a programmer keyer, a 19.5-kHz crystal oscillator, a power amplifier, a matching and monitoring network, a transfer relay receive preamplifier, a tiltable and trainable directional transducer, a receive calibration system, a tunable amplifier, a monitor oscilloscope, an oscillograph strip-film camera, a logarithmic amplifier, and a direct-writing recorder system. In the sea were three special free-floating sonobuoys. In the USS *Rockville* the components were (Fig. A3) three sonobuoy receivers, a tiltable and trainable directional transducer, a transducer preamplifier, a receive calibration system, four tuned amplifiers, a precision time standard, a monitor oscilloscope, a two-beam oscillograph strip-film camera, four logarithmic amplifiers, a direct-writing recorder system, and a recording time-control system.

The system functioned as follows. In the USS *Grouper* the precision time standard provided the programmer with accurate 10-sec reset pulses and a 1000-Hz time base. The programmer, a digital multichannel preset counter, generated keying pulses of determined interval and duration which gated the output of the 19.5-kHz crystal oscillator into the power amplifier. To achieve maximum acoustic power, the output of the power amplifier was matched to the impedance characteristics of a remotely controlled tiltable and trainable directional transducer by a matching network. Associated with the matching network was an output monitoring system to permit measurement of the power-amplifier output amplitude in order to establish known acoustic source levels from the calibrated directional transducer. For backscattered intensity measurements in the *Grouper*, the same directional transducer that was used for transmitting was used for receiving. A transfer relay, controlled by an auxiliary output of the programmer, transfered the transducer connections from the power-amplifier output to the input of the receive preamplifier at the end of the transmit pulse and remained in this condition until shortly before the next transmit pulse. The signal from the preamplifier

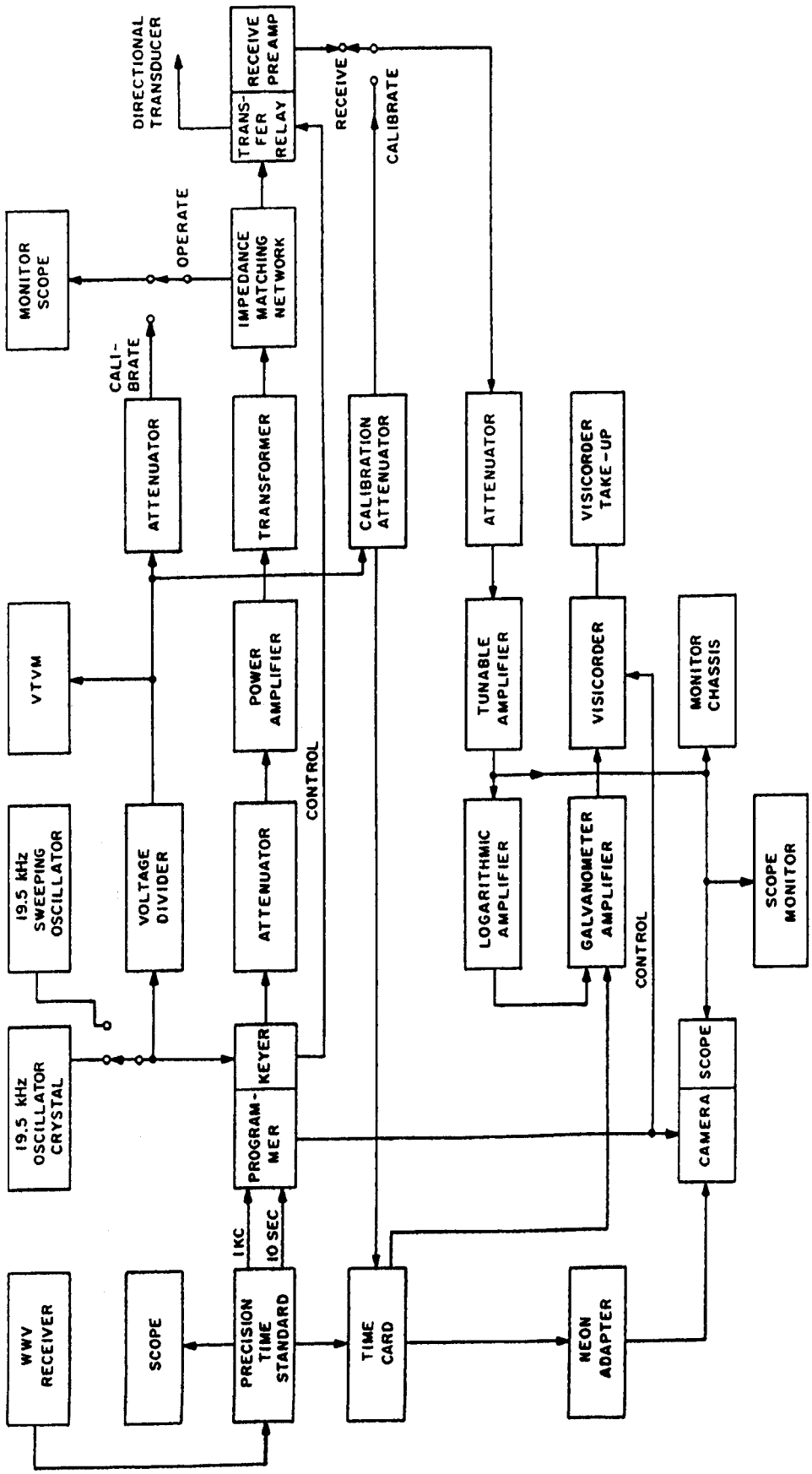

Fig. A2. Signal instrumentation in *Grouper*.

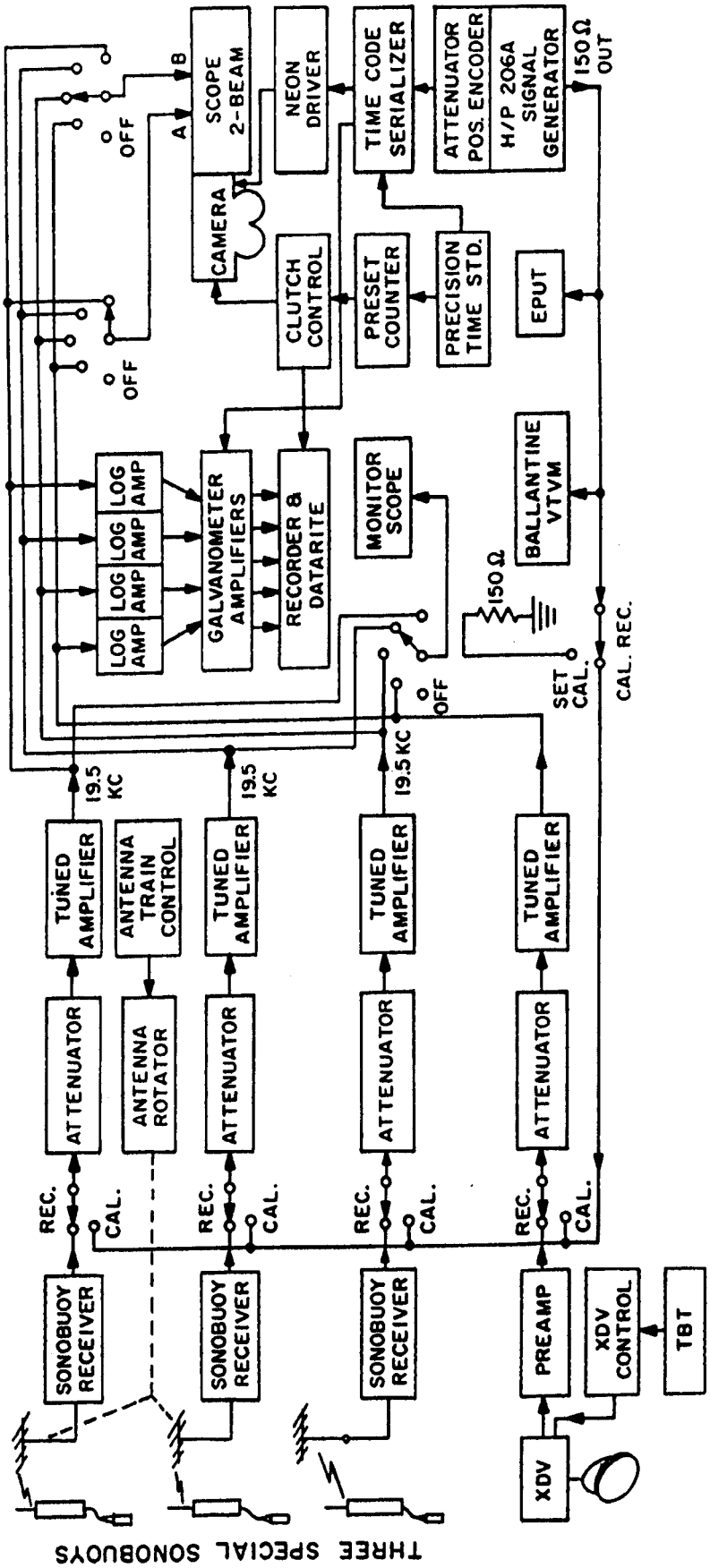

Fig. A3. Signal instrumentation in *Rockville*.

was further amplified in a tunable amplifier for presentation to the various display and recording instruments. Incorporated in the receiving system were attenuators and a calibrated test signal (obtained from the 19.5-kHz crystal oscillator) that could be switched into the system in order to accurately set and measure the gain of the receiving and recording instruments. By using these gain measurements along with the known calibration of the directional transducer, the levels of the received acoustic signals were measured.

The output of the tuned amplifier was fed to a monitor oscilloscope, where amplitudes of the backscattered signal were observed. In addition, the signal was fed to a linear oscilloscope display (recorded by a continuously running 35-mm oscillograph-recording camera) and to a logarithmic amplifier feeding one channel of a Visicorder direct-recording oscillograph. The logarithmic amplifier demodulated the signals and compressed the amplitudes, permitting measurement of the signal over a 60-dB dynamic range.

Also in the submarine was a motor-driven oscillator, mechanically swept over a narrow range of frequencies centered at 19.5 kHz. This oscillator could be substituted for the 19.5-kHz crystal oscillator. The rate of change in the transmitted frequency was adjusted to values calculated from the problem geometry and velocities, so as to control the effects of the submarine's motion on the instantaneous frequency differences across the insonified area of the bottom.

Auxiliary outputs of the precision time standard were serially coded to provided a continuous indication of time on the edge of the film and Visicorder records, in the form of coded pulse trains. Auxiliary outputs of the programmer started and stopped the recording system in order to eliminate wasted recording medium during dead time.

Floating freely in the sea were three special radio-sonobuoys, each consisting of a ceramic cavity-type hydrophone suspended about 4.5 m below the surface with the axis of its broad major lobe directed downward, a low-noise amplifier modulating a VHF-FM transmitter for transmission of the acoustic signals to the monitor vessel, and a long-service-life battery. All components except the hydrophone were housed in a watertight, buoyant,

stable cylindrical container. Each of the buoys was tuned to a different VHF transmitting frequency, to allow easy separation and identification of the forward-scattered signals as seen from each buoy. The buoys were equipped with means to enhance visual identification and to facilitate recovery.

In the USS *Rockville* the VHF signals from the sonobuoys were received by three precision FM receivers. The outputs of the receivers were reproductions of the signals existing at the output of the sonobuoy hydrophones but at a considerably higher level. Simultaneously the forward-scattered signal was also received at the *Rockville* by a tiltable and trainable directional transducer, set a known tilt and trained in the direction of the bottom area insonified by the transmitting vessel. The output of the transducer was amplified in a preamplifier.

The outputs of the VHF receivers and the transducer preamplifier went to four tuned amplifiers, preceded by attenuators. Switching arrangements were provided at the inputs to the attenuators to permit calibrated test signals to be substituted for the incoming signals, in order to set and measure the gain of the receiving and recording systems. The gains thus determined, along with the known calibrations of the sonobuoy/receiver combinations and of the directional transducer/preamplifier combination, enabled the actual levels of the received acoustic signals to be obtained. The outputs of the tuned amplifiers were fed to four logarithmic amplifiers that, through a multichannel galvanometer driver, recorded the signal envelope amplitudes on a multiple oscillographic recording system. The tuned-amplifier outputs also fed a monitor oscilloscope and a two-beam cathode-ray strip-film recording system. Selector switches were provided for selecting the desired tuned amplifier output for display on the monitor scope and for recording on either of the two beams of the strip-film recording system. Auxiliary digital outputs of the precision time standard were serialized for recording a coded time record on the recording paper and the strip film.

Geometric-Data Instrumentation

In the USS *Grouper* the components of the geometric-data instrumentation were (Fig. A4) a precision time standard, a sonar keyer unit, a submarine sonar transmitter, a sonar

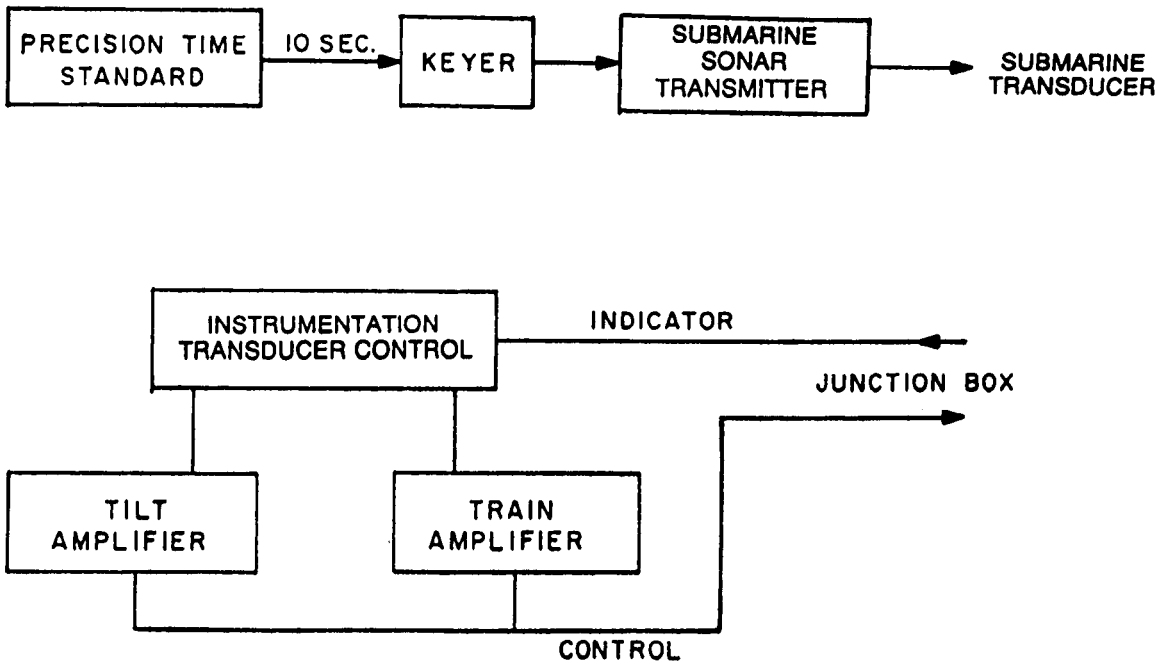

Fig. A4. Geometry instrumentation in *Grouper*.

transducer, a gyrocompass, a directional transducer tilt-train control system, a periscope, and a depth gauge. In the sea were three special free-floating sonobuoys. In the USS *Rockville* the components were (Fig. A5) a precision time standard, a sonar keyer unit, a sonar transmitter, a sonar transducer, an omnidirectional transducer, a transducer preamplifier, three sonobuoy receivers, four dual-frequency amplifiers, four dual-channel digital time-interval meters (storage units), a data control unit, a relay code converter, a tape punch, a digital printer, a time-code converter, a directional transducer tilt-train control system, a gyrocompass, an optical bearing transmission system, and a precision depth recorder.

The geometry (Fig. A6) was determined as follows. All of the station points (submarine, ship, and sonobuoys) established the vertices of a series of triangles whose sides were measured by the propagation times from submarine to ship, submarine to buoys, and ship to buoys. These triangles were geographically oriented by measuring the bearing of one of the sides and using that as a base line. Generally the line between the ship and the submarine was used as the base line for all the triangles. Knowledge of the direction of the base line, the lengths of the sides of all the triangles, the headings of the two vessels, the depth of the submarine, the depth of the water, the orientation of the directional transducers on the ship

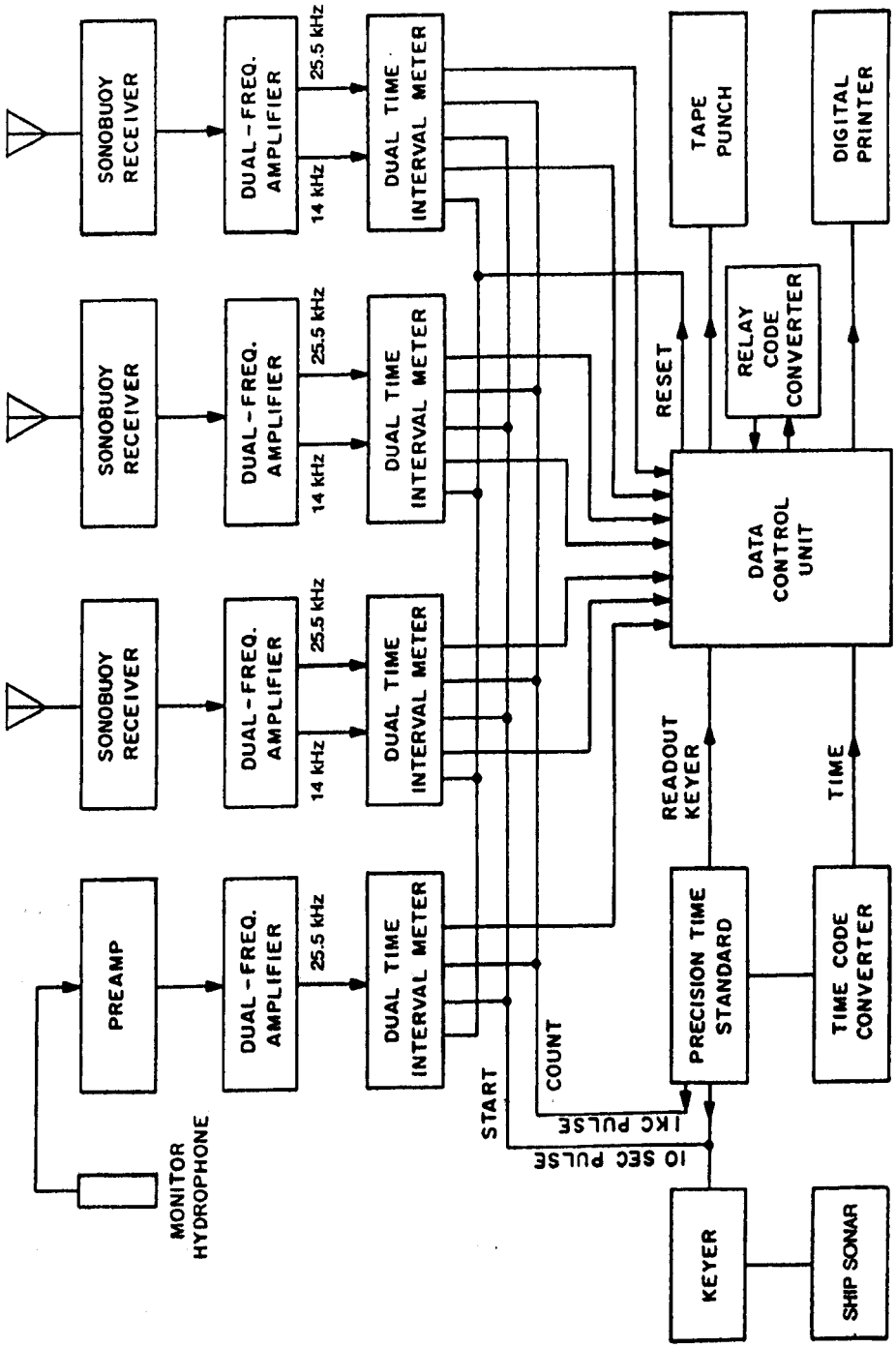

Fig. A5. Geometry instrumentation in *Rockville*.

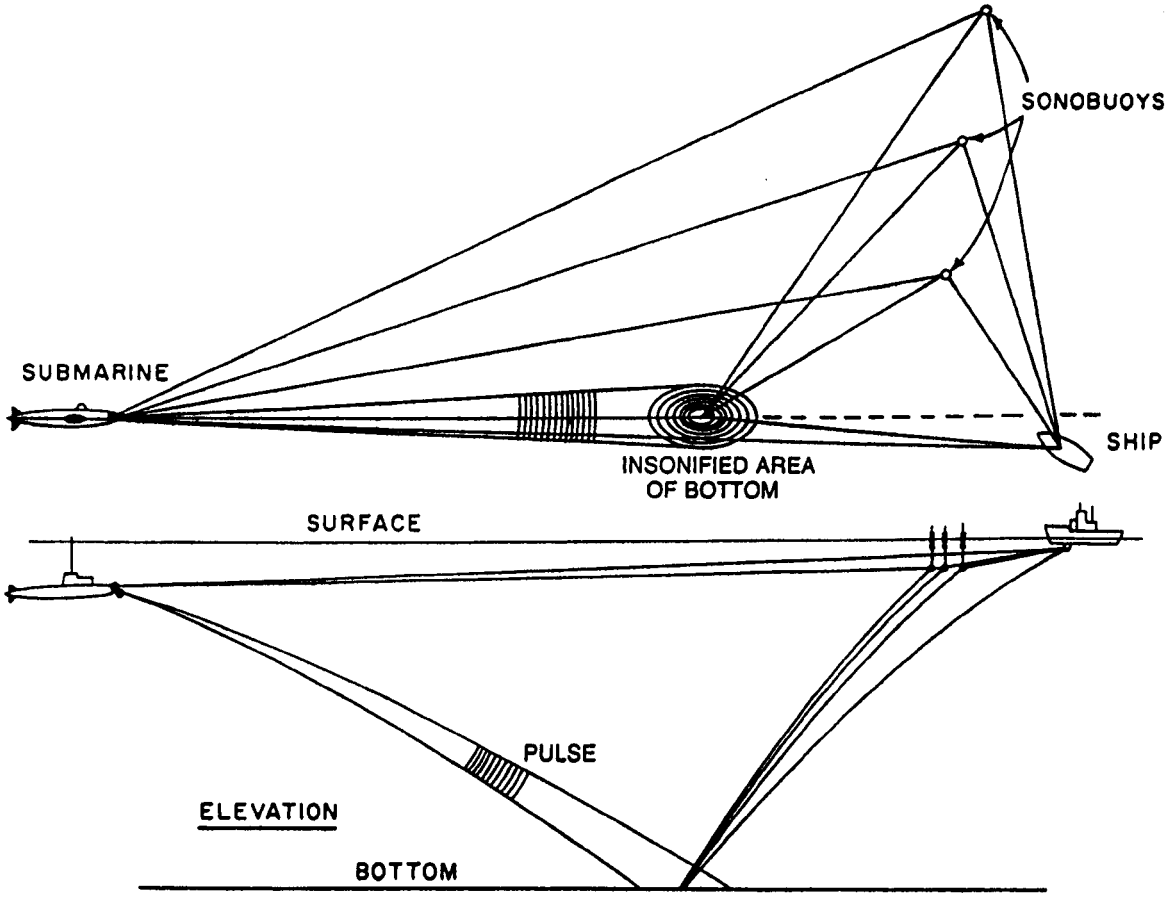

Fig. A6. Experiment geometry.

and the submarine, and the pertinent dimensions of the vessels were used to establish a complete picture of the geometry of the problem for every transmission of the signal.

The precision time standards on the *Grouper* and *Rockville* were synchronized with Station WWV, to at least 1/10 msec accuracy. By this means all sonar transmissions on both vessels were made to occur simultaneously every 10 sec, along with the start of the digital time-interval meters. The time-interval meters were scaled to count millisecond pulses from the precision time standard. Seven of the eight channels of the four dual-channel receivers and the four dual-channel time-interval meters were used. One of the receiver channels amplified and selected the sonar signal transmitted from the submarine, as received by the ship-mounted transducer, and, on receipt of such a pulse, stopped the count of its associated time-interval meter. The count represented the propagation time, in milliseconds, for direct sound transmission from the submarine to the ship and thereby, when multiplied by the sound speed, the range from the submarine to the ship. Each of the remaining three dual-channel

receivers was connected to each of the three sonobuoys receivers. In each of the dual-channel receivers one of the channels was tuned to the submarine's sonar transmission frequency while the other was tuned to the ship's sonar transmission frequency. The output of each channel was connected to an associated time-interval-meter channel. Thus, when a sonobuoy receives a pulse from the submarine's sonar or the ship's sonar, the signal was received by the buoy and telemetered by an FM radio link to the ship, where it was received, amplified, and selected to stop the count of the time-interval-meter channel associated with that buoy and received sonar frequency. As already described, the range from the submarine to each of the three buoys, as well as the range from the ship to each of the three buoys, was measured. Concurrently, other data such as the bearing from the ship to the submarine, the ship's course and speed, the submarine's course and speed and depth, the water depth, the sound propagation speed, the transducer tilt and train angles, the run number, and other numerical information were noted and set in on switches on the data control unit. The binary-coded-decimal outputs of the decade counting units in the time-interval units, as well as the outputs of the hours, minutes, and seconds decade counting units of the precision time standard, were brought into the data control unit. Within the unit were stepping switches which scanned all the data, digit by digit, and sent the impulses derived from the data to the tape punch. Interposed between the stepping-switch arms and the punch magnets was a relay unit which isolated the inductive load of the punch magnets from the switch contacts, as well as converting the binary-coded-decimal format of the decade counting units in the time-interval meters to the format required on the paper tape for direct entry into a computer. Functions such as carriage-return, tabular, space, and stop codes were incorporated in the line format by permanently wiring fixed voltages into selected points in the stepping switches. The stepping switches were synchronized with the tape punch by a contact on the punch shaft that actuated the stepping-switch magnet after each punching operation. The data-input switches on the front of the data control unit were wired to fixed voltages to produce the same voltages as the outputs of the decade counting units in the time-interval meters. Because the format and voltages from the precision time standard were different, a converter consisting of a diode matrix

and amplifier was interposed between the time standard and the data control unit to provide the time input in the same code and voltage levels as all the other inputs. The operation of the stepping switches was initiated by a signal derived from the precision time standard 6 sec after the initiation of the sound transmission. On completion of the cycling of the stepping relays and the punching of the data on paper tape, the time-interval meters were reset to zero, and the system was ready for the next sound transmission.

PROCEDURE

Calibration of Submarine Instrumentation

Submarine instrumentation was calibrated after adjusting the output of the master 19.5-kHz oscillator to a reference level and then switching that output through a calibration attenuator into the receiver and recording system. The calibration attenuator was switched through its range to provide simulated signals of accurately determined amplitude over the dynamic range of the system. These calibration signals were recorded to provide an accurate reference on the recording medium of levels against which the acoustic signals received during the data runs could be accurately compared. After that calibration was completed, the receiver input was switched back to the transducer-preamplifier output, for acoustic signal measurement. The acoustic signal was calibrated by measuring the transducer current during the transmit pulse by a cathode-ray oscilloscope connected across a series resistor in the transducer circuit. This remained connected into the transducer circuit during operation, to monitor the transmitted level and the waveform. The display on the oscilloscope was calibrated by comparison of the amplitude during operation with that obtained by occasionally switching the oscilloscope input to the output of an attenuator fed by the standardized master 19.5-kHz oscillator output.

Calibration of Ship-Mounted Instrumentation

Ship-mounted instrumentation was calibrated by switching the inputs of the four tuned amplifiers from the outputs of the three sonobuoy receivers and from the output of the special

instrumentation sonar receiving preamplifier to the output of the calibration signal generator, which provides simulated signals of various, accurately determined amplitudes, over the dynamic range of the system. The calibration signals were recorded to provide reference levels on the record against which the signals received during the data runs were compared for accurate measurements. On completion of the calibration, the inputs to the tuned amplifiers were then switched back to their appropriate signal sources, for reception and recording of acoustic signals.

Calibration of Sonobuoy Systems

Sonobuoy systems were calibrated before the sonobuoys were launched and after they were recovered. Each sonobuoy was opened, battery power was applied to the circuitry, and, when gain and output had reached a stable level, the hydrophone was disconnected, and a battery-powered signal generator was attached to the signal input. The output of the signal generator was stepped through the dynamic range of the sonobuoy's receiver/recording system, and the signal-generator levels were noted on the recorder chart opposite the corresponding recorded levels as well as in the logbook. The signal generator was then disconnected from the sonobuoy, and the hydrophone was reconnected. When a sonobuoy was calibrated before launch, it was kept powered and was closed and sealed. When a sonobuoy was calibrated after recovery, the power was turned off after the calibration. In each case the plate and heater voltages were logged for each sonobuoy, to account for changes in calibration and to estimate the remaining battery life. When the plate or heater voltage dropped below a given level, the battery was replaced.

Positioning of the Ship, Submarine, and Sonobuoys

The buoys were prepared for launching by turning on their power, calibrating them, sealing them, and attaching marker floats with a short length of line. A marker float was constructed by taping together three hula hoops (rings of polyethylene tubing that were about 8 cm in diameter) to form a roughly trihedral structure that would float on the water with most of the structure above the surface. Each of the sonobuoys launched was identified by a

marker of a distinctive color. The sonobuoys were dropped at intervals of approximately 450 m, or multiples thereof, as shown in Figs. A7a and A7b, depending on the type of runs to be used for that particular day. After dropping the sonobuoys, the ship then took up its assigned position relative to the buoy pattern. Because the sonobuoys plus their markers were structurally almost identical, wind and current would cause the entire buoy pattern to drift without substantially altering the locations of the buoys relative to each other. However, the ship showed a marked tendency to drift and to swing around in the wind. Therefore the ship had to be periodically repositioned.

The submarine positioned itself, relative to the ship, at the range and bearing specified for the particular type of run. After communication and time checks with the ship the submarine would submerge to snorkel depth and assume a heading to pass the ship as close aboard as safety would permit. The ship would remain stationary and attempt to maintain a heading reciprocal to the submarine's course, while the bearing optical-tracking operator would optically acquire and track the submarine's masts, measuring the reference bearing for system geometry. The submarine would then make its run in accordance with the dictates of the run specifications.

At the end of the day's operations the ship would maneuver to retrieve the sonobuoys by using grapnels cast into the marker floats, first bringing a marker aboard and then hauling the sonobuoys aboard by means of the attached line. The sonobuoys were rinsed off with fresh water, dried, opened, and calibrated. Then the batteries were disconnected, and the sonobuoys were closed and stowed for the night.

Run Calibration

Run signals were calibrated periodically during the day's operation, at the beginning and end of each run. Calibration signals were switched into the receiving system aboard the ship and the submarine, in place of the transducers output or the sonobuoy radio/receiver output. The calibrate attenuators were stepped through the full range of voltages, and the step levels on the oscillograph records were marked in pencil with the corresponding calibrate attenuator

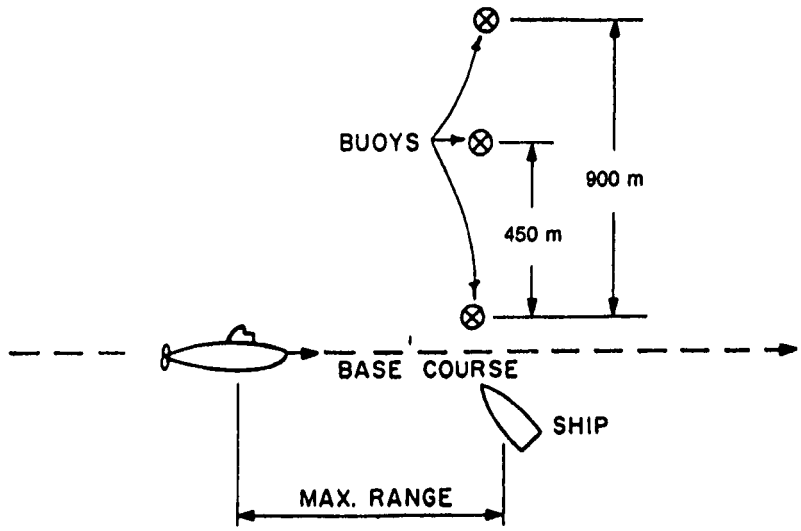

Fig. A7(a). Run type A.

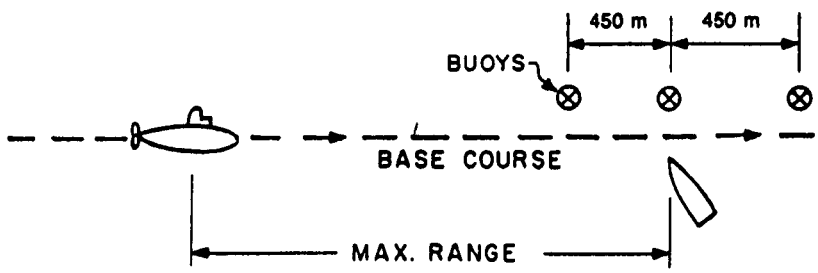

Fig. A7(b). Run type B.

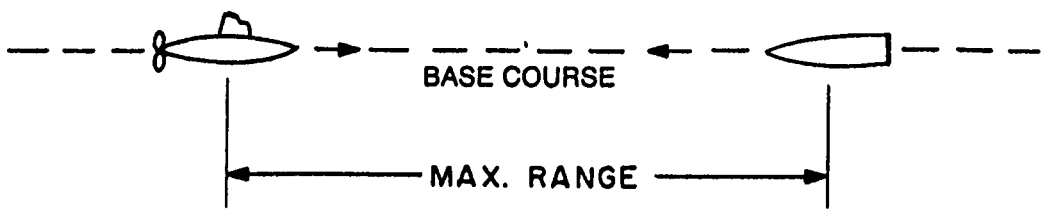

Fig. A7(c). Run type C.

Fig. A7(d). Run type D.

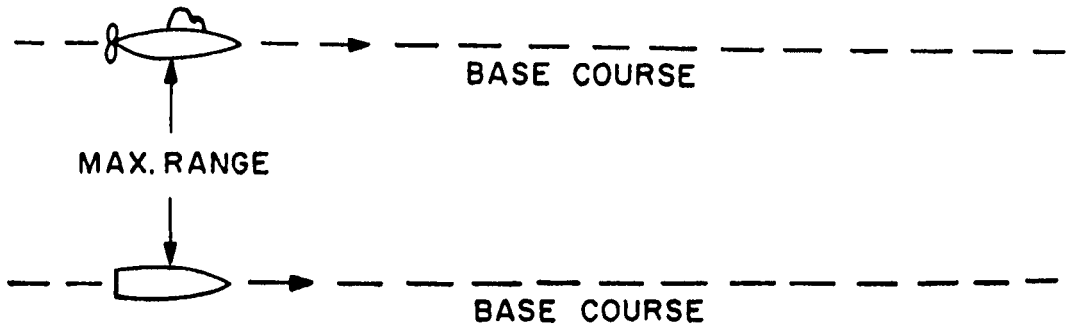

Fig. A7(e). Run type E.

settings, thus providing scales of levels on the record against which the received signal levels would be measured. This procedure also compensated for nonlinearities in the receiving and recording systems. The times and attenuator settings were also noted in the operation logbooks. The transmissions were calibrated by measuring the amplitude of the transmitted pulse against a calibrate signal on the graticule of the transmit monitor oscilloscope. After the transmissions and signals were calibrated, all transmit and receive circuits were returned to their operating configuration.

Run Data Recording

The recording of run data began after all the vessels and buoys had been positioned according to the particular specified category of runs, as shown in Fig. A7. When data were being recorded, all recording systems were running in the operate mode, and the submarine was at the ordered depth, course and speed, transmitting sonar pulses at the specified pulse length and depression angle. All components of the precision position-determining system were in operation, including the sonar transmissions aboard the submarine and the sonar transmissions aboard the ship. Personnel aboard the submarine and ship were monitoring the oscillographic recordings, prepared to adjust the various receiver gains as necessary to maintain the received levels roughly in the middle of the dynamic range of the recording system. Changes in attenuator settings were noted on the oscillograph records in pencil and also recorded in the operation logbooks. The man on the target-bearing transmitter tracked the

masts of the submarine throughout the run. The bearing was transmitted to the sonar laboratory and was read from the bearing indicator by the digital-data-panel operator, who entered the value on the data-panel switches as well as entering other data such as the ship's heading, the water depth, the train and tilt of the ship's sonar transducer, the submarine's ordered course, speed, and depth, the tilt of the submarine's sonar transducer, the water temperature, and the run number and designation. Another operator monitored the performance and operation of the seven start-stop time-interval counters, to ensure accurate geometric range information. It was necessary to reorient the ship at times during the longer runs so that the optical-bearing-tracker operator could continue optically tracking the submarine's bearing and the ship's sonar could continue maintaining sound paths to the buoys. The submarine took a heading directly toward the ship at the beginning of the run, adjusting its course slightly to avoid collision, passing close to the ship. At the end of the run the submarine opened out again to be in position for the next run, while the ship maneuvered to reestablish its position and heading relative to the buoy array. The punched-tape output of the digital data-recording system was loaded into the reader of a flexowriter on board ship, for duplicating the tape record as well as initially looking at the digital record to determine if the data just taken were valid.

Time Checks

Time checks were made at the beginning and end of a day's operations. Rough time checks were made by voice radio marks between ship and submarine for synchronizing bridge, CIC, conning-tower, and control clocks aboard the ship and the submarine for coordination of maneuvers. The precision digital clocks aboard the ship and the submarine were synchronized by tuning radio receivers to WWV and displaying the radio ticks on oscilloscope traces, whose sweeps were synchronized by the 0.1-msec outputs of the precision digital clocks. The clocks were advanced or retarded as necessary.

OPERATING AREAS

Most of the data for the experiments were obtained in the Blake Plateau area about 150 nmi east of Jacksonville, Florida (Fig. A8). The area was chosen because of the relative flatness of the bottom over an extended area, the intermediate water depth (consistent with the instrumentation being employed), and the uniformity of the bottom material (a calcareous sediment). The choice of the area was based on considerable geophysical exploration in its vicinity (Hersey et al., 1959, and Ericson et al., 1961). A second area, used primarily for volume-scattering experiments, was about 90 nmi southeast of Cape Hatteras (Fig. A8).

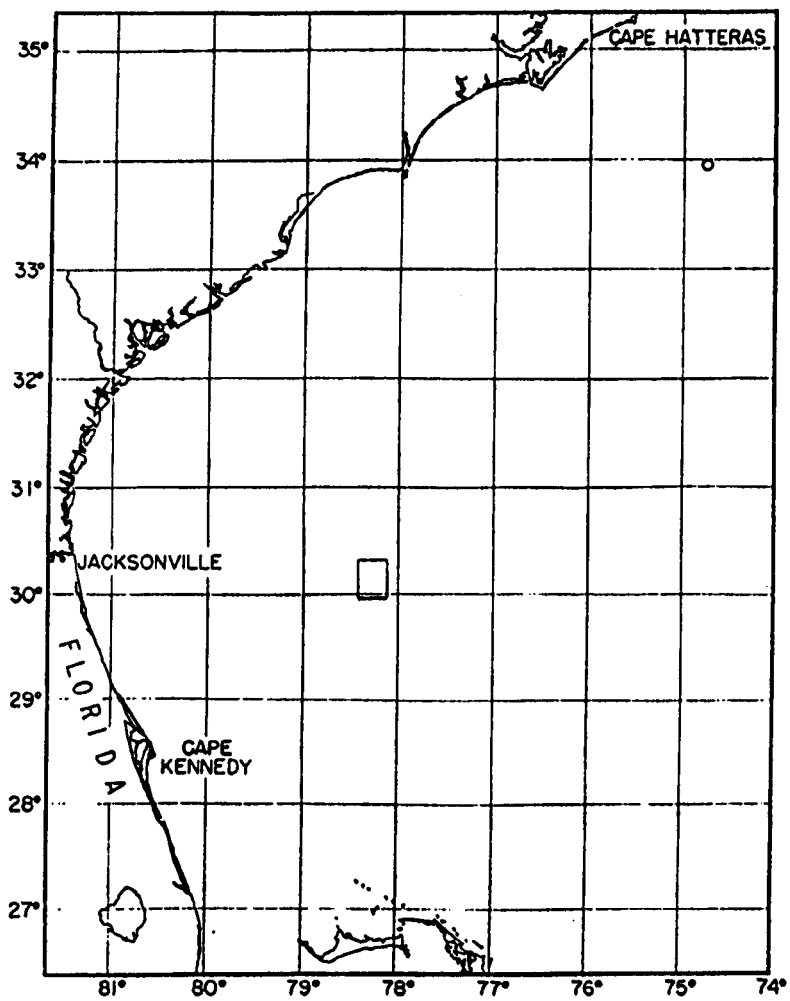

Fig. A8. Operating areas: Blake Plateau (rectangle) and Hatteras (small circle).

PROPAGATION IN THE BLAKE PLATEAU AREA

To help plan the experiments, a series of ray computations were made prior to the experiments at sea. These computations were based on data obtained from the Naval Oceanographic Office for the general area and the time of year. The ray computations assisted in positioning the buoys, in determining the limiting angle of the scattered bottom returns received at the surface, in determining the amount of refractive bending to be encountered, etc.

Environmental Data

Upon completion of the experiments a more precise set of ray computations were made for use in the analysis. These computations were based on the environmental data obtained during the experiments and on hydrographic data for the area and time of year. The environmental data consisted primarily of bathythermograms (BTs). Twenty-three 275-m BTs were taken. An analysis of the BTs indicated that the profile was sufficiently stable that a single composite temperature profile could be used for all of the experiments. The maximum standard deviation encountered was 0.8°C at a depth of 40 m. The average BT temperatures were combined with temperatures obtained from the Oceanographic Office for the greater depths to provide the profile of Fig. A9a.

A typical set of salinity data for the area supplied by the Oceanographic Office was used. The salinity-versus-depth profile is illustrated in Fig. A9b.

The sound speed was computed by following MacKenzie (1960), except DelGrosso's (1952) constant for the first term was used. Figure A9c illustrates the resulting sound-speed profile.

Ray Computations

The sound-speed profile was broken into a series of linear increments of constant gradient for the ray computations. The following propagational factors were computed (Fig. A10). The ray angle (in degrees) with respect to the horizontal for an increment i is

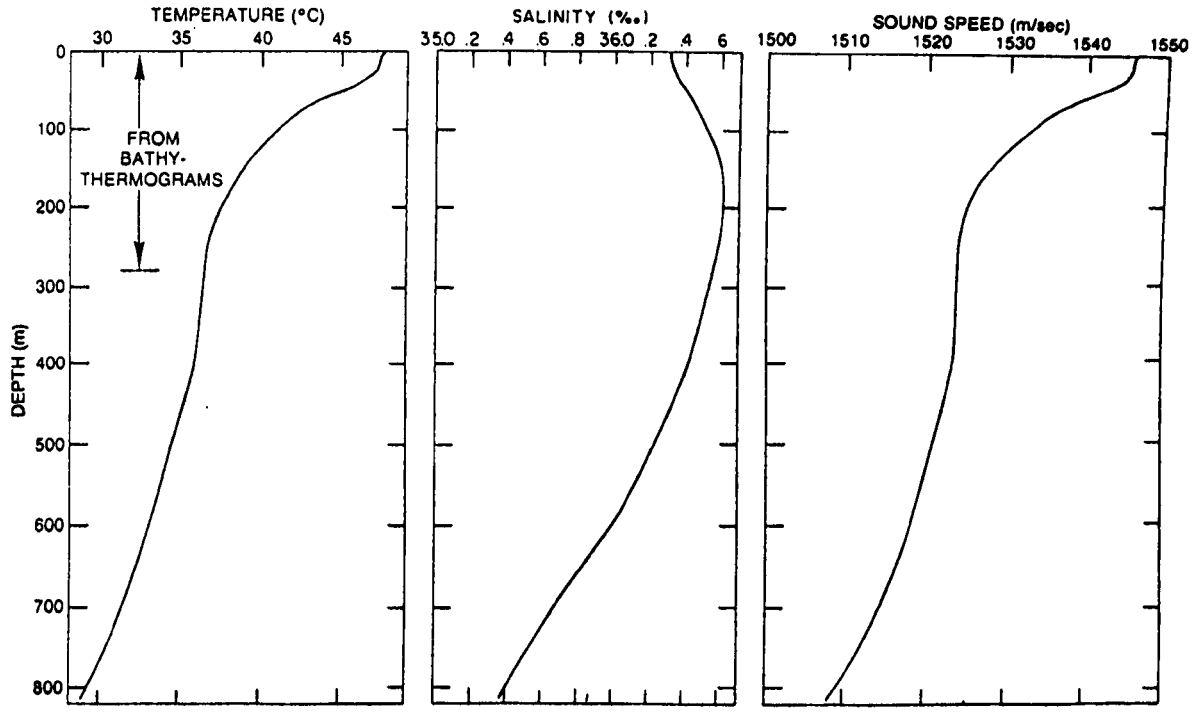

(a). Temperature profile. (b). Salinity profile. (c). Sound-speed profile.

Fig. A9. Environmental profiles.

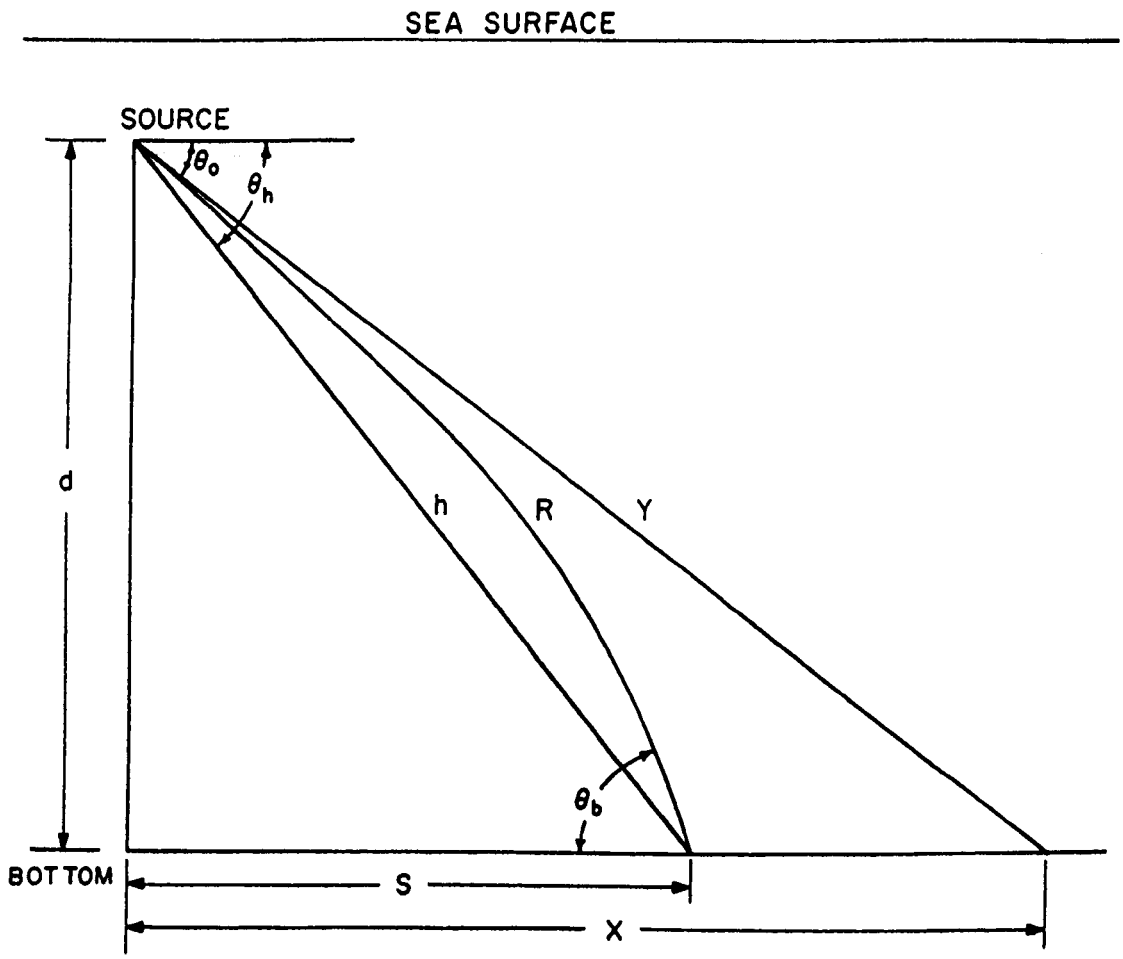

Fig. A10. Ray geometry.

$$\theta_i = \cos^{-1}\left[\frac{C_i}{C_v}\right], \tag{A1}$$

where C_i is the sound speed at depth d_i and C_v is the vertex velocity, which is $C_0/\cos\theta_0$. The ray path length R is

$$R = C_v \sum \frac{1}{g_i}(\theta_m - \theta_n), \tag{A2}$$

where θ_m is the entrance angle to the ith layer (degrees), θ_n is the exit angle from th ith layer (degrees), and g_i is the gradient (1/sec). The horizontal distance of the ray is

$$S = C_v \sum 2\left[\cos\left[\frac{\theta_m + \theta_n}{2}\right]\sin\left[\frac{\theta_m - \theta_n}{2}\right]\right]. \tag{A3}$$

The travel time over the ray path (seconds) is

$$t = \sum \frac{1}{2} \ln \frac{(1 - \sin\theta_m \sin\theta_n) + (\sin\theta_m - \sin\theta_n)}{(1 - \sin\theta_m \sin\theta_n) - (\sin\theta_m - \sin\theta_n)}. \tag{A4}$$

The distance over the nonrefractive ray path is

$$Y = d \csc\theta_0, \tag{A5}$$

where d is depth of water below the source. The horizontal distance of the nonrefractive ray path is

$$X = d \cot\theta_0. \tag{A6}$$

The distance between the source and the point of intercept of the refractive ray on the bottom is

$$h = \sqrt{d^2 + S^2}, \tag{A7}$$

with $\theta_h = \tan^{-1}\frac{d}{S}$. The spreading loss over the downward path (ratio) is

$$N = -S\frac{\sin\theta_b}{\cos\theta_0}\frac{dS}{d\theta_0}, \tag{A8}$$

where

$$\frac{dS}{d\theta_0} = \sum \frac{C_v}{g_i} \tan\theta_0 \left[\frac{1}{\sin\theta_m} - \frac{1}{\sin\theta_n}\right].$$

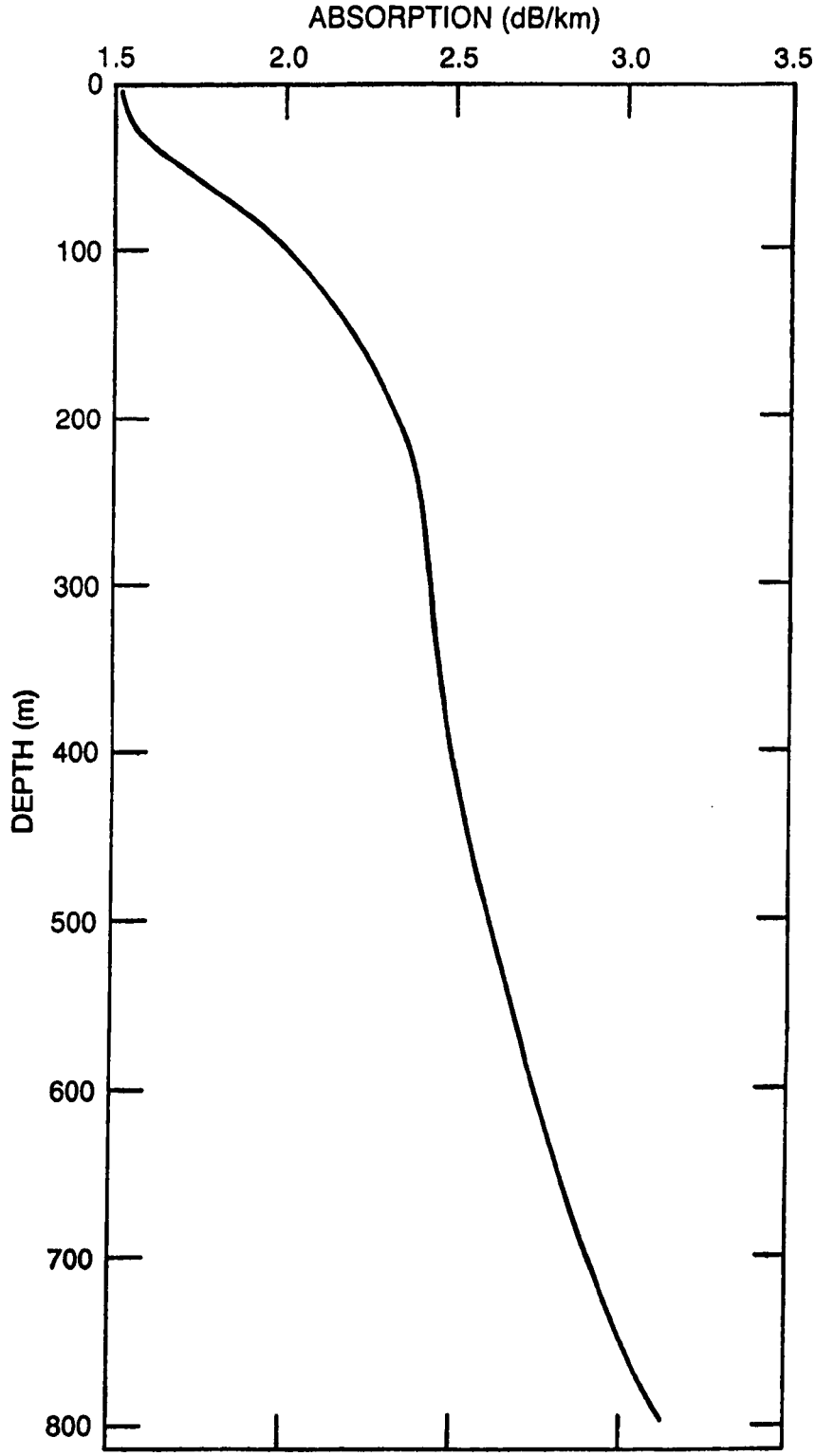

Fig. A11. Absorption profile.

The spreading-loss exponent over the downward path is

$$\gamma_d = \frac{10 \log N}{10 \log R} . \tag{A9}$$

The spreading-loss exponent over the upward path is

$$\gamma_u = \gamma_d + \frac{20 \log C_0 - 20 \log C_b}{10 \log R} . \tag{A10}$$

A set of computations were made, for each depth of source and receiver used in the experiments, as a function of depression angle θ_0, with θ_0 incremented in 0.5° steps.

Absorption

The sound absorption coefficient for the experiments was obtained by computing the absorption as a function of depth, making a numerical integration over the path, and then dividing by the path length to obtain the average coefficient. The values of temperature and salinity of Fig. A9a and A9b were used to obtain absorption values from Del Grosso's (1954) table. These values were modified by the pressure term of $1 - 0.000654\ P$ (where P is in kg/cm^2) following Shulkin and Marsh (1962). Figure A11 illustrates the resulting profile of absorption versus depth. An examination of the absorption constant for paths $15° < \theta_0 < 90°$ resulted in a change of absorption of 2.263 to 2.273 dB/km. The variation was sufficiently small that a signal value of 2.267 dB/km was employed for the entire analysis.

REFERENCES

1. V.A. DelGrosso, "The Velocity of Sound in Sea Water at Zero Depth," NRL Rept. 4002, 1952.
2. V.A. DelGrosso, "Dependence of Sound Absorption on Concentration, Frequency, and Temperature in $MgSO_4$ Solutions Equivalent to Sea Water-Graphs from Calculations Based on a Review," NRL Rept. 4279, 1954.
3. D.B. Ericson, M. Ewing, G. Wollin, and B. Herzen, "Atlantic Deep-Sea Sediment Cores," Geol. Soc. Am. Bull. **72**, 193-286 (1961).

4. J.B. Hersey, E.T. Bunce, R.F. Wyrick, and F.T. Dietz, "Geophysical Investigation of the Continental Margin Between Cape Henry, Virginia, and Jacksonville, Florida," Geol. Soc. Am. Bull. **70**, 437-466 (1959).

5. K.V. Mackenzie, "Formulas for the Computation of Sound Speed in Sea Water," J. Acoust. Soc. Am. **32**, 100-104 (1960).

6. M. Schulkin and H.W. Marsh, "Sound Absorption in Sea Water," J Acoust. Soc. Am. **34**, 864-865 (1962).

Glossary

Bistatic scattering	Scattering from a boundary or volume to any point or direction in the field, with the source and receiver not coincident.
Monostatic scattering	Scattering from a boundary or volume to the point of transmission, with the source and receiver coincident.
Multistatistic scattering	Scattering from a boundary or volume in a number of directions.
BT	Bathythermograph, which measures temperature as a function of depth.
XBT	Expendable bathythermograph.
AXBT	Air-deployed expendable bathythermograph.
CIC	Combat Information Center.
CZ	Converence zone, a region of high intensity in the sound field, these regions being spaced approximately 35 nmi apart in the Atlantic.
PDR	Precision depth recorder.
RR	Refracted-refracted rays, rays trapped in a sound channel.
SOFAR channel	Deep sound channel in the ocean.
Sonobuoy	An air- or ship-deployed buoy with a suspended acoustic transducer for reception, amplifiers, and VHF-FM (very high frequency-frequency modulated) radio transmitter and antenna. Recepetion is made in aircraft or on board ships with HF-FM receivers.
TL	Transmission loss.

TABLE OF ILLUSTRATIONS

Chapter 1

Chapter 2

Fig. 2 Geometry for monostatic scattering with a directive source.

Fig. 3. Square of the source/receiver beam function at 19.5 kHz.

Fig. 4. Normalized incident power as a function of time for various pulse lengths with the depression angle β constant (45°) and with d = 0.9 km (1000 yards) and C = 1460 m/sec (1600 yards/sec).

Fig. 5. Normalized incident power as a function of time for various depression angles with the pulse length τ constant (0.01 sec) and with d = 0.9 km and C = 1460 m/sec.

Fig. 6. Envelope of a single return and the mean envelope of the bottom scattered signal as a function of time (Blake Plateau, Sept. 1961; frequency 19.5 Hz; depression angle 90°; pulse length 0.910 sec; depth 805 m, and number of echoes 231).

Fig. 7. Measured bottom scattered signals and the predicted envelope as a function of time (frequency 19.5 kHz, pulse length 0.817 sec, depression angle 70°, depth 805 m, echoes averaged 99).

Fig. 8. Measured bottom scattered signals and the predicted envelope as a function of time (frequency 19.5 kHz, pulse length 0.060 sec, depression angle 70°, depth 805 m, echoes averaged 35).

Fig. 9. Measured bottom scattered signals and the predicted envelope as a function of time (frequency 19.5 kHz, pulse length 0.411 sec, depression angle 45°, depth 805 m, echoes averaged 89).

Fig. 10. Measured bottom scattered signals and the predicted envelope as a function of time (frequency 19.5 kHz, pulse length 0.050 sec, depression angle 45°, depth 805 m, echoes averaged 34).

Fig. 11. Measured bottom scattered signals and the predicted envelope as a function of time (frequency 19.5 kHz, pulse length 0.015 sec, depression angle, 45°, depth 805 m, echoes averaged 12).

Fig. 12. Measured bottom scattered signals and the predicted envelope as a function of time. (frequency 19.5 KHz, pulse length .510 sec, depression angle 30°, depth 805m, echoes averaged 84)

Fig. 13. Monostatic scattering strength curve for 19.5 kHz determined from short pulselength data.

Fig. 14. Measured scattered average intensities of long pulses at 19.5 kHz (circles) versus depression angle. The solid line represents a numerical evaluation of $I_s(\beta)$ using the scattering strength curve of Fig. 13. The bars represent the extreme range of ± 1.0 LSD about all of the observations. Note: $I_0 = 1$.

Fig. 15. Measured scattered average intensities of long pulses at 39.0 kHz using the 19.5-kHz scattering strength curve of Fig. 2. The bars represent the extreme range of ± 1.0 LSD about all of the observations. Note: $I_0 = 1$.

Fig. 2A1. Geometry for calculating the normalized incident power at unit distance.

Chapter 3

Chapter 4

Fig. 4. Scattering strength in the specular plane (± 10 ° in azimuth).

Fig. 5. Logarithmic standard deviation of the average values in Fig. 4f.

Fig. 6. Scattering strength in the upper half space for an incident grazing angle of 19.7°. The field is assumed symmetrical on either side of the specular plane. (The specular plane is perpendicular to the page along the lower edge of the plot; Fig. 4a is a side view of this plane.) The incident angle is marked with an ×, and the center of the scattering area is directly beneath the pole. The blank 10°-step areas are due to missing values.

Fig. 7. Scattering strength in the upper half space for an incident grazing angle of 32.4°.

Fig. 8. Scattering strength in the upper half space for an incident grazing angle of 46.4°.

Fig. 9. Scattering strength in the upper half space for an incident grazing angle of 60.8°.

Fig. 10. Scattering strength in the upper half space for an incident grazing angle of 70.5°.

Fig. 11. Computed ratio of scattered to incident power as a function of the incident angle.

Fig. 12. Three-dimensional model of the scattered field for an incident grazing angle of 70.5°. The incident and specular directions are indicated by the wires.

Fig. 4B1. Sonar ranges (obtained automatically every 10 sec) and periscope bearing α to the ship (manually recorded every minute).

Fig. 4B2. Horizontal ranges (identified in Fig. B1) versus time for run 11. The curves are plotter readouts of the original data on paper tapes, except for some points originally missing and subsequently filled in.

Chapter 5

Fig. 1. Bistatic scattering geometry

Fig. 2. Operating areas

Fig. 3a. Scattering strength S for a depression angle of 90° in operating area 1 (mud-coral bottom)

Fig. 3b. Scattering strength S for a depression angle of 70° in operating area 1 (mud-coral bottom)

Fig. 3c. Scattering strength S for a depression angle of 45° in operating area 1 (mud-coral bottom)

Fig. 3d. Scattering strength S for a depression angle of 30° in operating area 1 (mud-coral bottom)

Fig. 4a. Scattering strength S for a depression angle of 90° in operating area 2 (ooze bottom)

Fig. 4b. Scattering strength S for a depression angle of 70° in operating area 2 (ooze bottom)

Fig. 4c. Scattering strength S for a depression angle of 60° in operating area 2 (ooze bottom)

Fig. 4d. Scattering strength S for a depression angle of 45° in operating area 2 (ooze bottom)

Fig. 5. Scattering strength S for a depression angle of 90° in operating area 3 (mud-coral bottom)

Fig. 6. Lambert's-law fit of the measured scattering strength S of the scatter field (mud and coral bottom), with the fit being made at the normal-incidence (90°) monostatic point

Fig. 7. Results of an analysis of a two-layer model (water and bottom), with a water depth of 1400 m, a water gradient of -0.02 sec^{-1}, and a bottom gradient of $+10.2$ sec^{-1}

Fig. 5A1. Profile of the average measured temperature (left) and profile of the computed average sound speed (right) for the experiment

Fig. 5A2. Absorption of 20-kHz sound as a function of water temperature (left) and profile of the average absorption over a path to depth d

Chapter 6

Fig. 1. General geometry for volume scattering.

Fig. 2. Volume of integration for monostatic scattering.

Fig. 3. Measured beam function squared, at 19.5 kHz.

Fig. 4. Received intensity as a function of time.

Fig. 5. Location of the scatter volume.

Fig. 6. Typical scattering-strength profile. This profile was obtained at 0222 hours in the Blake Plateau area with $\beta = 45°$ and pulse length $\tau = 30$ msec.

Fig. 7. Composite of six scattering-strength profiles. These profiles were obtained at 0220 to 0225 hours in the Blake Plateau area with $\beta = 45°$ and pulse lengths τ from 15 to 60 msec.

Fig. 8. Scattering-strength profiles obtained at 2330 hours in the Cape Hatteras area with two pulse lengths and $\beta = 90°$.

Fig. 9. Comparison of two scattering-strength profiles taken at different times of day in the Blake Plateau area.

Fig. 1. Low-frequency propagation experiment.

Fig. 2a. Ship's track for the two Atlantic experiments.

Fig. 2b. Ship's track for the Pacific experiment.

Fig. 3. Four classes of sound-speed profiles found (Guthrie et al., 1974).

Fig. 4. Bathymetry and sound channels, where A is the subsurface-channel axis, B is the bottom of the subsurface channel, C is the SOFAR-channel axis, and D is the limit of the depth excess (Guthrie et al., 1974).

Fig. 5. Graphic recordings of the received CW acoustic pressure (Guthrie et al., 1974): (a) 13.89-Hz signal starting at 1394 km, (b) 111.1-Hz signal starting at 1394 km, (c) 13.89-Hz signal starting at 2744 km, and (d) 111.1-Hz signal starting at 2744 km.

Fig. 6. Acoustic transmissiom loss (TL) versus range (Guthrie et al., 1974): (a) 13.89-Hz TL, (b) 13.89-Hz TL for the received intensity averaged over 7 km, (c) 111.1-Hz TL, and (d) 111.1-Hz TL for the received intensity averaged over 7 km.

Fig. 7. Acoustic transmission loss versus range. This figure is the section of Fig. 6 between 400 and 1000 km plotted on an expanded range scale. The arrows show the shift in range between corresponding high- and low-frequency convergence zones.

Fig. 8. Interference-wavelength spectrum of signal powers.

Fig. 9. Ship's track in May 1974.

Fig. 10. Sample segment of data showing the smoothed and residual pressure amplitude curves, the residual distribution function (DF), the density histogram, the autocorrelation functions (ACF), and the sample statistics.

Fig. 11. Various statistics as a function of range or range rate, for a 1-hour smoothing time.

Fig. 12. Various statistics as a function of range or range rate, for a 3-hour smoothing time.

Fig. 13. Linear trends in the statistics as a function of range for the high-frequency 3-hour smoothing (H3), the high-frequency 1-hour smoothing (H1), and the low-frequency 3-hour smoothing (L3).

Fig. 14. Normalized density functions and correlation plots of the statistics for the low-frequency 3-hour smoothing

Fig. 15. Normalized density functions and correlation plots of the statistics for high-frequency (a) 3-hour smoothing and (b) 1-hour smoothing.

Fig. 16. Density functions for the residual signal amplitude as predicted using the fluctuation model. These functions are most often Rayleigh shaped (a) but may have a "cocked hat" appearance (b).

Fig. 17. Statistics for a 9.8-Hz signal. The open circles represent measured data, and the crosses represent values generated using a normal-mode-propagation model. (For this range segment the coefficient of variation appears to be increasing with range. When the coefficient is plotted for the complete range, a decrease with range is clear.)

Fig. 18. Aligned shot signatures. (Fitzgerald et al. 1974).

Fig. 19. Abstract of aligned shot signatures. (Fitzgerald et al. 1974).

Fig. 20. Details of shot signatures in region 1. Arrival classes are numbered. (Fitzgerald et al. 1974).

Fig. 21. Details of shot signatures in region 2. (Fitzgerald et al. 1974).

Fig. 22. Details of shot signatures in regions 3 and 4. (Fitzgerald et al. 1974).

Fig. 23. Evolution of a ray class as the range increases.

Chapter 8

Fig. 1. Sound-speed profile used in ocean model computations.

Fig. 2. Transmission loss as a function of range, with the top plot being the sum of the first 20 modes, the middle plot being SOFAR modes 1 through 16, and the bottom plot being RSR modes 17 through 20.

Fig. 3. Calculated amplitudes and beat frequencies of the received signals for the first 20 modes when the transmitted frequency is 13.8889 Hz and the source speed toward the receiver is 3.60 m/sec. Shown at the top left is the frequency-difference scale or beat-frequency scale.

Fig. 4a. Bilinear sound-speed profile and the locations of isointensity calculations of the interference field.

Fig. 4b. Isointensity field for the section in Fig. 4a between 50 and 100 km in range and 800 and 1400 m in depth.

Fig. 4c. Isointensity field for the section between 1200 and 1250 km in range and 800 and 1400 m in depth.

Fig. 5. Amplitude levels of the received signal in the Lloyd-mirror case (source or receiver moving at a fixed depth, with other being deeper) as a function of the source-to-receiver range.

Fig. 6. Isointensity contours of an interference field.

Fig. 7a. Sound-speed profiles and the location of the calculated intensity field.

Fig. 7b. Transmission loss between 450 and 625 km at a depth of 1000 m and a frequency of 14 Hz.

Fig. 7c. Isointensity contours in the section designated in Fig. 7a calculated for 14 Hz using the sound-speed profile indicated.

Fig. 7d. Isointensity contours in the section designated in Fig. 7a calculated for 14 Hz using the sound-speed profile indicated.

Fig. 7e. Superposition of Figs. 7c and 7d, shifted as indicated by the arrows at the bottom to emphasize the similarity of the patterns.

Fig. 7f. Isointensity contours in the section designated in Fig. 7a calculated for 14 Hz using the sound-speed profile indicated.

Fig. 7g. Superpostion of Figs. 7c and 7f.

Fig. 8. Mean sound speed and perturbation envelope (from Mooers (1975)) in the case of a 100-m-amplitude internal tide.

Fig. 9. Truncated parabolic profile used in simulating an Atlantic internal tide, given by: $C(z) = C_0 (1 - \alpha^2 z^2)^{-1/2}$, where $\alpha = h^{-1} [1 - (C_0/C_1)^2]^{1/2}$ and $|z| < h$, and, at the right, the acoustic geometry. The values for the calculations were $h = 1200$ m, $C_1 = 1544.63$ m/sec, $C_0 = 1489.55$ m/sec, and $\Delta C_0 = 0.196$ m/sec.

Fig. 10. Variation of the amplitude (b) and phase (c) from calculations simulating an Atlantic internal tide.

Fig. 11. Pattern of the pressure field (a) and the particle-velocity (b) in an interference field.

APPENDIX A

Fig. A1. Platform configuration.

Fig. A2. Signal instrumentation in *Grouper*.

Fig. A3. Signal instrumentation in *Rockville*.

Fig. A4. Geometry instrumentation in *Grouper*.

Fig. A5. Geometry instrumentation in *Rockville*.

Fig. A6. Experiment geometry.

Fig. A7(a). Run type A.

Fig. A7(b). Run type B.

Fig. A7(c). Run type C.

Fig. A7(d). Run type D.

Fig. A7(e). Run type E.

Fig. A8. Operating areas: Blake Plateau (rectangle) and Hatteras (small circle).

Fig. A9. Environmental profiles.

Fig. A10. Ray geometry.

Fig. A11. Absorption profile.

ACKNOWLEDGMENTS

As discussed earlier, ocean acoustic research requires the effort of an integrated team of scientists and technicians. It was the author's good fortune to lead the dedicated and competent team of scientists that conducted the experiments, analyzed the data, and developed the theory on the research contained in this work. The following are members of this team that evolved from the early 1960s through the 1970s: H. U. Criss, J. A. Desanto, R. H. Ferris, R. M. Fitzgerald, K. D. Flowers, G. Frisk, A. N. Guthrie, R. M. Lee, D. A. Nutile, D. Ramsdale, J. D. Shaffer, K. P. Thompson, and E. L. Wright. Their outstanding cooperation and contributions are gratefully acknowledged. The full support and encouragement of the Naval Research Laboratory and its staff in this work is also acknowledged.

With pleasure I gratefully acknowledge Mrs. Ann Grant for her typing and proofing efforts in preparing the work, Mrs. Dora Wilbanks in the preparation and formating, and Irene Jewett for her contributions to the illustrations. Special thanks are reserved for David Triantos for his editorial comments.

I am particularly indebted to my wife, Edith, for her advice, encouragement, and support which has been the basis for the existence of this work.

A debt of gratitude is owed to K. D. Flowers for his scientific critique and helpful comments on this research and to K. Attenborough and M. J. Buckingham, my internal and external advisors for their encouragement, guidance, and scientific wisdom in the preparation of this work. I thank B. K. Gazey and C. H. Harrison, my examiners for their interest and efforts. I greatly appreciate the Open University and its faculty's consideration of this work for the Degree of Doctor of Philosophy.

CONCLUDING NOTE

To: Dr. Keith Attenborough
Dr. Michael J. Buckingham
Dr. Brian K. Gazey
Dr. Christopher H. Harrison

Gentlemen:

It is my fervent hope that having read this thesis you will *not* be of a mind to reply as did Dr. Samuel Johnson to an aspiring writer:

> "Dear Sir:
>
> I have read your manuscript. It is both good and original. The trouble with it, however, is the part that's good is not original. And the part that's original is not good."

With my gratitude for your patience and consideration.

Respectfully yours,

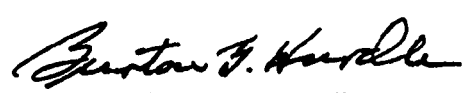

Burton G. Hurdle